

7-10-2012

# Advances in Rock Fabric Quantification and the Reconstruction of Progressive Dike Replacement in the Coastal Batholith of Central Chile

Jeffrey R. Webber  
*University of Vermont*

Follow this and additional works at: <http://scholarworks.uvm.edu/graddis>

---

## Recommended Citation

Webber, Jeffrey R., "Advances in Rock Fabric Quantification and the Reconstruction of Progressive Dike Replacement in the Coastal Batholith of Central Chile" (2012). *Graduate College Dissertations and Theses*. Paper 238.

This Thesis is brought to you for free and open access by the Dissertations and Theses at ScholarWorks @ UVM. It has been accepted for inclusion in Graduate College Dissertations and Theses by an authorized administrator of ScholarWorks @ UVM. For more information, please contact [donna.omalley@uvm.edu](mailto:donna.omalley@uvm.edu).

**ADVANCES IN ROCK FABRIC  
QUANTIFICATION AND THE  
RECONSTRUCTION OF PROGRESSIVE DIKE  
EMPLACEMENT IN THE COASTAL  
BATHOLITH OF CENTRAL CHILE**

A Thesis Presented

by

Jeffrey R. Webber

to

The Faculty of the Graduate College

of

The University of Vermont

In Partial Fulfillment of the Requirements  
for the Degree of Master of Science  
Specializing in Geology

October, 2012

# Abstract

The Coastal Batholith of central Chile preserves structures that record the concentration, migration, transportation, and emplacement of magma during the progressive construction of a sheeted dike complex. This sheeted dike complex is divided into three main structural-geographic domains. The northwestern domain contains an abundance of deformed microgranitoid enclaves that host features that facilitated the concentration of melt during crystallization. The formation of interconnected dilational sites produced an array of leocratic zones that may have formed larger dike networks that facilitated the transportation of melt-rich magma producing new magmatic units of similar mineralogy. The central domain is characterized by the presence of two tonalitic units that contain enclave swarms distinguished by their general packing arrangement and degree of elongation. Differences in the fabric architecture of these enclave swarms are displayed by two separate three-dimensional fabric analyses using the  $R_f/\phi$  method, which indicates an abrupt transition from low-distortion oblate fabrics to more distorted prolate geometries. These changes are compared to the statistical alignment of feldspar phenocrysts that indicate general flattening in both units with a higher degree of alignment within the XZ fabric plane for the younger tonalite. The third (southeastern) domain is distinguished by meter-scale, compositionally and texturally diverse sheeted dikes intercalated with biotite-rich migmatite screens of the host gneiss along the pluton margin.

The need to process large quantities of fabric data from central Chile presented the opportunity to establish a comprehensive method for the quantification of three-dimensional rock fabrics following the  $R_f/\phi$  and Fry methods. In order to test the utility of this procedure, a three-dimensional synthetic model of known strain shape, magnitude, and orientation was processed. The results of this assessment indicate that the procedure accurately calculated the expected state of strain within a small margin of error. Finally, a natural example is presented to test the method's ability to quantify the fabrics of deformed rocks. This example is a "lineation much greater than foliation" ( $L \gg S$ ) metagranite augen gneiss from the Coastal Batholith of central Chile. This analysis resulted in calculated fabric ellipsoids from both the  $R_f/\phi$  and Fry methods that clearly display significantly prolate geometries at moderate distortions.

The development of the three-dimensional rock fabric quantification procedure highlighted the need to teach analytical strain techniques in three-dimensions. To allow for this application, an interactive R script (FRY3D) was created specifically to aid in the instruction and visualization of three-dimensional strain calculation at the advanced undergraduate and graduate levels. This tutorial was presented to a structural geology course of 20 students at the undergraduate level with a two part semi-quantitative concept assessment before and after the presentation. The results of this assessment indicate a positive increase in student's understanding of three-dimensional finite strain.

Finally, a simple examination of analytical error associated with the Panozzo projection technique for strain analysis is presented and indicates relationships among population size, strain magnitude, and initial fabric. My results suggest that this method is most robust when applied to sections containing greater than approximately 125 lines. Moreover, the magnitude-dependent error indicates that the method may be better suited for rocks deformed at low to moderate strains. I recommend an adaption to the initial conditional assumptions for this method that lines exhibit an initial radial symmetry when recentered to a common point.

# Dedication

The patient Earth amassed documents and inscribed them with signs and pictures, which lay unnoticed and unused. Today, at last, they are waking up, because man has come to rouse them. Stones have begun to speak, because an ear is there to hear them. Layers become history and, released from the enchanted sleep of eternity, life's motley, never-ending dance rises out of the black depths of the past into the light of the present.

-Hans Cloos

This is for my family, for they know exactly who I am.

# Acknowledgments

This thesis is but a small representation of the thoughts and passions provided to me by an innumerable and eclectic population of individuals. As such, I cannot possibly acknowledge the roles of everyone that have influenced the culmination of this document. Nevertheless, I hold each of you in kind thoughts and truly appreciate all that has been done. Please understand, that although I may have personally typed the words of this thesis, you began writing this document many years ago.

I am truly grateful for the mentoring of my advisor Dr. Keith A. Klepeis, without whom, none of the progress of the previous years would have been possible. You have helped me through many trials, pushed me when I needed pushing, and accepted my faults as lessons yet to be learned. I am also grateful for the expertise and humor of Dr. Laura E. Webb and Gabriela Mora-Klepeis. This research was made possible by several collaborators; namely José Cembrano, Diego Morata, and Gloria Arancibia who graciously helped with a plethora of logistical nuances and showed us many of the critical features described herein. Inspiration to pursue computational applications was cultivated by Dr. Christian “*Le Lion Couchant*” Skalka during days spent in the Adirondacks and Green mountains.

I am indebted to Dr. Thomas J. Kalakay for the advice, guidance, and passion he has given during the past seven years. Without these qualities I would never have understood the limitless depth of history recorded within the mountains of Montana, and indeed, throughout the world. I am also grateful to several individuals at Montana

State University that furthered this passion and guided me as an undergraduate. As such, I would like to specifically thank Dr. David W. Mogk, Dr. David R. Lageson, and Dr. Colin A. Shaw, you all have taught me more than you realize.

I wish to acknowledge the individuals who struggled throughout these years along with me. To all of my peers: may we once again enjoy the satisfaction of a cold pint after a hard fought test, presentation, or stint in the field; may we all find peace in the simple tasks of the day and the honor of a job well done. To all of my students who accepted my teaching style as one of mutual learning, I thank you. It is with this synergistic combination of individuals comprising the Department of Geology at The University of Vermont that a productive environment is created. May you all continue to work together despite the obstacles that undoubtedly lie ahead. Finally, I am grateful for the financial support awarded by the *National Science Foundation* to Keith Klepeis (EAR 0635940) and to The University of Vermont Ronald Suiter Prize for travel support.

-Thank you

# Table of Contents

Contents	Page
Dedication . . . . .	iii
Acknowledgments . . . . .	iv
List of Figures . . . . .	xv
List of Tables . . . . .	xvii
Preface . . . . .	xviii
<b>1 Comprehensive Literature Review . . . . .</b>	<b>1</b>
1.1 Tectonic synthesis of Chile . . . . .	1
1.1.1 Rodinia . . . . .	2
1.1.2 Pampean tectonic cycle . . . . .	5
1.1.3 Famatinian tectonic cycle . . . . .	5
1.1.4 Gondwana tectonic cycle . . . . .	6
1.1.5 Pre-Andean tectonic cycle . . . . .	6
1.1.6 Andean tectonic cycle . . . . .	6
1.2 Quantification of rock fabric . . . . .	7
1.2.1 The $R_f/\phi$ method . . . . .	8
1.2.2 The Fry method . . . . .	11
1.2.3 Additional techniques . . . . .	13
1.2.3.1 Sanderson and Panozzo projection method . . . . .	13
1.2.3.2 DTNNM (triangulation method) . . . . .	15
1.2.3.3 The intercept method . . . . .	16
References . . . . .	19
<b>2 Reconstruction of progressive dike emplacement in the Coastal   Batholith, central Chile . . . . .</b>	<b>24</b>
2.1 Introduction . . . . .	25
2.2 Background . . . . .	27
2.2.1 Geologic framework . . . . .	27

2.2.2	Magmatic processes . . . . .	30
2.3	Observations of host rock . . . . .	37
2.4	Pluton divisions . . . . .	38
2.4.1	Northwestern domain . . . . .	39
2.4.1.1	Enclave textures . . . . .	39
2.4.1.2	Enclave structures . . . . .	40
2.4.1.3	Leucocratic dikes . . . . .	44
2.4.2	Central domain . . . . .	46
2.4.2.1	Field-based observations . . . . .	47
2.4.2.2	Enclave swarm architecture . . . . .	48
2.4.2.3	Mineral alignment . . . . .	53
2.4.3	Southeastern domain . . . . .	56
2.5	Discussion . . . . .	56
2.6	Conclusions . . . . .	63
	References . . . . .	66
<b>3</b>	<b>A methodology for the quantification and visualization of deformed rock fabrics within the statistical computing environment R . . .</b>	<b>72</b>
3.1	Introduction . . . . .	73
3.2	Methodology . . . . .	74
3.2.1	Data collection and extraction . . . . .	74
3.2.2	Sectional analyses . . . . .	75
3.2.3	Ellipsoid synthesis . . . . .	76
3.2.4	Visualization and presentation . . . . .	76
3.3	Synthetic analysis . . . . .	77
3.3.1	Model construction . . . . .	77
3.3.2	Results . . . . .	82
3.4	Application to a naturally deformed example . . . . .	87
3.4.1	Background . . . . .	87
3.4.2	Results . . . . .	89
3.5	Discussion and conclusions . . . . .	94
	References . . . . .	97
<b>4</b>	<b>FRY3D: an interactive R script for the visualization of rock fabrics in three-dimensions . . . . .</b>	<b>100</b>
4.1	Introduction . . . . .	101
4.2	Methodology . . . . .	103
4.3	Qualitative evaluation . . . . .	106
4.3.1	Evaluation setup . . . . .	106
4.4	Conclusions . . . . .	108
	References . . . . .	118



<b>5</b>	<b>Error evaluation of the Panozzo projection method for strain analysis (short note)</b>	<b>119</b>
5.1	Introduction	119
5.2	Methodology	121
5.2.1	General procedure	121
5.2.2	Statistical setup	123
5.3	Results	124
5.3.1	Least-squares ellipse fitting	124
5.3.2	Population size and strain magnitude errors	125
5.4	Conclusions and summary	127
	References	129
	<b>Comprehensive reference list</b>	<b>132</b>
<b>A</b>	<b>Additional field data</b>	<b>144</b>
A.1	Sample information	144
A.2	Las Cruces mylonites	145
A.3	Structure orientations	150
<b>B</b>	<b>Fabric quantification</b>	<b>162</b>
B.1	Preface	162
B.2	Getting Started	163
B.2.1	Understanding the manual	163
B.2.2	Requirements	165
B.2.3	Establishing the computer environment	166
B.2.4	Software	167
B.2.4.1	R: Statistical Computing	169
B.2.4.2	Graphics programs	171
B.2.4.3	Analytical software	172
B.3	Parameter extraction	172
B.3.1	Preparing the data	172
B.3.2	Digitization	174
B.3.3	Raster requirements	177
B.3.4	SAPE	178
B.4	Analytical methods	180
B.4.1	Setup	180
B.4.2	$R_f/\phi$ technique	182
B.4.2.1	Mulchrone and Meere 2001 method	182
B.4.2.2	Chew 2003 method	182
B.4.3	Fry method	185
B.4.4	Data Compilation	186
B.5	Ellipsoid construction	188
B.5.1	Ellipsoid	188

B.5.2	Visualization . . . . .	189
B.5.3	Quantifying shape and magnitude . . . . .	193
B.6	Data Collection . . . . .	199
B.6.1	Manual field measurement . . . . .	199
B.6.1.1	Manual $R_f/\phi$ data . . . . .	199
B.6.1.2	Manual Fry data . . . . .	201
B.6.2	Standardized photographs . . . . .	202
B.6.3	Scanned slabs . . . . .	204
B.6.4	Fabric from thin sections . . . . .	209
B.7	Concluding remarks . . . . .	211
<b>C</b>	<b>FRY3D user guide . . . . .</b>	<b>214</b>
C.1	Preface . . . . .	214
C.2	Getting Started . . . . .	215
C.2.1	R: Statistical Computing . . . . .	215
C.2.2	Tutorial scripts and data . . . . .	218
C.3	Operating procedure . . . . .	221
C.3.1	Concluding remarks . . . . .	228
<b>D</b>	<b>Three-dimensional synthetic model . . . . .</b>	<b>230</b>
D.1	Introduction . . . . .	230
D.2	Construction procedure . . . . .	231
D.3	Sectional tiles . . . . .	232
<b>E</b>	<b>R Scripts . . . . .</b>	<b>244</b>
E.1	Fry data setup and conversion . . . . .	244
E.2	$R_f/\phi$ data setup and conversion . . . . .	246
E.3	Standardized Fry plot . . . . .	247
E.4	Standardized $R_f/\phi$ plot . . . . .	251
E.5	Ellipsoid to Blender conversion (Fry) . . . . .	255
E.6	Ellipsoid to Blender conversion ( $R_f/\phi$ ) . . . . .	256
E.7	SYNTHETIC_P1 . . . . .	257
E.8	SYNTHETIC_P2 . . . . .	258
E.9	VT_P1 . . . . .	258
E.10	VT_P2 . . . . .	259
E.11	StructR functions . . . . .	259
E.12	Panozzo functions . . . . .	264
<b>F</b>	<b>Digital materials . . . . .</b>	<b>268</b>

# List of Figures

Figures	Page
1.1 Schematic cross section illustrating the tectonic evolution of South America. 1.) Formation of Rodinia (~1.0 Ga). 2.) Break up of Rodinia / Pannotia and the formation of the Iapetus and Puncoviscan oceans (~550 Ma). 3.) Closure of the Puncoviscan ocean with oceanic subduction beneath Gondwana (Pampean tectonic cycle ~540 Ma) 4.) Collision of the Pampean terrane and the formation of the Pampean mobile belt (~525 Ma). 5.) Closure of the Iapetus ocean with renewed subduction beneath Gondwana during the Famatinian tectonic cycle (490–470 Ma). 6.) Docking of the Precordillera terrane and subduction of the Proto-Pacific Ocean (430–390 Ma). 7.) Continued accretion of western terrains (e.g. Chilenia) with eastward directed subduction and the progression of the Gondwana, Pre-Andean and Andean Tectonic cycles (~390 through modern times). Modified from Loewy et al. (2004); Rapela et al. (1998); Durand (1996); Astini et al. (1995); Charrier et al. (2007). . . . .	2
1.2 A.) Global tectonic reconstruction of the major components of Rodinia. B.) Terranes of South America modified from Dalziel et al. (1994) and Ramos (2009). Those with Proterozoic affinities are shaded in dark gray.	4
2.1 Geologic overview map of the Andean coastal range in central Chile. Modified from SERNAGEOMIN (2002) and Wall et al. (1996). . . . .	32
2.2 Generalized geologic map of coastal exposures between Isla Negra and El Tabo. Stereographic projection contains data from region shown in map obtained in this study. Map lithologies and extent modified from Siña (1987). Mineral SPO relates to the shape preferred orientation of minerals within the outcrop. . . . .	34
2.3 Schematic cross-section illustrating the general architecture of magmatic phases and structures developed between Isla Negra and El Tabo. See Figure 2.2 for line of section (A-A'). . . . .	36
2.4 Basic enclave classification based on textures. The field of view in each photograph is 15 cm. . . . .	41

2.5	Photograph and sketch of folded enclaves with leucosome concentrated in fold hinges. Notebook width is $\sim 19$ cm. The finite strain axes are inferred and shown with black arrows. . . . .	42
2.6	Photograph and sketch of fractured enclaves with leucosome concentrated in an echelon tension gashes. Notebook width is $\sim 19$ cm. The finite strain axes are inferred and shown with black arrows. Tonalite is distinguished from leucosome by color and an increase in felsic minerals. Note that the shearband boudinage is defined by the small relative arrow symbol. . . . .	43
2.7	Photograph and sketch of boudinaged enclave with leucosome concentrated in boudin necks. Coin is roughly 2.5 cm in diameter. Section of view is roughly parallel to magmatic foliation The finite strain axes are inferred and shown with black arrows.. . . .	44
2.8	Photograph and sketch of partially dismembered xenolith with leucosome concentrated in strain shadows. Length of pen cap is approximately 3 cm. The finite strain axes are inferred and shown with black arrows. Gray arrows define inferred pressure gradient trajectories that illustrate the flow of melt prior to complete crystallization. . . . .	45
2.9	Photograph and sketch of a concentrated leucosome in diffuse undulating zones. Notebook length is $\sim 19$ cm. . . . .	46
2.10	Photograph and sketch of an overpressurized leucosome domain with a tapered proto-dike apophysis (likely representing the initial stage of dike formation) extending into background. Notebook length is $\sim 19$ cm. . . . .	47
2.11	Photograph and sketch of location 11-IN-01 (see Figure 2.2) illustrating two distinct tonalite phases. Enclave swarm fabrics are distinctive between the older northwest unit and the younger southeast phase, as explained in the text. . . . .	49
2.12	Sectional $R_f/\phi$ results from the northwestern unit at location 11-IN-01. Analyses “A”, “B”, and “C” correspond to the three mutually perpendicular principle fabric planes describe in Table 2.1. . . . .	51
2.13	Sectional $R_f/\phi$ results from the southeastern unit at location 11-IN-01. Analyses “A”, “B”, and “C” correspond to the three mutually perpendicular principle fabric planes describe in Table 2.1. . . . .	52
2.14	Rendered image of oriented fabric ellipsoids from the northwestern (A) and southeastern (B) units at 11-IN-01 corresponding to oblate and prolate fabric symmetries. Ellipsoids normalized to an equal volume. . . . .	53
2.15	A: equal area stereographic projection of principle fabric axes from two tonalitic sub-domains at 11-IN-01. B: Nadai plot illustrating the relationship between fabric symmetry ( $\nu$ ) and the octahedral shear fabric ( $\bar{\epsilon}_s$ ). . . . .	54

2.16	Normalized histograms of feldspar long axis orientations determined from two samples collected at location 11-IN-01 (see Figure 2.2). Individual plots correspond to the respective principle fabric plane and tonalitic unit. Histograms in upper row are from the northwestern enclave abundant tonalite unit shown in Figure 2.11. Lower plots are from the southeastern unit. The circular standard deviations (CSD) are displayed for each analysis. . . . .	55
2.17	Photograph and sketch of location 11-IN-03 (see Figure 2.2) illustrating the sheeted dike geometry of compositionally and texturally distinctive phases. . . . .	57
2.18	Schematic diagram displaying the general evolution of magmatic phases recorded within the igneous complex between Isla Negra and El Tabo. 1.) Incomplete interaction of compositionally distinctive magmas forming enclaves and schlieren. 2.) Rheological heterogeneities create dilational sites that concentrate melt during deformation of crystal rich mush. 3.) Small volumes of concentrated melt pool and become overpressurized causing diking. 4.) Dikes and melt rich domains become interconnected and increase in volume forming distinct magmatic phases and flow kinematics 5.) Magmatic phases emplace as dikes forming a composite sheeted pluton along margin with host rock. . . . .	64
3.1	Schematic diagram illustrating the construction of the synthetic dataset by scaling each principle plane proportionally about the axes defined in Table 3.1. . . . .	81
3.2	Figure highlighting the use of a camera frame device in collection of oriented and standardized digital images for error analysis of the fabric quantification procedure. Note that perspective foreshortening of XY-plane produces the appearance of a higher distortion than XZ, but is actually less than the XZ-plane. . . . .	83
3.3	Sectional $R_f/\phi$ results from the synthetic model. . . . .	84
3.4	Sectional Fry results from the synthetic model. . . . .	85
3.5	Comparison of fabric ellipsoid shapes and magnitudes obtained for the synthetic data test and expected results. . . . .	87
3.6	Comparison of orientation results from the synthetic data test. . . . .	88
3.7	Oriented sectional scans and traced objects of slabbed faces from 11-LC-03-C. The X-Z, X-Y, and Y-Z faces correspond to the non-genetic sectional nomenclature of A, B, C, respectively. . . . .	89
3.8	Sectional $R_f/\phi$ plots with normalized fitted ellipses from sample 11-LC-03-C. Abbreviations: s = index of symmetry; vm = vector mean; and hm = harmonic mean. . . . .	90
3.9	Sectional fry plots with normalized fitted ellipses. . . . .	91

3.10	Nadai plot displaying the theoretical octahedral shear strain ( $\bar{\epsilon}_s$ ) and Lode parameter $\nu$ for both $R_f/\phi$ and Fry methods. Rendered three-dimensional images correspond to the labeled points on the Nadai plot.	93
3.11	Equal area stereographic projections with measured fabric elements from the field (i.e. poles to gneissic foliations and gneissic mineral trace lineations) with the calculated principle fabric ellipsoid axes for the $R_f/\phi$ technique (left) and the Fry method (right). Great circles denote the calculated X-Y principle planes.	94
4.1	Cartoon illustrating the construction of the synthetic deformed conglomerate dataset accompanying the instructional tutorial. Part “A” denotes the two-dimensional strain ellipses for the principle planes of strain shown in “B” as constructed through constant volume deformation highlighted in “C.”	104
4.2	Screen images from the FRY3D tutorial depicting the two-dimensional strain analyses. A: object centroid selector tool. B: central void ellipse estimation.	105
4.3	Three-dimensional strain visualizers with an interactive Fry plot (A) and a modeled fitted strain ellipsoid.	106
4.4	Images from the FRY3D instructional tutorial highlighting the quantitative properties of the strain ellipsoid synthesis. A.) Equal-area lower-hemisphere stereographic projection of the principle strain axes; B: Nadai plot illustrating the Lode parameter and octahedral shear strain.	107
4.5	Results of the FRY3D evaluation compiled from a class of 20 students before and after the tutorial. Comprehension is divided into three qualitative categories with a “lacks substantial understanding” corresponding to the histogram bins on the left, “some concepts are developed but lack a comprehensive understanding” for the center bins, and “exhibits a comprehensive understanding of the nature of deformation in three-dimensions” on the right.	109
4.6	Schematic illustration highlighting the general procedure of the manual Fry method.	112
4.7	Deformed oolitic limestone: (Ramsay and Huber 1983, p. 112).	113
4.8	Plot the strain ellipse here and determine the properties listed above.	114
5.1	Plot of 150 undeformed (A) and deformed (B) synthetic lines centered at the plot origin. Initial dataset generated with a normal distribution of line lengths with a mean length of 25 units and a standard deviation of 6.25 that are rotated to create a uniform distribution of orientations. Undeformed data was subjected to a dextral shear strain ( $\gamma$ ) of one under homogeneous simple shear plane strain.	123

5.2	Panozzo projection results from line data presented in Figure 5.1. Polar plot of projected lengths based on one degree rotations defining an ellipse perimeter (A). Perimeter is statistically fitted with an ellipse (B) using a least-squares method from which the semi-major and semi-minor axial lengths are obtained. . . . .	124
5.3	A comparison of two different Panozzo $R_s$ methods involving: (A) the ratio of maximum to minimum projected line lengths; (B) the ratio of semi-major to semi-minor axial lengths of a least squares fitted ellipse. Differences in the two plots are indistinguishable. . . . .	125
5.4	Error associated with population size and strain magnitude. For each applied shear strain on a population size of 10 (A), 20 (B), 40 (C), 80 (D), 160 (E), and 320 (F). Thirty five initial datasets were generated with a normal distribution of line lengths and a uniform distribution of orientations. Applied shear strains ( $\gamma$ ) for each population size included 0.25 ( $R_s = 1.28$ ), 0.5 ( $R_s = 1.64$ ), 0.75 ( $R_s = 2.08$ ), 1 ( $R_s = 2.62$ ), 1.25 ( $R_s = 3.26$ ), 1.5 ( $R_s = 4$ ), 1.75 ( $R_s = 4.86$ ), 2 ( $R_s = 5.83$ ), 2.25 ( $R_s = 6.92$ ), 2.5 ( $R_s = 8.13$ ), 2.75 ( $R_s = 9.46$ ), and 3 ( $R_s = 10.91$ ). The thick black line in each plot forms a one to one relationship between the applied $R_s$ and the expected $R_s$ . Gray polygons display a two $\sigma$ confidence interval based on 35 analyses per applied deformation. Lower limits of confidence region is truncated by $R_s = 1$ in some plots (at lower population sizes). A total of 2,520 Panozzo projection analyses were used at a one degree rotation interval to construct the plots requiring a total of 264,600 lines. . . . .	127
5.5	Calculated $R_s$ versus applied $R_s$ on lines of initial radial symmetry and equal lengths. Gray line forms a one to one expected relationship. Note that this "radial symmetry" distribution does not consider translational line location and is not analogous to radial crystal growth habits. Points are plotted for applied shear strains of 0.25 ( $R_s = 1.28$ ), 0.5 ( $R_s = 1.64$ ), 0.75 ( $R_s = 2.08$ ), 1 ( $R_s = 2.62$ ), 1.25 ( $R_s = 3.26$ ), 1.5 ( $R_s = 4$ ), 1.75 ( $R_s = 4.86$ ), 2 ( $R_s = 5.83$ ), 2.25 ( $R_s = 6.92$ ), 2.5 ( $R_s = 8.13$ ), 2.75 ( $R_s = 9.46$ ), and 3 ( $R_s = 10.91$ ). . . . .	129
A.1	Mylonite plane solutions for discrete shear zones documented in augen gneiss near Las Cruces. . . . .	146
A.2	Composite mylonite plane solution derived from the measurements shown in Figure A.1. Solution suggests mylonite zones are compatible with general top to the north-north-east directed contraction. . .	148
B.1	Basic organizational description of the various components to the folder structure implemented in each three-dimensional analysis . . . . .	168
B.2	How to change the working directory for R. . . . .	170
B.3	Selecting a mirror to download R-packages. . . . .	194

B.4	Digitization of objects with Inkscape. . . . .	195
B.5	Difference between gray scale (A) objects and two color objects (B). . .	195
B.6	Manual inspection of fitted ellipses in SAPE. . . . .	196
B.7	R console output for the ELLIP2BLEND scripts. . . . .	196
B.8	Basic use of the Blender GUI. . . . .	197
B.9	R console display of the NADAI plotting utility. . . . .	198
B.10	Photographic Aperture Device for the collection of standardized digital images. . . . .	203
B.11	Basic table for collection of standardized photographic field data. . .	204
B.12	Scanned, oriented, and traced images for three mutually perpendicular faces on a deformed granite aguen gneiss. . . . .	210
B.13	The use of thin sections in a fabric analysis requires the documentation of the direction of sight in order for photomicrographs to be correctly oriented. . . . .	211
C.1	Selecting a mirror to download R-packages. . . . .	217
C.2	Folder structure and R scripts accompanying the manual. . . . .	219
C.3	Loaded R script from which the configuration parameters can be edited.	220
C.4	Centroid locator tool in new window of sectional data. . . . .	222
C.5	Central void apogee and perigee locator tool. . . . .	223
C.6	Three-dimensional Fry plot with sectional fabric ellipses. Lower view is zoomed in from upper plot. . . . .	225
C.7	Three-dimensional fitted ellipsoid calculated by the program Ellip- soid2003. . . . .	226
C.8	Nadai plot corresponding to the fitted fabric ellipsoid. . . . .	227
C.9	Stereographic projection of the principle fabric axes and XY plane for the fitted ellipsoid. . . . .	229
D.1	Sectional tile A of the XY principle plane of strain. . . . .	232
D.2	Sectional tile B of the XY principle plane of strain. . . . .	233
D.3	Sectional tile C of the XY principle plane of strain. . . . .	234
D.4	Sectional tile D of the XY principle plane of strain. . . . .	235
D.5	Sectional tile A of the XZ principle plane of strain. . . . .	236
D.6	Sectional tile B of the XZ principle plane of strain. . . . .	237
D.7	Sectional tile C of the XZ principle plane of strain. . . . .	238
D.8	Sectional tile D of the XZ principle plane of strain. . . . .	239
D.9	Sectional tile A of the YZ principle plane of strain. . . . .	240
D.10	Sectional tile B of the YZ principle plane of strain. . . . .	241
D.11	Sectional tile C of the YZ principle plane of strain. . . . .	242
D.12	Sectional tile D of the YZ principle plane of strain. . . . .	243



# List of Tables

Tables	Page
1.1 List of symbols used throughout the text as related to fabric quantification. . . . .	18
2.1 Analytical enclave section orientations vs fitted L-S fabric data. . . . .	50
3.1 Scale percentage values for the three principle strain axes used to produce the deformed synthetic dataset . . . . .	82
3.2 Relative differences between the results of the calculated sectional strain ratios and the expected values. . . . .	84
A.2 Overview of the primary geochronological constraints for the Isla Negra Igneous Complex. . . . .	149
A.3 Structural orientations from: 11-AS-01 . . . . .	150
A.3 Structural orientations from: 11-AS-01 . . . . .	151
A.3 Structural orientations from: 11-AS-01 . . . . .	152
A.4 Structural orientations from: 11-AS-02 . . . . .	152
A.5 Structural orientations from: 11-AS-03 . . . . .	152
A.5 Structural orientations from: 11-AS-03 . . . . .	153
A.6 Structural orientations from: 11-IN-01 . . . . .	153
A.6 Structural orientations from: 11-IN-01 . . . . .	154
A.7 Structural orientations from: 11-IN-02 . . . . .	154
A.7 Structural orientations from: 11-IN-02 . . . . .	155
A.8 Structural orientations from: 11-IN-03 . . . . .	155
A.9 Structural orientations from: 11-IN-04 . . . . .	155
A.9 Structural orientations from: 11-IN-04 . . . . .	156
A.10 Structural orientations from: 11-LC-01 . . . . .	156
A.11 Structural orientations from: 11-LC-02 . . . . .	156
A.11 Structural orientations from: 11-LC-02 . . . . .	157
A.12 Structural orientations from: 11-LC-03 . . . . .	158
A.12 Structural orientations from: 11-LC-03 . . . . .	159
A.13 Structural orientations from: 11-LC-04 . . . . .	159
A.14 Structural orientations from: 11-QT-01 . . . . .	159

A.14	Structural orientations from: 11-QT-01 . . . . .	160
A.15	Structural orientations from: 11-QT-02 . . . . .	160
A.15	Structural orientations from: 11-QT-02 . . . . .	161
B.1	List of available software resources used within the tutorial. . . . .	167
B.2	Required R Packages. . . . .	171
B.3	Example field data text file. Each field is separated with a tab character.	173
B.4	Basic file structure for a .sda file, columns from left to right in output file. . . . .	199
D.1	Sectional orientations following right hand rule convention to reorient a physical model of the synthetic dataset implemented in the FRY3D tutorial . . . . .	230

# Preface

This thesis is a combination of fabric analysis methodology, application, and education. Chapter one presents a general synopsis of previous work and background information pertaining to the tectonic evolution of South America, as well as several analytical strain techniques. In order to reduce redundancy I have simplified this chapter. The reference lists throughout the text provide more information. Chapter two forms the basis of a manuscript focused on the significance of mesoscopic structures developed within the Coastal Batholith of central Chile. This chapter is the foremost topic within my thesis and best captures the research completed during the past two years. Chapter three resulted from addressing obstacles in calculating three-dimensional fabrics from multiple data sources. The need for a comprehensive procedure outlining this method became evident once I was faced with the task of processing massive quantities of fabric data. Eventually I expanded the method to enable both  $R_f/\phi$  and Fry analyses, as well as the use of multiple data sources including photomicrographs, outcrop images, and scanned hand-samples. Through this process, I realized the inadequacy of two-dimensional fabric analysis and the need to better teach deformation in three-dimensions at the undergraduate level. As such, Chapter four was designed as a tutorial to help visualize the application of sectional strain analyses within a three-dimensional context. The final chapter presents a short note on the assessment of error in the Panozzo method that came about in the final days of writing. Although this thesis is complete, the ideas presented herein will remain a work in progress.

# Chapter 1

## Comprehensive Literature Review

### 1.1 Tectonic synthesis of Chile

The geologic history of South America is a product of plate tectonic processes that document episodes of continental amalgamation, accretion, rifting, and the development of a long lived oceanic-continental convergent margin (Fig. 1.1). This evolution follows the breakup of Rodinia and Pannotia (see definition in Finney et al. 2003 pg. 351), through the construction of Gondwana, and the ultimate formation of the South American continent. The following sections describe these tectonic phases in the context of the Coastal Batholith in central Chile, which is the focus of my research presented in Chapter 2. As such, they do not provide an exhaustive review of the tectonic evolution of South America, but rather, a select collection of generally distinct geologic events. This history begins with the Proterozoic configuration of Rodinia (and subsequently Pannotia) to provide the cratonic core of the modern South American continent. Following the breakup of Pannotia, two temporally distinct tectonic phases (Pampean and Famatinian) are described that document deformation, metamorphism, and accretion of domains with Laurentian affinities. These phases are succeeded by the development of a subduction related magmatic arc during the cul-

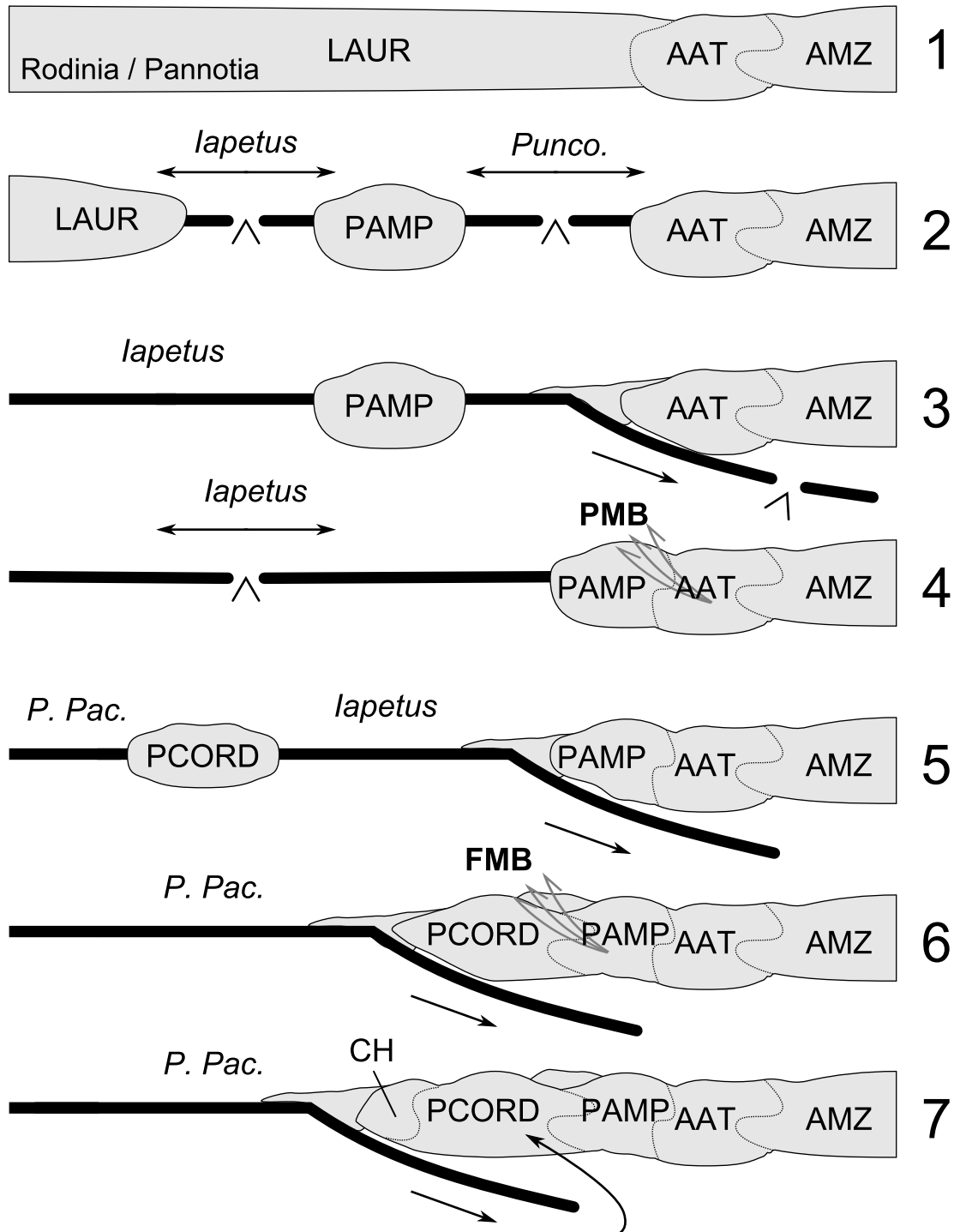
mination of Gondwana construction that ultimately produces the Coastal Batholith. Finally, two more cycles are described that lead to the rifting of Gondwana and the development of the modern Andean orogeny.

### 1.1.1 Rodinia

The existence of a late Proterozoic supercontinent has long been hypothesized since the proliferation of plate tectonic theory (Valentine and Moores 1970). This continent is now widely accepted as Rodinia and is believed to be one of only two supercontinents (the other being Pangaea) that included nearly all crustal fragments of continental lithosphere (see synthesis by Li et al. 2008). The formation of this supercontinent persisted for roughly 150 million years with the culmination of amalgamation at roughly 900 Ma. It is prior to this culmination that the initial history of Chile is recorded. The Arequipa-Antofalla Terrane, located in northern Chile, has commonly been ascribed to the Oclayic orogeny (Bahlburg and Hervé 1997) during the Famatinian tectonic cycle. However, Loewy et al. (2004) concluded that the Arequipa-Antofalla Terrane is a single basement block accreted to the Amazonian

---

Figure 1.1: Schematic cross section illustrating the tectonic evolution of South America. 1.) Formation of Rodinia ( $\sim 1.0$  Ga). 2.) Break up of Rodinia / Pannotia and the formation of the Iapetus and Puncoviscan oceans ( $\sim 550$  Ma). 3.) Closure of the Puncoviscan ocean with oceanic subduction beneath Gondwana (Pampean tectonic cycle  $\sim 540$  Ma) 4.) Collision of the Pampean terrane and the formation of the Pampean mobile belt ( $\sim 525$  Ma). 5.) Closure of the Iapetus ocean with renewed subduction beneath Gondwana during the Famatinian tectonic cycle (490–470 Ma). 6.) Docking of the Precordillera terrane and subduction of the Proto-Pacific Ocean (430–390 Ma). 7.) Continued accretion of western terrains (e.g. Chilenia) with eastward directed subduction and the progression of the Gondwana, Pre-Andean and Andean Tectonic cycles ( $\sim 390$  through modern times). Modified from Loewy et al. (2004); Rapela et al. (1998); Durand (1996); Astini et al. (1995); Charrier et al. (2007).



Formation of the Coastal Batholith

LAUR: Laurentia  
 AAT: Arequipa-Antofalla Terrane  
 AMZ: Amazonia  
 PAMP: Pampean Terrane  
 PCORD: Precordillera Terrane  
 CH: Chilenia and other western terranes

*Iapetus*: Southern Iapetus Ocean  
*Punco.*: Puncoviscan Ocean  
*P. Pac.*: Proto Pacific Ocean

**PMB**: Pampean Mobile Belt  
**FMB**: Famatinian Mobile Belt

craton during the Sunsás orogeny<sup>1</sup> (Fig. 1.1). This accretion occurred prior to both the Pampean and Famatinian tectonic cycles at approximately 1.05 Ga. Although this the only unequivocal Proterozoic terrane exposed in Chile, several other terranes and blocks throughout South America have been documented to contain Rodinian affinities (see review by Li et al. 2008). Figure 1.2 shows a simplified plate tectonic reconstruction of the of the Rodinia supercontinent (A) and the Proterozoic terranes, cratons, and blocks of South America (B), which places the Arequipa-Antofalla Terrane directly in between Laurentia and Amazonia (Fig. 1.1-1).

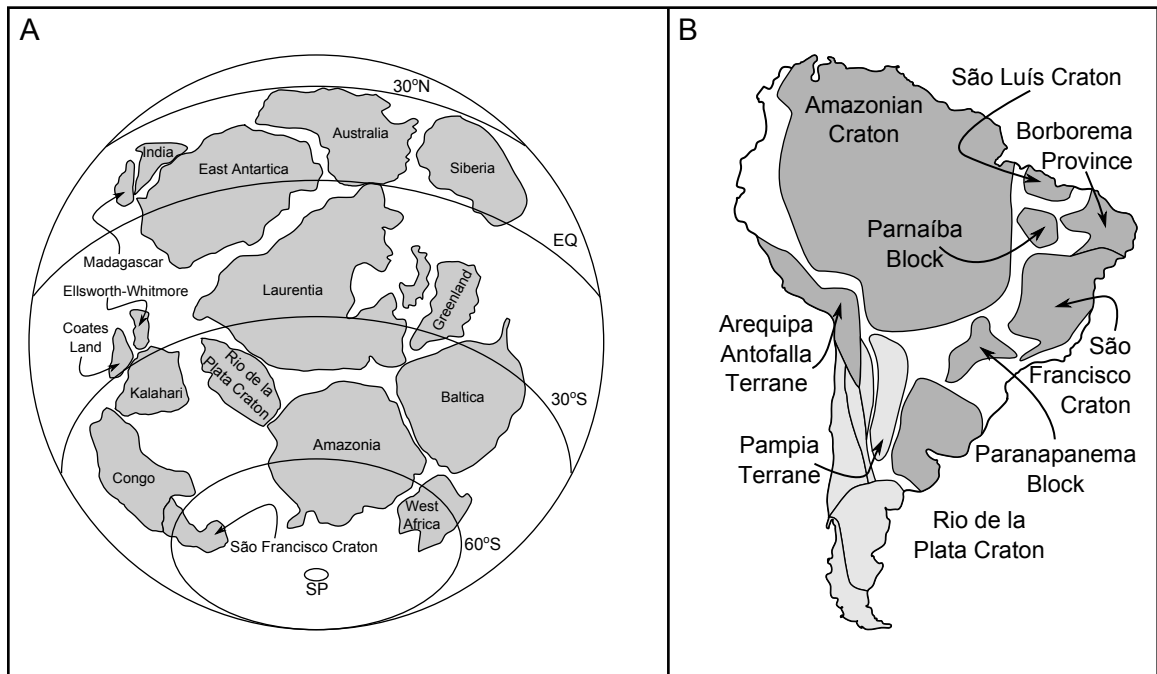


Figure 1.2: A.) Global tectonic reconstruction of the major components of Rodinia. B.) Terranes of South America modified from Dalziel et al. (1994) and Ramos (2009). Those with Proterozoic affinities are shaded in dark gray.

<sup>1</sup>Even this assertion made by Loewy et al. (2004) is in contrast to early suggestions for the origin of the Arequipa-Antofalla Terrane made by this group (Loewy) as interpreted by Murphy et al. (2004).

### **1.1.2 Pampean tectonic cycle**

The Pampean tectonic cycle occurred from the Early to Middle Cambrian (Rapela et al. 1998; Durand 1996) upon the initiation of subduction along the Gondwana margin and the closure of the Puncoviscan ocean (Fig. 1.1-2) (Dalziel 1997; Rapela et al. 1998). The beginning of this cycle is marked by the transition from a stable continental margin distinguished by the Puncoviscana Formation (Turner 1960; Do Campo and Guevara 2005) to one dominated by accretionary wedge deposits (Rapela et al. 1998) (Fig. 1.1-3). Furthermore, exposures of the Eastern Sierras Pampeanas contain a belt of I-type granitoids (Lira et al. 1997) dated at  $530 \pm 4$  Ma by Rapela et al. (1998) that is interpreted to represent a subduction related magmatic arc along the Gondwana margin (Fig. 1.1-3). Metamorphism and partial melting in this region dated at  $522 \pm 8$  Ma has been interpreted to represent the collision of a semiautochthonous terrane known as the Pampean Terrane (Rapela et al. 1998)(Fig. 1.1-4). Continued deformation of the Puncoviscana Formation is accompanied by a low pressure high temperature metamorphic event at ca. 520 Ma. speculated to represent ridge subduction processes (Piñán-Llamas and Simpson 2006).

### **1.1.3 Famatinian tectonic cycle**

The Famatinian tectonic cycle extends from the Late Cambrian to the Early Devonian and documents the restoration of subduction related magmatism (Pankhurst et al. 1998, and references therein) following the development of a passive margin after Pampean Terrane accretion. Furthermore, the latter portion of this tectonic cycle is dominated by the Ocoyic orogeny (Astini et al. 1995; Casquet et al. 2001; Astini and Dávila 2004; Thomas et al. 2002). This extensive contractional phase is associated with the docking of the Precodillera Terrane (equivalent to the Cuyania Terrane) now located in north western Argentina.



#### **1.1.4 Gondwana tectonic cycle**

The Late Paleozoic geologic evolution of Chile is defined as the Gondwana tectonic cycle and signifies the continental assembly of Gondwana (Charrier et al. 2007). This cycle establishes a paleogeographic environment typical of oceanic-continental convergent settings with an accretionary prism, forearc basin, magmatic arc, and a backarc basin situated from west to east. Voluminous intrusive rocks were emplaced throughout the Late Carboniferous and Permian times (Gana and Tosdal 1996) now exposed as the Coastal Batholith (Fig. 2.1) throughout the Coastal Cordillera (SER-NAGEOMIN 2002, and references therein).

#### **1.1.5 Pre-Andean tectonic cycle**

The temporary cessation of subduction along the western margin of Gondwana during the Late Permian to the Early Jurassic is distinguished as the Pre-Andean tectonic cycle (Charrier et al. 2007). The 55 million year long absence of orogenic magmatism (Charrier et al. 2007; Mpodozis and Cornejo 1988; Nasi et al. 1985; Coira et al. 1982) is believed to reflect the final assembly followed by the initial break up of Gondwana. During this tectonic cycle within the Triassic, numerous NNW-SSE trending extensional basins (Uliana and Biddle 1988; Mpodozis and Kay 1992) developed that record extensive silicic volcanic and plutonic activity interpreted to mark a transition from arc to intraplate magmatism (Llambías and Sato 1995) and possibly elevated heat flow associated with the supercontinent Pangea.

#### **1.1.6 Andean tectonic cycle**

The final, and currently active, tectonic cycle is denoted as the Andean tectonic cycle and initiated during the Late Jurassic at the recommencement of eastward directed subduction beneath Gondwana and South America. This tectonic setting forms the

archetypal oceanic-continent convergent margin (Dewey and Bird 1970). As such, this modern setting can provide a type locality to study subduction related processes. Variations along the western margin of South America with respect to volcanism (Thorpe and Francis 1979), earthquake distribution (Barazangi and Isacks 1976), subduction angle (Wortel 1984), and stress regime (Lavenu and Cembrano 1999) have long been established. Subduction angle is often invoked as the predominant tectonic control responsible for trench-normal deformation along oceanic-continental convergent margins (Coney and Reynolds 1977; Dickinson and Snyder 1978; Bird 1988). However, recent studies have established higher order processes affecting the structural regime of deformation within the overriding continental plate as a function of the nature of subducted oceanic crust (Cembrano et al. 2007; Yáñez and Cembrano 2004; English et al. 2003), trench sediment supply (Lamb and Davis 2003), and mantle delamination (Wells and Hoisch 2008). These factors likely control the deformation style of the Andean orogen that is characterized by short intervals of contractional deformation between longer periods of time dominated by extensional tectonics (Charrier et al. 2007).

## **1.2 Quantification of rock fabric**

The ability to quantify rock deformation in three-dimensions provides an incredible tool for geologists to address the kinematics of large crustal structures that may localize and de-localize deformation through time and space. The opening quote presented by Ramsay and Huber (1983) after Sorby (1908) states: “In the case of nearly all branches of science a great advance was made when accurate quantitative methods were used instead of more qualitative. One great advantage of this is that it necessitates more accurate thought, points out what remains to be learned, and sometimes small residual quantities, which otherwise would escape attention,

indicate important facts.” In the context of geology, the ability to identify the rotations of strain ellipsoids in a spatial context with gradients in both the octahedral shear strain and Lode parameter (explained later in text) can provide crucial information on crustal scale tectonic motions through time that are not reflected by local strain regimes obtained through the traditional use of asymmetric fabrics at a small scale. For example, it has been shown by several workers that rheologically competent lozenges enveloped within shear zones will produce conflicting kinematic indicators if the lozenge propagates through the shear zone much like a zipper (see for a conceptual model: Hudleston 1999). The following sections describe several methods in which deformational fabrics developed in rocks may be elucidated and applied to this large-scale approach.

### 1.2.1 The $R_f/\phi$ method

The  $R_f/\phi$  method<sup>2</sup> is an analytical strain technique that utilizes the mathematical relationship between the sectional orientations and ellipticities (for example plots refer to Figures: 2.12; 2.13; 3.3; and 3.8) of deformed ellipsoidal objects to calculate the two-dimensional magnitude and orientation of finite strain (Ramsay 1967; Dunnet 1969; Ramsay and Huber 1983; Lisle 1985). The primary assumptions of this method are threefold: deformation at the scale of analysis is homogeneous, the distributions of undeformed object orientations were originally uniform, and objects deform passively. This latter requirement can be corrected for if the properties of differing viscosity can be constrained following Lisle et al. (1983). Ramsay (1967) first presented the mathematical proof of this concept, which was then expanded on by Dunnet (1969). However, Lisle (1985) presented the first comprehensive manual for the application of the  $R_f/\phi$  method to deformed rocks and has since been widely

---

<sup>2</sup>For a complete list of symbols used in this thesis, refer to Table 1.1.

applied to a variety of geologic problems. In this section, I present the basic concepts of the  $R_f/\phi$  method and expand on recent software advances that allow for fast and accurate strain calculations.

A suite of elliptical markers will define a curve given by Equation 1.1 after a given amount of finite strain if the initial  $R_i$  values are equal and the initial orientations define a uniform distribution. Similarly, if the initial object orientations are held at a constant angle but contain a uniform distribution of initial ratios a curve is defined for a given magnitude of finite strain following Equations 1.2 and 1.3.

$$\phi = \left(\frac{1}{2}\right) \arccos \left( \frac{(R_f + 1/R_f) \times (R_s + 1/R_s) - 2 \times (R_i + 1/R_i)}{(R_f - 1/R_f) \times (R_s - 1/R_s)} \right) \quad (1.1)$$

$$\text{Where } \theta \neq \pm 45^\circ : R_f = \sqrt{\frac{\tan 2\theta \times (R_s^2 - \tan^2 \phi) - 2R_s \tan \phi}{\tan 2\theta \times (1 - R_s^2 \tan^2 \phi) - 2R_s \tan \phi}} \quad (1.2)$$

$$\text{Where } \theta = \pm 45^\circ : R_f = \sqrt{\frac{\tan^2 \phi - R_s^2}{R_s^2 \tan^2 \phi - 1}} \quad (1.3)$$

Therefore, a series of these curves can be constructed from each of the above equations for a given  $R_s$  value defining a range of  $R_i$  and  $\phi$  values respectively. These composite plots are known as deformation marker grids and are the traditional means for calculating the  $R_s$  value. The application of statistical software packages (Peach and Lisle 1979; Mulchrone and Meere 2001; Chew 2003) has allowed for the automation of  $R_s$  calculation by iteratively de-straining<sup>3</sup> an  $R_f/\phi$  dataset and calculating a  $\chi^2$  goodness of fit for a uniform distribution. The  $R_s$  used in Equations 1.1 and 1.2 that produces the lowest  $\chi^2$  value is inferred to represent the magnitude of finite tectonic

---

<sup>3</sup>Refer to Lisle 1985 for description of this terminology used synonymously to “un-straining.”

strain if the assumptions of the  $R_f/\phi$  method are constrained.

The vector and harmonic means for a given  $R_f/\phi$  data set allow for the determination of the maximum extension axis direction, as well as the nature of symmetry within the plot. As deformation progresses, the long axes of elliptical markers will rotate into parallelism with the maximum extension axis. Therefore, the vector mean (Equation 1.4) of long axis orientations provides the direction of maximum extension. The harmonic mean (Equation 1.5, where  $n$  is the population size) together with the vector mean will divide an  $R_f/\phi$  plot into four regions that can be used to address the nature of distribution asymmetry. In an ideal scenario, the final distribution of  $R_f/\phi$  points will be divided equally into these four regions. However, if the assumptions of no initial preferred orientation, or the absence of multiple non-collinear superimposed deformation events is invalid, the plot will be skewed producing lower values of the index of symmetry (Lisle 1985). As such, this forms a qualitative way to address the validity of several assumptions of the method.

$$\bar{\phi} = \left(\frac{1}{2}\right) \times \arctan \left(\frac{\sum \sin 2\phi}{\sum \cos 2\phi}\right) \quad (1.4)$$

$$H = \frac{n}{\sum_{i=1}^n 1/R_{f_i}} \quad (1.5)$$

In general, a statistically valid population size requires 50 to 75 markers (Borradaile 1984). This number is somewhat dependent on the initial conditions of markers such that lower initial ellipticities (e.g. ooids) will require a smaller population size relative to objects of higher initial ellipticities (e.g. conglomerate pebbles) for a given degree of accuracy (Dunnet 1969; Lisle 1985). Nevertheless, analyses with as few as six objects have been presented in the literature (see for example Treagus and Treagus 2002) while others fail to report any population size for their analyses (Czeck

et al. 2009). Due to this disparity in data presentation, I propose that the following properties be reported for a complete  $R_f/\phi$  analysis:

1. The orientation of the sectional face for an analysis with respect to the principle fabric planes if applicable (e.g. parallel to foliation etc.).
2. The number of objects used in a single analysis.
3. The object lithology.
4. The reference frame used in determining the orientations of objects.
5. The method used in extracting object parameters (i.e. manual vs. object fitting software).
6. The method of  $R_s$  determination (i.e.  $\chi^2$  vs. deformation marker grid fitting).
7. The calculated vector and harmonic means.
8. The index of symmetry.

The data presented within this thesis conforms to these standards and has been generated with a  $\chi^2$  test.

### **1.2.2 The Fry method**

The Fry method, originally presented by Fry (1979), is an all object separation method that is based on a single polar plot of all object centroid pairs (for an example of a fry plot construction refer to Figures 4.6; 3.4; 3.9; and 4.2). This method requires six assumptions to be addressed in order to calculate finite strain: strain is homogeneous at the scale of deformation; the strain history is coaxial such that simple shear, as accommodated by infinitesimally narrow shear planes, is not accounted for by the analysis (Genier and Epard 2007); objects contain a minimum threshold distance;

the initial centroid distribution is considered random (Poisson) (Lisle 2010), and the object centroids do not migrate relative to the object’s enveloping surface during deformation. This method has been applied (with variable degrees of success) to a number of entities from deformed ooids Fry (1979) to salt domes (Rönnlund and Koyi 1988; Paterson et al. 1989). The general aspects of this method are presented below.

After some amount of finite coaxial strain the distribution of centroid pairs will develop a non-random anisotropic pattern such that the original minimum threshold distance will produce a elliptical central void. The ellipticity of this central void is analogous to the shape and orientation of the finite strain ellipse. Traditional methods use a visual estimation of the ellipse apogee and perigee to calculate  $R_s$ . Recently, several workers have attempted to integrate a statistical destraining approach to automatically calculate this value (see for example Waldron and Wallace 2007; Lisle 2010). However, the application of these “objective” fitting methods depend heavily on estimated inputs provided by the user that can have significantly different results. Furthermore, the non-unique results from these statistical tests introduce a level of subjectivity. As such, caution is advised in applying this methodology without addressing the degree of central void development.

A major problem in producing a well defined central void ellipse is the degree of object centroid clustering and anti-clustering. Erslev (1988) presented a modification to the Fry method in order to correct for the phenomenon of clustering and anti-clustering of objects in two-dimensional sections. This modification can be applied to objects that have roughly equal ellipticities following Equation 1.6 where  $K$  is a scale constant.

$$D_n = \frac{D}{\sqrt{X_a \times Z_a} + \sqrt{X_b \times Z_b}} \times K \quad (1.6)$$

Fry (1979) established a theoretical minimum population size of 260 centroids but

recommended upwards of 1,000 objects. This issue of a large required population size is further exacerbated in the production of the Fry plot following Equation 1.7 where the total number of points plotted is determined.

$$\text{Fry plot population} = n \times (n - 1) \quad (1.7)$$

As such a “good” fry plot would require 67,340 points per section with a minimum of three sections for a three-dimensional strain analysis requiring 202,020 coordinate pairs to be plotted. Obviously, this application is best processed with the use of computerized scripts to alleviate the logistical problems of data reduction. Nevertheless, the application of this technique together with other methods such as the  $R_f/\phi$  technique may provide insight to the nature of deformation in terms of vorticity or the validity of assumptions used in either procedure.

### **1.2.3 Additional techniques**

Although the  $R_f/\phi$  and Fry methods are the most widely applied techniques in calculating finite deformation in rocks, several other methods have been presented in the literature. As such, a brief explanation is warranted, which may form the basis of future research on rock fabrics. The following paragraphs briefly describe these additional methods including the Sanderson method (Sanderson 1977), Panozzo projection technique (Panozzo 1984), the Delaunay triangulation nearest neighbor method (Mulchrone 2005), and the intercept method (Launeau and Robin 1996).

#### **1.2.3.1 Sanderson and Panozzo projection method**

Although the Sanderson and Panozzo techniques are considered separate methods, the difference between them is minor and presents slightly different sensitivities in their results (Trayner 1986). In both methods, deformation is assumed to be homogeneous



at the scale of observation and that objects can be approximated by lines, which are initially randomly oriented. In the Sanderson technique, the distributions of material line orientations with respect to a fixed reference frame will deviate from a uniform distribution into a normal distribution with progressive deformation where the frequency of lines, out of the total number of lines ( $n$ ), in a sector subtended by  $\phi_1$  and  $\phi_2$  is given by Equation 1.8 (Sanderson 1977).

$$Frequency = \frac{n}{2\pi} \times (\arctan(R_s \times \tan \phi_2) - \arctan(R_s \times \tan \phi_1)) \quad (1.8)$$

This allows a standard set of histograms to be constructed and compared to an empirical data set.

In the Sanderson method, the lengths of lines are not considered. This lack of sensitivity to the extension of material lines can be accounted for by the Panozzo projection method. In this technique, the horizontal components of a population of lines are projected onto a horizontal line and summed. The dataset is then iteratively rotated and the components are again added to produce a histogram where the maximum projected length corresponds to the maximum extension direction and the quotient between the maximum and minimum projected lengths is equal to the ratio of strain.

Trayner (1986) applied these two methods to an identical data set of grain boundary orientations from a deformed limestone and recommended against using the Sanderson technique. The reasoning of this stemmed from the ability of the Panozzo method to address the calculated angle between semi-major and minor axes. In the case that this angle is not  $90^\circ$ , the assumptions of initial uniform distribution and homogeneous deformation can be called into question. However, I propose that the Sanderson method may provide information on the nature of deformation if applied

in conjunction with the Panozzo technique. Assuming the results of the Panozzo method are deemed acceptable, I propose that the relative difference, as shown in Equation 1.9, between the calculated  $R_s$  values may yield a proxy for the degree of solid-body rotation versus passive material flow (i.e. viscosity contrast). This proposal assumes the  $R_s$  value generated from the Panozzo method is less than or equal to the Sanderson result. To clarify, if the resultant strain ratio of the Panozzo method is less than what is predicted by the distribution of line orientations, the lines have likely rotated into a higher degree of alignment than suggested for passive material flow.

$$Rotation\ index = 2 \times \frac{R_s^{san} - R_s^{pan}}{R_s^{san} + R_s^{pan}} \quad (1.9)$$

Higher values would likely imply higher viscosity contrasts, while a relative difference of zero would suggest passive deformation (i.e. both  $R_s$  alues are equal). This premise, however, is entirely conceptual as Chapter 5 discusses the error associated with the Panozzo method that would need to be considered prior to applying this rotation index.

### 1.2.3.2 DTNNM (triangulation method)

Mulchrone (2005) presented a method (Delaunay triangulation nearest neighbor method modified from a previous version by Mulchrone 2003) based on principles first considered by Ramsay (1967) that calculates the finite strain ratio from objects that are assumed to have an initially even distribution (see assumptions presented for the Fry method in section 1.2.2). Due to the complexity of internal calculations used in this technique, the details are omitted herein and the reader is encouraged to seek the references listed above. Conceptually, this method simply takes a series of lines connecting each point with its nearest neighbor and translates the lines to the origin of the plot. This produces a plot that resembles a Fry plot with significantly fewer

points (roughly the square root of the population size used to create a Fry plot) that defines an elliptical region corresponding to the orientation and ellipticity of the finite strain ellipse. The major draw back to this method is the fact that at higher and higher strains the method begins to break down in that nearest neighbor pairs oriented roughly parallel to the maximum extension direction are less likely to occur.

### **1.2.3.3 The intercept method**

The intercept method (Launeau and Robin 1996) is not considered an analytical strain technique, but rather a process to quantify the shape preferred orientation of markers, such as mineral grains, within a two-dimensional section. This method uses a series of parallel lines at a given spacing that traverse a plane containing object traces. At equal intervals along these lines a boolean expression is executed defining whether or not each point falls within a defined object. Each time this test changes from object to matrix an intercept is counted and summed for each grid line. As such a total intercept value is obtain for a set of grid lines proceeding in a given direction. This procedure is repeated iteratively through  $180^\circ$  and a polar plot can be constructed of the intercepts. This plot can then be inversely fitted with an ellipse that corresponds to the sectional fabric ellipse. An interesting aspect of the intercept method is the nature of object surface irregularities in producing more intercepts. Consider for example a perfectly elliptical object. If the intercept method is applied to this object we would obtain an ellipse geometrically similar to the object. However, imagine this object has an undulatory surface (e.g pinch and swell proto-boudin necks) but can still be approximated by the previous ellipse. In this case the intercept method will produce a fabric ellipse that is lower in ellipticity. This change is a function of increased intercepts produced by the irregular surface. For this reason, the nature of object digitization can have a great affect on the resultant fabric ellipse

such that smoother traces will tend to provide more intercept anisotropy for a given object. As an extension to this method, I propose the simple application of fitted object ellipses as a proxy for the object shape. This proposal shifts the conundrum of object digitization to a different stage because the procedure that ultimately fits an ellipse to the object may be dependent on the nature of boundary smoothness. However, based on experimentation with boundary smoothness and the program SAPE (Mulchrone et al. 2005) following a seed grow algorithm implemented therein (Adams and Bischof 1994), I assert this procedure is substantially less sensitive to boundary irregularities<sup>4</sup>. Therefore the application of the intercept method to sections containing fitted ellipses of objects, as the object itself (i.e. the intercept method applied to the boundaries of ellipses as opposed to the actual object boundaries), may better reflect the most consistent values of fabric, and indeed may relate directly to finite strain if the assumptions of homogeneous and passive deformation can be constrained. However, this remains to be confirmed with future research.

---

<sup>4</sup>SAPE statistically fits an ellipse to the object region while the intercept method simply counts the number of boundaries. As such, the fitting of objects by SAPE will effectively smooth asperities and not significantly change the overall fitted ellipse.

Table 1.1: List of symbols used throughout the text as related to fabric quantification.

Symbol	Description
$R$	The axial ratio the semi-major axis and semi-minor axis of an ellipse.
$R_i$	The initial undeformed axial ratio of an elliptical object.
$R_f$	The final deformed axial ratio of an elliptical object.
$R_s$	The ratio of principle stretches in an undefined 2D section (strain ratio).
$R_s^{XY, XZ, YZ}$	The strain ratio corresponding to a specific principle plane of strain.
$(X, Y, Z)_{t_1}$	Normalized strain ellipsoid principle axial lengths at the initial measure of time.
$(X, Y, Z)_{t_2}$	Normalized strain ellipsoid principle axial lengths after a given finite strain from $t_1$ to $t_2$ .
$(X, Z)_{a, b}$	Axial lengths (semi major and minor, respectively) of object “a” and “b.”
$\theta$	Angle between the maximum extension and an object’s semi-major axis before deformation.
$\phi$	Angle between the maximum extension axis and an object’s semi-major axis of after deformation. <sup>1</sup>
s	The index of symmetry for a sectional $R_f/\phi$ analysis.
vm, $\bar{\phi}$	The vector mean of the $\phi$ angles.
hm, $H$	The harmonic mean of $R_f$ values.
$\bar{\epsilon}_s$	The octahedral shear strain of finite deformation
$\nu$	Lode parameter defining the symmetry of strain.
$D_n, D$	Normalized distance between object centroids and actual distance, respectively.
$R_3^{pan}, R_s^{san}$	The calculated strain ratio as given by the Panozzo and Sanderson techniques, respectively.
$\gamma$	Geological shear strain: $\gamma = \tan \psi$ .

---

<sup>1</sup>Angle with respect to strike following right hand rule, positive angles are defined down-dip from the line of strike.

## References

- Adams, R. and L. Bischof (1994). Seeded region growing. *Pattern Analysis and Machine Intelligence, IEEE Transactions on* 16(6), 641–647.
- Astini, R., J. Benedetto, and N. Vaccari (1995). The early paleozoic evolution of the argentine precordillera as a laurentian rifted, drifted, and collided terrane: A geodynamic model. *Geological Society of America Bulletin* 107(3), 253–273.
- Astini, R. and F. Dávila (2004). Ordovician back arc foreland and oclotic thrust belt development on the western gondwana margin as a response to precordillera terrane accretion. *Tectonics* 23(4), TC4008.
- Bahlburg, H. and F. Hervé (1997). Geodynamic evolution and tectonostratigraphic terranes of northwestern argentina and northern chile. *Bulletin of the Geological Society of America* 109(7), 869.
- Barazangi, M. and B. Isacks (1976). Spatial distribution of earthquakes and subduction of the nazca plate beneath south america. *Geology* 4(11), 686–692.
- Bird, P. (1988). Formation of the rocky mountains, western united states: A continuum computer model. *Science* 239(4847), 1501.
- Borradaile, G. (1984). Strain analysis of passive elliptical markers: success of de-straining methods. *Journal of structural geology* 6(4), 433–437.
- Casquet, C., E. Baldo, R. Pankhurst, C. Rapela, C. Galindo, C. Fanning, and J. Saavedra (2001). Involvement of the argentine precordillera terrane in the famatinian mobile belt: U-pb shrimp and metamorphic evidence from the sierra de pie de palo. *Geology* 29(8), 703.
- Cembrano, J., A. Lavenu, G. Yáñez, R. Riquelme, M. García, G. González, and G. Hérail (2007). Neotectonics. *The geology of Chile (Moreno, T.; Gibbons, W.; editors). The Geological Society, London*, 231–261.
- Charrier, R., L. Pinto, M. Rodríguez, T. Moreno, and W. Gibbons (2007). Tectonostratigraphic evolution of the andean orogen in chile. *The Geology of Chile (Moreno, T.; Gibbons, W.; editors). The Geological Society*, 21–114.
- Chew, D. (2003). An excel spreadsheet for finite strain analysis using the rf/phi technique. *Computers & geosciences* 29(6), 795–799.
- Coira, B., J. Davidson, C. Mpodozis, and V. Ramos (1982). Tectonic and magmatic evolution of the andes of northern argentina and chile. *Earth-Science Reviews* 18(3-4), 303–332.
- Coney, P. and S. Reynolds (1977). Cordilleran benioff zones. *Nature* 270, 403–406.

- Czeck, D., D. Fissler, E. Horsman, and B. Tikoff (2009). Strain analysis and rheology contrasts in polymictic conglomerates: An example from the seine metaconglomerates, superior province, canada. *Journal of Structural Geology* 31(11), 1365–1376.
- Dalziel, I. (1997). Overview: Neoproterozoic-paleozoic geography and tectonics: Review, hypothesis, environmental speculation. *Geological Society of America Bulletin* 109(1), 16–42.
- Dewey, J. and J. Bird (1970). Mountain belts and the new global tectonics. *Journal of Geophysical Research* 75(14), 2625–2647.
- Dickinson, W. and W. Snyder (1978). Plate tectonics of the laramide orogeny. *Geological Society of America Memoir* 151, 355–366.
- Do Campo, M. and S. Guevara (2005). Provenance analysis and tectonic setting of late neoproterozoic metasedimentary successions in nw argentina. *Journal of South American Earth Sciences* 19(2), 143–153.
- Dunnet, D. (1969). A technique of finite strain analysis using elliptical particles. *Tectonophysics* 7(2), 117–136.
- Durand, F. (1996). La transición precámbrico-cámbrico en el sur de sudamérica. *Early Paleozoic evolution in NW Gondwana. Universidad Nacional de Tucumán, Argentina, Serie Correlación Geológica* 12, 195–205.
- English, J., S. Johnston, and K. Wang (2003). Thermal modelling of the laramide orogeny: testing the flat-slab subduction hypothesis. *Earth and Planetary Science Letters* 214(3), 619–632.
- Finney, S., J. Gleason, G. Gehrels, S. Peralta, and G. Acenolaza (2003). Early gondwanan connection for the argentine precordillera terrane. *Earth and Planetary Science Letters* 205(3-4), 349–359.
- Gana, P. and R. Tosdal (1996). Geocronología u-pb y k-ar en intrusivos del paleozoico y mesozoico de la cordillera de la costa, región de valparaíso, chile. *Andean Geology* 23(2), 151–164.
- Genier, F. and J. Epard (2007). The fry method applied to an augen orthogneiss: Problems and results. *Journal of structural geology* 29(2), 209–224.
- Hudleston, P. (1999). Strain compatibility and shear zones: is there a problem? *Journal of Structural Geology* 21(8-9), 923–932.
- Lamb, S. and P. Davis (2003). Cenozoic climate change as a possible cause for the rise of the andes. *Nature* 425(6960), 792–797.
- Launeau, P. and P. Robin (1996). Fabric analysis using the intercept method. *Tectonophysics* 267(1-4), 91–119.
- Lavenu, A. and J. Cembrano (1999). Compressional-and transpressional-stress pattern for pliocene and quaternary brittle deformation in fore arc and intra-arc

- zones (andes of central and southern chile). *Journal of Structural Geology* 21(12), 1669–1691.
- Li, Z., S. Bogdanova, A. Collins, A. Davidson, B. De Waele, R. Ernst, I. Fitzsimons, R. Fuck, D. Gladkochub, J. Jacobs, et al. (2008). Assembly, configuration, and break-up history of rodinia: a synthesis. *Precambrian Research* 160(1-2), 179–210.
- Lira, R., H. Millone, A. Kirschbaum, and R. Moreno (1997). Calc-alkaline arc granitoid activity in the sierra norte-ambargasta ranges, central argentina. *Journal of South American Earth Sciences* 10(2), 157–177.
- Lisle, R. (1985). Geological strain analysis, a manual for the rf/phi method.
- Lisle, R. (2010). Strain analysis from point fabric patterns: An objective variant of the fry method. *Journal of Structural Geology* 32(7), 975–981.
- Llambías, E. and A. Sato (1995). El batolito de colangüil: transición entre orogénesis y anorogénesis. *Revista de la Asociación Geológica Argentina* 50(1-4), 111–131.
- Mpodozis, C. and P. Cornejo (1988). *Hoja Pisco Elqui: IV region de Coquimbo*. Servicio nacional de geología y minería.
- Mpodozis, C. and S. Kay (1992). Late paleozoic to triassic evolution of the gondwana margin: Evidence from chilean frontal cordilleran batholiths (28 {degrees} s to 31 {degrees} s). *Bulletin of the Geological Society of America* 104(8), 999.
- Mulchrone, K. (2003). Application of delaunay triangulation to the nearest neighbour method of strain analysis. *Journal of Structural Geology* 25(5), 689–702.
- Mulchrone, K. (2005). Dtnnm: A windows program for strain analysis using the delaunay triangulation nearest neighbour method. *Computers & geosciences* 31(8), 978–988.
- Mulchrone, K. and P. Meere (2001). A windows program for the analysis of tectonic strain using deformed elliptical markers. *Computers & geosciences* 27(10), 1251–1255.
- Mulchrone, K., P. Meere, and K. Choudhury (2005). Sape: a program for semi-automatic parameter extraction for strain analysis. *Journal of structural geology* 27(11), 2084–2098.
- Nasi, C., C. Mpodozis, P. Cornejo, R. Moscoso, and V. Maksaev (1985). El batolito elqui-limarí (paleozoico superior triásico): características petrográficas, geoquímicas y significado tectónico. *Revista geológica de Chile* 25, 26.
- Pankhurst, R., C. Rapela, J. Saavedra, E. Baldo, J. Dahlquist, I. Pascua, and C. Fanning (1998). The famatinian magmatic arc in the central sierras pampeanas: an early to mid-ordovician continental arc on the gondwana margin. *Geological Society, London, Special Publications* 142(1), 343–367.



- Panozzo, R. (1984). Two-dimensional strain from the orientation of lines in a plane. *Journal of structural geology* 6(1-2), 215–221.
- Paterson, S., P. Rönnlund, and H. Koyi (1989). Comment and reply on” fry spacing of deformed and undeformed modeled and natural salt domes”. *Geology* 17(2), 193–195.
- Peach, C. and R. Lisle (1979). A fortran iv program for the analysis of tectonic strain using deformed elliptical markers. *Computers & Geosciences* 5(3-4), 325–334.
- Piñán-Llamas, A. and C. Simpson (2006). Deformation of gondwana margin turbidites during the pampean orogeny, north-central argentina. *Geological Society of America Bulletin* 118(9-10), 1270–1279.
- Ramsay, J. (1967). *Folding and fracturing of rocks*, Volume 56. McGraw-Hill ^ eNew York New York.
- Ramsay, J. and M. Huber (1983). *The techniques of modern structural geology*. Number v. 1 in The Techniques of Modern Structural Geology. Academic Press.
- Rapela, C., R. Pankhurst, C. Casquet, E. Baldo, J. Saavedra, and C. Galindo (1998). Early evolution of the proto-andean margin of south america. *Geology* 26(8), 707–710.
- Rönnlund, P. and H. Koyi (1988). Fry spacing of deformed and undeformed modeled and natural salt domes. *Geology* 16(5), 465–468.
- Sanderson, D. (1977). The analysis of finite strain using lines with an initial random orientation. *Tectonophysics* 43(3-4), 199–211.
- SERNAGEOMIN (2002). *Mapa Geológico de Chile. Servicio Nacional de Geología y Minería, Chile. Carta geológica de Chile. Serie Geología básica No. 75, 1 mapa en 3 hojas, escala 1:1.000.000.*
- Thomas, W., R. Astini, and G. Bayona (2002). Ordovician collision of the argentine precordillera with gondwana, independent of laurentian taconic orogeny. *Tectonophysics* 345(1-4), 131–152.
- Thorpe, R. and P. Francis (1979). Variations in andean andesite compositions and their petrogenetic significance. *Tectonophysics* 57(1), 53–70.
- Trayner, P. (1986). A comparison of sanderson’s and panozzo’s strain measurement methods using calcite grain boundaries from the variscan fold and thrust belt in ireland. *Journal of structural geology* 8(2), 205–207.
- Treagus, S. and J. Treagus (2002). Studies of strain and rheology of conglomerates. *Journal of Structural Geology* 24(10), 1541–1567.
- Turner, J. C. M. (1960). Estratigrafía de la sierra de santa victoria y adyacencias. *Boletín de la Academia Nacional de Ciencias* 41(2), 163–196.

- Uliana, M. and K. Biddle (1988). Mesozoic-cenozoic paleogeographic and geodynamic evolution of southern south america. *Revista Brasileira de Geociencias* 18(2), 172–190.
- Valentine, J. and E. Moores (1970). Plate-tectonic regulation of faunal diversity and sea level: a model.
- Waldron, J. and K. Wallace (2007). Objective fitting of ellipses in the centre-to-centre (fry) method of strain analysis. *Journal of Structural Geology* 29(9), 1430–1444.
- Wells, M. and T. Hoisch (2008). The role of mantle delamination in widespread late cretaceous extension and magmatism in the cordilleran orogen, western united states. *Geological Society of America Bulletin* 120(5-6), 515–530.
- Wortel, M. (1984). Spatial and temporal variations in the andean subduction zone. *Journal of the Geological Society* 141(5), 783–791.
- Yáñez, G. and J. Cembrano (2004). Role of viscous plate coupling in the late tertiary andean tectonics. *Journal of Geophysical Research* 109(B02407).

## Chapter 2

# Reconstruction of progressive dike emplacement in the Coastal Batholith, central Chile

### Abstract

The Coastal Batholith of central Chile preserves structures that record the concentration, migration, transportation, and emplacement of magma during the progressive construction of a sheeted dike complex. This sheeted dike complex, located on the Pacific Coast near the town of El Tabo, is divided into three main structural-geographic domains. The northwestern domain contains an abundance of deformed microgranitoid enclaves that host features such as fold hinges, tension gashes, boudin necks, and strain shadows that are filled with leucosome. We relate these structures to features developed in migmatite terrains that facilitate the concentration of melt. The formation of inter-connected dilational sites produced an array of leucocratic zones that contain apophyses with tapered tips suggesting fracture propagation related to magma overpressurization. The coalescence of multiple proto-dikes may have formed larger dike networks that facilitated the transportation of melt-rich magma producing new magmatic units of similar mineralogy. The central domain is characterized by the presence of two tonalitic units emplaced under syn-magmatic conditions that contain two enclave swarms distinguished by their general packing arrangement (i.e. enclave vs. matrix supported) and degree of elongation. Cross-cutting field relationships indicate a younging of emplacement towards the southeastern domain associated with a decrease in enclave abundance. Differences in the fabric architecture of these enclave swarms are displayed by two separate three-dimensional fabric analyses using the  $R_f/\phi$  method, which indicates an abrupt transition from low-distortion oblate fabrics to more distorted prolate geometries. This change in fabric architecture suggests that either the nature of hypersolidus flow affected the packing arrangement of enclaves and their corresponding geometries, or that the nature of enclave packing induced a characteristically different hypersolidus flow, and allowed enclaves to become more aligned and distorted in a colinear manner. These changes are compared to the statistical alignment of feldspar phenocrysts, which indicate general

flattening in both units with a higher degree of alignment within the XZ fabric plane for the younger tonalite. This application of analytical strain techniques to magmatic fabrics may help decipher changes in the nature of hypersolidus flow despite the lack of finite strain significance. The third (southeastern) domain is distinguished by meter-scale, compositionally and texturally diverse sheeted dikes intercalated with biotite-rich migmatite screens of the host gneiss along the pluton<sup>1</sup> margin. These observations indicate that the mechanisms of granitic magmatism including melt extraction, migration, transportation, and emplacement do not necessarily occur in series, and may operate concomitantly throughout a single pluton. This concentration and movement of magma within the pluton is dependent on deformation of variable styles.

---

## 2.1 Introduction

The transportation and emplacement of subduction-related magmas within oceanic-continent convergent settings is an important process resulting in the growth of continental crust through magma addition. Although numerous models establish a genetic relationship between hypersolidus deformation and the transportation and emplacement of plutonic complexes (Petford 1996; Miller and Paterson 1999; Hutton et al. 1990; Grocott et al. 1994; Kalakay et al. 2001) the role of deformation during magmatic arc construction can be difficult to interpret in many settings. A major impediment to the resolution of this uncertainty is derived from the complex, ambiguous kinematic significance of magmatic structures that are commonly incompletely preserved such as mineral alignment fabrics (Paterson et al. 1989; Nicolas 1992a; Paterson et al. 1998; Blumenfeld and Bouchez 1988) microgranitoid enclave swarm geometries (Tobisch et al. 1997), microgranitoid enclave shapes (Paterson et al. 2004), geometries of schlieren (Wiebe et al. 2007), and hypersolidus folds (Paterson et al. 1998). Although these structures must form in response to differential stresses, complex spatial and temporal variations in strain make distinguishing flow regimes difficult, which are dependent on properties that can vary both spatially and

---

<sup>1</sup>The definition of a pluton used within this text is a generic term for an igneous rock as adapted from Winter et al. (2001, pg. 59).

temporally, including compositional heterogeneity (Frost and Mahood 1987), viscosity contrast (Williams and Tobisch 1994; Vigneresse and Tikoff 1999; Petford 2003), strain rate (Johnson et al. 2004), and vorticity (Vigneresse and Tikoff 1999). As such, the processes that produce magmatic fabrics within a pluton can be difficult to completely constrain. For this reason the application of traditional structural mechanics (e.g. pure shear vs. simple shear) to the quantification of deformation within polyphase systems (i.e. solid and liquid constituents) has been met with warranted resistance (for a discussion on the complexity of strain and stress see: Paterson et al. 1998). Therefore, progressive homogenous deformation is not likely a viable assumption. Despite this complexity, a large body of literature has established the genetic role of hypersolidus flow and host rock deformation in the transportation of magma through the crust.

In this chapter I present a field-based study of magmatic structures observed from the Coastal Batholith of central Chile (Fig. 2.1) that record a progressive emplacement history involving the concentration, migration, and transportation of melt-rich magmas during pluton construction. This location provides an excellent opportunity to study the role of deformation in magmatic transport processes due to the variety of compositionally distinctive phases, structures, and mineral fabric geometries within a well-exposed, easily accessible coastal transect (Fig. 2.2).

The Coastal Batholith is an extensive belt of late Paleozoic and early Mesozoic calcalkaline intrusive rocks located in the Coastal Range that developed in response to the east-directed subduction of oceanic crust beneath Gondwana. Diachronous eastward migration of magmatism is documented by a progressive younging of plutons to the east (Levi 1973; Vergara et al. 1995), which are generally interpreted to have been emplaced at increasingly shallower crustal levels through time (Parada et al. 1999). Therefore, the Coastal Range of central Chile broadly exposes a tempo-

ral section of magmatism from the late Paleozoic to modern times. This long-lived subduction related arc magmatism provides a link between the modern archetypal volcanic arc of the Andes and intrusive processes occurring at deeper crustal levels.

My analysis of hypersolidus structures, including magmatic fabrics, tension gashes, folds, boudins, dikes, and strain shadows, define a progressive evolution of dike emplacement involving pulses of compositionally distinctive magmas, the partitioning of leucosome into dilational sites, the formation of melt-rich dike networks, and the construction of a sheeted dike complex. This progression involved the mingling of dominantly tonalitic and dioritic magmas to produce rheological contrasts that helped concentrate melt into fold hinges, tension gashes, boudin necks and strain shadows during synmagmatic deformation. This concentration of melt into interconnected networks of leucocratic zones focused flow and mobilized melt aiding in the construction of a composite dike complex along the pluton margin. In contrast to suggestions made by Petford et al. (2000), these observations indicate that the mobilization, transportation, and emplacement of granitic magma can proceed concomitantly during pluton construction and can produce a highly diverse array of mesoscale structures and different deformation styles that together facilitated the migration and transportation of magma during the construction of the Coastal Batholith in central Chile.

## **2.2 Background**

### **2.2.1 Geologic framework**

Central Chile, from 33° S to 34° S (Fig. 2.1), comprises three physiographic provinces that include the western flank of the Main Cordillera, the Central Valley, and the Coastal Cordillera. The Main Cordillera forms the physical expression of the modern volcanic arc and contains folded and faulted Paleogene volcanoclastic sequences that host Neogene plutonic rocks (SERNAGEOMIN 2002). The Central Valley separates

the Main Cordillera from the Coastal Cordillera and is bounded by a kinematically complex array of basin-bounding fault systems (Lavenu and Cembrano 1999; Farías et al. 2005; Fock et al. 2005) that have accommodated 1.5–5.0 km. of subsidence from the Oligocene to the Holocene (Elgueta et al. 2000). The Coastal Cordillera is composed of late Paleozoic to Mesozoic plutons, hypabyssal intrusive rocks, and volcanic sequences (Wall et al. 1996). The eastern flank of the Coastal Range consists of Mesozoic sedimentary, volcanoclastic, and volcanic rocks that constitute a 15 km thick sequence, which developed during extension driven subsidence within a series of intra-arc basins (Vergara et al. 1995). In central Chile, these deposits overlie an intrusive basement, which is exposed as the Coastal Batholith. This batholith is composed of three plutonic belts including the Cretaceous Illapel Complex, the Middle Jurassic Papudo-Quintero Complex, and the Carboniferous Santo Domingo Complex (Parada et al. 1999). This eastward migration of magmatism led to the preservation of structures produced during pluton construction in the Coastal Cordillera.

Coastal granitoids of the Santo Domingo Complex (Figs. 2.1 and 2.2) between Isla Negra and El Tabo (Isla Negra igneous complex) display coarse-grained porphyritic hornblende and biotite-bearing tonalites that host fine grained mafic and microgranitoid enclaves (henceforth referred to as enclaves) (Siña and Parada 1985; Siña 1987; Parada et al. 1999). Enclave abundances are spatially variable within the tonalites, ranging from < 1% to >50% by volume (Siña 1987). The close association of enclave swarms with mafic dikes has led previous workers to suggest a dismembered syn-plutonic<sup>2</sup> dike origin for these enclaves (Parada et al. 1999). However, their exact provenance remains equivocal. These large tonalitic units transition towards the

---

<sup>2</sup>Syn-plutonic, as defined by Pitcher (1991, pg. 384) indicates intrusion of a dike prior to complete crystallization of the host rock. As such this terminology refers to the state of the host rock and not the state of the dike, which by definition is obviously magmatic. This definition *sensu-stricto* is carried throughout the following text.

host margin to sheeted dikes that are compositionally variable including megacrystic granodiorites, granites, tonalites, and fine-grained biotite-rich granitoids (Figs. 2.1, 2.2, and 2.3) (Siña 1987). The sheeted dikes range in thickness from  $\sim 10$  cm to  $>1$  km and are cut by relatively undeformed mafic dikes.

To our knowledge, no crystallization ages have been obtained directly from outcrops near Isla Negra. However, a U-Pb zircon age of  $291 \pm 1$  Ma (Godoy and Loske 1988) and a Rb-Sr whole rock isochron age of  $292 \pm 2$  Ma (Hervé et al. 1988) constrain an Early Permian age for similar rocks of the Santo Domingo Complex. One geobarometric pressure obtained for hornblende crystallization of 7 kbar is reported in the literature (Siña and Parada 1985) and suggests mid-crustal emplacement (Petrini and Podladchikov 2000). The relatively undeformed cross-cutting mafic dikes were emplaced from 163 Ma to 157 Ma (Creixell et al. 2011) and have been reported to truncate brittle epidotiferous faults and fractures (Creixell et al. 2009). This relationship suggests exhumation to relatively shallow crustal levels by the Middle Jurassic.

The Santo Domingo Complex is hosted by granitic metaigneous gneiss and metasedimentary rocks of the Valparaíso Metamorphic Complex that are locally migmatitic (Wall et al. 1996). These metamorphic units are well exposed south of the Isla Negra igneous complex near the town of Las Cruces (Fig. 2.1). One K-Ar radiometric age of  $278 \pm 6$  Ma was obtained from garnet-bearing quartzofeldspathic gneiss roughly one kilometer east of Punta Lacho (Cordani et al. 1976). This date has previously been interpreted as the age of metamorphism (Wall et al. 1996). However, based on the host relationship of the Valparaíso Metamorphic Complex to the Isla Negra igneous complex, we suggest that this date may indicate a cooling or partial resetting age following emplacement of late Paleozoic plutons.



### 2.2.2 Magmatic processes

Granitic magmatism requires the partial melting of some protolith, segregation of leucosome, ascent of magma, and the emplacement of plutons or dikes (Petford et al. 2000). During these phases, changing flow regimes may completely obscure earlier features, limiting the record available within many plutons to younger events. Nevertheless, the recognition of dilational structures, magmatic foliations, lineations, enclave swarms and dike networks can provide key information on the evolution of igneous complexes during the construction of batholiths.

The physical segregation of melt from grain ( $\mu\text{m}$ ) to sample scale (dm) zones requires driving forces such as gravitational buoyancy or pressure gradients (Brown and Rushmer 1997). The formation of low pressure “dilation sites” caused by deformation include the development of interboudin partitions (Strömgård 1973; Van der Molen and Paterson 1979; Mancktelow 1995; Brown and Rushmer 1997), folds (Hand and Dirks 1992; Brown 1994; Williams et al. 1995; Collins and Sawyer 1996), tension gashes (Shaw 1980; Sleep 1988; Rutter and Neumann 1995), and shear zones (Brown and Solar 1998). If sufficient volumes of melt are concentrated at the mesoscopic scale, interconnected networks of dikes and veins can initiate ascent (Brown 2010) that may transport magma through the crust. The mechanisms of large-scale magma transportation are widely debated in the literature and typically involve combinations of two end member models that include the diapiric rise of plutons versus dike-driven ascent (see for example: Petford 1996 Miller and Paterson 1999; Paterson and Vernon 1995; Clemens and Mawer 1992; Clemens et al. 1997).

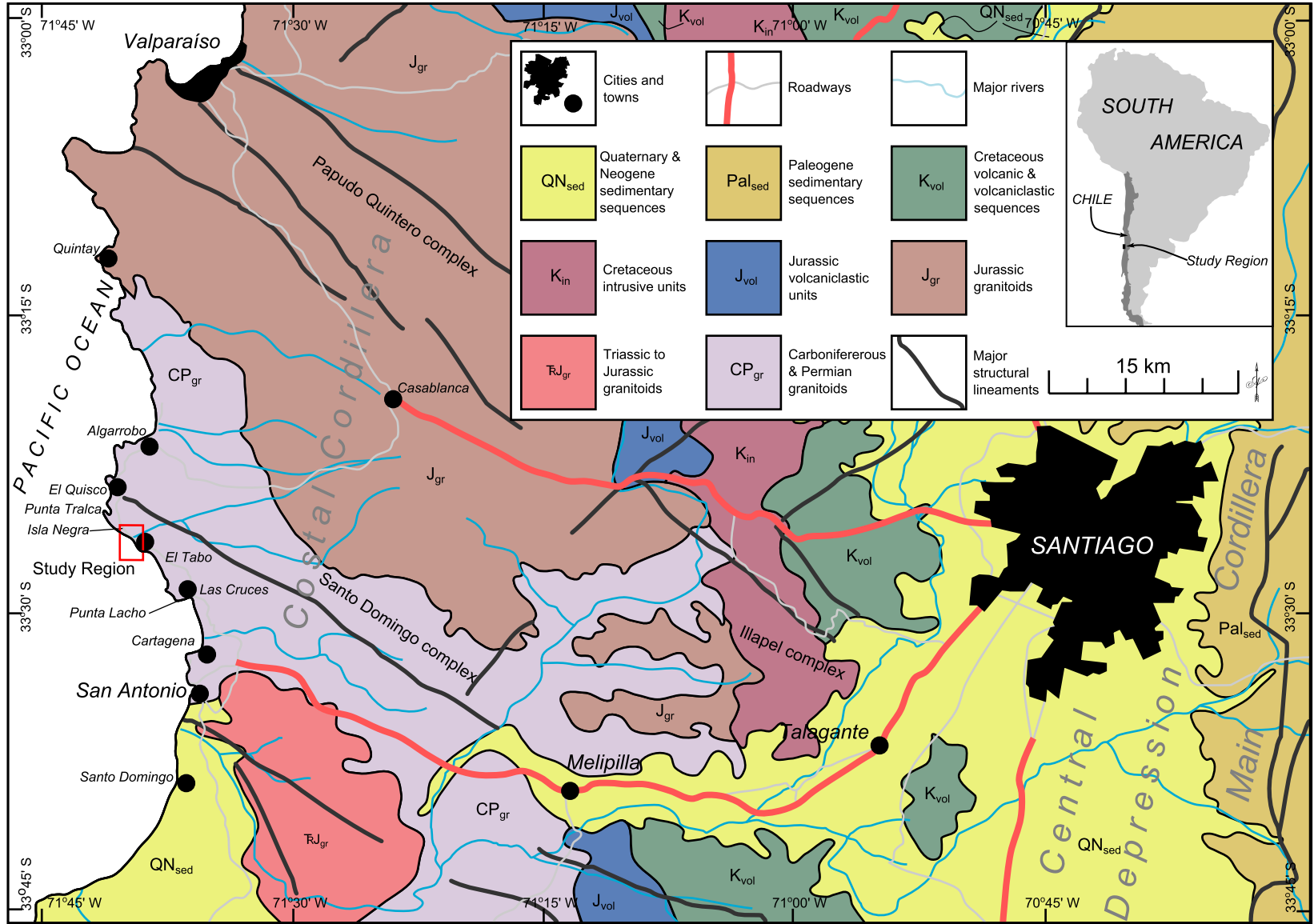
The mechanisms of magma ascent are difficult to ascertain based on the ambiguity of kinematic indicators (Nicolas 1992b) and the significance of foliations and lineations (Paterson et al. 1998). Due to this limitation, many workers (e.g. John

and Blundy 1993; Molyneux and Hutton 2000) have attempted to use the shapes and orientations of enclaves and xenoliths to determine changes in strain throughout a pluton. However, the use of enclaves as strain markers to evaluate these mechanisms has been challenged (Paterson and Vernon 1995; Paterson et al. 1998). This challenge is due to difficulties in constraining key properties such as the initial characteristics of enclave populations, enclave rheology, enclave-host viscosity contrasts, the passive nature of enclave deformation under homogeneous strain, and the final distributions of enclave populations (Paterson et al. 2004). However, geometric changes in the architecture of enclave swarms can provide information on the nature of hypersolidus flow and may be used to distinguish geometric domains within a magmatic complex that may correlate to other regional structures.

The switch from magma transportation to emplacement may be controlled by numerous feed-back systems that involve properties such as stress, strain, and rheology (see discussion on emplacement by Brown 2001), which are incompletely understood. Although the previously mentioned processes for granitic magmatism are qualitatively believed to occur in series (Petford et al. 2000), observations presented herein suggest that melt segregation, ascent, and emplacement may occur concomitantly during the progressive construction of magmatic arcs.

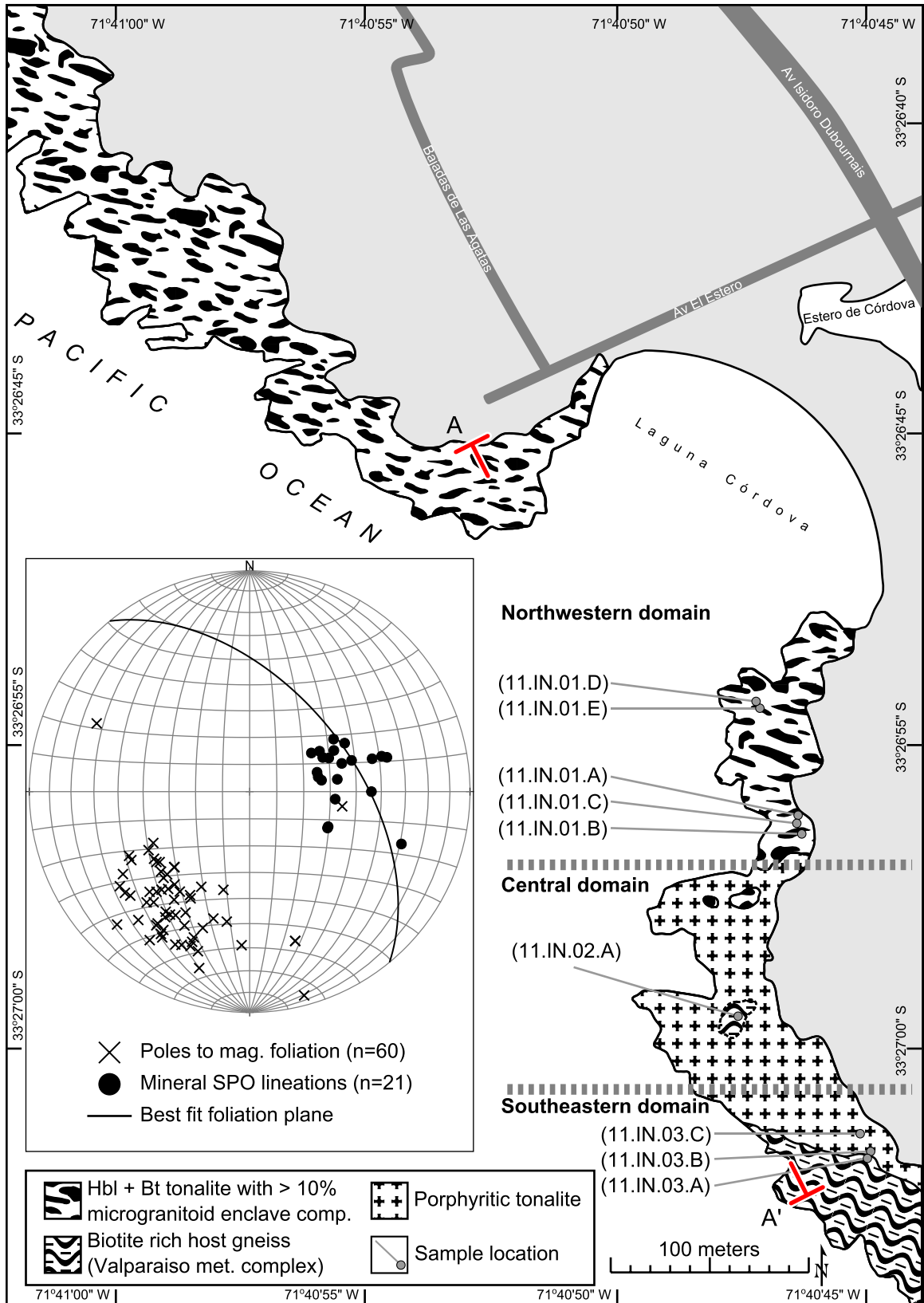
---

Figure 2.1: Geologic overview map of the Andean coastal range in central Chile. Modified from SERNAGEOMIN (2002) and Wall et al. (1996).



---

Figure 2.2: Generalized geologic map of coastal exposures between Isla Negra and El Tabo. Stereographic projection contains data from region shown in map obtained in this study. Map lithologies and extent modified from Siña (1987). Mineral SPO relates to the shape preferred orientation of minerals within the outcrop.



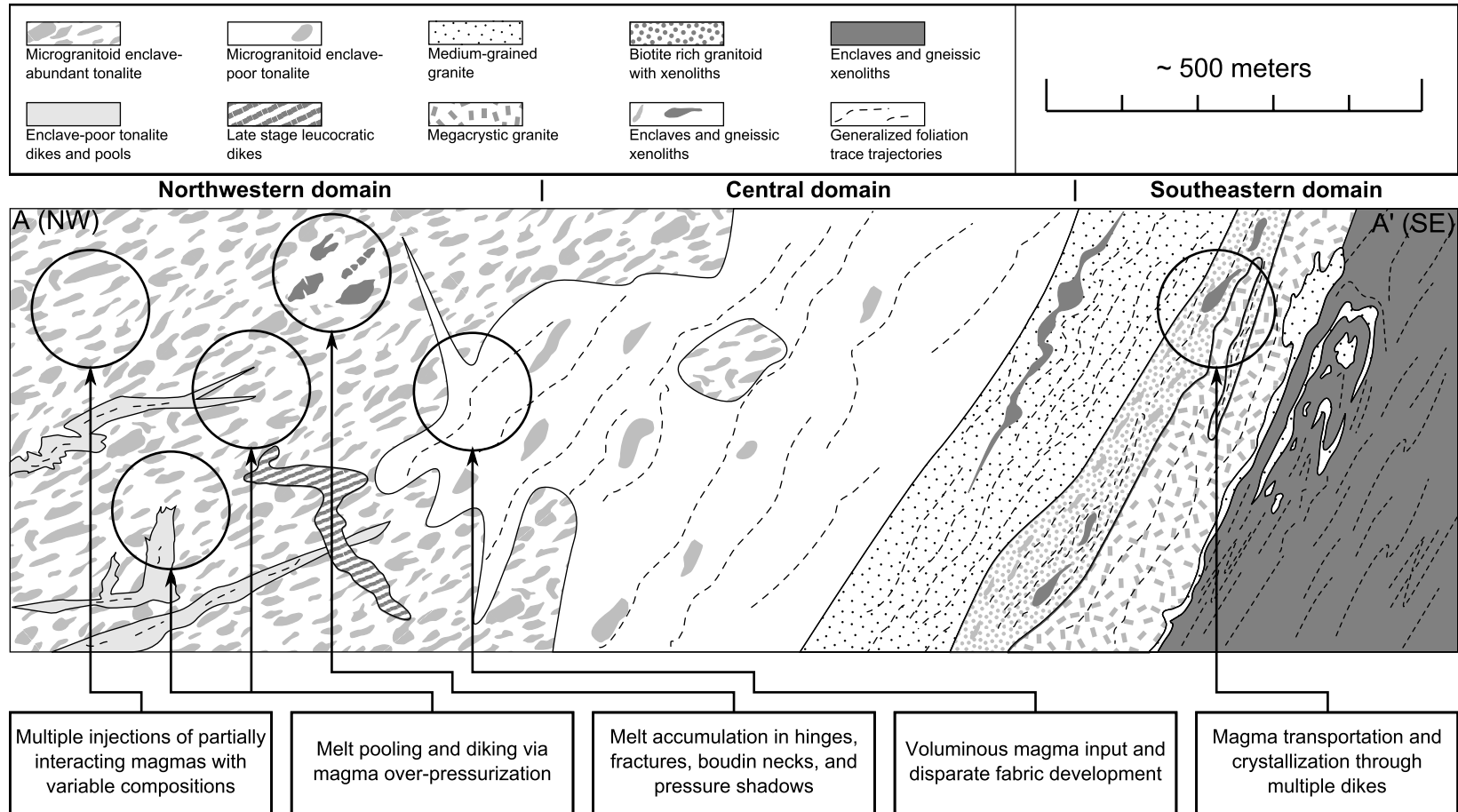


Figure 2.3: Schematic cross-section illustrating the general architecture of magmatic phases and structures developed between Isla Negra and El Tabo. See Figure 2.2 for line of section (A-A').

## 2.3 Observations of host rock

Granite augen gneiss of the Valparaíso Metamorphic Complex displays a metamorphic foliation that is defined by the alignment of plagioclase and potassium feldspar porphyroclasts within a matrix of fine-grained biotite, quartz, and hornblende minerals. The foliation dips steeply to the north–northeast and contains an east-trending mineral lineation. The three-dimensional geometry of fabrics developed throughout the granite augen gneiss varies locally from  $L \gg S$  (see for example section 3.4 in Chapter 3) to  $L < S$  tectonites. Feldspar porphyroclasts commonly exhibit strain shadows that are weakly asymmetric and tend to lack robust kinematic indicators. Moreover asymmetric porphyroclasts are observed in sections orthogonal to the mineral stretching lineation and suggest a complex triclinic deformation history, the details of which remain unresolved.

Discrete, low-displacement, mylonitic shear zones cross-cut the granite augen gneiss fabric and deflect foliations into parallelism with the shear zone. These discrete shear zones display significant grain size reduction and are frequently ultramylonitic. The orientations and kinematics of the mylonites vary throughout the region and do not define a coherent displacement direction. However, fault plane solutions<sup>3</sup> constructed for each shear zone (this study) and plotted on one composite stereographic projection indicate well defined contractional and extensional quadrants that are compatible with north–northeast directed contraction (see Appendix A). The use of fault

---

<sup>3</sup>I have used fault plane solutions on these low displacement mylonites to characterize the regional shortening and lengthening directions. Although this technique is typically restricted to brittle deformation structures, I assert that in this unique case the method is valid for the following reasons. First, all displacements observed are low (I concede that the actual magnitude of displacement is not directly obtainable due to a lack of offset markers, however, none of the described shear zones are regionally traceable, nor do any offset discernible compositional units). Secondly, deformation is highly localized and occurs within a narrow zone of reduced grain size. Finally, all measured shear zones of this style in this region define clear contractional and extensional domains. As such, the formation of these mylonites likely represent (or closely approximate) the orientations of the instantaneous state of strain.



plane solutions assumes deformation under brittle conditions and is generally not applied to ductile structures. The use of fault plane solutions in this study, however, is supported by the fact that displacement is low for each shear zone and is constrained in a narrow (1 - 5 cm) localized domain (see footnote for expansion on this idea). Moreover, these mylonites do not display any evidence for progressive deformation (e.g. folding) and likely represent orientations approximating the instantaneous state of strain. Although the timing of these structures are poorly constrained, none are observed within the Isla Negra igneous complex, suggesting pre-emplacement development.

Biotite-rich quartzofeldspathic gneiss near Punto Lancho host lit-par-lit granitoid dikes that are commonly folded, yet preserve magmatic textures and generally lack evidence for solid state deformation. Additionally, dikelets of ptlygmatically folded leucosome are observed with euhedral garnet, indicative of a peritectic crystallization. Leucosome and granitoid dikes are generally concordant to the gneissic foliation.

## **2.4 Pluton divisions**

The Isla Negra igneous complex is divided into three domains defined by the spatial distribution of structures, compositions, and textures. The northwestern domain (Figs. 2.2 and 2.3) is characterized by a hornblende-biotite tonalite that hosts abundant enclaves and diffuse leucocratic zones and dikes. The central domain is distinguished by a series of tonalitic units that show progressively lower enclave abundances towards the southeast. The third domain is located to the southeast and is defined by a composite sheeted dike complex that occurs along the southeast margin of the Isla Negra igneous complex. The following subsections document these divisions in detail.

Throughout all domains, magmatic foliations are moderately well developed and

are defined by the preferential alignment of subhedral tabular, bladed, and platy minerals such as plagioclase, hornblende, and biotite. Mineral trace lineations, defined by the alignment of mineral long axes within the magmatic foliation, are weakly developed. The best fit magmatic foliation throughout the complex dips moderately to the northeast and contains a bulk down-dip magmatic lineation (Fig. 2.2). Although the orientations of these features vary locally, a well-defined and consistent bulk magmatic fabric is found throughout the region. The orientations of sheeted dikes are generally concordant to the magmatic foliation as well as the flat surfaces of lenticular enclaves and zones of schlieren.

#### **2.4.1 Northwestern domain**

The northwestern domain consists of outcrops just south of Laguna Cordóva (Fig. 2.2 and 2.3) and exposures to the north towards Punta Tralca (Figs. 2.1). This domain is distinguished by tonalites with abundant enclaves that display a variety of shapes, sizes, and compositions. Enclaves frequently display strain shadows within the surrounding tonalite host and are commonly folded, boudinaged, and fractured with leucosome preferentially concentrated inside these small-scale structures. The northwestern domain also contains leucocratic dikes that display a wide variety of spatial relationships and geometries. The details of these structural associations are described below.

##### **2.4.1.1 Enclave textures**

Enclaves are prophyritic and are divided into three groups on the basis of the relative percentage and distribution of feldspar phenocrysts (Fig. 2.4). Groups one and two consist of evenly distributed phenocrysts (Fig. 2.4A & B), while the third group contains a heterogeneous phenocryst distribution (Fig. 2.4C). Group two is distinguished from group one by a relatively high percentage of feldspar phenocrysts (Fig. 2.4B).

Feldspar phenocryst distributions in heterogeneous enclaves are concentrated at the margin of the enclaves and grade directly into the tonalite host (Fig. 2.4C). Furthermore, feldspar grains within the host tonalite are petrographically indistinguishable from many of the phenocrysts found in the enclaves. Additionally, variations in enclave color indices indicate that the relative abundance of mafic constituents changes between enclaves throughout the region. Although these enclaves lack evidence for pervasive solid-state deformation, interstitial anhedral quartz grains do appear to have a crystallographic preferred orientation as qualitatively determined with the use of a lambda plate. Schlieren are associated with enclaves and tend to grade into diffuse, cusped (Fig. 2.4B) to lobate (Fig. 2.4C) enclave protrusions. This relationship is best observed in outcrop sections oriented parallel to the bulk magmatic lineation and perpendicular to the bulk magmatic foliation. These features, in the absence of evidence for pervasive solid-state deformation, suggest that material exchange between enclaves and the host tonalite may have occurred prior to complete crystallization of the enclaves.

#### **2.4.1.2 Enclave structures**

The hinges of folded enclaves ( $\sim 1\text{--}5$  cm in width) are filled with crescentic zones of leucosome that narrow along fold limbs and grade into the host (Fig. 2.5). The leucosome is characterized by a higher abundance of felsic minerals, such as feldspar and quartz, as compared to the tonalite host. Several of the folds are bounded by neighboring enclaves and display leucosome zones that widen into strain shadows. Magmatic textures within the host rock, such as aligned subhedral to euhedral plagioclase phenocrysts that lack evidence for pervasive crystal-plastic deformation, indicate folding was synmagmatic. As such, this association suggests enclave folding produced pressure gradients that transferred melt into fold hinges (see review by

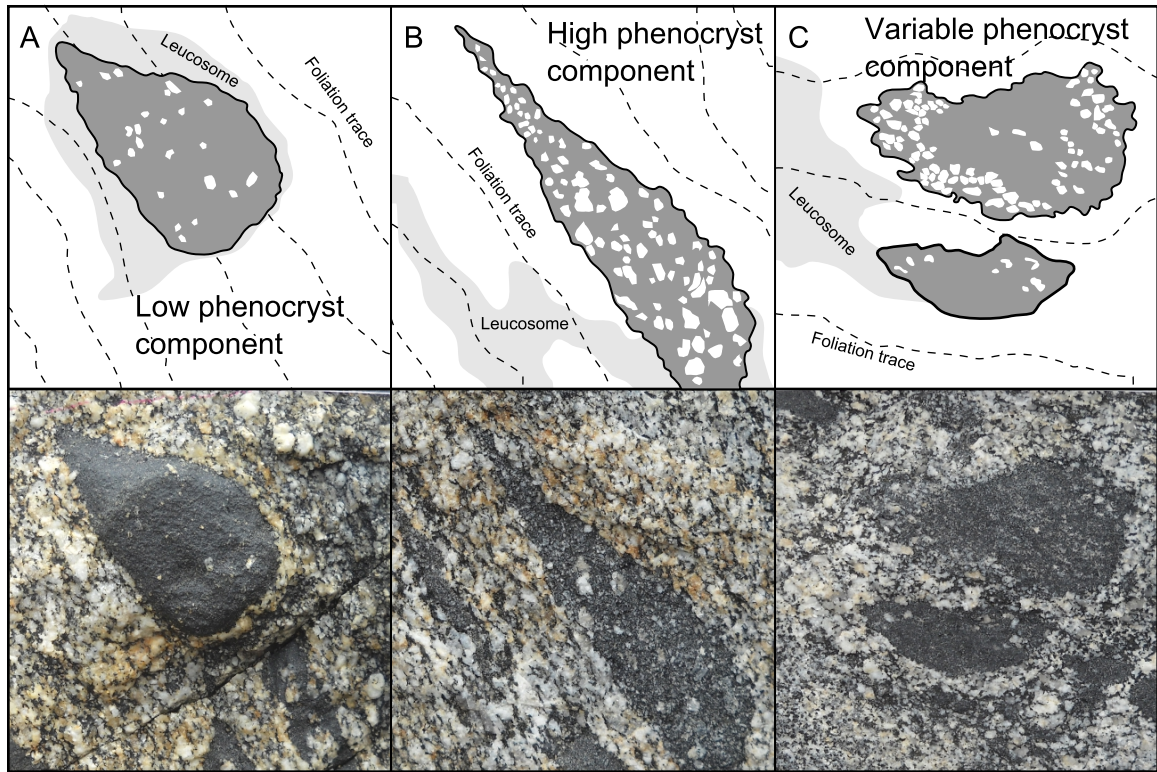


Figure 2.4: Basic enclave classification based on textures. The field of view in each photograph is 15 cm.

Brown and Rushmer 1997).

Enclaves frequently display wedge-shaped en echelon fracture arrays filled with leucosome (Fig. 2.6). These fractures occur in a variety of shapes from planar to sigmoidal with tapered tips and often occur together with shear band boudins. Figure 2.6 documents an example of this relationship where an array of three fractures display an approximate maximum stretching direction that is compatible with the dextral sense of shear developed along a neighboring shear band. Although it is tempting to discuss the angular relationship of these arrays to zones of shear<sup>4</sup>, the inability to constrain the three-dimensional orientations of these features invalidates the use

<sup>4</sup>For example, the angle between the shear plane and instantaneous shortening direction is often used to distinguish simple shear versus transpression or transtension regimes.

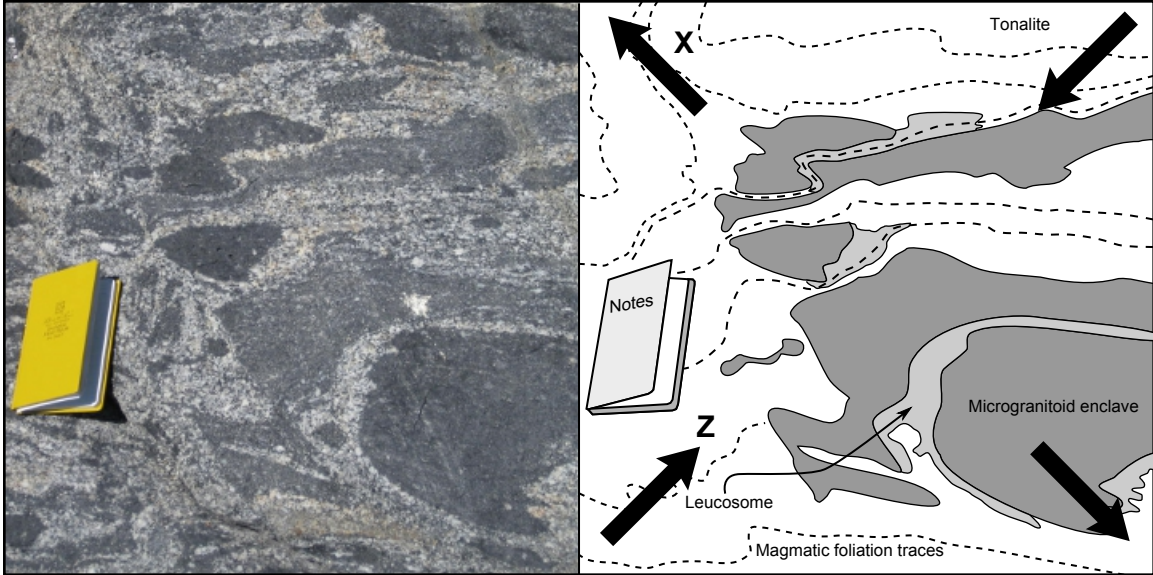


Figure 2.5: Photograph and sketch of folded enclaves with leucosome concentrated in fold hinges. Notebook width is  $\sim 19$  cm. The finite strain axes are inferred and shown with black arrows.

of general flow models. Nevertheless, we interpret these fracture arrays to be the result of tensile deformation under high fluid pressures and strain rates based on the presence of tapered tips, sigmoidal shapes, and their en echelon geometry. A component of shear may be accommodated by these tension gashes as evidenced by offset enclave boundaries and the neighboring shear band boudinage. Multiple tension gashes can form in a single enclave with non-parallel orientations and intersect such that isolated enclave fragments may be enveloped in leucosome as shown in Figure 2.6. Furthermore, the lengths of tension gashes can exceed half the width of the enclave and may record the initial stages of deformation prior to boudinage. The presence of tension gashes suggests high magmatic pressures together with high strain rates that can produce tensile deformation allowing for the concentration of melt.

Boudinaged enclaves commonly contain leucosome preferentially concentrated in interboudin partitions. The leucosome is preserved as medium to coarse-grained

feldspar and quartz preferentially aligned parallel to the boudin axis (Fig. 2.7). Mafic minerals observed within enclave boudin necks typically occur as lithic fragments likely derived from partial disaggregation of the enclave during boudinage. The development of tension gashes and boudins suggests changes in the general style of deformation (i.e. brittle vs. ductile) likely in response to either increases in the local strain rate or the progressive rigidification of enclaves such that fracture propagation becomes the preferred mechanism of deformation (Blake and Fink 2000; Paterson et al. 2004).

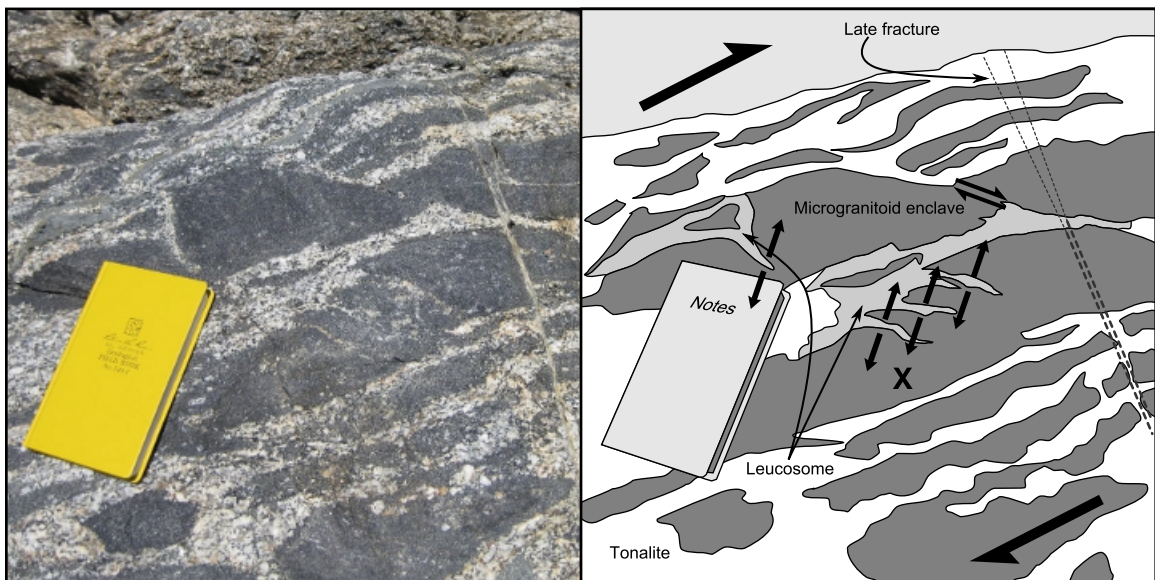


Figure 2.6: Photograph and sketch of fractured enclaves with leucosome concentrated in an echelon tension gashes. Notebook width is  $\sim 19$  cm. The finite strain axes are inferred and shown with black arrows. Tonalite is distinguished from leucosome by color and an increase in felsic minerals. Note that the shearband boudinage is defined by the small relative arrow symbol.

Enclaves and mafic xenoliths are commonly enclosed by magmatic foliations of the host tonalite and form strain shadows with increased leucosome concentrations (Fig. 2.8). Figure 2.8 documents a plagioclase hornblendite xenolith within a hornblende-biotite bearing tonalite. In this example, tonalite magmatic foliation traces symmet-

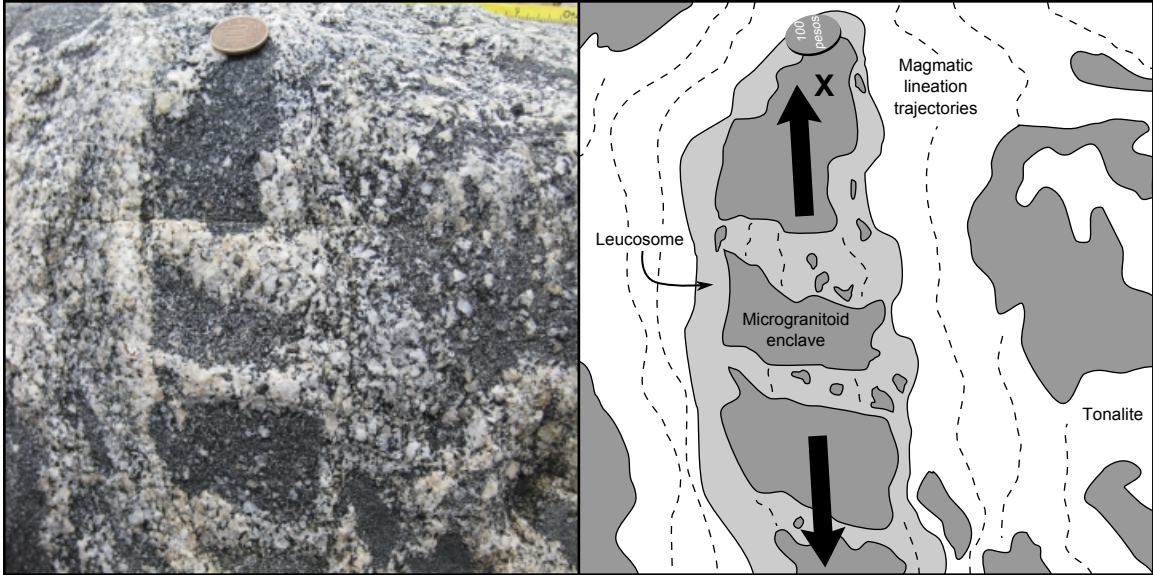


Figure 2.7: Photograph and sketch of boudinaged enclave with leucosome concentrated in boudin necks. Coin is roughly 2.5 cm in diameter. Section of view is roughly parallel to magmatic foliation. The finite strain axes are inferred and shown with black arrows..

rically deflect around, and envelope, the xenolith. The alignment of host minerals defining the magmatic foliation is better developed along the upper and lower surfaces of the object and become tangential to wedge shaped strain shadows. These strain shadows also contain lithic fragments identical to the xenolith that imply mechanical plucking of a rheologically competent object within hypersolidus flow (Fig. 2.8).

#### 2.4.1.3 Leucocratic dikes

Zones of leucosome throughout the enclave bearing tonalite unit at Isla Negra display a variety of geometries from globular domains to narrow dikes (Figs. 2.9 and 2.10). The boundaries of these domains range from diffuse and gradational with undulating and scalloped geometries (Fig 2.9) to discrete and planar. Leucosome domains also frequently surround and entrain enclaves (Fig. 2.9) whereas others directly truncate enclaves without entrainment (Fig. 2.10). Moreover, some leucosome domains

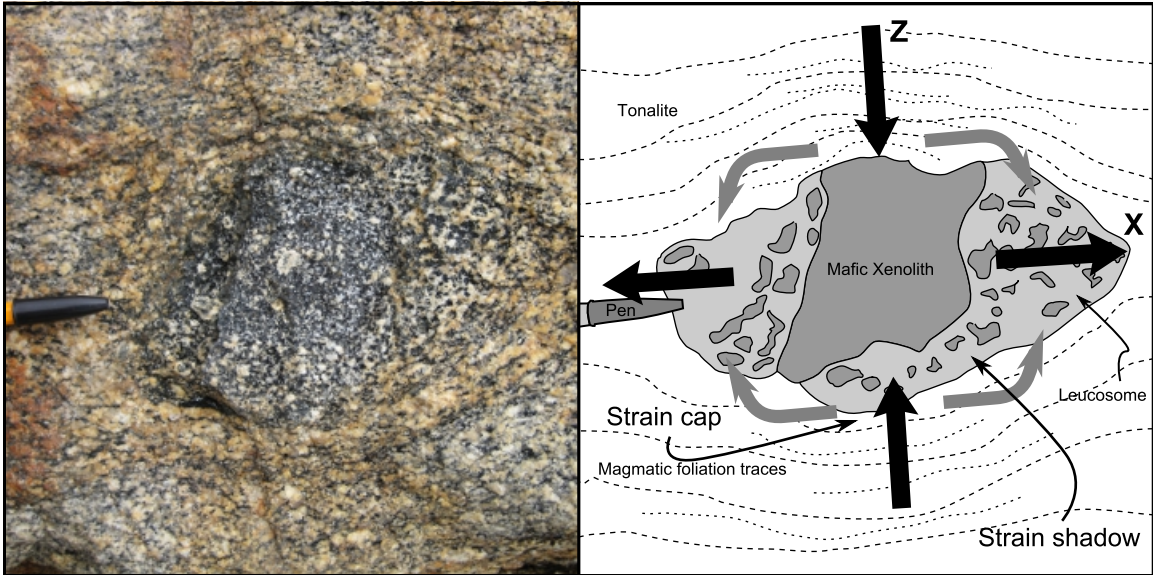


Figure 2.8: Photograph and sketch of partially dismembered xenolith with leucosome concentrated in strain shadows. Length of pen cap is approximately 3 cm. The finite strain axes are inferred and shown with black arrows. Gray arrows define inferred pressure gradient trajectories that illustrate the flow of melt prior to complete crystallization.

show planar apophyses with tapered tips that cross-cut fabrics within the tonalite host (Fig. 2.10). This suggests that leucosome domains may form from multiple mechanisms including fracture propagation (proto-dike formation) and inundation of low melt-fraction magmas via pooling. Leucocratic zones range in thickness from centimeter to meter scale and frequently bifurcate to form interconnected networks. The diversity of leucosome dike geometries with mutually cross-cutting relationships is indicative of the collection of magma within diffuse zones forming incipient dikes followed by hydraulic overpressurization and fracture propagation (see discussion on dike formation by Gudmundsson 1984). The formation of these interconnected dikes likely accommodated the extraction of melt from a crystal mush into larger networks of melt-rich magma.



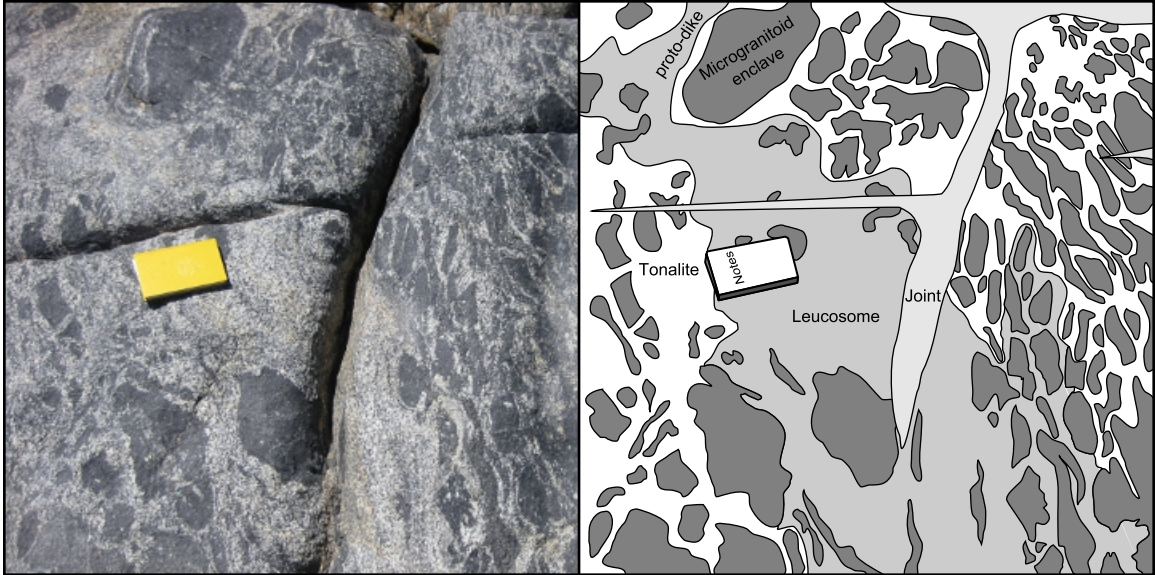


Figure 2.9: Photograph and sketch of a concentrated leucosome in diffuse undulating zones. Notebook length is  $\sim 19$  cm.

#### 2.4.2 Central domain

In contrast to the northwestern domain, which is characterized by the shortening and stretching of enclaves and xenoliths to produce structures that mobilized melt and formed proto-dikes, the central domain documents the transportation and emplacement of magmatic pulses under variable flow regimes. This domain, located south of Laguna Cordóva (Figs. 2.2 and 2.3), is characterized by the progressive decrease in enclave abundance and the variable geometries of enclave swarms through a series of approximately tabular tonalitic units. Cross-cutting relationships, such as rafted xenoliths and narrow truncating apophyses indicate emplacement younging to the southeast. Contacts between tonalitic units display non-planar cusped-lobate geometries that are locally diffuse and gradational. The following sections describe the quantification of fabrics defined by both the orientations and ellipticities of enclaves, as well as the statistical alignment of feldspar grains from two tonalitic units

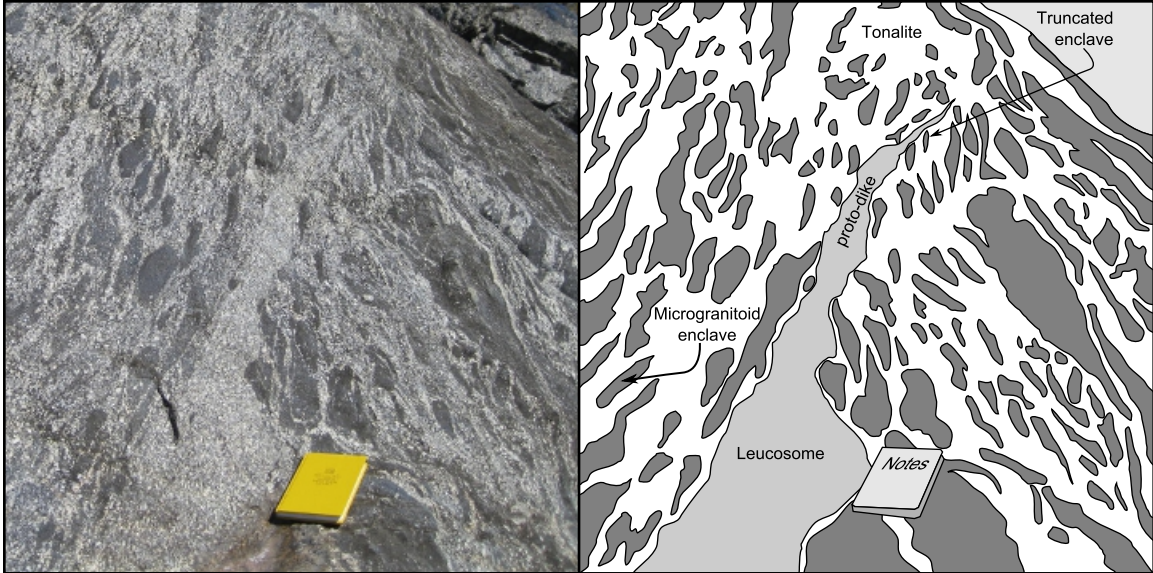


Figure 2.10: Photograph and sketch of an overpressurized leucosome domain with a tapered proto-dike apophysis (likely representing the initial stage of dike formation) extending into background. Notebook length is  $\sim 19$  cm.

at location 11-IN-01 (Fig. 2.2).

I documented the development of distinctive fabrics in response to the influx of new magma and how these relate to hypersolidus flow regimes. Despite the lack of variance in magmatic foliation and lineation orientations across these units (see stereographic projection in Figure 2.2), the architecture of enclave swarms change as indicated by three-dimensional fabric analyses. This suggests that subsequent magmatic pulses display widely different flow regimes, yet maintain a larger-scale fabric likely imposed by boundary conditions such as the margins of the host rock or more viscous dikes.

#### 2.4.2.1 Field-based observations

Location 11-IN-01 (Fig. 2.2) documents the interaction of two tonalitic units distinguished by enclave swarm concentrations, packing, and three-dimensional fabric

geometries. The northwestern unit is the left portion of the outcrop face as shown in Figure 2.11. The southeastern unit contains rafts of the northwestern one indicating that it is younger in age. The contact between the units show thin diffuse leucocratic dikes with undulating cusped-lobate geometries that grade into the southeastern unit, near the base of the outcrop (Fig 2.11). Splays of this dike intrude the northwestern unit and terminate with tapered tips. Enclaves within the northwestern unit are highly concentrated and display a large degree of impingement. Enclaves are frequently bent around neighboring enclaves from which they are separated by thin layers of tonalite matrix. Although the enclaves in this unit generally impinge one another, they do not completely coalesce. This clast-supported enclave swarm creates<sup>5</sup> a network of interconnected volumes separated by impinged enclaves that are filled with tonalite matrix. The southeastern unit contains a significantly lower enclave fraction where neighboring enclaves only locally impinge and form a matrix supported enclave swarm. Although both units are hornblende-biotite bearing tonalites, the southeastern unit contains a smaller modal fraction of mafic minerals. Nevertheless, modal percentages of these mafic constituents locally vary in both units. Thus, 11-IN-01 records the boundary between two syn-plutonic dikes with different compositions and enclave packing.

#### **2.4.2.2 Enclave swarm architecture**

In order to better define the characteristics of different flow regimes within the Central domain, I quantified changes in the three-dimensional architecture of enclave swarms. These calculations are based on the orientations and shapes of enclaves at location 11-IN-01 as determined by the  $R_f/\phi$  technique. The details of this methodology are

---

<sup>5</sup>This clast-supported network refers only to the northwestern unit shown on the left side of Figure 2.11. The probability of intersecting a surface (i.e. the outcrop surface) through a point of impingement is low compared to the intersection area of the matrix, that is, the corpuscle effect following Burger and Skala 1976.

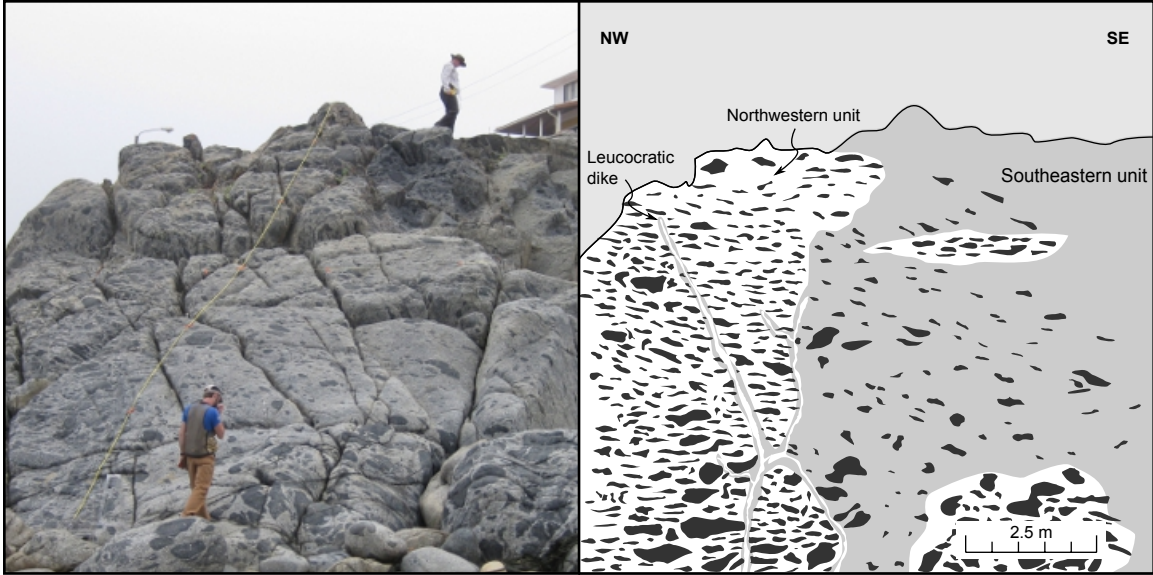


Figure 2.11: Photograph and sketch of location 11-IN-01 (see Figure 2.2) illustrating two distinct tonalite phases. Enclave swarm fabrics are distinctive between the older northwest unit and the younger southeast phase, as explained in the text.

explained with detail in Chapter 3 and Appendix B. Data collection involved both manual measurements and digital imagery on faces aligned approximately parallel to the three principle fabric planes. The orientations of the principle fabric planes were calculated using magmatic foliation and lineation measurements as proxies (see stereographic projection in Fig. 2.2). Therefore, the best fit lineation corresponds to the fabric X-axis contained within the best fit foliation plane. By definition, the foliation plane also contains the fabric Y-axis and is orthogonal to the fabric Z-axis. As such the orientations of the poles to the principle fabric planes are defined as shown in Table 2.1. Outcrop faces closely aligned to these fabric planes were grouped into three mutually perpendicular sections such that the largest angular difference between any outcrop face and the corresponding principle fabric plane is  $11^\circ$  (Table 2.1). Section “A” correlates the X-Y fabric plane, “B” to the X-Z fabric plane, and “C” to the Y-Z fabric plane. Changes in the properties of the enclave swarms provide

details on the nature of changing hypersolidus flow regimes during injection of new tonalitic phases within the central domain.

Table 2.1: Analytical enclave section orientations vs fitted L-S fabric data.

Correlation	Pole to section	Pole to fabric axis	Angular difference
A-XY	240° 41°	231° 38°	8°
B-XZ	334° 02°	330° 14°	11°
C-YZ	065° 49°	078° 54°	10°

In total, the axial lengths and orientations of 203 enclaves were measured for six sectional  $R_f/\phi$  analyses that contained an average population size of 34 enclaves per section (Figs. 2.12 and 2.13). Section “A” from the northwestern tonalite produced a fairly symmetric  $R_f/\phi$  plot with an index of symmetry = 0.8 and a moderate harmonic mean of 2.13 (Fig. 2.12). An  $R_S$  value of 1.54 was obtained from the Microsoft® Excel macro written by Chew (2003) using a  $\chi^2$  function. Section “B” produced a significantly different  $R_f/\phi$  plot with a much lower index of symmetry value ( $s = 0.75$ ) and a higher harmonic mean (2.71). Furthermore, the enclave traces display a high degree of alignment with higher ellipticities and produced a fabric ellipse ratio of 2.55 ( $R_S$ ). The third section (“C”) produced a moderate  $R_S$  value of 2.03 with a harmonic mean of 2.39 and a high index of symmetry ( $s = 0.86$ ). These sectional analyses indicate the highest degree of enclave alignment and ellipticity in outcrop sections oriented parallel to the bulk magmatic mineral trace lineation and perpendicular to the magmatic foliation. Sectional analyses from the southeastern unit produced substantially different results. Section “A” from the first unit displayed a symmetric plot (index of symmetry  $\sim 1$ ) with a moderate harmonic mean of 2.44 and a value of 2.36 for the sectional fabric ellipse. Section “B” also displayed an extremely symmetrical plot ( $s = 0.9$ ) but contained a higher harmonic mean and  $R_S$

value of 5.11 and 4.45 respectively. Finally, section “C” produced results similar to section “A” (harmonic mean = 2.42;  $R_S = 2.04$ ) aside from a much more skewed index of symmetry ( $s = 0.78$ ). Not unlike the first unit, the sectional results from the southeastern domain indicate the highest degree of enclave alignment and ellipticity in sections parallel to magmatic lineations and perpendicular to magmatic foliations. Nevertheless, the axial ratios of sectional fabric ellipses are generally higher in this unit with respect to the northwestern unit.

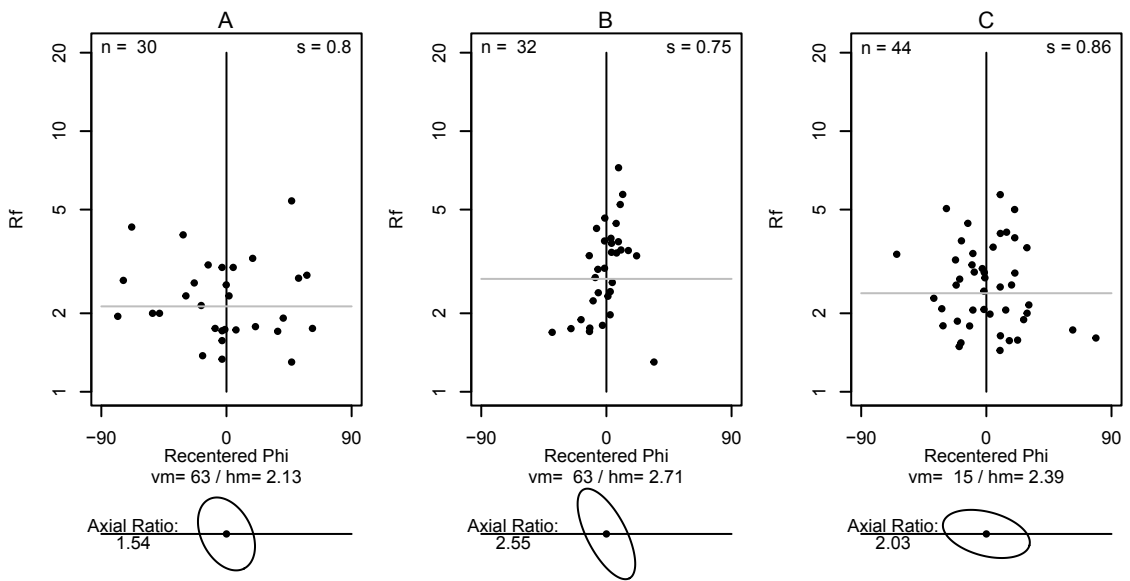


Figure 2.12: Sectional  $R_f/\phi$  results from the northwestern unit at location 11-IN-01. Analyses “A”, “B”, and “C” correspond to the three mutually perpendicular principle fabric planes describe in Table 2.1.

The sectional results from the two units at 11-IN-01 yielded two best-fit fabric ellipsoids using the software program *Ellipsoid 2003* (Launeau and Robin 2005). From this program, the orientations and normalized lengths of fabric ellipsoid axes were obtained and modeled using code explained in Chapter 3. Figure 2.14 contains rendered views of the synthesized fabric ellipsoids from the northwestern unit (Fig. 2.14A) and

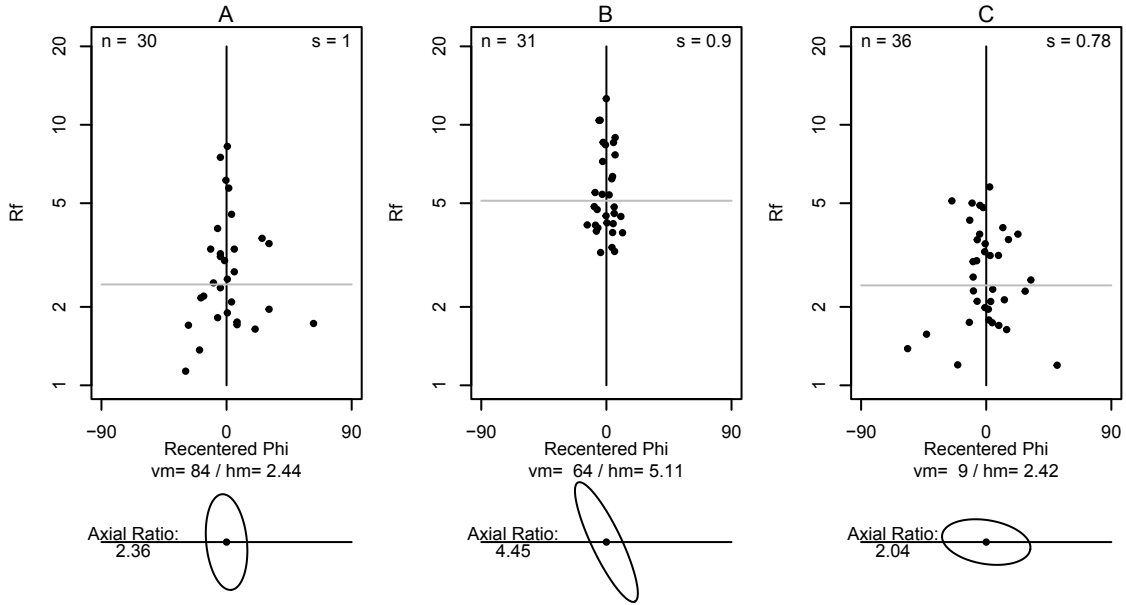


Figure 2.13: Sectional  $R_f/\phi$  results from the southeastern unit at location 11-IN-01. Analyses “A”, “B”, and “C” correspond to the three mutually perpendicular principle fabric planes describe in Table 2.1.

the southeastern phase (Fig. 2.14B) that clearly display distinct geometries. The orientations of the calculated fabric ellipsoids are plotted in Figure 2.15A and contain closely aligned X-Y principles planes, as well as X-axes.

The calculated best-fit fabric ellipsoid axes are parallel to the bulk magmatic foliation (corresponding to the calculated X-Y planes) and magmatic mineral lineation (X-axis) (Fig. 2.15A). Although the ellipsoid orientations are similar, the corresponding shapes are clearly different. This disparity is best illustrated by the Nadai plot in Figure 2.15B. The Nadai plot represents strain magnitude space, used herein as a proxy for “fabric magnitude space,” and compares the magnitude of distortion ( $\bar{\epsilon}_s$ ) to the fabric symmetry ( $\nu$ ) (see review of strain magnitude space by Brandon 1995). These parameters are based on Equations 3.10 and 3.9 which are described with detail in the corresponding chapter. The calculated fabric ellipsoid from the northwestern

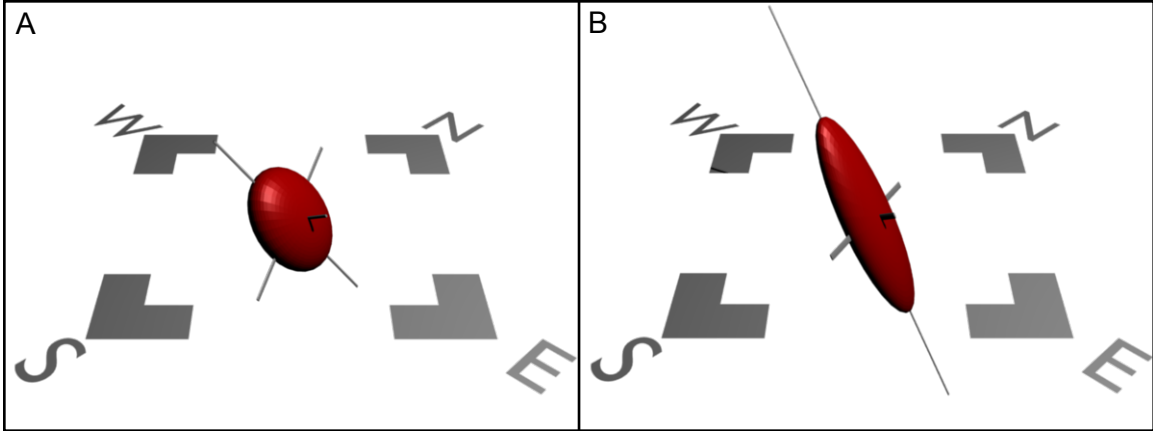


Figure 2.14: Rendered image of oriented fabric ellipsoids from the northwestern (A) and southeastern (B) units at 11-IN-01 corresponding to oblate and prolate fabric symmetries. Ellipsoids normalized to an equal volume.

unit plots well within the oblate field (i.e.  $\nu = 0.46$ ) and has a relatively low magnitude of distortion (i.e.  $\bar{\epsilon}_s = 0.73$ ). The fabric ellipsoid from the southeastern unit, however, plots within the prolate field (i.e.  $\nu = -0.24$ ) and is substantially more distorted (i.e.  $\bar{\epsilon}_s = 1.36$ ).

### 2.4.2.3 Mineral alignment

In order to determine if the distributions of feldspar long axes from the tonalite host record similar changes in fabric architecture as displayed by the enclave swarms, the two-dimensional orientations of 1,726 feldspar grains were measured. These data were collected from three mutually-perpendicular sections of two samples corresponding to the units at 11-IN-01. The outlines of individual feldspar grains were traced from scanned images of known orientation and processed in the program SAPE to extract the rake of each long axis (Mulchrone et al. 2005). Figure 2.16 contains six histograms corresponding to the principle fabric planes (e.g.  $XY \sim$  foliation) of the two samples. Each histogram is normalized to the population size and re-centered along the vector



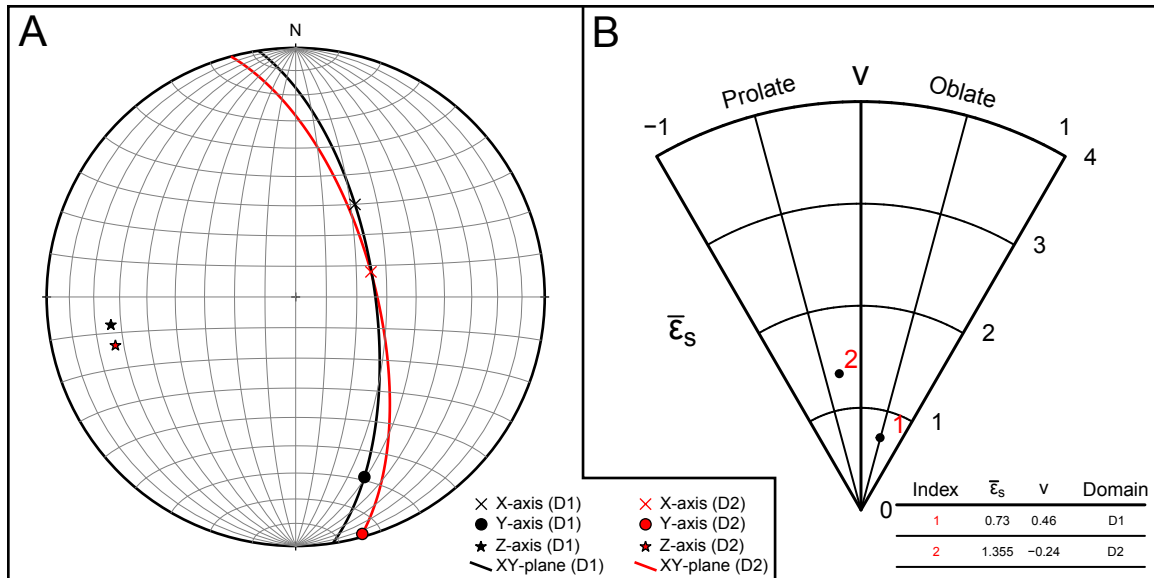


Figure 2.15: A: equal area stereographic projection of principle fabric axes from two tonalitic sub-domains at 11-IN-01. B: Nadai plot illustrating the relationship between fabric symmetry ( $\nu$ ) and the octahedral shear fabric ( $\bar{\epsilon}_s$ ).

mean (calculations presented by Lisle 1985). The circular standard deviation (Fisher 1996) and population size are also presented for each analysis. Histograms that display a more pronounced peak and lower circular standard deviation indicate sections where two-dimensional feldspar axes are more aligned. Conversely, histograms without pronounced peaks and higher circular standard deviations correspond to sections with poorly aligned grains. For both units at 11-IN-01, sections oriented parallel to the bulk magmatic lineation and perpendicular to the magmatic foliation (XZ) have the most pronounced peaks, indicating a greater degree of mineral alignment. Mineral alignment within this section from the southeastern unit is higher than the north-western unit as determined from the circular standard deviations. Sections oriented parallel to the XY and YZ principle fabric planes display a lower degree of alignment and are similar between the domains. As expected from the bulk magmatic foliation

orientation where traces of mineral alignment can be followed across corners, feldspar grains observed in the XY fabric plane are slightly more misaligned than the YZ plane. The preferential alignment of feldspar grains in the XZ fabric plane mimics the enclave swarm architecture and roughly defines a common X-axis. This style of mineral alignment suggests a hypersolidus flow regime where feldspar phenocrysts are allowed to rotate within the bulk foliation plane and can more freely spin about their long axes suggesting a general flattening style of hypersolidus flow.

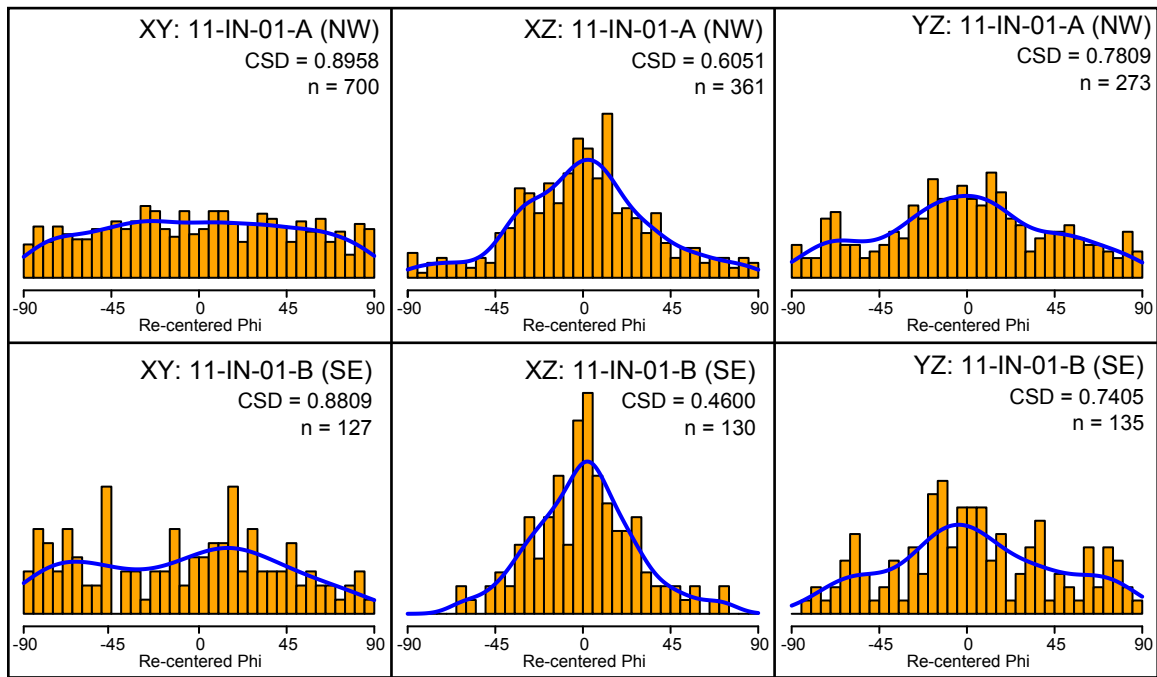


Figure 2.16: Normalized histograms of feldspar long axis orientations determined from two samples collected at location 11-IN-01 (see Figure 2.2). Individual plots correspond to the respective principle fabric plane and tonalitic unit. Histograms in upper row are from the northwestern enclave abundant tonalite unit shown in Figure 2.11. Lower plots are from the southeastern unit. The circular standard deviations (CSD) are displayed for each analysis.

### 2.4.3 Southeastern domain

The southeastern domain is located along the margin of the Isla Negra igneous complex (Fig. 2.2 and 2.3) and is characterized by the occurrence of sheeted dikes that are intercalated with screens of biotite-rich migmatitic host gneiss that frequently grade into schlieren (Fig 2.17). These dikes consist of numerous compositionally and texturally distinctive phases that can be grouped into three major lithological classifications. These include porphyritic granitoids, enclave bearing granitoids, and migmatic biotite-rich host gneiss. The porphyritic granitoids contain several sub-phases that include megacrystic granodiorites, granites, and tonalites. Enclave-rich granitoid sheets are similar in composition to the hornblende-biotite tonalites described previously, yet generally tend to contain higher mafic mineral percentages. Biotite rich migmatitic screens display wide variations in leucosome concentrations and are commonly difficult to distinguish from schlieren zones in the granitoids. Moreover, several porphyritic granitoid dikes host biotite rich pods and isolated ribbons of concentrated schlieren (Fig. 2.17). The orientations of sheeted dikes are concordant to the bulk magmatic foliation, which is generally well-developed within individual dikes. Location 11-IN-03 also hosts late-stage mafic dikes (Fig. 2.17) that truncate magmatic foliations and sheeted dike contacts. Although the relative timing of all magma injections cannot be ascertained from these field relationships (excluding those previously described in section 2.4.2), the syn-plutonic style of dike emplacement is well evidenced by the folded cusped-lobate geometry of dike contacts as well as exceptionally well preserved magmatic mineral textures.

## 2.5 Discussion

The Coastal Batholith of central Chile forms the archetypal example of a mid-crustal igneous complex developed during oceanic-continent convergence. This batholith is

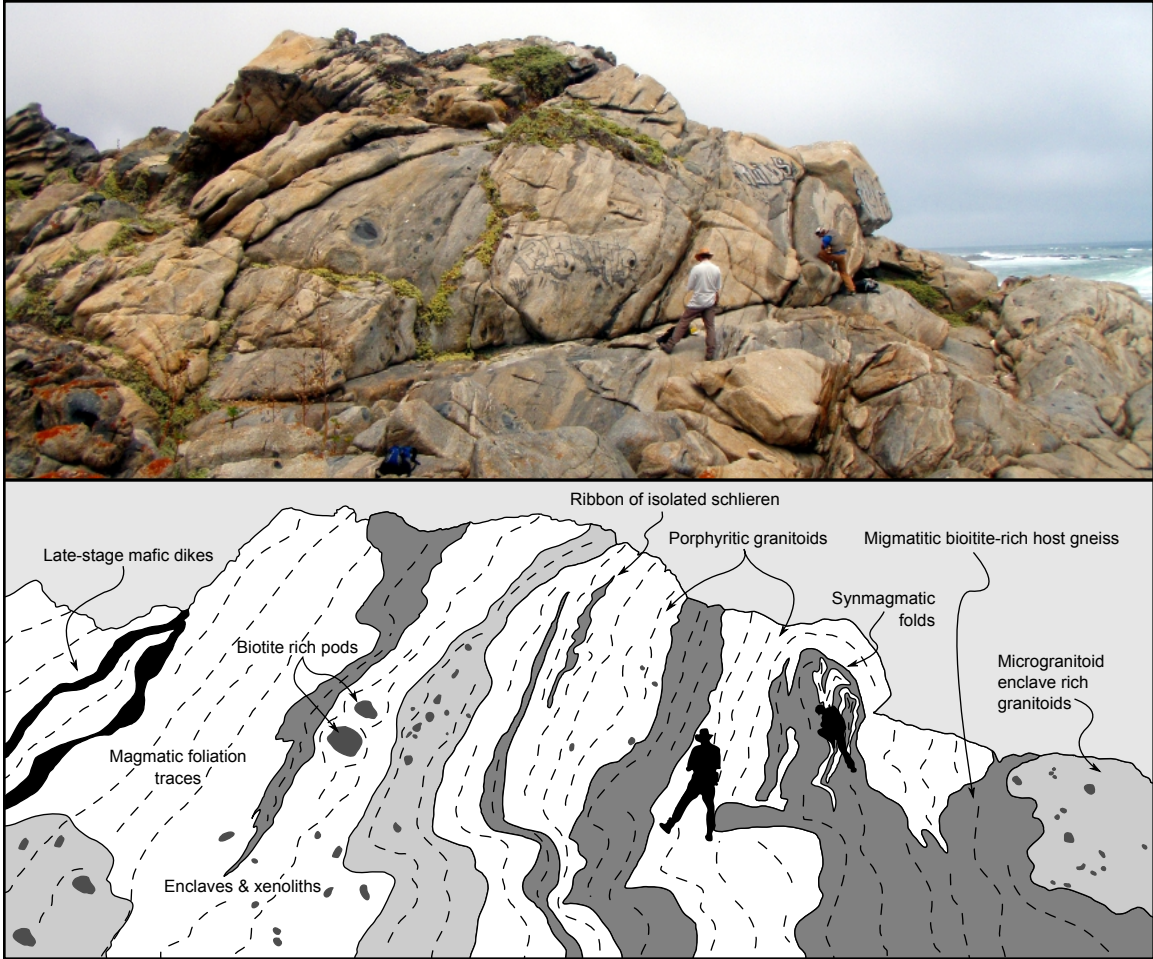


Figure 2.17: Photograph and sketch of location 11-IN-03 (see Figure 2.2) illustrating the sheeted dike geometry of compositionally and texturally distinctive phases.

comprised of three main plutonic belts that record an eastward migration of magmatism. The oldest of these complexes is the Santo Domingo Complex that is Late Paleozoic in age. Due to the eastward shift of magmatism, the exposures of the Santo Domingo Complex lack the overprinting of younger magmatism. As such, features observed within these rocks likely record processes that may be occurring beneath the modern arc.

One of the most poorly understood aspects of granitic magmatism has to do with

the significance of structures preserved in plutons and batholiths. These features include the formation and relative development of magmatic foliations and lineations, enclave swarms, hypersolidus folds, and dikes. Although these structures must form in response to differential stresses, complex spatial and temporal variations in strain make distinguishing flow regimes, in a continuum mechanics sense, ambiguous. As such, the application of traditional structural mechanics (e.g. pure shear vs. simple shear) to the quantification of deformation within polyphase systems (i.e. solid and liquid constituents) has been met with warranted resistance<sup>6</sup>. This is complicated by the non-linear changes in strain rates, viscosities, and composition through crystallization. Therefore, assumptions of progressive homogenous deformation are difficult to constrain. Despite this complexity, a large body of literature has established the genetic role of hypersolidus flow and host rock deformation in the transportation of magma through the crust.

Structures preserved within the Isla Negra igneous complex document the concentration of melt-rich magma (evidenced by the presence of leucosome) within dilational sites (Figs. 2.5, 2.6, 2.7, 2.8, and 2.18). These sites developed in association with rheologically competent enclaves and are analogous to structures widely documented in migmatite terrains (see review by Brown and Rushmer 1997). The preferential formation of leucosome in saddle reefs (hinges of folded enclaves), tension gashes, interboudin partitions, and strain shadows indicate that melt can be freely extracted from a crystal mush. Although specific structures may develop in response to changes in local stresses, many features are compatible with the orientations of regional shortening and extension as determined by the bulk foliations and lineations. For example, boudinaged enclaves are best observed in sections oriented parallel to the magmatic

---

<sup>6</sup>Criteria outlined by Tikoff and Fossen 1995, for identifying vorticity in naturally deformed rocks are genetically solid-state, whereas the application of vorticity to the magmatic state has largely been experimental; see for example Dlugogorski et al. 1994

mineral trace lineation. Moreover, the occurrence of en echelon tension gash arrays are compatible with the sense of shear expressed by shear band boudinage in neighboring enclaves. Many of these shear bands are observed in sections orthogonal to the mineral trace lineation, which suggests shear across the principle stretching direction if the development of these features are assumed to be contemporaneous. This triclinic deformation symmetry may be a product of local (internal) magmatic stresses and regional (external) stresses. However, the details of this possibility remain unconstrained. The presence of sigmoidal tension gashes may suggest simultaneous ductile shear and brittle fracture propagation facilitated by fluctuations in local strain rate<sup>7</sup> during the rigidification of enclaves (following nomenclature of properties presented by Blake and Fink (2000) to define the cessation of enclave distortion). Nevertheless, the concentration of leucosome within mesoscale features associated with enclaves and xenoliths suggests that rheological heterogeneities are important in the mobilization of melt from within a crystal mush.

The association of tabular enclave swarms and zones of increased schlieren concentration that resemble syn-plutonic dikes has led previous workers to interpret the origin of enclaves as dismembered mafic intrusions prior to the full crystallization of the host. Although the exact provenance of the enclaves I studied remains poorly understood, variations in enclave textures suggest several processes involving the exchange of material. This textural heterogeneity may be the result of multiple batches of magma or a single heterogeneous magma source. The localized increase in plagioclase phenocrysts near the margin of some enclaves suggests a possible partial mixing of the tonalite host. This texture could represent xenocrysts that were mechanically

---

<sup>7</sup>The presence of features that display both brittle and ductile mechanisms of formation (e.g folded tension gashes) with mutually cross-cutting relationships indicates that temperature fluctuation is unlikely a dominate control on deformation style. Therefore, strain rate fluctuation is a plausible control on deformation style following experiments by Gumbsch et al. 1998.

entrained within the host and are therefore not chemically mixed (*sensu stricto*). Nevertheless, the elongation of enclaves suggests some degree of magma mixing (Vernon et al. 1988). This reasoning remains equivocal due to the occurrence of foliations within enclaves defined by the alignment of hornblende and biotite grains that contain interstitial anhedral quartz, which displays a crystallographic preferred orientation<sup>8</sup>. The application of geochemical analysis to these enclaves may elucidate the nature of magma interaction in future work. Finally, the occurrence of enclaves with cusped wispiness that grade into schlieren highly suggests the mechanical abrasion of grains from the enclaves by a less viscous matrix. The general orientation of these tips, as observed in outcrop sections perpendicular to the bulk magmatic foliation and parallel to the mineral trace lineation (i.e. XZ principle fabric plane), may indicate up-dip matrix flow to the southwest relative to the enclave swarm from the northwestern domain of Isla Negra.

The three domains of the Isla Negra igneous complex characterize a progression of melt concentration, mobilization, and transportation into interconnected networks that permit the transportation of progressively higher volumes of magma into tabular bodies, which produced a sheeted dike complex (Fig. 2.18). The formation of melt-rich networks within the pluton may produce younger dikes that can interact under syn-magmatic conditions with older phases. The tonalite units within the central domain document changes in fabrics developed with the emplacement of new magma pulses as evidenced by both cross-cutting relationships and fabric analyses. These fabric analyses document the transition from oblate low-magnitude distortion fabrics developed in older enclave swarms that are characterized by enclave supported networks to moderately distorted prolate swarms within younger units characterized by matrix supported enclave swarms. One sectional  $R_f/\phi$  analysis (XZ plane) from the

---

<sup>8</sup>See Section 2.4.1.1.

northwestern unit displays a low index of symmetry ( $S = .75$ ) and may have resulted from the superposition of multiple igneous fabrics (see Section 2.4.2.2). The change in enclave swarm architecture is accompanied by a slight change in host mineral alignment. This suggests that the alignment of matrix minerals is sensitive to changing flow regimes that also appear to affect the shapes and orientation of enclaves. Nevertheless, the orientations of all fabric elements such as mineral foliations, mineral lineations, enclave foliation (XY) planes, and stretching directions (X-axes) indicate the orientation of magma flow during transportation just prior to emplacement below the particle locking threshold (Paterson et al. 1998; Vigneresse and Tikoff 1999).

The notion of “last gasp” magmatic fabric development has led previous workers to suggest that magmatic fabrics may reflect the instantaneous state of strain developed under regional paleostresses (Paterson et al. 1998). This, however, remains as conjecture for the time being within the Coastal Batholith, and likely for most areas as studies continue to show heterogeneous deformation in many plutons. The fact that the orientations of these sheeted dikes are concordant to the orientations of the previously mentioned fabric elements indicates that, although flow regimes are unique developed within dikes, external boundary conditions (e.g pluton margin<sup>9</sup> or older dikes) likely determine the bulk orientations of features developed in the complex.

Although it is tempting to describe the enclave swarm fabric analyses in terms of strain, numerous factors clearly invalidate the assumptions required to address the magnitude and symmetry of strain. These assumptions include the state of homogeneous deformation at the scale of analysis, the passive nature of markers, the ability to constrain the initial properties of marker populations, the identification of single

---

<sup>9</sup>This statement does not preclude the fact that pluton margins are frequently structurally controlled. See for example Kalakay et al. (2001).



marker geometries in three-dimensions, the belief that all markers are the same age, the use of a sufficient number of markers to be statistically viable, the degree of viscosity contrasts can be determined, and that data are collected at a scale in which principle planes of strain exist (see requirements presented in Paterson et al. 2004 p. 1467).

The enclave swarms at Isla Negra violate many of these assumptions. Even if we assume homogenous deformation, the three-dimensional geometries of enclaves cannot be assumed ellipsoidal. We have clearly shown enclaves that contain fractures and are folded with wispy cusped tips. Moreover, viscosity contrasts are nearly impossible to constrain due to the clear variety in deformation styles including enclave elongation, fracturing, folding, and abrasion. This implies a large spectrum of enclave rheologies that was likely highly variable through time. This variety of deformation mechanisms also invalidates the notion of passive marker deformation. For example, the boudinage of enclaves will essentially reset the  $R_f$  value determined for that enclave. Moreover, shear band boudinage is observed at variety of levels of development and suggests that the slightly asymmetric shapes of many enclaves may have been produced by this process. Nevertheless, variations in the index of symmetry obtained from  $R_f/\phi$  analyses as well as gradients in fabric shape and orientation may provide information on the possibility of multiple superimposed fabrics with regional scale kinematic implications.

Although the finite state of strain is not reflected in my results, they indicate a change in the architecture of enclave swarms with respect to different pulses of magma. This change in architecture is most likely due to differences in the nature of hypersolidus flow as imposed by the packing arrangement of enclaves, pressure gradients, viscosities, and pluton boundaries. One promising aspect of regional fabric studies is the ability to sub-divide regions of plutonic complexes in terms of structural

domains that record stages of emplacement. This may elucidate regional trends in flow style with respect to fabric rotation (and therefore, imply regional kinematics) and magnitude of development. Despite the difficulties previously mentioned in ascertaining the kinematics of plutonic features developed during emplacement, this style of fabric quantification may aid in the reconstruction of progressive continental growth via batholith construction. The associations of these features within the context of cross-cutting relationships indicates that melt concentration, mobilization, migration, transportation, and emplacement are not genetically linked in series<sup>10</sup>, and may in fact occur diachronously or simultaneously within a spatially complex system.

## 2.6 Conclusions

The Coastal Batholith of central Chile preserves structures that document the progressive construction of a sheeted dike complex within a pluton that was emplaced along the margin of western Gondwana during late Paleozoic and Jurassic times. Exposures between Isla Negra and El Tabo record diverse magma types, including tonalites, diorites, granites, and granodiorites. These magmas interacted with each other under hypersolidus conditions forming enclaves and syn-plutonic dikes with viscosity contrasts that locally exchanged material forming schlieren and compositionally variable enclaves.

Deformation of rheologically competent phases was associated with the partitioning of leucosome into mesoscale structures such as fold hinges, boudin necks, tension gashes and strain shadows. The deformation that produced these structures concentrated melt from the crystallizing host tonalite and produced interconnected domains of leucosome. The contacts between leucosome domains and host tonalite are diffuse, undulating, and scalloped. Other leucocratic zones display contacts that are more

---

<sup>10</sup>For a review of granitic magmatism terminology see Brown (2001).

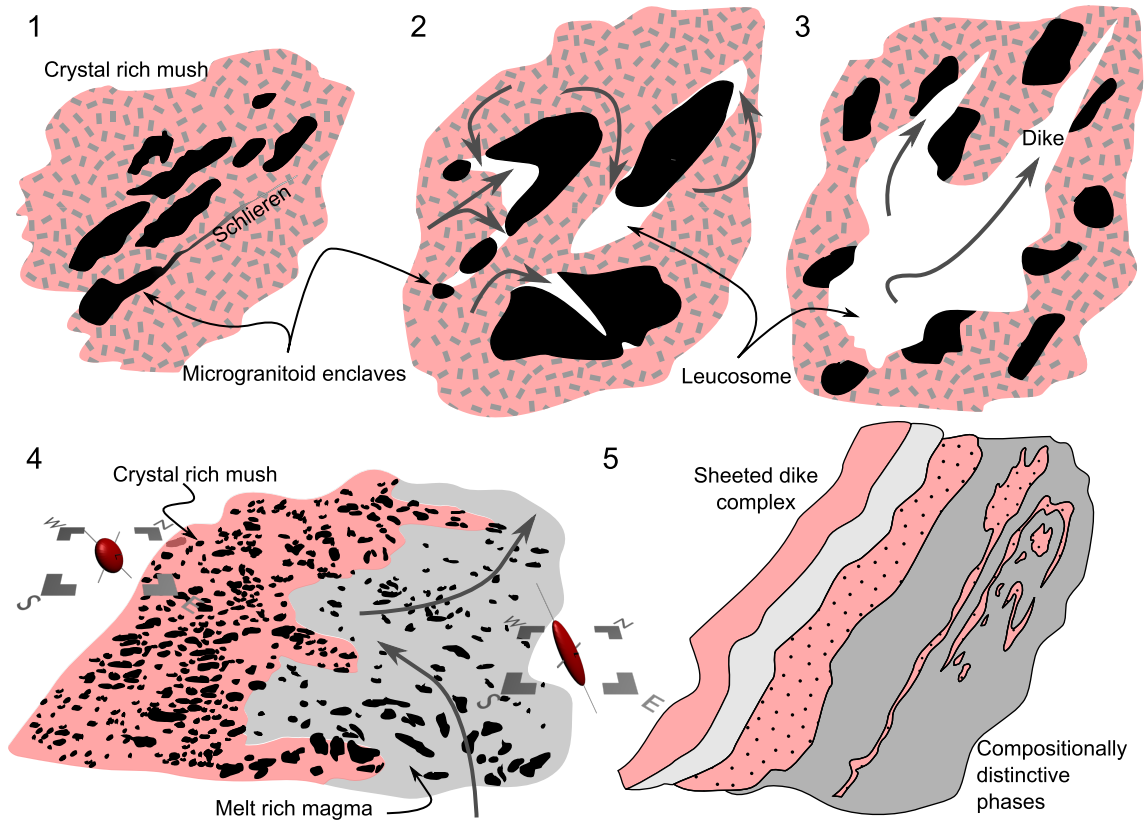


Figure 2.18: Schematic diagram displaying the general evolution of magmatic phases recorded within the igneous complex between Isla Negra and El Tabo. 1.) Incomplete interaction of compositionally distinctive magmas forming enclaves and schlieren. 2.) Rheological heterogeneities create dilational sites that concentrate melt during deformation of crystal rich mush. 3.) Small volumes of concentrated melt pool and become overpressurized causing diking. 4.) Dikes and melt rich domains become interconnected and increase in volume forming distinct magmatic phases and flow kinematics 5.) Magmatic phases emplace as dikes forming a composite sheeted pluton along margin with host rock.

planar and well defined. The presence of tapered apophyses originating from diffuse leucocratic zones suggests locally fluctuating strain rates and magmatic overpressurization that facilitated fracture propagation and formed proto-dikes.

The formation of interconnected dikes implies the transportation of higher volumes of melt-rich magmas through the crystal mush that produced subsequent magmatic pulses. Synmagmatic folds and cusped-lobate contacts between these magmatic pulses indicate emplacement of new phases prior to complete crystallization of host units below the particle locking threshold (Vigneresse and Tikoff 1999). This progressive emplacement of numerous magmatic phases along the pluton margin formed a sheeted dike complex with diverse textures and compositions.

The progressive emplacement of sheeted dikes was accompanied by distinctive flow regimes that are distinguished by changes in the architecture of enclave swarms and mineral fabrics. The results of three-dimensional fabric analyses applied to enclave swarms within two tonalitic units indicate a clear difference in fabric symmetry as a function of the arrangement of enclave shapes and orientations. Additionally, the statistical alignment of feldspar phenocrysts within the host tonalite for the enclave swarms indicates a general flattening flow regime that is relatively similar for both units. The orientations of the calculated fabric ellipsoid X-Y planes and Z-axes are concordant to the regional magmatic foliations and mineral trace lineations, respectively. This association allowed me to recognize commonalities in fabric orientations at a variety of scales (e.g. large dike orientations, mineral orientations, and enclave swarm geometries) that is indicative of a flow regime imposed by conditions likely resulting from the boundaries of the igneous complex or previously emplaced dikes. This concordance of multiple features throughout the Isla Negra igneous complex suggests that regional boundary conditions establish the final statistical orientations of magmatic foliations, enclave swarms, and dikes.

These observations indicate that the mobilization, transportation, and emplacement of granitic magma can proceed concomitantly during pluton construction. This progression concentrates and moves melt-rich magma into pulses of higher volume that are emplaced along the pluton margin forming a sheeted dike complex. These pulses are characterized by changes in fabric architecture, which may be useful in mapping zones of focused flow and circulation within other magmatic complexes. Our results highlight the role of deformation to produce a highly diverse array of structures that allowed for the migration and transportation of magma during the construction of the Coastal Batholith in central Chile.

## References

- Blake, S. and J. Fink (2000). On the deformation and freezing of enclaves during magma mixing. *Journal of Volcanology and Geothermal Research* 95(1-4), 1–8.
- Blumenfeld, P. and J. Bouchez (1988). Shear criteria in granite and migmatite deformed in the magmatic and solid states. *Journal of Structural Geology* 10(4), 361–372.
- Brandon, M. (1995). Analysis of geologic strain data in strain-magnitude space. *Journal of Structural Geology* 17(10), 1375–1385.
- Brown, M. (1994). The generation, segregation, ascent and emplacement of granite magma: the migmatite-to-crustally-derived granite connection in thickened orogens. *Earth-Science Reviews* 36(1-2), 83–130.
- Brown, M. (2001). Orogeny, migmatites and leucogranites: a review. *Journal of Earth System Science* 110(4), 313–336.
- Brown, M. (2010). The spatial and temporal patterning of the deep crust and implications for the process of melt extraction. *Philosophical Transactions of the Royal Society A: Mathematical, Physical and Engineering Sciences* 368(1910), 11–51.
- Brown, M. and T. Rushmer (1997). The role of deformation in the movement of granitic melt: views from the laboratory and the field. In M. Holness (Ed.), *Deformation-enhanced fluid transport in the Earths crust and mantle*, pp. 111–144. Mineralogical Society Series vol. 8.
- Brown, M. and G. Solar (1998). Granite ascent and emplacement during contrac-

- tional deformation in convergent orogens. *Journal of Structural Geology* 20(9), 1365–1393.
- Burger, H. and W. Skala (1976). Comparison of sieve and thin-section technique by a monte-carlo model. *Computers & Geosciences* 2(2), 123–139.
- Clemens, J. and C. Mawer (1992). Granitic magma transport by fracture propagation. *Tectonophysics* 204(3-4), 339–360.
- Clemens, J., N. Petford, and C. Mawer (1997). Ascent mechanisms of granitic magmas: causes and consequences. In M. Holness (Ed.), *Deformation-enhanced fluid transport in the Earths crust and mantle*, pp. 145–172. Mineralogical Society Series vol. 8.
- Collins, W. and E. Sawyer (1996). Pervasive granitoid magma transfer through the lower–middle crust during non-coaxial compressional deformation. *Journal of Metamorphic Geology* 14(5), 565–579.
- Cordani, U., F. Munizaga, F. Hervé, and M. Hervé (1976). Edades radiométricas provenientes del basamento cristalino de la cordillera de la costa de las provincias de valparaíso y santiago, chile. In *Congreso Geológico Chileno*, Number 1, pp. F213–F222.
- Creixell, C., M. Parada, D. Morata, P. Roperch, and C. Arriagada (2009). The genetic relationship between mafic dike swarms and plutonic reservoirs in the mesozoic of central chile (30°–33° 45' s): insights from ams and geochemistry. *International Journal of Earth Sciences* 98(1), 177–201.
- Creixell, C., M. Parada, D. Morata, P. Vásquez, C. Pérez de Arce, and C. Arriagada (2011). Middle-late jurassic to early cretaceous transtension and transpression during arc building in central chile: evidence from mafic dike swarms. *Andean geology* 38(1), 37–63.
- Dlugogorski, B., M. Grmela, P. Carreau, and G. Lebon (1994). Rheology of several hundred rigid bodies. *Journal of non-newtonian fluid mechanics* 53, 25–64.
- Elgueta, S., O. Baeza, R. Aguirre, R. Charrier, N. Muñoz, and P. Gans (2000). Mecanismos de la depositación volcanoclástica oligo–miocena del cajón del maipo, chile central. 2, 21–25.
- Farías, M., R. Charrier, A. Fock, D. Campbell, J. Martinod, and D. Comte (2005). Rapid late cenozoic surface uplift of the central chile andes (33-35 s). In *International Symposium on Andean Geodynamics (ISAG)*, Number 6, pp. 261–265.
- Fisher, N. (1996). *Statistical analysis of circular data*. Cambridge Univ Pr.
- Fock, A., R. Charrier, M. Farías, V. MaksaeV, M. Fanning, and P. Álvarez (2005). Exhumation and uplift of the western main cordillera between 33° and 34° s. In *Proceedings of International Symposium on Andean Geodynamics (ISAG)*, Number 6, pp. 273–276.
- Frost, T. and G. Mahood (1987). Field, chemical, and physical constraints on mafic-felsic magma interaction in the lamarck granodiorite, sierra nevada, california. *Geological Society of America Bulletin* 99(2), 272.

- Godoy, E. and W. Loske (1988). Tectonismo sinplutónico de dioritas jurásicas al sur de valparaíso: datos u-pb sobre la 'fase quintay'. *Andean Geology* 15(2), 119–127.
- Grocott, J., M. Brown, R. Dallmeyer, G. Taylor, and P. Treloar (1994). Mechanisms of continental growth in extensional arcs: An example from the andean plate-boundary zone. *Geology* 22(5), 391.
- Gudmundsson, A. (1984). Formation of dykes, feeder-dykes, and the intrusion of dykes from magma chambers. *Bulletin of Volcanology* 47(3), 537–550.
- Gumbsch, P., J. Riedle, A. Hartmaier, and H. Fischmeister (1998). Controlling factors for the brittle-to-ductile transition in tungsten single crystals. *Science* 282(5392), 1293–1295.
- Hand, M. and P. Dirks (1992). The influence of deformation on the formation of axial-planar leucosomes and the segregation of small melt bodies within the migmatitic napperby gneiss, central australia. *Journal of structural geology* 14(5), 591–604.
- Hervé, F., F. Munizaga, M. Parada, M. Brook, R. Pankhurst, N. Snelling, and R. Drake (1988). Granitoids of the coast range of central chile: geochronology and geologic setting. *Journal of South American Earth Sciences* 1(2), 185–194.
- Hutton, D., T. Dempster, P. Brown, and S. Becker (1990). A new mechanism of granite emplacement: intrusion in active extensional shear zones.
- John, B. and J. Blundy (1993). Emplacement-related deformation of granitoid magmas, southern adamello massif, italy. *Geological Society of America Bulletin* 105(12), 1517–1541.
- Johnson, S., R. Vernon, and P. Upton (2004). Foliation development and progressive strain-rate partitioning in the crystallizing carapace of a tonalite pluton: microstructural evidence and numerical modeling. *Journal of Structural Geology* 26(10), 1845–1865.
- Kalakay, T., B. John, and D. Lageson (2001). Fault-controlled pluton emplacement in the sevier fold-and-thrust belt of southwest montana, usa. *Journal of Structural Geology* 23(6-7), 1151–1165.
- Launeau, P. and P. Robin (2005). Determination of fabric and strain ellipsoids from measured sectional ellipses—implementation and applications. *Journal of structural geology* 27(12), 2223–2233.
- Lavenu, A. and J. Cembrano (1999). Compressional-and transpressional-stress pattern for pliocene and quaternary brittle deformation in fore arc and intra-arc zones (andes of central and southern chile). *Journal of Structural Geology* 21(12), 1669–1691.
- Levi, B. (1973). Eastward shift of mesozoic and early tertiary volcanic centers in the coast range of central chile. *Bulletin of the Geological Society of America* 84(12), 3901.
- Lisle, R. (1985). Geological strain analysis, a manual for the rf/phi method.
- Mancktelow, N. (1995). Deviatoric stress and the interplay between deformation

- and metamorphism. In *Geological Society of Australia, Abstracts, Clare Valley Conference*, Volume 40, pp. 95–96.
- Miller, R. and S. Paterson (1999). In defense of magmatic diapirs. *Journal of Structural Geology* 21(8-9), 1161–1173.
- Molyneux, S. and D. Hutton (2000). Evidence for significant granite space creation by the ballooning mechanism: the example of the ardara pluton, Ireland. *Geological Society of America Bulletin* 112(10), 1543.
- Mulchrone, K., P. Meere, and K. Choudhury (2005). Sape: a program for semi-automatic parameter extraction for strain analysis. *Journal of structural geology* 27(11), 2084–2098.
- Nicolas, A. (1992a). Kinematics in magmatic rocks with special reference to gabbros. *Journal of Petrology* 33(4), 891.
- Nicolas, A. (1992b). Kinematics in magmatic rocks with special reference to gabbros. *Journal of Petrology* 33(4), 891.
- Parada, M., J. Nyström, and B. Levi (1999). Multiple sources for the coastal batholith of central Chile (31–34°S): geochemical and Sr–Nd isotopic evidence and tectonic implications. *Lithos* 46(3), 505–521.
- Paterson, S., T. Fowler Jr, K. Schmidt, A. Yoshinobu, E. Yuan, and R. Miller (1998). Interpreting magmatic fabric patterns in plutons. *Lithos* 44(1-2), 53–82.
- Paterson, S., G. Pignotta, and R. Vernon (2004). The significance of microgranitoid enclave shapes and orientations. *Journal of Structural Geology* 26(8), 1465–1481.
- Paterson, S. and R. Vernon (1995). Bursting the bubble of ballooning plutons: A return to nested diapirs emplaced by multiple processes. *Geological Society of America Bulletin* 107(11), 1356–1380.
- Paterson, S., R. Vernon, and O. Tobisch (1989). A review of criteria for the identification of magmatic and tectonic foliations in granitoids. *Journal of structural geology* 11(3), 349–363.
- Petford, N. (1996). Dykes or diapirs? *Geological Society of America Special Papers* 315, 105–114.
- Petford, N. (2003). Rheology of granitic magmas during ascent and emplacement. *Annual Review of Earth and Planetary Sciences* 31(1), 399–427.
- Petford, N., A. Cruden, K. McCaffrey, and J. Vigneresse (2000). Granite magma formation, transport and emplacement in the earth's crust. *Nature* 408(6813), 669–673.
- Petrini, K. and Y. Podladchikov (2000). Lithospheric pressure–depth relationship in compressive regions of thickened crust. *Journal of Metamorphic Geology* 18(1), 67–78.
- Rutter, E. and D. Neumann (1995). Experimental deformation of partially molten westerly granite under fluid-absent conditions, with implications for the extraction of granitic magmas. *Journal of Geophysical Research* 100(B8), 15697–15.



- SERNAGEOMIN (2002). *Mapa Geológico de Chile. Servicio Nacional de Geología y Minería, Chile. Carta geológica de Chile. Serie Geología básica No. 75, 1 mapa en 3 hojas, escala 1:1.000.000.*
- Shaw, H. (1980). The fracture mechanisms of magma transport from the mantle to the surface. *Physics of magmatic processes*, 201–264.
- Siña, A. (1987). El batolito de la costa entre algarrobo y rocas de santo domingo (chile central, 33° 30' s): geología e interpretaciones petrogenéticas. *Comunicaciones* 38, 47–66.
- Siña, A. and M. Parada (1985). Los granitoides de rocas de santo domingo: antecedentes de terreno, petrográficos y de química de elementos mayores para una mezcla de magmas. In *Proc. Congreso Geológico Chileno, 4th, Antofagasta, Chile*, Volume 3, pp. 512–530.
- Sleep, N. (1988). Tapping of melt by veins and dikes. *Journal of Geophysical Research* 93(B9), 10255–10272.
- Strömberg, K. (1973). Stress distribution during formation of boudinage and pressure shadows. *Tectonophysics* 16(3-4), 215–248.
- Tikoff, B. and H. Fossen (1995). The limitations of three-dimensional kinematic vorticity analysis. *Journal of Structural Geology* 17(12), 1771–1784.
- Tobisch, O., B. McNulty, and R. Vernon (1997). Microgranitoid enclave swarms in granitic plutons, central sierra nevada, california. *Lithos* 40(2-4), 321–339.
- Van der Molen, I. and M. Paterson (1979). Experimental deformation of partially-melted granite. *Contributions to Mineralogy and Petrology* 70(3), 299–318.
- Vergara, M., B. Levi, J. Nyström, and A. Cancino (1995). Jurassic and early cretaceous island arc volcanism, extension, and subsidence in the coast range of central chile. *Geological Society of America Bulletin* 107(12), 1427.
- Vernon, R., M. Etheridge, and V. Wall (1988). Shape and microstructure of microgranitoid enclaves: indicators of magma mingling and flow. *Lithos* 22(1), 1–11.
- Vignerresse, J. and B. Tikoff (1999). Strain partitioning during partial melting and crystallizing felsic magmas. *Tectonophysics* 312(2-4), 117–132.
- Wall, R., P. Gana, and A. Gutiérrez (1996). *Mapa geológico del area de Valparaiso-Curacavi, Regiones de Valparaiso y Metropolitana*. Servicio Nacional de Geología y Minería.
- Wiebe, R., M. Jellinek, M. Markley, D. Hawkins, and D. Snyder (2007). Steep schlieren and associated enclaves in the vinalhaven granite, maine: possible indicators for granite rheology. *Contributions to Mineralogy and Petrology* 153(2), 121–138.
- Williams, M., S. Hanmer, C. Kopf, and M. Darrach (1995). Syntectonic generation and segregation of tonalitic melts from amphibolite dikes in the lower crust, striding-athabasca mylonite zone, northern saskatchewan. *Journal of Geophysical Research* 100(B8), 15717–15.

Williams, Q. and O. Tobisch (1994). Microgranitic enclave shapes and magmatic strain histories: Constraints from drop deformation theory. *Journal of Geophysical Research* 99(B12), 24359–24.

## Chapter 3

# A methodology for the quantification and visualization of deformed rock fabrics within the statistical computing environment R

### Abstract

A comprehensive method for the quantification of three-dimensional rock fabrics following the  $R_f/\phi$  and Fry methods is presented herein. This method outlines the steps required to construct a three-dimensional fabric ellipsoid from a variety of data sources including standardized outcrop images, scanned hand-sample slabs, and photomicrographs of thin sections. This methodology utilizes a series of scripts written within the open-source statistical computing environment R to convert data formats between preexisting strain software packages. Moreover, these scripts produce an array of graphical figures and models including sectional and three-dimensional Fry plots, sectional  $R_f/\phi$  plots, interactive three-dimensional fabric ellipsoid models, a Nadai plot of the Lode parameter and octahedral shear strain, and a stereographic projection of the calculated fabric ellipsoid axial orientations. In order to test the utility of this procedure, a three-dimensional synthetic model of known strain shape, magnitude, and orientation was tested. The results of this assessment indicate that the procedure accurately calculated the expected state of strain within a small margin of error. Finally, a natural example is presented to test the method's ability to quantify the estimated tectonite fabric properties. This example is an  $L \gg S$  metagranite augen gneiss from the Coastal Batholith of central Chile. This analysis resulted in calculated fabric ellipsoids from both the  $R_f/\phi$  and Fry methods that clearly display significantly prolate geometries at moderate distortions.

---

### 3.1 Introduction

The recognition and quantification of rock fabrics can provide crucial insight to the nature of finite deformation. Numerous studies have directly correlated changes in fabric geometry (i.e.  $L > S$ ;  $L \sim S$ ;  $L < S$  tectonites) to large scale structural features such as thrust nappes (Flinn 1956; Hossack 1968), metamorphic core complex detachments (Wells 2001), oroclinal fold hinges (Sullivan 2006), and mid-crustal extensional shear zones (Klepeis et al. 2007). Nevertheless, a major restriction to the application of classic analytical strain techniques to geologic scenarios is the time consuming and commonly subjective nature of data collection, reduction, and synthesis (Dunnet 1969; Borradaile 1984; Lisle 1985; Fry 1979). Although several advances in computational software have greatly reduced the tedious nature of applying analytical strain techniques to deformed rocks, a comprehensive integration of these tools from data extraction to fabric modeling remains unestablished (Mulchrone et al. 2005; Chew 2003; Waldron and Wallace 2007; Mookerjee and Nickleach 2011). This limitation is partially the result of data format incompatibilities and a lack of visualization functionality. In order to elucidate regional trends from numerous three-dimensional fabric analyses, a standard methodology that enables efficient processing and visualization of extensive datasets is a fundamental requirement.

In this chapter, I present a procedure that integrates several widely available computer programs to rapidly process large quantities of three-dimensional rock fabric data and produce a series of standardized figures. This procedure is accompanied by a set of templates and scripts written in the open-source statistical computing environment R (R Development Core Team 2010) that establish a standard operational convention to produce three-dimensional fabric ellipsoids, following both the Fry (Fry 1979) and the  $R_f/\phi$  techniques (Ramsay 1967; Dunnet 1969; Ramsay and

Huber 1983; Lisle 1985). The results of two separate analyses applied to a deformed synthetic model with a known three-dimensional strain geometry and a natural example with an  $L \gg S$  gneissic fabric (determined from visual estimations) indicate the validity of this procedure. My results closely align to the expected values of these tests and clearly establish the ability of this procedure to distinguish changes in the calculated fabric ellipsoid distortion, shape, and orientation.

## 3.2 Methodology

In order to quantify the three-dimensional architecture of a rock fabric, data must be collected, extracted, analyzed, synthesized, and presented. This involves collecting measurements on three mutually perpendicular sections where the properties of objects (locations, orientations, and ellipticities) can be obtained and analyzed with either the  $R_f/\phi$  technique or the Fry method. The results of these analyses are then synthesized into a fabric ellipsoid and presented in terms of shape, distortion, and orientation. Although the details of this procedure are explained with detail in the accompanying manual (see Appendix B), the following paragraphs provide a brief outline of the major steps required.

### 3.2.1 Data collection and extraction

Data used for fabric analysis can be obtained from a variety of sources including standardized outcrop images, slabbed hand sample scans, thin section photomicrographs, and manual measurements<sup>1</sup>. These data (excluding manual measurements) are obtained from digital imagery that is tagged with orientation information such that the section can be placed within a three-dimensional context. Object traces within the images are manually outlined to ensure correct selection of data (B.4) and

---

<sup>1</sup>Manual measurements will bypass the *SAPÉ* parameter extraction procedure as explained later in text.

allow for the statistical fitting of ellipses to each object. Although object detection software may be viable in certain circumstances, it is not discussed further herein due to complexities involved in distinguishing like-colored objects or boudin trains. The object traces are exported to binary color bitmap files (B.5) and processed within the program *SAPÉ* (Mulchrone et al. 2005). This program fits an ellipse to each of the object traces and extracts the locations, axial lengths, and the orientations of semi-major and minor axes throughout the image. These data are processed by an R script to convert and write output files that are compatible with software designed for two-dimensional strain analyses.

### 3.2.2 Sectional analyses

Two-dimensional fabric analyses are applied to each of the three-mutually perpendicular sections by running the output files created within the previous stages through several widely available analytical strain programs. Programs currently compatible with this technique include *Rf/Phi v1.0* (Mulchrone and Meere 2001), a Microsoft® Excel macro for  $R_f/\phi$  analysis (Chew 2003), and an objective central void fitting macro for the Fry method (Waldron and Wallace 2007). The details of these specific analyses are presented in the accompanying manual (Appendix B) and the original citations. The analytical results are then tagged to the corresponding sections and processed through another R-script that generates an array of standardized plots. The plots are saved as portable document files that can easily be imported into most vector based graphic programs for production of publication-quality figures. Additionally, a file is automatically generated in the previous script that is formatted for use in the program *Ellipsoid 2003* (Launeau and Robin 2005).

### 3.2.3 Ellipsoid synthesis

*Ellipsoid 2003* (Launeau and Robin 2005) statistically fits a fabric ellipsoid to the sectional data and returns the ellipsoid properties including normalized axial lengths, axis orientations, and an “incompatibility index” ( $\sqrt{\tilde{F}}$ ) that is a proxy for the degree of misfit between the ellipsoid and the sectional ellipses. Although this program provides all the raw data necessary to completely address the nature of fabric architecture, it does not present these results in elegant format, nor does it quantify the fabric symmetry or magnitude of distortion. Therefore, the results can be save into a file for further processing in R.

### 3.2.4 Visualization and presentation

In order to produce high quality standardized figures that aid in the visualization and presentation of the calculated fabric ellipsoid, the output from *Ellipsoid 2003* must be processed with scripts in R. These scripts enable the generation of a real-time interactive ellipsoid model that is correctly oriented relative to a geographic reference frame, a Nadai plot, and a stereographic projection of the calculated XY principle fabric plane and principle axes. The ellipsoid model is also saved as a three-dimensional mesh object that can be manipulated in the open source programs MeshLab<sup>TM</sup> and Blender<sup>TM</sup>. Within these programs the ellipsoids can be stylized and exported to a variety of images from any view point to best communicate the results. As with the other plots, the Nadai plot and stereographic projection are saved as portable document files and can easily be incorporated into publishable figures.

### 3.3 Synthetic analysis

#### 3.3.1 Model construction

The application of this procedure to a synthetic model is the most direct means to address the nature of error introduced. In order to construct a viable model for strain analysis, an undeformed dataset that upholds the initial conditions assumed for the  $R_f/\phi$  and Fry methods must be created (see review by Ramsay and Huber 1983 and Chapter 1 of this thesis). The  $R_f/\phi$  technique requires an initial set of randomly oriented elliptical objects with varying ellipticities (Ramsay 1967; Dunnet 1969; Ramsay and Huber 1983; Lisle 1985). As this medium undergoes homogeneous finite deformation, a statistical relationship between object orientations and ellipticities forms as a product of the imposed strain magnitude and orientation. Similarly, the locations of the object centroids will translate relative to each other in a predictable manner. This translation forms the fundamental premise of the Fry method<sup>2</sup> if the initial population of markers roughly fits a “random” Poisson distribution and contains a minimum nearest-neighbor threshold distance (Fry 1979; Lisle 2010).

The initial undeformed dataset used to create the synthetic model was generated by a script written for the program R to maintain the assumptions of both strain techniques. This script automatically creates a list of 1,000 axial ratios that fit a normal distribution characterized by a known mean ( $\bar{R}_i = 1.5$ ) and standard deviation ( $\sigma = 0.167$ ). This distribution limits the range of initial axial ratios from roughly one to two, which are subsequently normalized to a common ellipse area. The script also produces a population of values ranging from zero to 180 with a uniform distribution to properly orient each ellipse. Although this criteria is sufficient for an  $R_f/\phi$  analysis, the distribution of ellipse centroids must be constrained for the Fry analysis. This

---

<sup>2</sup>For more information refer to Section 1.2.1.



requires the determination of ellipse to background percentage and the prevention of overlapping objects. In order to adequately produce a population of objects, the script must determine the window size for plotting, as a function of the number of clasts and the total clast area following Equation 3.1 where  $A_e$  is the summation of all individual ellipse areas.

$$Window\ Area = \left( \frac{100 \times A_e}{Clast\ Percentage} \right) + A_e \quad (3.1)$$

Once the script has calculated the window size for plotting within Cartesian space, the range of centroid coordinate values is determined. To prevent any ellipses from overlapping, I designed an algorithm that randomly generates an X and Y coordinate from a uniform distribution (limited by the window size) and tests the value against previously accepted coordinates that are buffered by the summation of long axis pairs. If the buffer length is greater than the centroid distance, the test coordinates are rejected and new values are generated. Finally, the script will plot the set of 1,000 ellipses, which represents any two-dimensional section through an undeformed state of strain.

In order to develop a three-dimensional strain ellipsoid with known geometric properties, the initial undeformed dataset must be systematically distorted for each principle plane such that the finite strain ellipsoid volume is preserved (Fig. 3.1). If the initial measure of time ( $t_1$ ) represents the undeformed dataset, the initial geometry of strain can be represented by a sphere. In this unique case, the Lode parameter ( $\nu$ , also referred to as the *strain symmetry*) and the octahedral shear strain ( $\bar{\epsilon}_s$ ) are both equivalent to zero<sup>3</sup> (Lode 1926; Nadai 1963; Hsu 1966; Hossack 1968). The Lode

---

<sup>3</sup>The octahedral shear strain of an ellipsoid as the principle axes approach a length of one:

$$\lim_{(X, Y, \& Z) \rightarrow 1} \bar{\epsilon}_s = 0$$

parameter, analogous to the  $k$  value of Flinn (1962), allows for the quantification of ellipsoid shape such that prolate geometries range in value from negative one to zero, and oblate shapes from zero to one. The octahedral shear strain describes the magnitude of ellipsoid distortion with increasing value. Therefore, after the initial dataset has undergone homogeneous finite strain through a given increment of time ( $t_2$ ), the sphere is deformed into an ellipsoid that is characterized by the nature of material flow (i.e. constrictional vs flattening determined by the Lode parameter) and the magnitude of distortion. Assuming the conservation of volume during deformation, Equation 3.2 will hold true.

$$X_{t_1} \times Y_{t_1} \times Z_{t_1} = X_{t_2} \times Y_{t_2} \times Z_{t_2} \quad (3.2)$$

The values of  $X$ ,  $Y$ , and  $Z$  are the normalized axial lengths (see Equation 3.3) of the strain ellipsoid before deformation ( $t_1$ ) and after deformation ( $t_2$ ). By convention, the initial volume of the undeformed ellipsoid is equivalent to the unitless value:  $(4/3)\pi$ , such that Equation 3.2 can reduce to Equation 3.3. Furthermore, this normalizes the ellipsoid axial lengths such that  $X$ ,  $Y$ ,  $Z$  are equal to one.

$$X_{t_2} \times Y_{t_2} \times Z_{t_2} = 1 \quad (3.3)$$

The conservation of volume fundamentally constrains the strain ratios observed in each principle plane of strain. Therefore, if the finite strain ratios for any two principle planes of strain are determined, the third is mathematically defined. In order to properly distort the undeformed dataset, the two-dimensional strain ratio defined by the  $X$  and  $Z$  principle strain axes ( $R_s^{XZ}$ ) is established at a value of six (Fig. 3.1

---

XZ). Additionally, the two-dimensional strain ratio defined by the  $X$  and  $Y$  strain axes ( $R_s^{XY}$ ) is set to four (Fig. 3.1 XY). This will produce a moderately deformed model that is a reasonable representation of many geologic scenarios (for example, see values reported by Czeck et al. 2009). As such, Equations 3.4 and 3.5 are defined.

$$R_s^{XZ} = X_{t_2}/Z_{t_2} = 6 \quad (3.4)$$

$$R_s^{XY} = X_{t_2}/Y_{t_2} = 4 \quad (3.5)$$

Equations 3.4 and 3.5 can rearrange to produce Equations 3.6 and 3.7.

$$Z_{t_2} = X_{t_2}/6 \quad (3.6)$$

$$Y_{t_2} = X_{t_2}/4 \quad (3.7)$$

This allows the length of  $X_{t_2}$  to be determined by substituting Equations 3.6 and 3.7 into Equation 3.3. By substituting the value of  $X_{t_2}$  into Equations 3.6 and 3.7, the values of  $Z_{t_2}$  and  $Y_{t_2}$  are obtained. Furthermore, the quotient of Equations 3.7 and 3.6 will give the sectional strain ratio for the YZ principle plane as shown in Equation 3.8. This requires the principle strain axes to be scaled according to the percentages listed in Table 3.1. From these percentages, the principle planes of strain for  $t_2$  can be constructed by scaling the corresponding principle planes of strain at  $t_1$  disproportionately about the given axes to create a strain ellipsoid where the octahedral shear strain and Lode parameter are obtained from Equations 3.9 and 3.10, respectively.

$$R_s^{YZ} = Y_{t_2}/Z_{t_2} = 1.5 \quad (3.8)$$

$$\bar{\epsilon}_s = \frac{\sqrt{(\ln X_{t_2} - \ln Y_{t_2})^2 + (\ln Y_{t_2} - \ln Z_{t_2})^2 + (\ln Z_{t_2} - \ln X_{t_2})^2}}{\sqrt{3}} = 1.329 \quad (3.9)$$

$$\nu = \frac{2 \times \ln Y_{t_2} - \ln X_{t_2} - \ln Z_{t_2}}{\ln X_{t_2} - \ln Z_{t_2}} = -0.56 \quad (3.10)$$

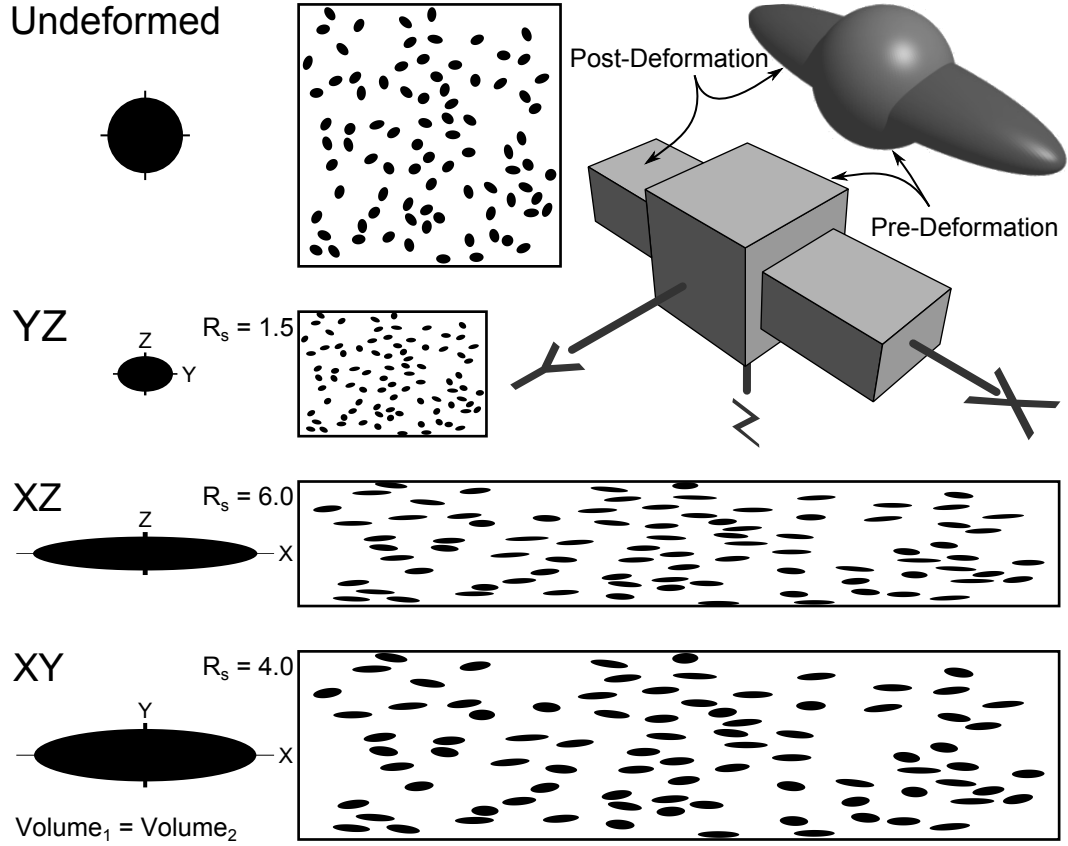


Figure 3.1: Schematic diagram illustrating the construction of the synthetic dataset by scaling each principle plane proportionally about the axes defined in Table 3.1.

To physically construct the synthetic model for error analysis, the undeformed dataset must be appropriately distorted, printed, and applied to a cubic object such as a cardboard box. This is accomplished by importing the portable document file (PDF) with plotted undeformed elliptical objects into a vector based graphic program

Table 3.1: Scale percentage values for the three principle strain axes used to produce the deformed synthetic dataset

$X_{\%}$	$Y_{\%}$	$Z_{\%}$
288.45%	72.11%	48.07%

and scaling the horizontal and vertical axes according to the values in Table 3.1 for each principle plane of strain. The deformed datasets are then printed on tiled sections of paper that are aligned and pasted to the outside of a robust cubic cardboard box with edge lengths of approximately 12 inches. Appendix D contains accurately distorted tiles for additional model construction. After construction, the model is securely mounted in the laboratory for data collection and processing.

### 3.3.2 Results

Although the analysis of a synthetic data set cannot possibly address all sources of error that may arise in the application of this procedure to natural examples, discrepancies between the expected and calculated results form a baseline level of inherent procedural error. These results are described in terms of the properties of the final fitted ellipsoids as derived from the  $R_f/\phi$  and Fry techniques. In general, this comparison addresses strain symmetry (Lode parameter), octahedral shear strain, and the relative orientations of principle axes. The methodology previously presented was applied to the synthetic conglomerate model from photographs taken with an aperture camera device as illustrated in Figure 3.2. A total of 198 objects were traced from the images (average of 66 objects per face, which exceeds the accepted adequate population size as discussed in section 1.2.1) and processed in *SAPÉ*. The parameters of the fitted object ellipses were then used to determine the fabric architecture as explained in the following text.

The parameters extracted in *SAPÉ* were analyzed with the  $R_f/\phi$  and Fry tech-

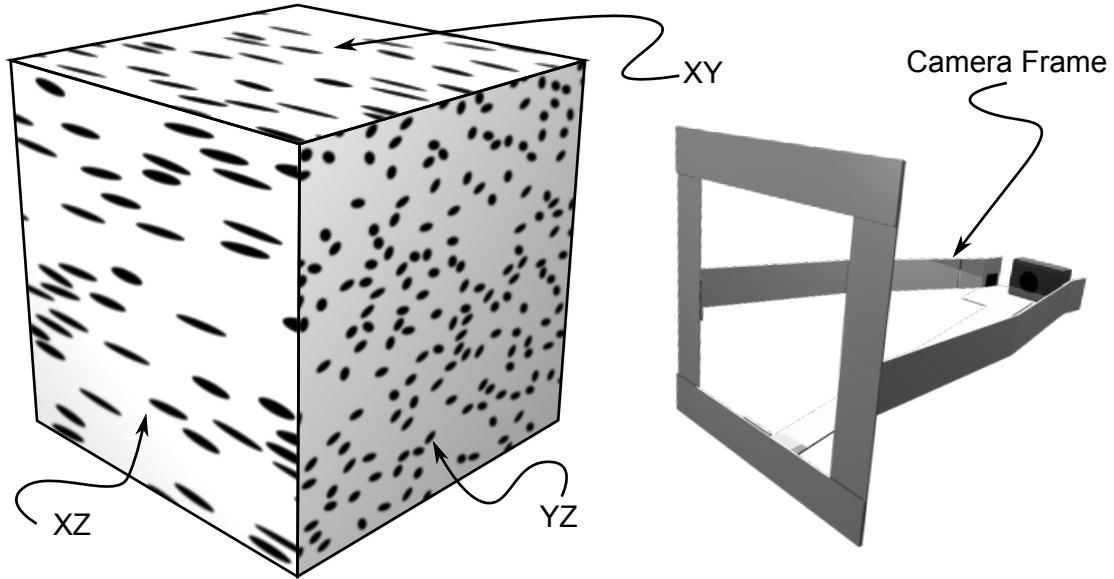


Figure 3.2: Figure highlighting the use of a camera frame device in collection of oriented and standardized digital images for error analysis of the fabric quantification procedure. Note that perspective foreshortening of XY-plane produces the appearance of a higher distortion than XZ, but is actually less than the XZ-plane.

niques. The sectional results of the  $R_f/\phi$  analysis are presented in Figure 3.3. Section “A” corresponds to the XY principle plane of strain and has a theoretical  $R_s$  value of four as established in Equation 3.4. The calculated strain ratio of this section is 3.9, which is quite close to the expected value. The XZ principle plane (shown in section B of Figure 3.3) deviates slightly from the expected strain ratio value of 6 with a calculated value of 5.6 when calculated with the macro by Chew (2003). However, when the exact same dataset was processed with the program *Rf/Phi* by Mulchrone and Meere (2001) an  $R_s$  value of 5.95 was calculated, which suggests this program may be more robust at higher strains than the Chew (2003) macro. However, future research will need to be completed to assess this difference. The final section (YZ) produces a lower strain value of 1.4 compared to the theoretical ratio of 1.5 and clearly demonstrates the validity of the procedure thus far. The relative differences

in expected and calculated results is listed in Table 3.2.

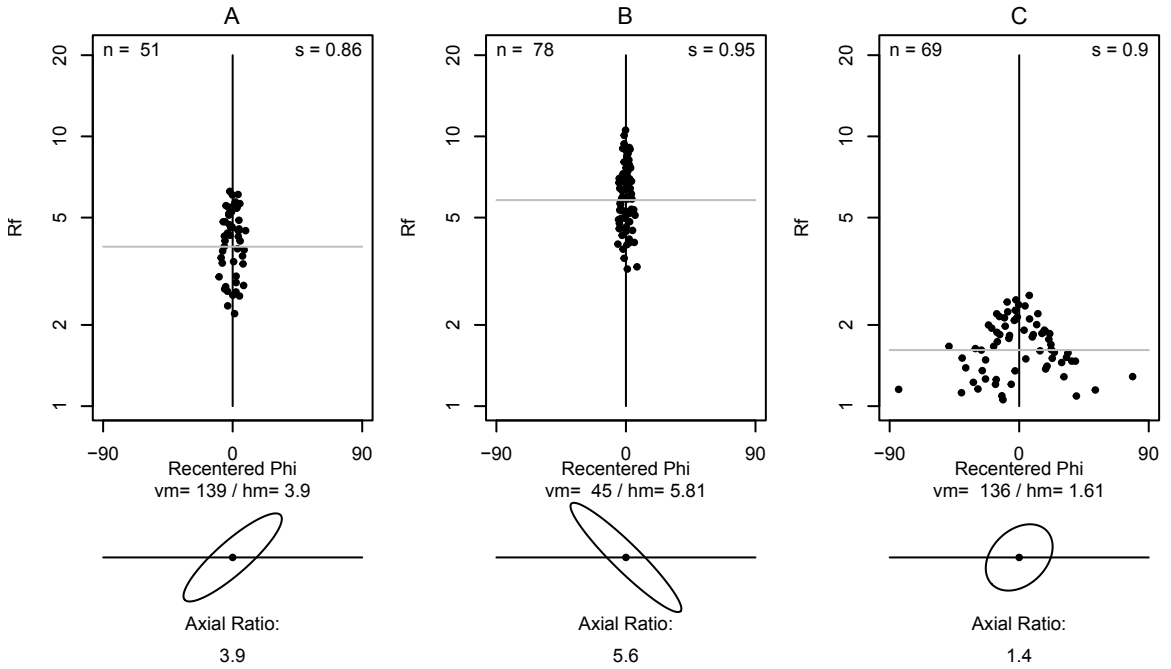


Figure 3.3: Sectional  $R_f/\phi$  results from the synthetic model.

Table 3.2: Relative differences between the results of the calculated sectional strain ratios and the expected values.

Method	XY	XZ	YZ
$R_f/\phi$	2.5%	0.6%	4.7%
Fry	17.7%	5.1%	19.8%

The sectional results of the Fry method were slightly less robust than for the  $R_f/\phi$  method as shown in Figure 3.4 and Table 3.2. The XY, XZ, and YZ principle plane strain ratios were calculated at 3.35, 5.7, and 1.83, respectively. At most, the long axis orientation differs by 13 degrees with respect to the vector means calculated in each section and indicates that the central void ellipse orientation is reasonably well constrained.

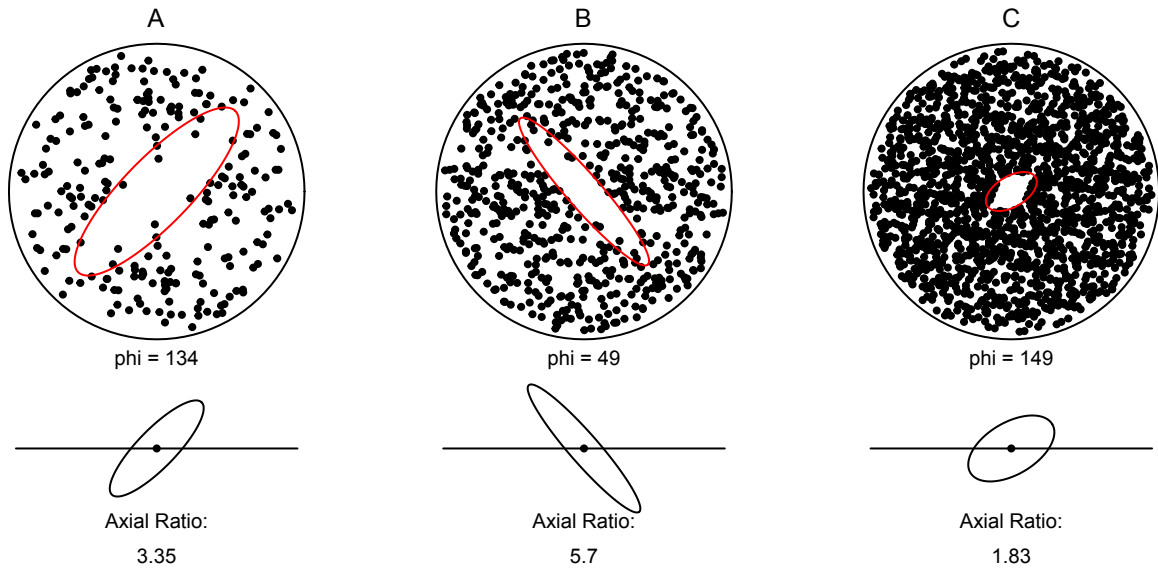


Figure 3.4: Sectional Fry results from the synthetic model.

The sectional results obtained from both the  $R_f/\phi$  and Fry methods were fitted with two strain ellipsoids and compared to the expected theoretical shape, distortion, and orientation of finite strain. This comparison addresses the nature of error introduced through the entire procedure and gives a general level of analytical resolution to which gradients in strain may be determined. The inability to judge the quality of a three-dimensional strain analysis based on a single stage of the procedure is highlighted in this example where the incompatibility index for ellipsoid fitting from the Fry method was slightly better than that for the  $R_f/\phi$  ( $\sqrt{F} = 0.1$  *versus* 0.2 for the Fry and  $R_f/\phi$  results, respectively), despite the better sectional results obtained from the  $R_f/\phi$  technique. As such, error should be addressed directly in terms of strain symmetry, octahedral shear strain, and orientation and not based on any one given component of the procedure. With that said, the total calculated error may be a product of error propagated from an individual component.



The expected theoretical strain symmetry value, as given by the Lode parameter (Equation 3.10), falls well within the prolate field (Fig. 3.5). The ellipsoid shape obtained from the  $R_f/\phi$  analysis is slightly more prolate than the expected value. However, the difference between the two is less a tenth of the Lode parameter. A slightly higher difference between the results of the Fry analysis and the expected value is observed in this example. As such, the Fry results produced a moderately less prolate ellipsoid. Nevertheless, the general shape of this calculated ellipsoid still represents an  $L > S$  tectonite fabric.

Octahedral shear strain values obtained in this analysis are remarkably consistent with the expected values (Fig. 3.5). In general, both the  $R_f/\phi$  and Fry methods slightly underestimated the expected value (less than a tenth of a decimal difference). Both analyses produced nearly identical values with the  $R_f/\phi$  technique marginally closer to that expected. This difference is visually indistinguishable and is an insignificant source of total error.

The orientations of the calculated fabric ellipsoids deviate slightly from the true orientation of the synthetic model. Figure 3.6 displays three stereographic projections containing the plotted principle axes for the  $R_f/\phi$  technique, Fry method, and the expected fabric ellipsoid, as well as great circles defining the X-Y principle planes. The X axis orientations are extremely consistent, with a largest angular distance from the expected of  $3.8^\circ$  (Fry method). Although the X-axis orientations are quite consistent and provide a good measure of the theoretical “mineral lineation,” they do not constrain the alignment of the “foliation” planes. The angular distance between the Z-axis orientation for the Fry method and the expected orientation ( $16^\circ$ ) is considerably higher than that obtained for the  $R_f/\phi$  method ( $2.6^\circ$ ). Although the Fry method tends to be the least consistent technique, it produced acceptable results within a fairly small margin of error (Fig. 3.5).

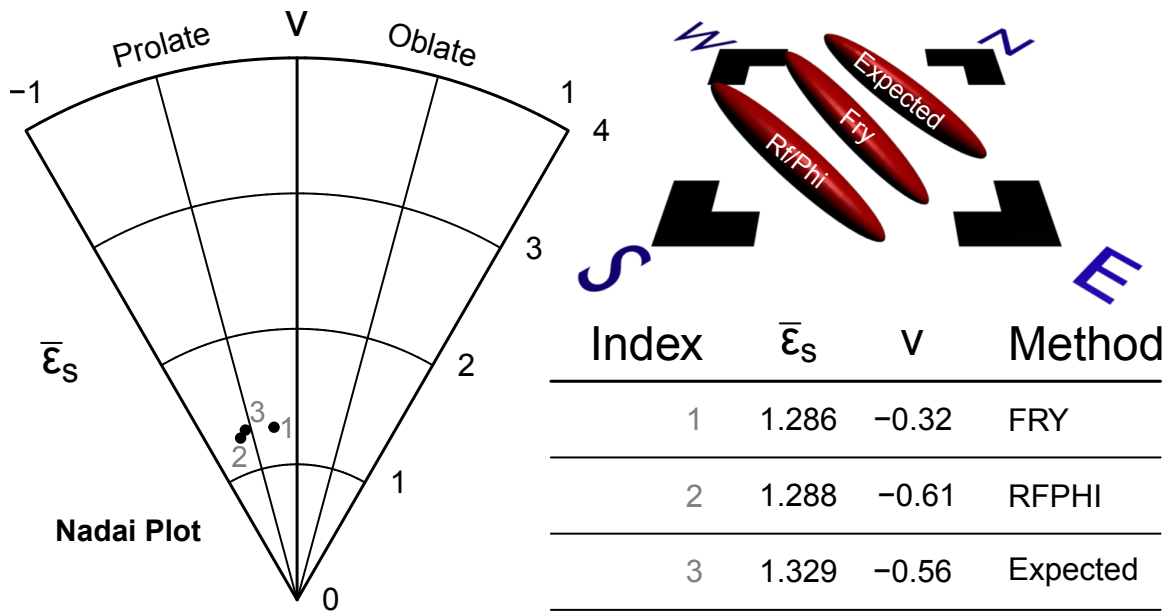


Figure 3.5: Comparison of fabric ellipsoid shapes and magnitudes obtained for the synthetic data test and expected results.

### 3.4 Application to a naturally deformed example

#### 3.4.1 Background

Sample 11-LC-03-C is a granite augen gneiss collected near the town of Las Cruces, central Chile. This sample is interpreted to be part of the Valparaíso Metamorphic Complex, which hosts voluminous magmatic rocks of late Paleozoic and Jurassic ages (Wall et al. 1996; Gana and Tosdal 1996). The geometry of gneissic fabrics within this metagranite vary spatially from regions dominated by foliations ( $L < S$ ), and lineation dominated domains ( $L > S$ ). The advantage of fabric quantification is the ability to quantitatively distinguish fabric gradients within a region that has experienced inhomogeneous deformation at large scales. Therefore, the results of natural analyses should compare well to visual fabric estimates such that  $L > S$

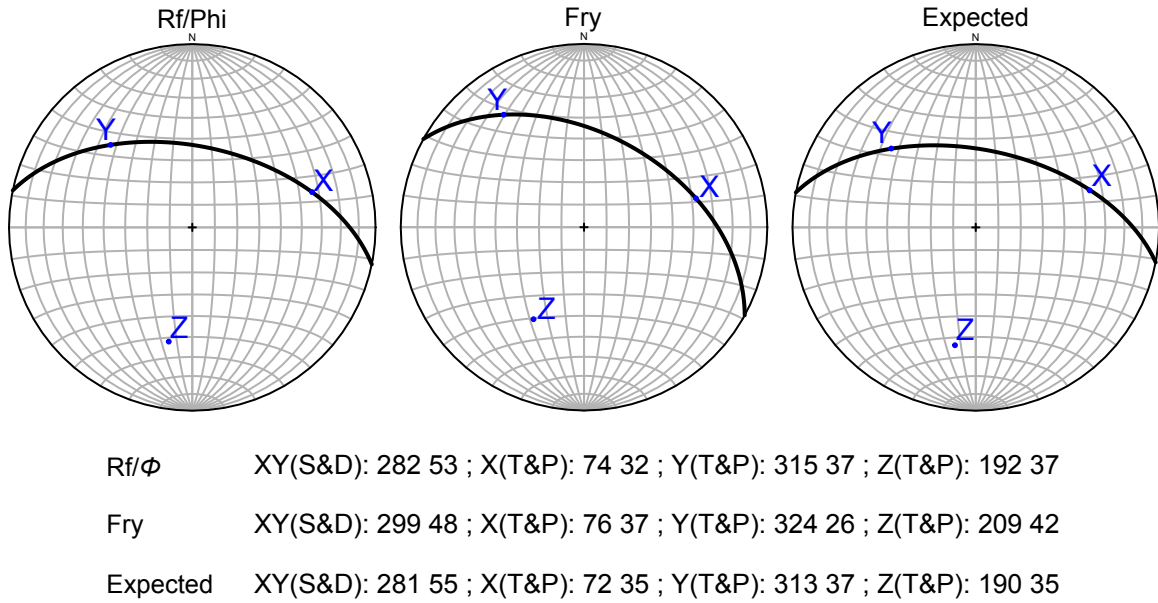


Figure 3.6: Comparison of orientation results from the synthetic data test.

and  $L < S$  tectonites are distinguished by prolate and oblate fabric geometries, respectively. The natural example presented herein is derived from an  $L > S$  domain as determined visually within the field. Therefore, we expect the results of this analysis to produce a prolate fabric ellipsoid.

Sample 11-LC-03-C was slabbed on three mutually perpendicular faces and reoriented in the laboratory. The orientation of each face was measured following right hand rule convention and directly marked with the line of strike. These faces were then scanned in color at a high resolution and saved (Fig. 3.7). Each scan was modified following the procedure outlined in the accompanying manual (Appendix B) to produce correctly aligned images of known orientation. The traces of 181 feldspar porphyroclasts were outlined and exported to bitmap files for processing in the program *SAPE* (Fig. 3.7), from which a file containing object properties was obtained. The *SAPE* output was processed in R to reformat the data for sectional fabric analy-

ses. Both the  $R_f/\phi$  (Fig. 3.8) and Fry methods (Fig. 3.9) were applied to the section data, which calculated the orientations and axial ratios of fitted fabric ellipses. These results were processed in *Ellipsoid 2003* and are describe in the following text.

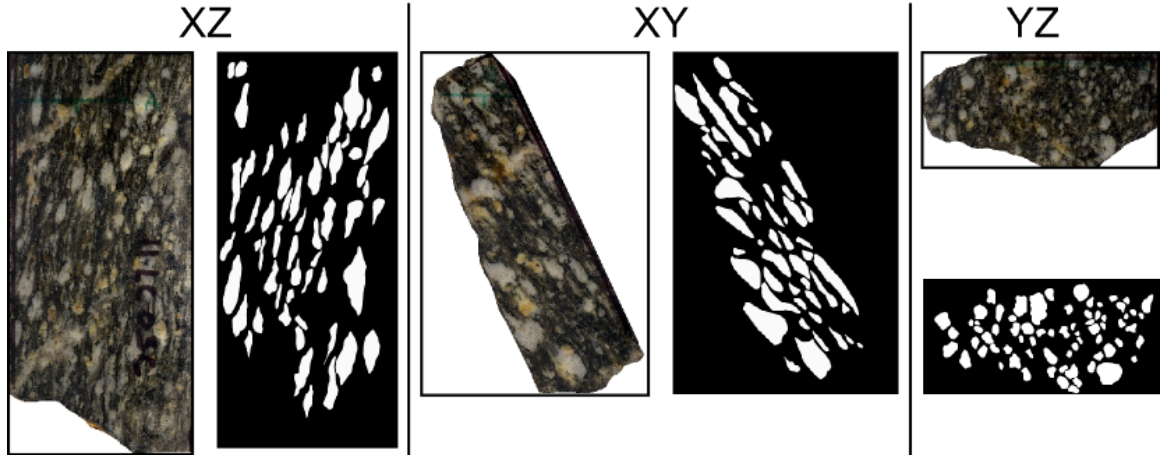


Figure 3.7: Oriented sectional scans and traced objects of slabbed faces from 11-LC-03-C. The X-Z, X-Y, and Y-Z faces correspond to the non-genetic sectional nomenclature of A, B, C, respectively.

### 3.4.2 Results

The results of both the  $R_f/\phi$  and Fry analyses applied to sample 11-LC-03-C produced fabric ellipsoids that closely resemble the visually estimated fabric shape and magnitude obtained in the field. These results are described in terms of the appearance of sectional analyses, the nature of fabric symmetries, the magnitudes of distortion, and the principle fabric element orientations. Not only do my results correspond closely to the fabric shape and magnitude from the field, but the orientations of the calculated maximum stretching axes are concordant to the bulk mineral stretching lineation. Although the XY fabric plane calculated for the  $R_f/\phi$  analysis is parallel to the bulk augen gneiss foliation, the orientation of the Fry XY-plane deviates ( $\sim 60^\circ$ ) substantially from this attitude.

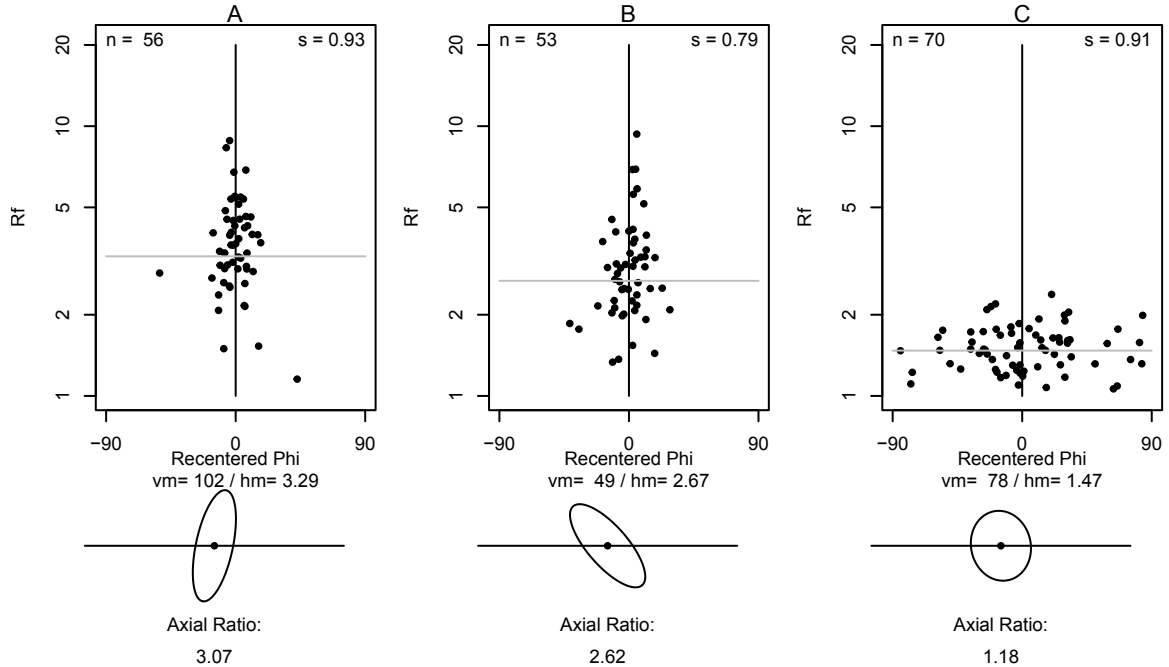


Figure 3.8: Sectional  $R_f/\phi$  plots with normalized fitted ellipses from sample 11-LC-03-C. Abbreviations:  $s$  = index of symmetry;  $vm$  = vector mean; and  $hm$  = harmonic mean.

The sectional  $R_s$  fabric values obtained from the  $R_f/\phi$  technique display two moderately deformed sections (Fig. 3.8 A & B) while the third exhibits a low fabric ellipse axial ratio (1.18). This relationship is expected based on the well-defined mineral trace lineation and less developed gneissic foliation. The sectional results from the Fry method are similar with the third section containing an isotropic fabric value of one. However, section “B” (Fig. 3.9) produced a substantially lower fabric ellipse relative to the  $R_f/\phi$  method (Fig: 3.8) with a 46.6% difference. Moreover, a  $38^\circ$  angular difference in long axis orientations between the methods is obtained.

Due to the premise that the orientation of the  $R_f/\phi$  fabric ellipse is determined directly from the vector mean of object long axes, while the Fry orientation is determined from the central void, differences between the two results suggests that either

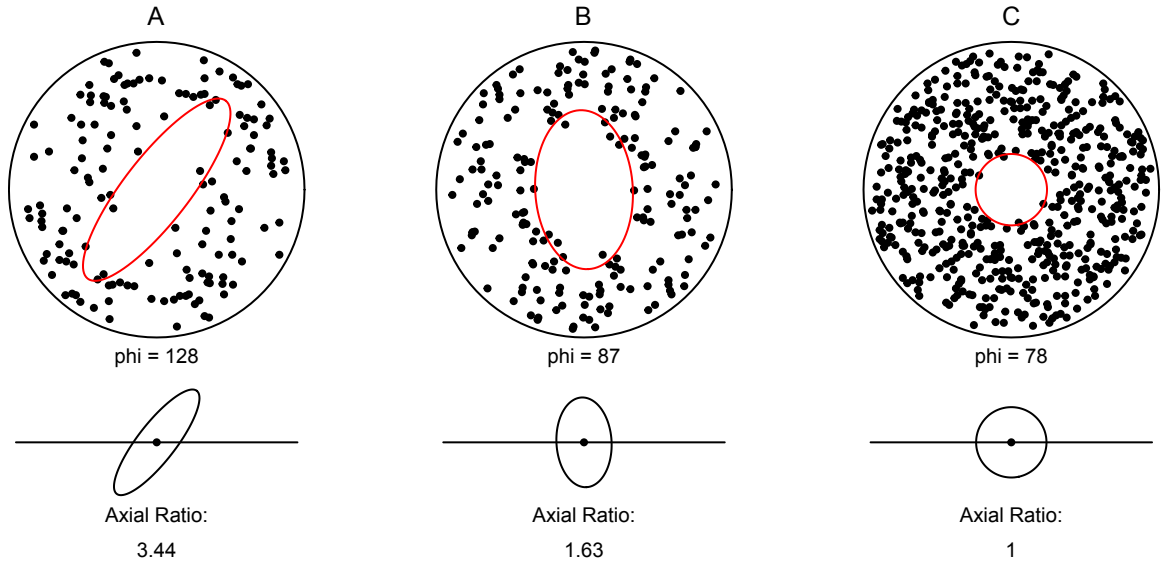


Figure 3.9: Sectional fry plots with normalized fitted ellipses.

a component of non-rotational object translation, or non-translational object rotation has been superimposed on a former anisotropy. To clarify, non-rotational object translation would cause the distribution of object centroids to change but would not affect the orientations or ellipticities of objects. This would produce a deviation in the Fry plot central void relative to the  $R_f/\phi$  result. Conversely, non-translational object rotation would change the  $R_f/\phi$  results relative to the Fry method. This discrepancy is supported by the low index of symmetry obtained for the  $R_f/\phi$  section “B” analysis ( $s = 0.79$ ) and indicates the possibility of superimposed fabrics that are best developed within this section. The incompatibility indexes obtained during ellipsoid fitting are substantially different ( $\sqrt{\tilde{F}} = 0.2$  vs. 4.7 for the  $R_f/\phi$  and Fry methods, respectively). This large degree of misfit obtained from the Fry sectional analyses indicates that the fabric ellipse determined for section “B” is not representative of the three-dimensional state of fabric architecture implied by the other two sections

and their close approximation to the values obtained from the corresponding sections of the  $R_f/\phi$  analyses. As such, it is possible the Fry method may be more sensitive to some violation of the assumptions of finite homogeneous deformation relative to the  $R_f/\phi$  technique for sample 11-LC-03-C.

The calculated fabric symmetry from both  $R_f/\phi$  and Fry analyses correspond to values in the prolate field of the Nadai plot (Fig. 3.10). The Lode parameter calculated from the  $R_f/\phi$  analysis very similar to the Lode parameter of the Fry analysis at  $\sim -0.75$  (Fig. 3.10: upper right and lower right, respectively). The calculated octahedral shear strains from this example plot at moderate distortions on the Nadai graph (Fig. 3.10). The  $R_f/\phi$  analysis resulted with a  $\bar{\epsilon}_s$  value inappreciably above one, while the Fry method produced a slightly higher value. Both methods are reasonably consistent with each other and tend to support field observations of rounded feldspar porphyroclasts with fairly well developed strain shadows. In light of the high incompatibility index determined for the Fry analysis ellipsoid fitting, the validity of this shape and magnitude may be called into question. However, the close association to the values obtained for the  $R_f/\phi$  ellipsoid suggests that effects of the sectional ellipse determined for face “B” may be mitigated by the other two sections, albeit, this could also be coincidental. Nevertheless these parameters for both analyses are effectively constrictional in geometry and moderate in distortion, as expected from the  $L \gg S$  estimation and mineral elongations obtained in the field, which supports the utility of the procedure.

The orientation of fitted principle axes from both methods is the most disparate property obtained in this example. Figure 3.11 displays two stereographic projections comparing the axial orientations for each method, as well as gneissic foliation and mineral trace lineation data recorded in the field. The calculated X-axis from the  $R_f/\phi$  analysis plots within the cluster of measured mineral trace lineations throughout

the region. The Z-axis also corresponds well to the orientations of several poles-to-foliation. Therefore, the  $R_f/\phi$  analysis is consistent with the regional field data. However, orientations of fabric axes obtained from the Fry method are significantly less congruous as shown in Figure 3.11. Not only does the X-axis plot outside the cluster of mineral trace lineations, the calculated X-Y plane deviates substantially from any foliation measurement (nearest pole to foliation measurement is approximate  $30^\circ$  from the Z-axis). However, the angular difference between the XY-plane and the gneissic foliation is greater than that for the mineral trace and X-axis, indicating that the orientations of prolate fabrics are more constrained by the lineation as is expected from the poor development of foliation at location 11-LC-03.

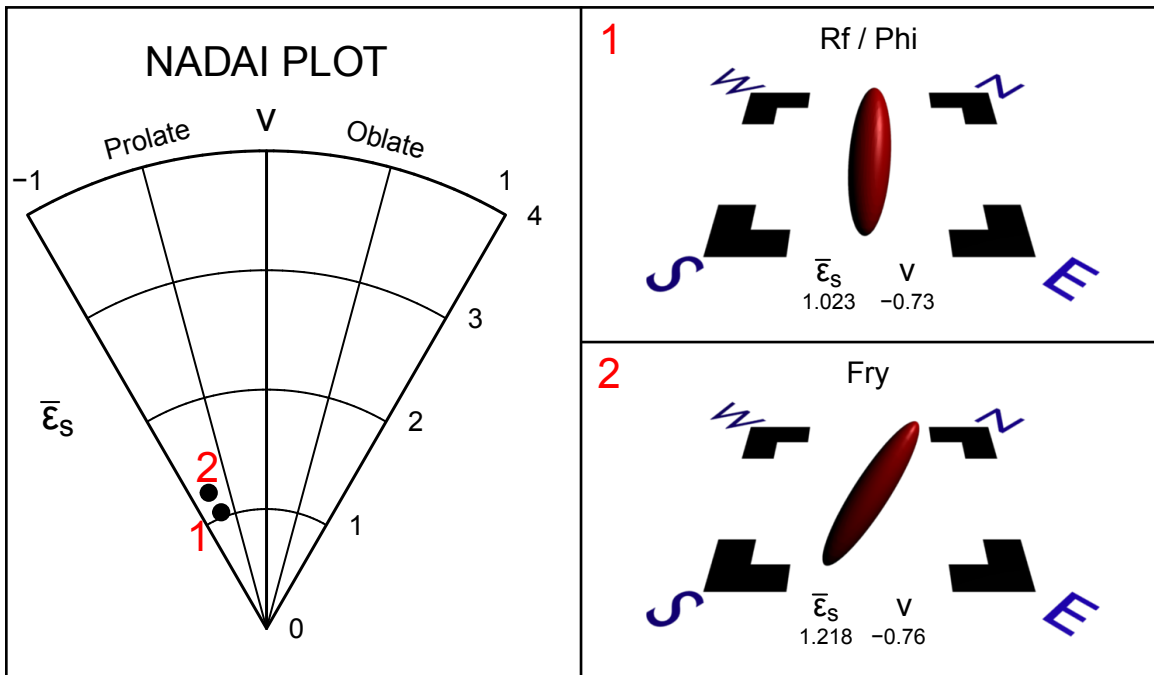


Figure 3.10: Nadai plot displaying the theoretical octahedral shear strain ( $\bar{\epsilon}_s$ ) and Lode parameter  $\nu$  for both  $R_f/\phi$  and Fry methods. Rendered three-dimensional images correspond to the labeled points on the Nadai plot.



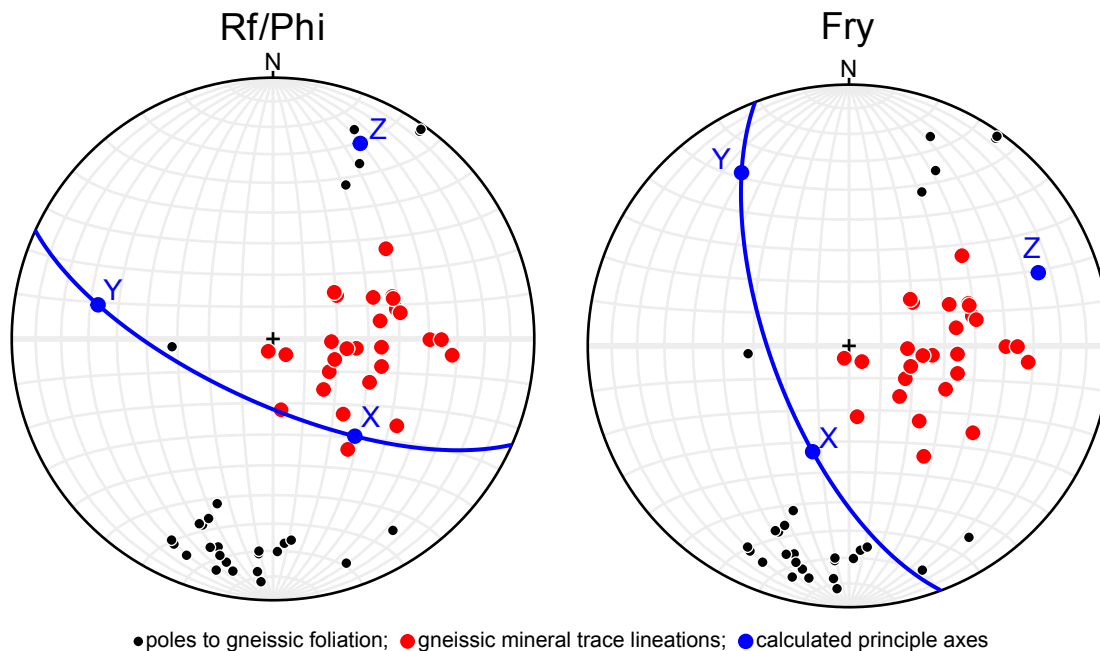


Figure 3.11: Equal area stereographic projections with measured fabric elements from the field (i.e. poles to gneissic foliations and gneissic mineral trace lineations) with the calculated principle fabric ellipsoid axes for the  $R_f/\phi$  technique (left) and the Fry method (right). Great circles denote the calculated X-Y principle planes.

### 3.5 Discussion and conclusions

The power of fabric quantification within deformed terrains has been established by correlating changes in fabric shape, magnitude, and orientation to regional structures. However, this procedure requires an enormous quantity of data<sup>4</sup> that is traditionally arduous to process following classic analytical strain techniques. This problem has been partially alleviated by advancements in computational software designed for geological strain applications. Despite this advance, there remains an absence within the literature of a comprehensive procedure outlining the steps of fabric quantification

<sup>4</sup>Assuming a minimum of 50 objects per each of the three mutually perpendicular sections that require the collection of semi-major axis lengths, semi-minor axis lengths, and the long axis orientation, one three-dimensional analysis involves a total of 450 measurements not including the computation required to produce a fabric ellipsoid.

from the field to an integrated result. The primary limitation to this stems from incompatibilities in data format between these programs and a lack of standardized visualization and presentation functions. The method presented herein outlines a new integration of several preexisting and widely available programs for strain analysis within the statistical computing environment R to convert data formats and produces an array of standardized graphs that can be directly incorporated into figures for publication.

This R-based quantification procedure described herein requires five main stages that include the collection and extraction of data from multiple two-dimensional sections, the analysis of these data through analytical strain techniques (Fry and  $R_f/\phi$ ), the synthesis of sectional fabric data into a fabric ellipsoid, and the visualization of the results. However, the assessment of error introduced in the procedure is difficult to address in a theoretical manner due to the potential propagation of errors throughout each of the stages outlined above. As such, I constructed a three-dimensional synthetic model with a known strain symmetry, octahedral shear strain, and orientation to empirically test the utility of the procedure. This model is based on the conservation of volume through coaxial, passive, and homogeneous finite deformation that resulted in principle planes of strain exhibiting sectional strain ratios of known magnitudes (i.e. 6, 4, and 1.5) and orientations. This state of strain corresponds to a Lode parameter of -0.56 and an octahedral shear strain of 1.33 such that the style of flow is general constriction at moderate distortions. With this model, the validity of the procedure was tested by comparing the calculated results to the expected theoretical state of strain.

The results of this assessment correspond closely to the expected state of strain and indicate several components of potential error. In general, the  $R_f/\phi$  method produced the most precise and accurate results compared to the Fry method. However, this

comparison is partially biased in that the population size of markers used for both analyses satisfied the requirements presented by Lisle (1985) but not for the Fry method (Fry 1979). Nevertheless, the sectional results were fairly consistent for each corresponding plane between the two methods. This assessment emphasizes the need to address analytical error in terms of shape, distortion, and orientation for a given ellipsoid and not by error determined from individual procedural stages. This is highlighted by the fact that the sectional Fry data produced an ellipsoid with a smaller degree of misfit compared to the  $R_f/\phi$  analysis despite the greater variation in sectional strain calculation. This affirms the fact that the “incompatibility index” generated by the program *Ellipsoid 2003* (Launeau and Robin 2005) corresponds only to the degree in which the relative parameters of ellipses in three-dimensional space define the surface of any possible triaxial ellipsoid, and not the accuracy of data collection or analysis. This error assessment produced ellipsoids that very closely approximated the expected state of strain. In general, the Fry analyses were slightly less robust, however, this may be a product of sample population size (see previous note on population sample size). Therefore, this procedure is deemed valid within a small margin of error (Figs. 3.5 and 3.6).

The applicability of this procedure to determine regional structures from changes in rock fabric must directly relate to visual estimates of tectonite fabrics. In order to highlight this application, a deformed metagranite with a characteristic  $L \gg S$  augen gneiss fabric from central Chile was processed. Results from both  $R_f/\phi$  and Fry analyses produced moderately distorted prolate ellipsoids that match field-based observations closely. However the orientation of the XY-fabric plane from the Fry analysis deviated considerably from the orientation of the bulk gneissic foliation, yet the orientation of the X axis remained fairly concordant to the mineral stretching direction. This relationship is expected from regions dominated by  $L \gg S$  fabrics

in that foliations will be poorly defined and the significance of their orientation is reduced. The fabric ellipse calculated from section “B” of the Fry analysis deviated substantially from the corresponding  $R_f/\phi$  section. I interpret this association as a possible result of either non-translational rotation, or non-rotational translation of objects superimposed on a preexisting fabric. It is tempting to suggest that this deviation may be produced by a component of plane-strain simple shear within section “B” that is not recorded by the Fry analysis (refer to Fry technique discussion in Chapter 1 for expansion on this concept) that may relate to vorticity. However, this possibility remains unexplored. My results highlight the need to address a given calculated fabric ellipsoid in terms of methodology and object type such that discrepancies in the assumptions of different methods or object deformation characteristics are not directly compared. To clarify, the results obtained from the Fry method can deviate from those produced by the  $R_f/\phi$  technique, which does not imply a change in the fabric architecture in a spatial context. Nevertheless, the application of multiple analytical strain techniques to a single sample may provide information on characteristics of the nature of deformation and the acceptability of specific strain assumptions.

## References

- Borradaile, G. (1984). Strain analysis of passive elliptical markers: success of de-straining methods. *Journal of structural geology* 6(4), 433–437.
- Chew, D. (2003). An excel spreadsheet for finite strain analysis using the rf/phi technique. *Computers & geosciences* 29(6), 795–799.
- Czeck, D., D. Fissler, E. Horsman, and B. Tikoff (2009). Strain analysis and rheology contrasts in polymictic conglomerates: An example from the seine meta-conglomerates, superior province, canada. *Journal of Structural Geology* 31(11), 1365–1376.
- Dunnet, D. (1969). A technique of finite strain analysis using elliptical particles.

- Tectonophysics* 7(2), 117–136.
- Flinn, D. (1956). On the deformation of the funzie conglomerate, fetlar, shetland. *The Journal of Geology* 64(5), 480–505.
- Fry, N. (1979). Random point distributions and strain measurement in rocks. *Tectonophysics* 60(1-2), 89–105.
- Gana, P. and R. Tosdal (1996). Geocronología u-pb y k-ar en intrusivos del paleozoico y mesozoico de la cordillera de la costa, región de valparaíso, chile. *Andean Geology* 23(2), 151–164.
- Hossack, J. (1968). Pebble deformation and thrusting in the bygdin area (southern norway). *Tectonophysics* 5(4), 315–339.
- Hsu, T. (1966). The characteristics of coaxial and non-coaxial strain paths. *The Journal of Strain Analysis for Engineering Design* 1(3), 216–222.
- Klepeis, K., D. King, M. De Paoli, G. Clarke, and G. Gehrels (2007). Interaction of strong lower and weak middle crust during lithospheric extension in western new zealand. *Tectonics* 26(4), TC4017.
- Launeau, P. and P. Robin (2005). Determination of fabric and strain ellipsoids from measured sectional ellipses—implementation and applications. *Journal of structural geology* 27(12), 2223–2233.
- Lisle, R. (1985). Geological strain analysis, a manual for the rf/phi method.
- Lisle, R. (2010). Strain analysis from point fabric patterns: An objective variant of the fry method. *Journal of Structural Geology* 32(7), 975–981.
- Lode, W. (1926). Versuche über den einfluß der mittleren hauptspannung auf das fließen der metalle eisen, kupfer und nickel. *Zeitschrift für Physik A Hadrons and Nuclei* 36(11), 913–939.
- Mookerjee, M. and S. Nickleach (2011). Three-dimensional strain analysis using mathematica. *Journal of Structural Geology*.
- Mulchrone, K. and P. Meere (2001). A windows program for the analysis of tectonic strain using deformed elliptical markers. *Computers & geosciences* 27(10), 1251–1255.
- Mulchrone, K., P. Meere, and K. Choudhury (2005). Sape: a program for semi-automatic parameter extraction for strain analysis. *Journal of structural geology* 27(11), 2084–2098.
- Nadai, A. (1963). Theory of fracture and flow of solids. *Vol. II) McGraw-H111, New York*.
- R Development Core Team (2010). *R: A Language and Environment for Statistical Computing*. Vienna, Austria: R Foundation for Statistical Computing. ISBN 3-900051-07-0.
- Ramsay, J. (1967). *Folding and fracturing of rocks*, Volume 56. McGraw-Hill ^ eNew York New York.

- Ramsay, J. and M. Huber (1983). *The techniques of modern structural geology*. Number v. 1 in *The Techniques of Modern Structural Geology*. Academic Press.
- Sullivan, W. (2006). Structural significance of 1 tectonites in the eastern-central laramie mountains, wyoming. *Journal of Geology* 114(5), 513–532.
- Waldron, J. and K. Wallace (2007). Objective fitting of ellipses in the centre-to-centre (fry) method of strain analysis. *Journal of Structural Geology* 29(9), 1430–1444.
- Wall, R., P. Gana, and A. Gutiérrez (1996). *Mapa geológico del area de Valparaiso-Curacavi, Regiones de Valparaiso y Metropolitana*. Servicio Nacional de Geología y Minería.
- Wells, M. (2001). Rheological control on the initial geometry of the raft river detachment fault and shear zone, western united states. *Tectonics* 20(4), 435–457.

## Chapter 4

# FRY3D: an interactive R script for the visualization of rock fabrics in three-dimensions

### Abstract

FRY3D is an interactive R script designed to aid in the instruction and visualization of three-dimensional strain calculation at the advanced undergraduate and graduate levels. This tutorial helps mitigate the logistics of multiple manual strain calculations by maintaining the orientations and properties of sectional data within a three-dimensional context. This tutorial allows the centroids of objects from three images of known orientations to be selected by the user and processed in the open-source program R to create three sectional Fry plots. The properties of the central void ellipse are determined by the user and an interactive, three-dimensional Fry plot is constructed. The sectional strain parameters are exported to a file compatible with the program *Ellipsoid 2003* for statistical ellipsoid fitting. The output generated from *Ellipsoid 2003* is read back into R to construct a Nadai plot of the calculated Lode parameter and octahedral shear strain, as well as a stereographic projection displaying the orientations of the principle strain axes. Additionally, the script generates an interactive, three-dimensional model of the strain ellipsoid correctly oriented with respect to a geographic reference frame so that the result can be directly compared to the three-dimensional Fry plot. This tutorial was presented to an upper-level structural geology course of 20 undergraduate students with a two part semi-quantitative concept assessment before and after the presentation. The results of this assessment indicate a positive increase in student's understanding of three-dimensional finite strain.

---

## 4.1 Introduction

The ability to visualize the characteristics of finite deformation in three-dimensions is a fundamental requirement of structural geology. Traditionally, strain concepts are taught at the undergraduate level through the use of static perspective diagrams and figures. Recently however, several workers have produced resources for structural geology education that utilize computer animations to help better convey the geometry and evolution of features such as dipping strata, folds, and faults (e.g. Burger and Harms 2006; Cockett 2012). Although these resources are widely available for general structural concepts<sup>1</sup>, there is an absence of computer-based tools that help students visualize the application of analytical strain techniques to three-dimensional deformation. Many structural geology courses, textbooks, and laboratory manuals (see for example: Rowland et al. 2007; Twiss and Moores 2007) provide examples and assignments that describe two-dimensional strain analyses using a variety of techniques such as the Fry method (Fry 1979), the Wellman procedure (Wellman 1962), and the  $R_f/\phi$  technique (Ramsay 1967; Dunnet 1969; Lisle 1985). However, these do not directly illustrate the three-dimensional context of these analyses.

The lack of three-dimensional strain examples in educational curricula is likely due to logistical impediments that include the time intensive nature of multiple plane strain analyses, the synthesis of two-dimensional data, and the ability to visualize the shape and orientation of the calculated strain ellipsoid. Nevertheless, a single two-dimensional analysis cannot describe the three-dimensional state of strain because the geometry of a strain ellipse is dependent on the orientation of the analytical section relative to the finite strain ellipsoid. As such, a single analysis not only fails to address the magnitude of deformation, it cannot provide information concerning the

---

<sup>1</sup>For a list of computer applications refer to the SERC website: [http://serc.carleton.edu/NAGTWorkshops/structure/computer\\_resources.html](http://serc.carleton.edu/NAGTWorkshops/structure/computer_resources.html)



orientation and symmetry of strain. The ability to completely constrain the geometry of finite deformation is an essential tool to describe strain gradients and thereby quantitatively distinguish shear zones. I believe the lack of discussion on deformation in three-dimensions creates the misconception that a single two-dimensional analysis can effectively address the nature of pervasive deformation. Therefore, I highlight the need to provide a three-dimensional context for analytical strain techniques taught at the undergraduate and graduate levels.

In this chapter I present a new instructional approach to help students better visualize three-dimensional deformation. This instructional procedure implements the script FRY3D written within the open source statistical computing environment R (R Development Core Team 2010) to alleviate the impediments of teaching traditional three-dimensional strain analyses. This script allows for the collection and analysis of two-dimensional strain data in order to produce a coherent interactive three-dimensional Fry plot, from which a finite strain ellipsoid is calculated. Accompanying this script is a deformed synthetic dataset (Fig. 4.1) that can be physically constructed with a known orientation, strain symmetry (i.e. the Lode parameter), and octahedral shear strain to aid in student visualization. For a discussion of these properties see: Brandon (1995). The details of this model are explained in Chapter 3 and can be reproduced following the instructions outlined in Appendix D. A replica of this model can easily be made and oriented (following the attitudes in Table D.1). In addition to the classroom application of this tutorial, FRY3D provides an excellent resource to train individuals interested in conducting analytical fabric research, as the program introduces the user to the primary components of three-dimensional fabric quantification.

In order to address the qualitative effectiveness of this instruction, a general assessment of three-dimensional strain concepts was administered to a class of 20 under-

graduate students before and after a presentation of the FRY3D script. The results document a general decrease in the number of misconceptions associated with three-dimensional deformation after the presentation of the instruction proposed herein. For example, many students incorrectly stated that a two-dimensional strain analysis accurately elucidates the orientation and magnitude of principle strain axes prior to the tutorial. After the FRY3D instruction, a significant population of the class indicated the importance of multiple strain analyses on three mutually-perpendicular sections to define all principle strain axes. Therefore, I assert the effectiveness of this tutorial in dismantling misconceptions concerned with strain quantification in three-dimensions.

## 4.2 Methodology

FRY3D is an R script that uses functions within the add on package *StructR* (Weber 2012) designed primarily for this tutorial and available for free download on the *Comprehensive R Archive Network*<sup>2</sup>. In order to successfully run the script, the open-source statistical computing environment R must be correctly installed and the *StructR* package loaded. The *StructR* package combines operations from other R packages and may require additional downloads of these modules (see the accompanying manual in Appendix C, and R documentation for additional help). Once the computer environment is established, the FRY3D instructional tutorial can be executed. This procedure involves two parts including the construction of a three-dimensional Fry plot and analysis of the fitted strain ellipsoid. As such, FRY3D is broken into two scripts that read and write files associated with the program *Ellipsoid 2003* (Launeau and Robin 2005) to completely define the three-dimensional state of strain.

---

<sup>2</sup>For more information visit: <http://cran.r-project.org/>

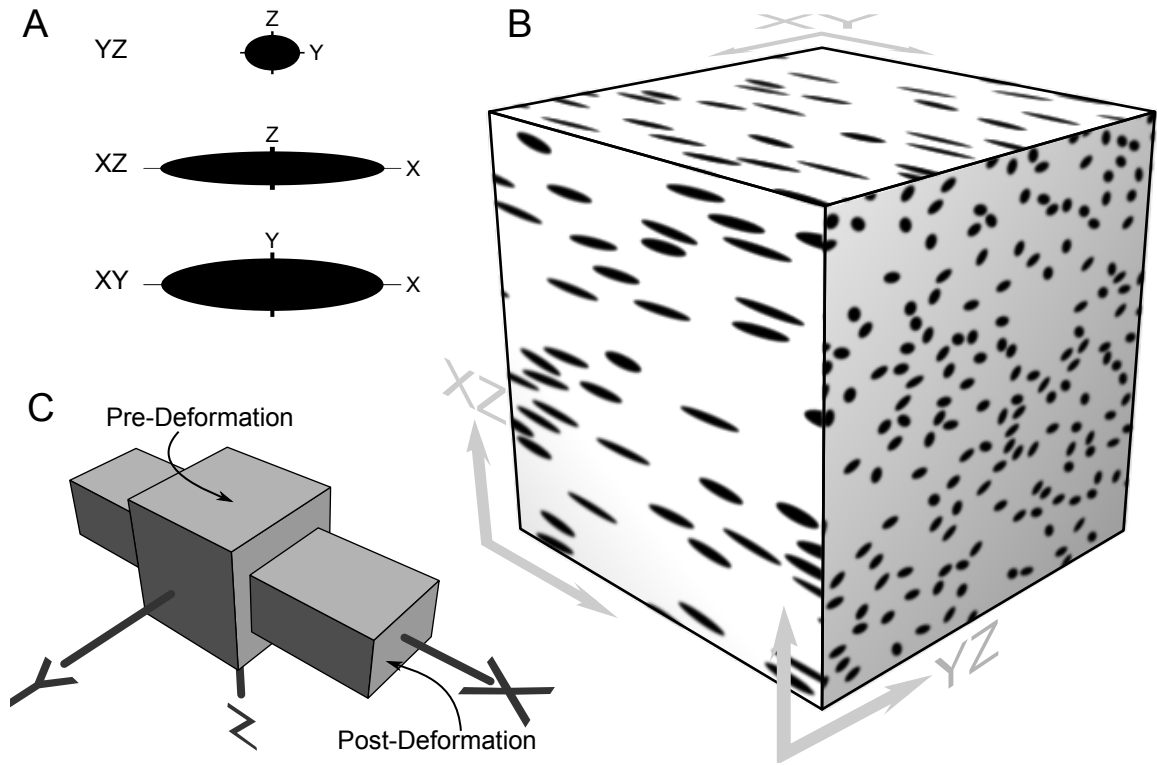


Figure 4.1: Cartoon illustrating the construction of the synthetic deformed conglomerate dataset accompanying the instructional tutorial. Part “A” denotes the two-dimensional strain ellipses for the principle planes of strain shown in “B” as constructed through constant volume deformation highlighted in “C.”

FRY3D enables the user to load a sectional image, with a known geographic orientation, into the R-console and select the locations of object centroids (Fig. 4.2-A). The sectional image is derived from a synthetic dataset based on the parameters explained in Chapter 3, illustrated in Figure 4.1, and available for construction following the procedure in Appendix D. Once all objects are selected, a two-dimensional Fry plot is produced that allows the user to visually estimate the central void apogee and perigee (Fig. 4.2-B). The geometric parameters of this central void estimation are extracted and a strain ellipse is plotted directly on the diagram. This process is repeated for the remaining two sectional images and a three-dimensional Fry plot is

produced (Fig. 4.3-A). The three-dimensional diagram simply orients and combines the previous two-dimensional Fry plots and plane strain ellipses into an interactive window so that the user may navigate throughout the point cloud and better visualize the resultant strain ellipsoid. In addition, a file is written and saved to the output folder that is directly compatible with the program “Ellipsoid 2003.”

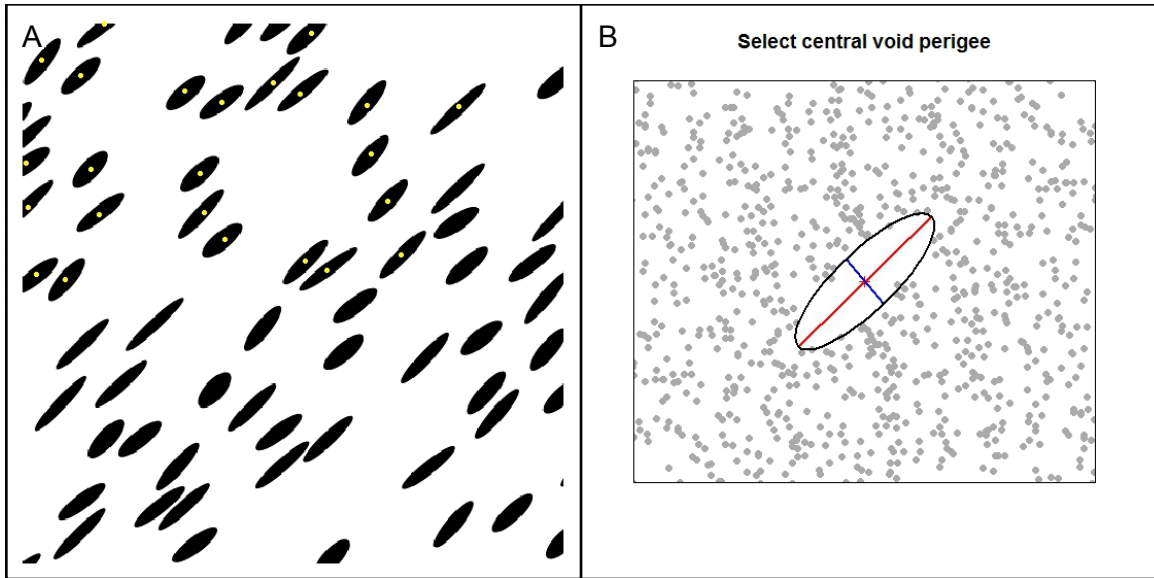


Figure 4.2: Screen images from the FRY3D tutorial depicting the two-dimensional strain analyses. A: object centroid selector tool. B: central void ellipse estimation.

Although the three-dimensional Fry plot helps students better visualize the context of the sectional data, no quantitative parameters defining the true geometry of finite strain are produced. However, running the output file through *Ellipsoid 2003* statistically fits a strain ellipsoid to the sectional data<sup>3</sup>. The results of this synthesis can be read into the R-console with the use of a second script and an array of graphs are produced. Specifically, the script will construct another three-dimensional plot with a model of the calculated ellipsoid (Fig. 4.3-B) so that a comparison to the Fry

<sup>3</sup>For a detailed methodology of the program *Ellipsoid 2003* and the statistical properties of ellipsoid fitting see Launeau and Robin 2005 and section 3.2.3.

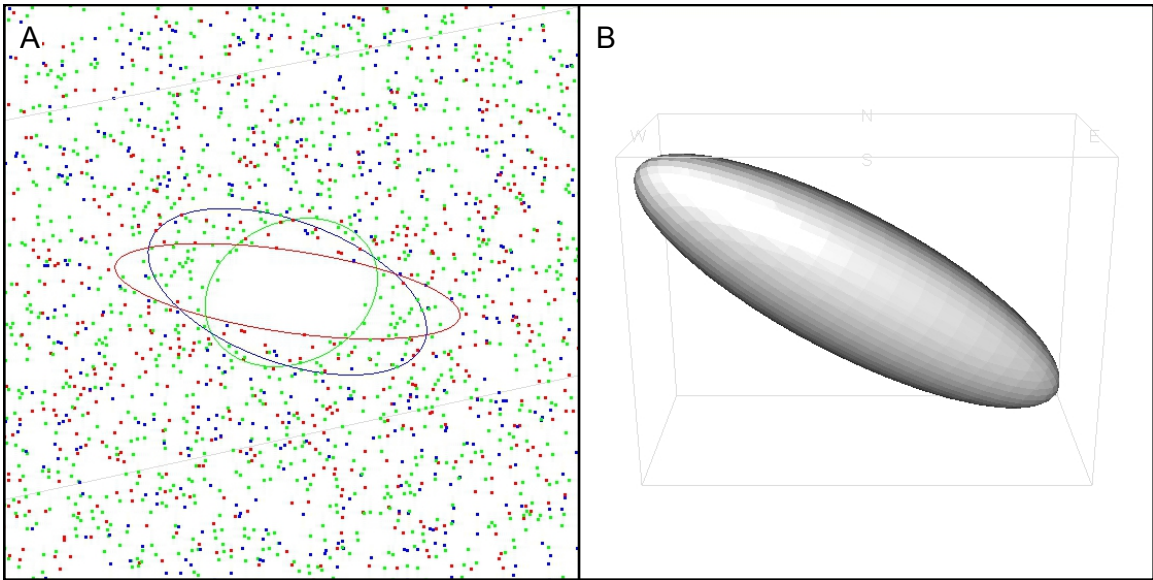


Figure 4.3: Three-dimensional strain visualizers with an interactive Fry plot (A) and a modeled fitted strain ellipsoid.

point cloud can be made. Furthermore, the script will run functions written by Lees (2011), to create a standardized equal-area lower-hemisphere stereographic projection directly in R that displays the orientations of the principle strain axes (Fig. 4.4-A). A final plot is generated containing a Nadai graph, which allows both the magnitude of distortion and strain symmetry to be compared (Fig. 4.4-B).

## 4.3 Qualitative evaluation

### 4.3.1 Evaluation setup

In order to qualitatively address the effectiveness of this instruction, a simple two part questionnaire concerning student comprehension of three-dimensional deformation was developed. The first assignment requires students to manually construct a Fry plot from a photomicrograph of a deformed oolitic limestone (Ramsay and Huber 1983, p. 112). From this plot, the central void ellipse is estimated and plotted on

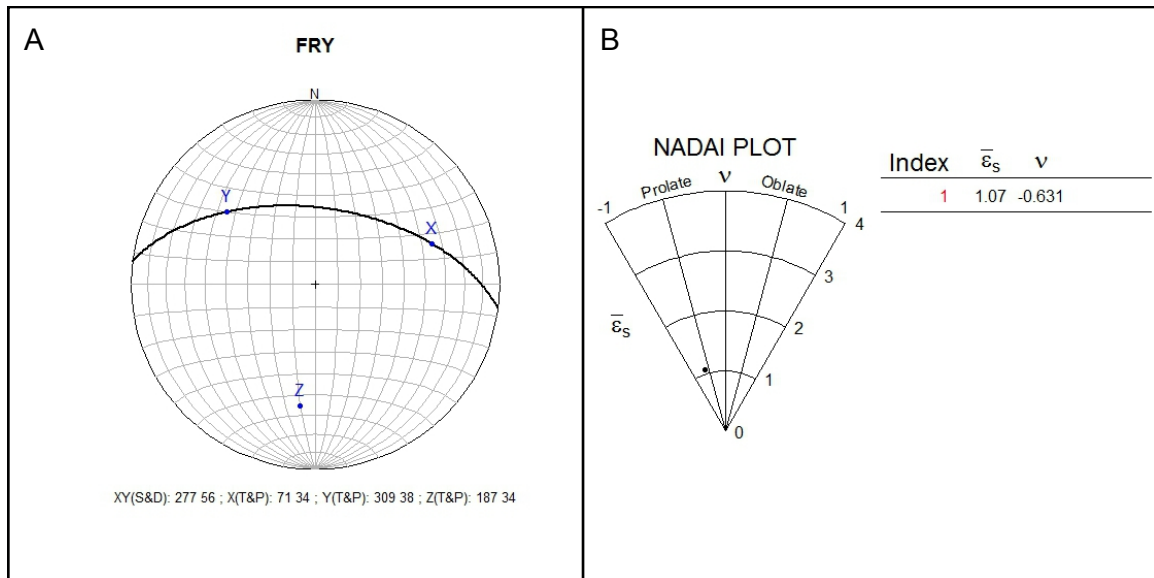


Figure 4.4: Images from the FRY3D instructional tutorial highlighting the quantitative properties of the strain ellipsoid synthesis. A.) Equal-area lower-hemisphere stereographic projection of the principle strain axes; B: Nadai plot illustrating the Lode parameter and octahedral shear strain.

a separate graph, from which the strain ratio and orientation is calculated (see this chapter's additional materials for an example assignment). Finally, students are asked to discuss how this section relates to three-dimensional deformation as stated below:

*What does this two-dimensional representation of strain inform us about deformation in three-dimensions?*

Although previous lectures have established the basic concepts of fabric symmetry (i.e.  $L > S$  vs.  $L < S$ ) the details of three-dimensional strain have not been discussed prior to this exercise. Therefore, I expect a significant number of incorrect student responses to the above question, which helps to establish a general baseline level of understanding prior to the FRY3D tutorial. Each response is categorized as follows: 1.) lacks substantial understanding; 2.) some concepts are developed but lack a comprehensive understanding 3.) exhibits a comprehensive understanding

of the nature of deformation in three-dimensions. The relative proportions of these categories are then determined.

After completion of the two-dimensional fry assignment, the FRY3D instructional tutorial is implemented during lecture and projected on a large screen. This instruction is accompanied with a simple in-class worksheet to help focus the attention of students. Additionally, the tutorial calls for volunteers to actively select object centroids and fit sectional ellipses. This interaction with students helps motivate interest and better solidify the process of data collection. After executing the tutorial, students are able to individually navigate the modeled Fry plot and fitted ellipsoid. Before the end of class, students are asked to complete a short answer questionnaire containing the statement:

*What does a calculated strain ellipsoid describe and why must the state of strain be represented with this geometry and not an ellipse?*

Once again, the results are categorized as described above and tabulated into relative proportions. These data are then compared to the base level understanding and a general assessment of effectiveness is obtained. Our tutorial evaluation highlights several common misconceptions students have about three-dimensional deformation after completing only the two-dimensional Fry assignment. However, after the tutorial was administered, the majority of students provided acceptable answers to the previous question (Fig. 4.5).

#### **4.4 Conclusions**

The FRY3D script provides instructors with a tool to aid in teaching three-dimensional deformation. The primary qualities of this instruction include the ability to quickly produce three mutually perpendicular Fry plots of known orientation, combine multiple two-dimensional data sets into a single three-dimensional viewer, and quantify

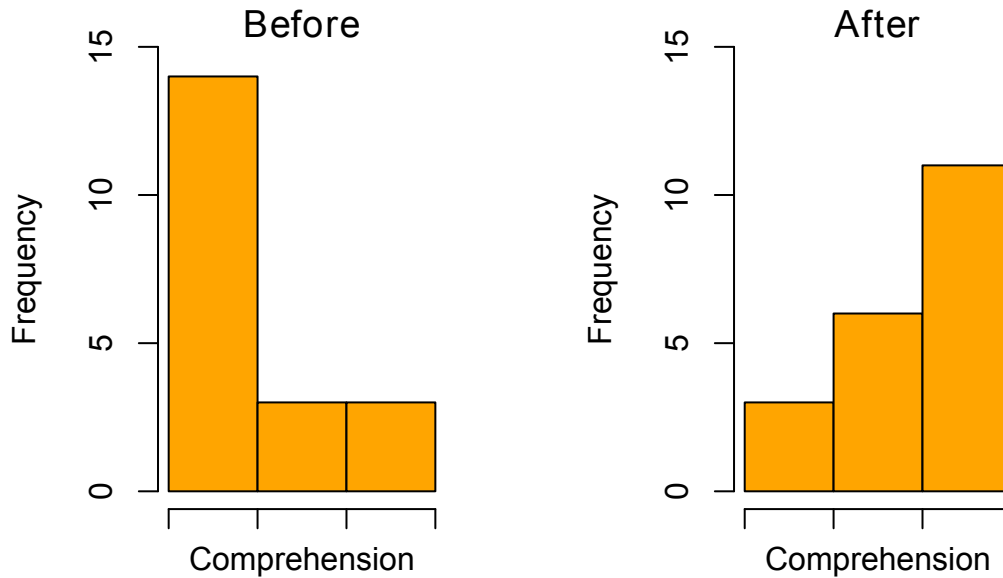


Figure 4.5: Results of the FRY3D evaluation compiled from a class of 20 students before and after the tutorial. Comprehension is divided into three qualitative categories with a “lacks substantial understanding” corresponding to the histogram bins on the left, “some concepts are developed but lack a comprehensive understanding” for the center bins, and “exhibits a comprehensive understanding of the nature of deformation in three-dimensions” on the right.

the geometric properties of a three-dimensional strain ellipsoid. With this functionality, the audience is able to physically see the manner in which non-unique sectional data constrains a single unique strain ellipsoid. Although this tutorial aids in three-dimensional visualization, students must have a prior knowledge of two-dimensional strain techniques (i.e. the Fry method in this role) in order to be an effective learning technique. Therefore, I recommend this procedure as an augmentation to lectures after students have manually completed a single Fry plot. The results of our qualitative evaluation document a favorable increase in the perception of three-dimensional deformation.

Although this tutorial is generally designed as an educational tool for an upper-level structural geology course, it can be expanded and used as a preparatory lesson



for fabric analysis research (see Chapter 3). From the tutorial I expect users to gain an more comprehensive understanding of the Fry method, the nature of a two-dimensional strain in the context of three-dimensional deformation, and the geometric properties of finite strain. Furthermore, this method clearly displays the advantages of model representation for the visualization of deformation and the use of the Lode parameter and octahedral shear strain to quantify strain gradients.

---

### **Additional materials**

The following is an example assignment designed to better evaluate student comprehension of finite strain in three-dimensions.

NAME: \_\_\_\_\_

GEOL 260: STRUCTURE

## **Part one: two-dimensional strain**

### **Introduction**

The Fry method, also known as a nearest-neighbor center-to-center analysis, is an analytical strain technique used to calculate the “amount” of deformation a rock has experienced using the final distribution of object centers. The primary assumption of this technique is that object centers (centroids) were randomly distributed with a minimum nearest neighbor threshold distance prior to deformation. As such, this method is best suited for scenarios that involve objects of similar sizes, similar shapes, and a random distribution or packing. For example, well-sorted “structureless” sandstones, oolitic limestones, and even phenocrysts in an igneous rock can be used with the Fry method. The Fry method graphically plots the centers of all objects for each object so that variations in the statistical distance between nearest neighbors will be determined. This produces an elliptical region at the center of the plot known as the central void that mimics the shape of the finite strain ellipsoid.

### **Procedure**

1. Use a colored pencil or pen to mark the centers of each ooid in Figure 4.7 directly on the figure. Keep each point as small as possible but large enough to clearly see through tracing paper (Fig. 4.6).
2. Take a sheet of tracing paper or mylar and place a small “X” roughly in the center of the sheet. Make sure this sheet has straight and square edges.
3. Pick an ooid close to the center of Figure 4.7 and place the tracing paper “X” directly on the ooid center you have marked. Align the the edge of the tracing

paper to the edge of the figure so that the two are parallel.

4. On the tracing paper, copy the centers of all other ooids with small dots. Be careful not to rotate the tracing paper as this will distort the plot.
5. Translate the tracing paper to another ooid and repeat step 4 for all other ooids. Once again, make sure the edges of the figure and tracing paper are aligned parallel. Do this for all ooid centers to clearly establish a central void. Yes, this is tedious and it will take a while.
6. Transfer your Fry plot to Figure 4.8 and calculate the long axis length, short axis length, strain ratio and orientation.

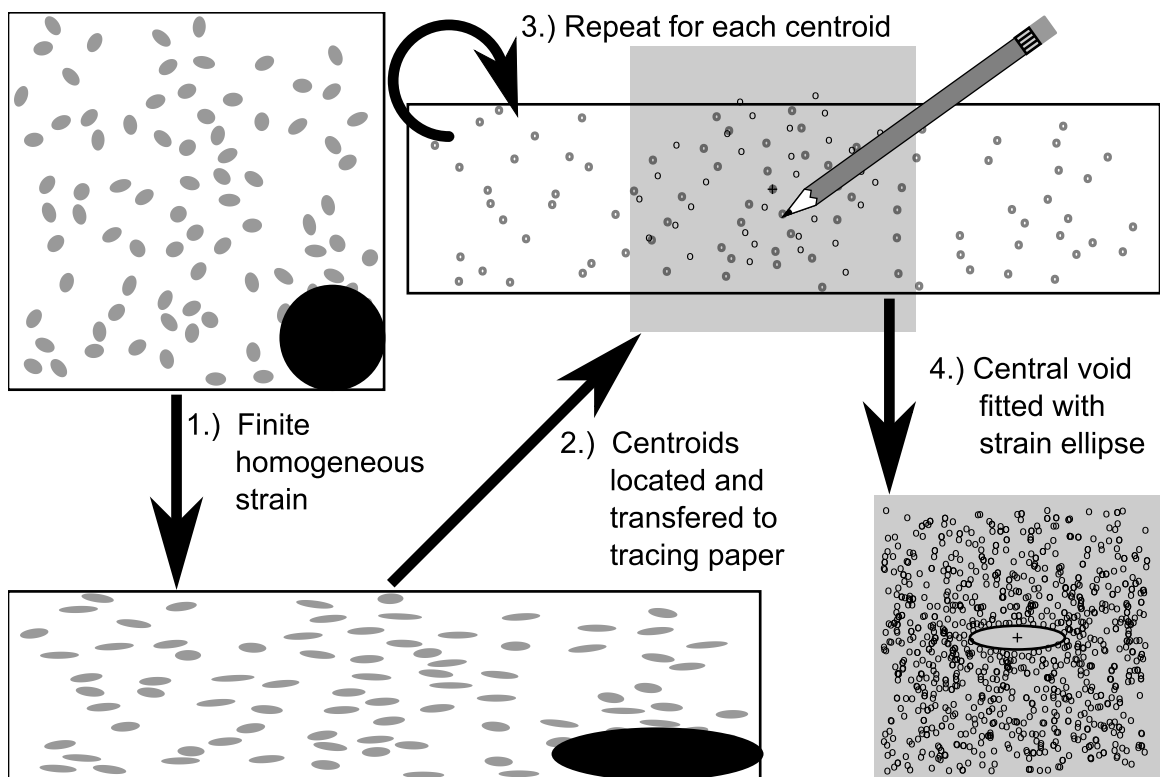


Figure 4.6: Schematic illustration highlighting the general procedure of the manual Fry method.

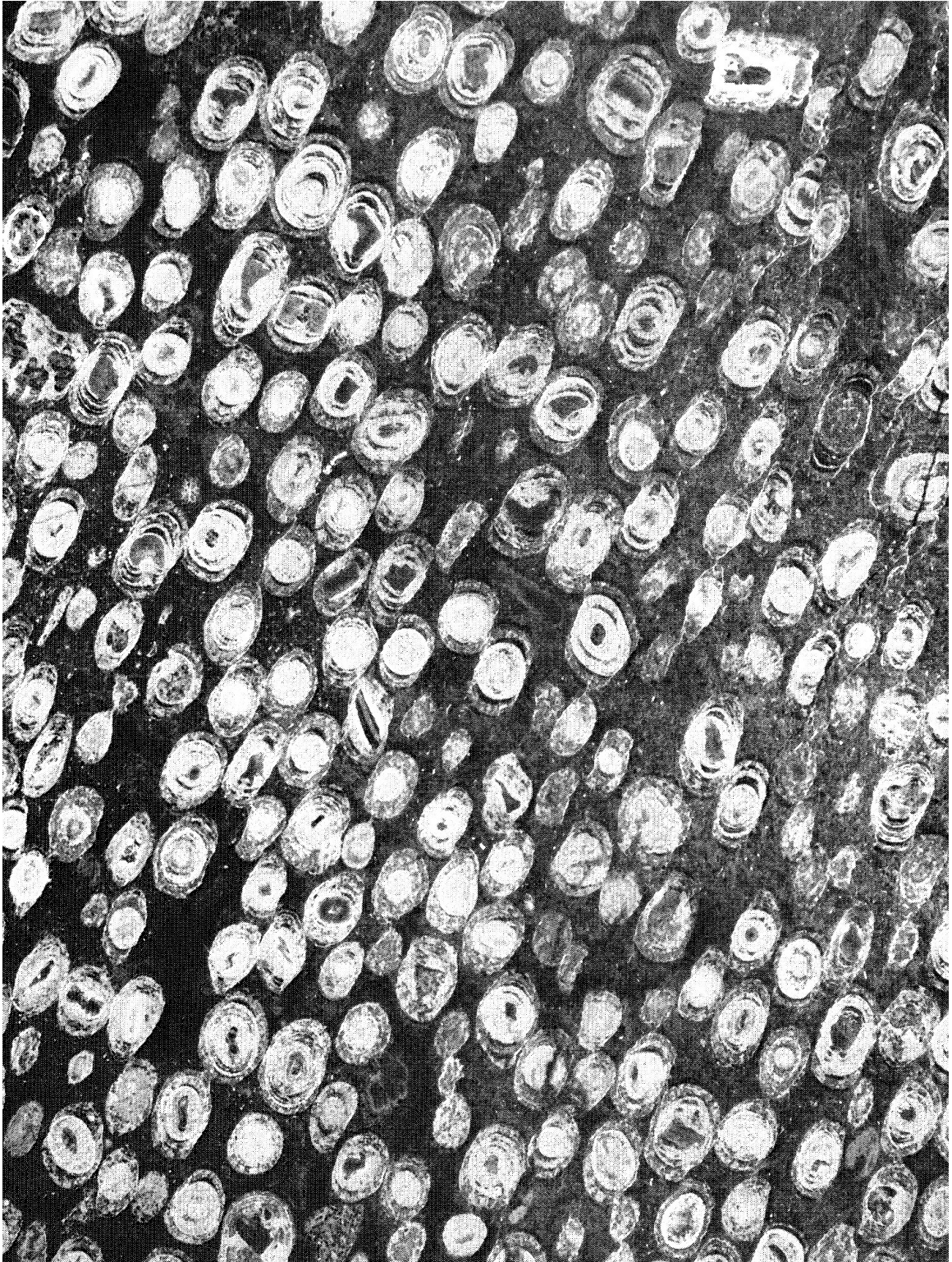
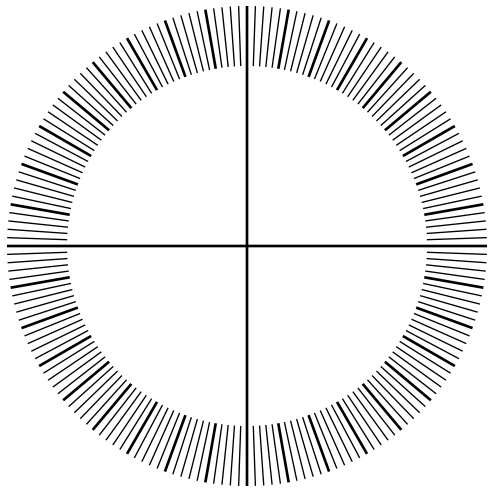


Figure 4.7: Deformed oolitic limestone: (Ramsay and Huber 1983, p. 112).



Long axis length:

Short axis length:

Strain ratio:

Long axis orientation:

Figure 4.8: Plot the strain ellipse here and determine the properties listed above.

### Questions and deliverables

What is a strain ellipse?

---

---

What does this two dimensional representation of strain inform us about deformation in three-dimensions?

---

---

---

---

---

Also turn in the following for credit:

***Ooid centers:*** Original figure with ooid centers marked.

***Fry plot:*** Staple your tracing paper with the fry plot.

***Strain ellipse:*** Complete Figure 4.8 and calculate the strain ratio.

NAME: \_\_\_\_\_

GEOL 260: STRUCTURE

### **Part two: three-dimensional strain**

Follow along in class with the three-dimensional strain tutorial and answer the basic questions listed below.

What is the general shortening direction for section A (e.g. left-right)? \_\_\_\_\_

What is the general shortening direction for section B (e.g. left-right)? \_\_\_\_\_

Is section B more or less deformed than A? \_\_\_\_\_

What is the general shortening direction for section C (e.g. left-right)? \_\_\_\_\_

Is section C more or less deformed than B? \_\_\_\_\_

In the space below sketch the general ellipsoid shape and orientation given by the 3D Fry plot.

What is the approximate direction of the maximum stretch axis? \_\_\_\_\_

What is a strain ellipsoid?

---

---

---

---

Why must the state of strain be represented by an ellipsoid and not an ellipse?

---

---

---

---

---

---

---

---

---

---

---



## References

- Burger, H. and T. Harms (2006). *An introduction to structural methods*. Tasa graphical arts inc.
- Cockett, R. (2012). *Visible Geology*.
- Dunnet, D. (1969). A technique of finite strain analysis using elliptical particles. *Tectonophysics* 7(2), 117–136.
- Fry, N. (1979). Random point distributions and strain measurement in rocks. *Tectonophysics* 60(1-2), 89–105.
- Launeau, P. and P. Robin (2005). Determination of fabric and strain ellipsoids from measured sectional ellipses—implementation and applications. *Journal of structural geology* 27(12), 2223–2233.
- Lisle, R. (1985). Geological strain analysis, a manual for the rf/phi method.
- R Development Core Team (2010). *R: A Language and Environment for Statistical Computing*. Vienna, Austria: R Foundation for Statistical Computing. ISBN 3-900051-07-0.
- Ramsay, J. (1967). *Folding and fracturing of rocks*, Volume 56. McGraw-Hill ^ eNew York New York.
- Ramsay, J. and M. Huber (1983). *The techniques of modern structural geology*. Number v. 1 in The Techniques of Modern Structural Geology. Academic Press.
- Rowland, S., E. Duebendorfer, and I. Schiefelbein (2007). *Structural Analysis and Synthesis: a laboratory course in Structural Geology*. Wiley-Blackwell.
- Twiss, R. and E. Moores (2007). *Structural geology second edition*. WH Freeman and Company.
- Webber, J. R. (2012). *StructR: Structural geology tools*. R package version 1.1.
- Wellman, H. (1962). A graphical method for analysing fossil distortion caused by tectonic deformation. *Geol. Mag* 99(4), 348–352.

## Chapter 5

# Error evaluation of the Panozzo projection method for strain analysis (short note)

### Abstract

A brief assessment of analytical error associated with the Panozzo projection technique for strain analysis is presented herein and indicates relationships among population size, strain magnitude, and initial fabric. My results suggest that this method is most robust when applied to sections containing greater than approximately 125 lines. Moreover, the magnitude-dependent error indicates that the method may be better suited for rocks deformed at low to moderate strains. I recommend an adaption to the initial conditional assumptions for this method that lines exhibit an initial radial symmetry when recentered to a common point. A least-squares fitting modification is presented to better define the calculated strain ratio mathematically. However, this modification does not effectively reduce the analytical error I document in this chapter.

---

### 5.1 Introduction

The Panozzo projection method is an analytical strain technique that involves summing the lengths of the horizontal components of a population of lines as projected onto a horizontal line. The population of lines is then iteratively rotated and the components are again added. From these data a plot is constructed that relates the summed lengths of projected lines to the rotation step forming a sinusoidal wave re-

flecting the strain ratio. The maximum projected length corresponds to the maximum extension direction and the quotient between the maximum and minimum projected lengths is equal to the ratio of strain. This method provides a fairly quick check for inherited fabrics (using computational scripts I have written) if the direction of the minimum projected length is not  $90^\circ$  from the maximum projected length (Trayner 1986).

The Panozzo projection method for two-dimensional strain analysis uses the orientation and lengths of lines within a planar section to calculate finite strain (Panozzo 1984). The assumptions of this method include the following: deformation is homogeneous at the scale of analysis, markers deform in a passive nature, the viscosity contrast between the objects and the matrix is zero, and the orientations of lines are uniformly distributed prior to deformation. Although Panozzo (1984) does not explicitly describe the nature of initial line lengths, all examples presented therein appear to have initially equal lengths. This criteria is not generally applicable to geologic scenarios where objects will likely form a range of lengths, therefore, it must be assumed that there is no orientation dependent lengths.

In this paper I address the nature of analytical error that must be expected in applying the Panozzo projection technique to deformed material lines. I present an array of guidelines that address the magnitude of error expected under ideal conditions with respect to both the magnitude of deformation and population size. This error analysis is based on a series of synthetic datasets produced with highly ideal initial undeformed conditions that are subjected to a range of known shear strains. Variations in the calculated strain ratios are statistically compared to the expected values. My results highlight the sensitivity of the Panozzo projection technique to slight preferred orientations in the initial rock fabric despite a uniform distribution of line orientations. I conclude that the Panozzo analytical strain method exacerbates

these initial fabric anisotropies through finite strain even when the basic assumptions of the method, as outlined in Panozzo (1984), are constrained. Based on these results, I recommend that the initial conditions of the Panozzo projection technique be modified from lines of uniform distribution to lines that exhibit a radially symmetric initial pattern when recentered about a common point within the section. Moreover, I suggest that sections with population sizes below  $\sim 125$  lines are not statistically robust. Finally, my results clearly show an increase in width of the confidence interval with increasing strain magnitude, which indicates that this method may be best suited for low strain fabrics ( $R_s \sim 1.5$  to 5).

## 5.2 Methodology

The methodology presented herein uses a series of scripts written in the statistical computing environment R to construct, deform, analyze and calculate the magnitude of two-dimensional strain from a series of lines following the Panozzo projection method (Panozzo 1984). The functions used in this procedure are freely available within the R-package “StructR” (Webber 2012) and are briefly explained in the following paragraphs. The details of individual methods presented throughout the various tests are explained later in the text (Section 5.2.2) and are simple modifications of these routines.

### 5.2.1 General procedure

In order to empirically determine the errors associated with this method a series of ideal undeformed datasets were generated based on an input population size and plot width. The lengths of lines are produced with a random normal population generator based on the average line length and a standard deviation one quarter this value. I assert that a normal distribution of line lengths in most geological situations is more reasonable an assumption than lines of equal length due to natural

variation in cross-sectional lengths of objects. The end point coordinates of these lines are transformed based on a rotation matrix constructed from a uniform distribution of angles and are plotted with tie-lines as shown in Figure 5.1-A. Note that the translational distribution of lines is irrelevant and not incorporated in the Panozzo projection method. For simplicity, the lines are centered at the plot origin.

The undeformed line coordinates are transformed with a separate function that displaces the node abscissae in such a manner to deform the lines under plane strain simple shear as determined by the input shear strain value (Fig. 5.1-B). This value directly relates to the strain ratio ( $R_s$ ) as given by Equation 5.1<sup>1</sup> (modified from Ramsay 1967, page 85 Equation 3-67). This enables the comparison of applied shear strain to the expected strain ratio and the calculated strain ratio.

$$R_s = \frac{\sqrt{\frac{1}{2} \times (\gamma^2 + 2 + \gamma \times \sqrt{\gamma^2 + 4})}}{\sqrt{\frac{1}{2} \times (\gamma^2 + 2 - \gamma \times \sqrt{\gamma^2 + 4})}} \quad (5.1)$$

The function used to determine the projected lengths of a given deformed dataset simply applies an iterative rotation matrix to the line node coordinates and calculates the summation of the absolute value of the difference in line node abscissae for each each rotational step (all data presented herein is based on a one degree rotational step). These data are then modified and plotted on a polar graph to define an elliptical perimeter (Fig. 5.3-A). The method used in the following analyses fits a least-squares ellipse to the perimeter point data to define the shape-preferred orientation mathematically (Fig. 5.3). However the reduction in error following this modification is insignificant as explained in Section 5.3.1. Based on the parameters of this ellipse (i.e. semi-major axis length, semi-minor axis length, and angular orientation) the

---

<sup>1</sup>For variable definitions refer to Table 1.1.

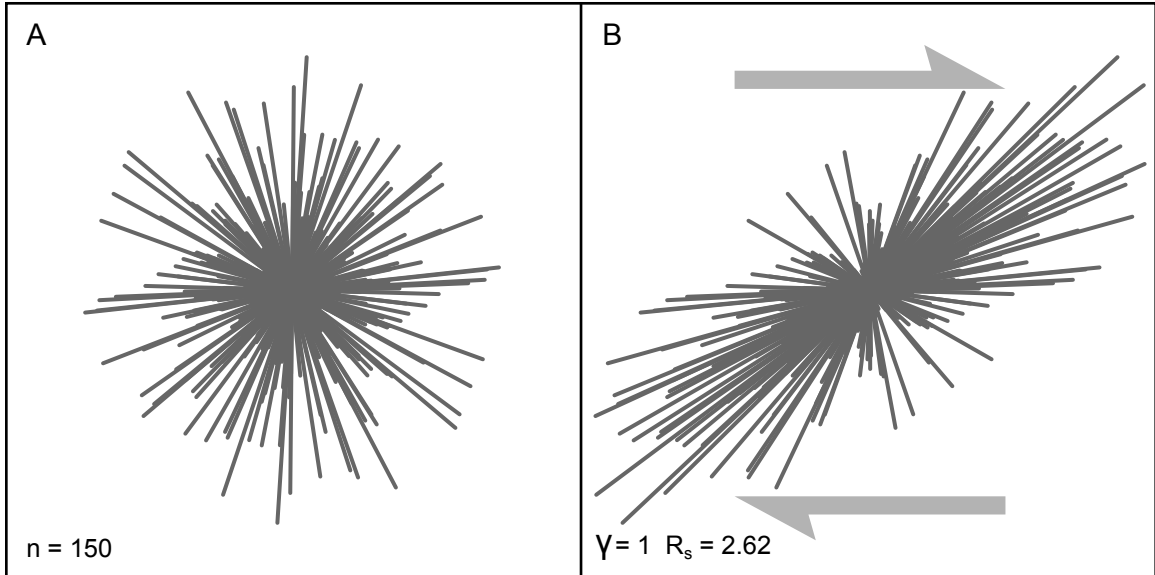


Figure 5.1: Plot of 150 undeformed (A) and deformed (B) synthetic lines centered at the plot origin. Initial dataset generated with a normal distribution of line lengths with a mean length of 25 units and a standard deviation of 6.25 that are rotated to create a uniform distribution of orientations. Undeformed data was subjected to a dextral shear strain ( $\gamma$ ) of one under homogeneous simple shear plane strain.

two-dimensional state of strain is theoretically defined.

### 5.2.2 Statistical setup

The primary statistical test presented here compares the magnitude of error obtained from the Panozzo projection method to population size and strain magnitude. This requires numerous undeformed datasets of different population sizes that are deformed through a spectrum of strain magnitudes. Each Panozzo projection calculation, for a given shear strain and population size, is repeated on a new (yet statistically identical) initial dataset for 35 iterations. This produces a statistically viable distribution of values, from which the average strain ratio and a two  $\sigma$  confidence interval can be compared to the expected result. To generate these data, I wrote an R-script to determine the errors within a range of population sizes ( $n = 5, 10, 20, 40, 80, 160,$

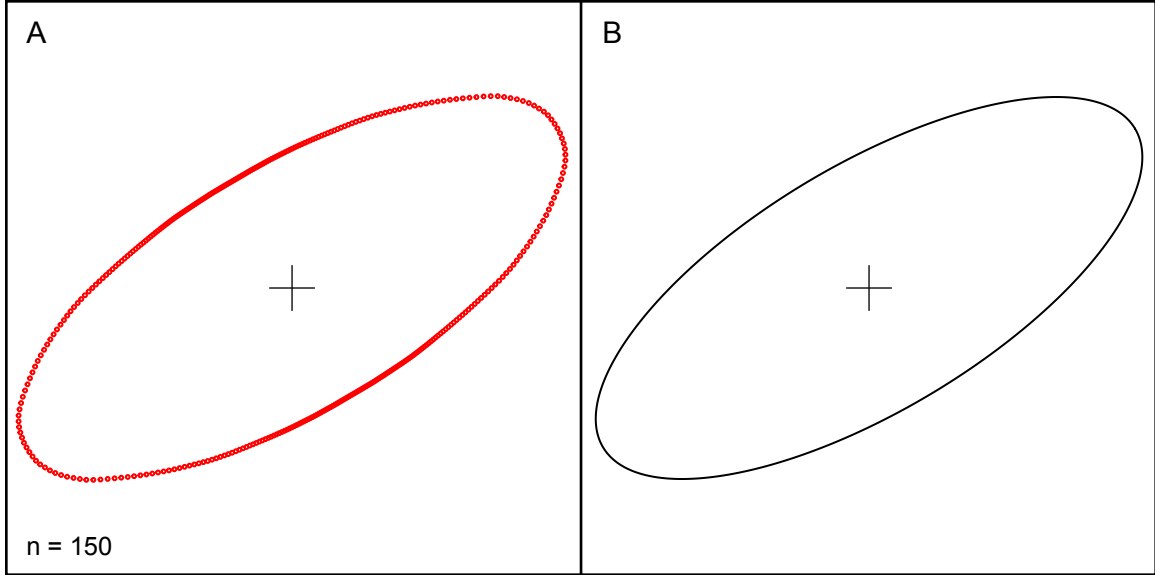


Figure 5.2: Panozzo projection results from line data presented in Figure 5.1. Polar plot of projected lengths based on one degree rotations defining an ellipse perimeter (A). Perimeter is statistically fitted with an ellipse (B) using a least-squares method from which the semi-major and semi-minor axial lengths are obtained.

and 320) based on 35 Panozzo projection calculations at one degree step rotations through a spectrum of shear strains ( $\gamma = 0.25, 0.50, 0.75, 1.00, 1.25, 1.50, 1.75, 2.00, 2.25, 2.50, 2.75, \text{ and } 3.00$ ). In total, 2,520 Panozzo projection analyses were used to obtain the mean and standard deviations of each population size at a given strain magnitude. The following sections describe these results.

## 5.3 Results

### 5.3.1 Least-squares ellipse fitting

In order to better define the mathematical properties of a projected line population, a least-squares ellipse is fitted to a radial plot of lengths and rotational steps. Although I originally hypothesized that this ellipse fitting modification would reduce error associated with the Panozzo method, a simple comparison of the modification to the

standard procedure produced a negligible difference (5.3). The premise of the original idea stemmed from an observation of irregularities in the radial plot perimeter that are likely due to an initial length preferred orientation. However, because each line is added to the rotational projection length (except when the line is perpendicular to the projection) the resultant perimeter ellipse distributes the effects of outliers throughout the ellipse and cannot simply be reduced by a statistical ellipse fitting.

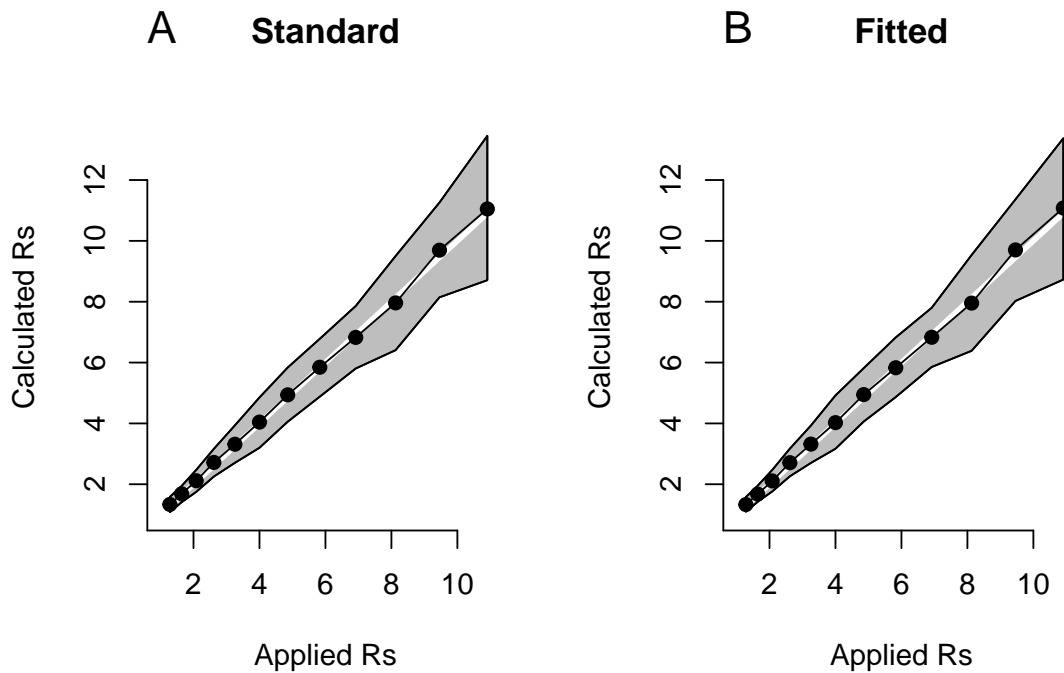


Figure 5.3: A comparison of two different Panozzo  $R_s$  methods involving: (A) the ratio of maximum to minimum projected line lengths; (B) the ratio of semi-major to semi-minor axial lengths of a least squares fitted ellipse. Differences in the two plots are indistinguishable.

### 5.3.2 Population size and strain magnitude errors

The statistical tests described in the previous section indicate an increase in error with increasing strain magnitude and decreasing population size (Fig. 5.4). Figure



5.4 contains six plots corresponding to different population sizes. Gray polygons in each plot define the region given by a two  $\sigma$  error confidence from the calculated mean of 35 Panozzo calculations at increasing strain magnitudes relative to the expected result. By definition, confidence intervals are truncated by a strain ratio of one even if the lower limit of the two  $\sigma$  error falls below this value. With increasing population sizes, the width of the confidence interval clearly narrows about the one-to-one calculated-to-expected line (thick black lines on plots). This confidence interval becomes progressively less narrow at increasing population sizes. As such, this relationship, together with the practicality of sectional application to geologic scenarios, suggests that population sizes below 125 lines per analysis are not statistically robust. A clear association of strain magnitude to confidence interval width can be seen in Figure 5.4. As the magnitude of strain increases, the degree of uncertainty also increases. The width of this interval, even at large population sizes (i.e. 160 lines) can be as large as 3.5  $R_s$  values. As such the Panozzo method may be better suited for smaller population sizes.

The source of error determined by these statistical tests is likely due to the difficulty in producing an isotropic initial dataset. Figure 5.5 displays the results of a similar statistical test as described previously to datasets that exhibit initial radial symmetry. Due to the highly constrained initial conditions imposed on this test, only one projection analysis was applied to a given strain magnitude and population size. My results indicate that the initial condition of radial symmetry produces highly accurate results at low population sizes (i.e.  $\sim 20$  lines). Datasets with lower than 20 lines will likely underestimate the true magnitude of strain at higher distortions. This relationship indicates that projected lengths of lines from lower populations do not accurately define the finite strain ratio (i.e. material lines have a lower probability of being closely aligned to the maximum stretching direction). Nevertheless, in situ-

ations where radial symmetry can be assumed (some potential fossils exist) smaller population sizes may be acceptable.

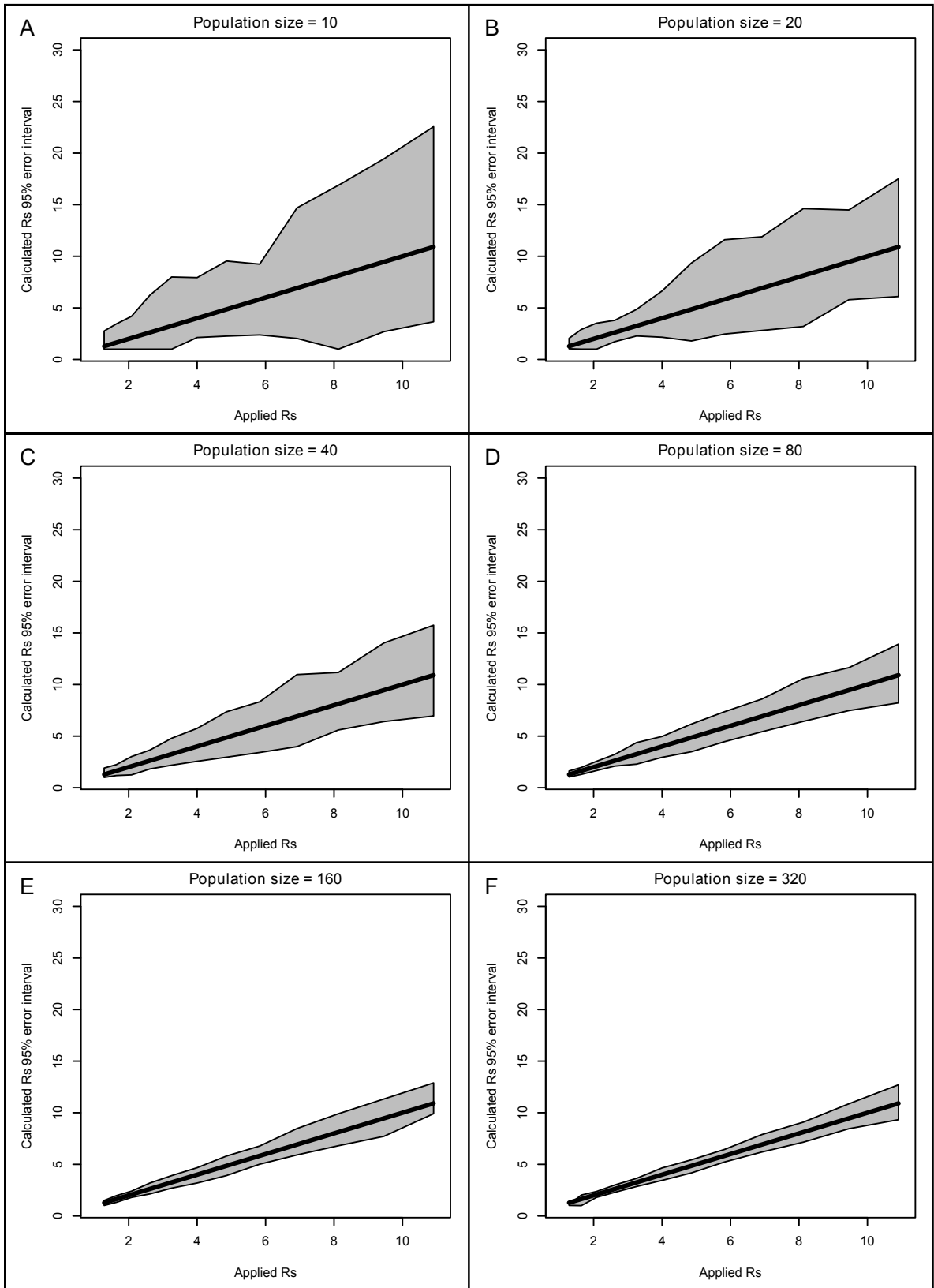
## 5.4 Conclusions and summary

The results presented in this short note indicate several considerations in the application of the Panozzo projection method, including the initial condition of material lines, population size, strain magnitude, and methodology. My data indicate that least-squares ellipse fitting does not significantly change the error associated with the Panozzo projection technique but does better define the strain ellipse mathematically. The range of calculated strain ratio error at the two  $\sigma$  confidence interval increases with increasing strain and indicates a potential limit to the applicability of the method. The population sample size has a significant effect on the magnitude of error, which is best mitigated by populations over  $\sim 125$  lines. The relationship of error reduction to sample size is less pronounced at high population sizes (e.g. 320 lines) but is probably impracticable for most geological scenarios.

The close approximation of the calculated  $R_s$  value to the expected strain ratio for initial datasets of “radial symmetry” indicates that the error associated with

---

Figure 5.4: Error associated with population size and strain magnitude. For each applied shear strain on a population size of 10 (A), 20 (B), 40 (C), 80 (D), 160 (E), and 320 (F). Thirty five initial datasets were generated with a normal distribution of line lengths and a uniform distribution of orientations. Applied shear strains ( $\gamma$ ) for each population size included 0.25 ( $R_s = 1.28$ ), 0.5 ( $R_s = 1.64$ ), 0.75 ( $R_s = 2.08$ ), 1 ( $R_s = 2.62$ ), 1.25 ( $R_s = 3.26$ ), 1.5 ( $R_s = 4$ ), 1.75 ( $R_s = 4.86$ ), 2 ( $R_s = 5.83$ ), 2.25 ( $R_s = 6.92$ ), 2.5 ( $R_s = 8.13$ ), 2.75 ( $R_s = 9.46$ ), and 3 ( $R_s = 10.91$ ). The thick black line in each plot forms a one to one relationship between the applied  $R_s$  and the expected  $R_s$ . Gray polygons display a two  $\sigma$  confidence interval based on 35 analyses per applied deformation. Lower limits of confidence region is truncated by  $R_s = 1$  in some plots (at lower population sizes). A total of 2,520 Panozzo projection analyses were used at a one degree rotation interval to construct the plots requiring a total of 264,600 lines.



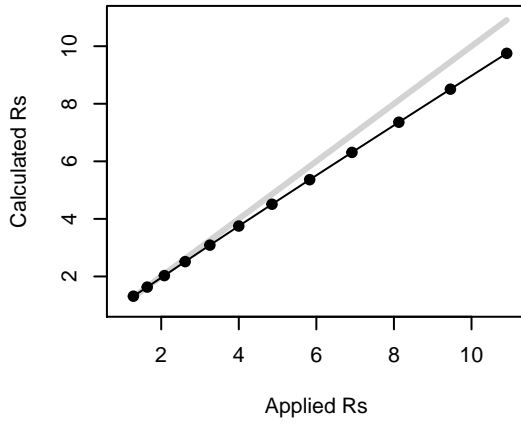
populations of statistically uniform orientations and normally distributed line lengths is a function of error propagation through progressive deformation based on a subtle initial shape-preferred orientation. This indicates that although a population may be defined as statistically uniform, subtle deviations from a truly isotropic population will decrease the probability of calculating the actual strain ratio. Even if the initial orientations of lines are perfectly uniform in distribution (i.e. radially symmetric with respect to orientation alone) a single line of extended length will define an initial shape preferred orientation. This is further complicated with lower population sizes due to the fact that this initial length preferred direction is a higher proportion of the projected length values produced by the other lines.

My results indicate that at relatively high strain magnitudes ( $R_s > 4$ ) and a population size of approximately 120 lines, the two  $\sigma$  confidence interval for a single  $R_s$  calculation is approximately between three and five. At higher strains (e.g.  $R_s \sim 9.5$ ) this range can be as large as 7.5 to 11.5 for a calculated strain ratio. Due to this range in possible sectional strain magnitude, the construction of a three-dimensional strain ellipsoid may occupy a large field of strain-magnitude space within error and could be difficult to accurately determine prolate from oblate strain symmetries. As such, caution is advised in applying the Panozzo projection technique to geologic scenarios without addressing the nature of initial radial symmetry and possible error introduced by initial fabric anisotropy.

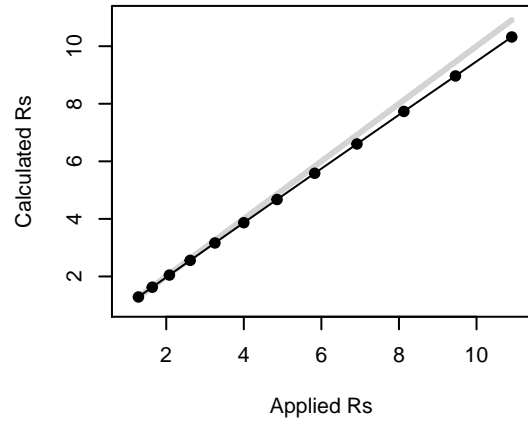
---

Figure 5.5: Calculated  $R_s$  versus applied  $R_s$  on lines of initial radial symmetry and equal lengths. Gray line forms a one to one expected relationship. Note that this "radial symmetry" distribution does not consider translational line location and is not analogous to radial crystal growth habits. Points are plotted for applied shear strains of 0.25 ( $R_s = 1.28$ ), 0.5 ( $R_s = 1.64$ ), 0.75 ( $R_s = 2.08$ ), 1 ( $R_s = 2.62$ ), 1.25 ( $R_s = 3.26$ ), 1.5 ( $R_s = 4$ ), 1.75 ( $R_s = 4.86$ ), 2 ( $R_s = 5.83$ ), 2.25 ( $R_s = 6.92$ ), 2.5 ( $R_s = 8.13$ ), 2.75 ( $R_s = 9.46$ ), and 3 ( $R_s = 10.91$ ).

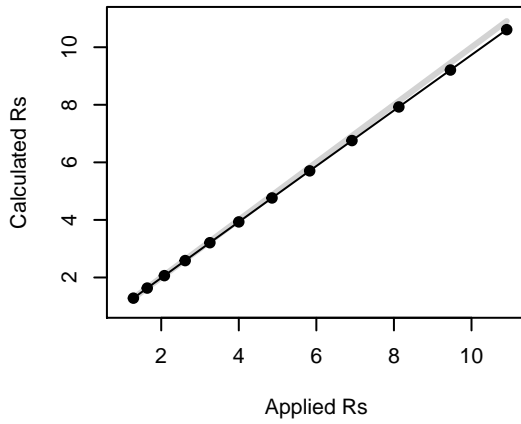
**A Population size = 10**



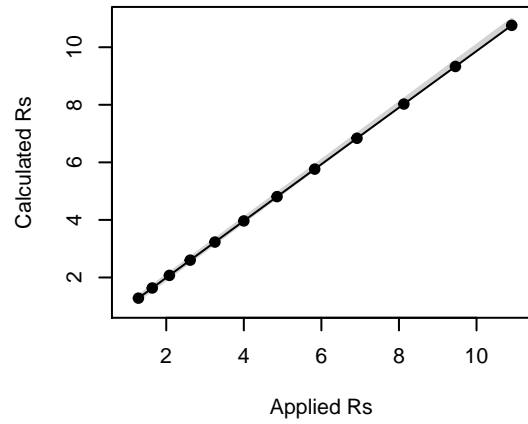
**B Population size = 20**



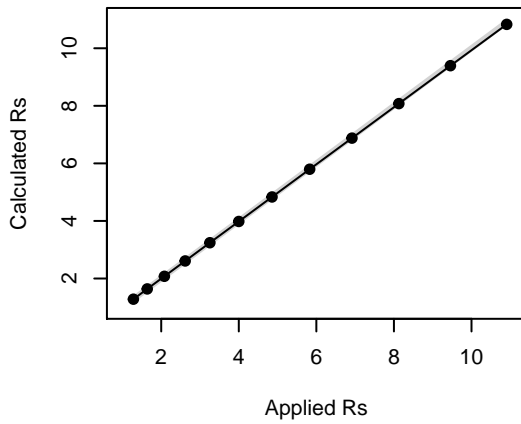
**C Population size = 40**



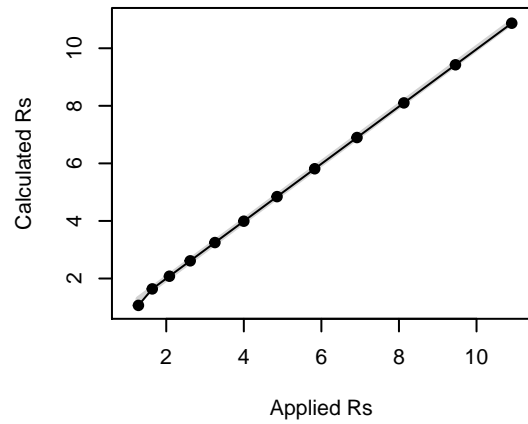
**D Population size = 80**



**E Population size = 160**



**F Population size = 320**



## References

- Panozzo, R. (1984). Two-dimensional strain from the orientation of lines in a plane. *Journal of structural geology* 6(1-2), 215–221.
- Ramsay, J. (1967). *Folding and fracturing of rocks*, Volume 56. McGraw-Hill ^ eNew York New York.
- Trayner, P. (1986). A comparison of sanderson's and panozzo's strain measurement methods using calcite grain boundaries from the variscan fold and thrust belt in ireland. *Journal of structural geology* 8(2), 205–207.
- Webber, J. R. (2012). *StructR: Structural geology tools*. R package version 1.1.

## Comprehensive reference list

- Abràmoff, M., P. Magalhães, and S. Ram (2004). Image processing with imagej. *Biophotonics international* 11(7), 36–42.
- Adams, R. and L. Bischof (1994). Seeded region growing. *Pattern Analysis and Machine Intelligence, IEEE Transactions on* 16(6), 641–647.
- Adler, D. and D. Murdoch (2011). *rgl: 3D visualization device system (OpenGL)*. R package version 0.92.798.
- Astini, R., J. Benedetto, and N. Vaccari (1995). The early paleozoic evolution of the argentine precordillera as a laurentian rifted, drifted, and collided terrane: A geodynamic model. *Geological Society of America Bulletin* 107(3), 253–273.
- Astini, R. and F. Dávila (2004). Ordovician back arc foreland and oclroyic thrust belt development on the western gondwana margin as a response to precordillera terrane accretion. *Tectonics* 23(4), TC4008.
- Bahlburg, H. and F. Hervé (1997). Geodynamic evolution and tectonostratigraphic terranes of northwestern argentina and northern chile. *Bulletin of the Geological Society of America* 109(7), 869.
- Barazangi, M. and B. Isacks (1976). Spatial distribution of earthquakes and subduction of the nazca plate beneath south america. *Geology* 4(11), 686–692.
- Betka, P. M. (2008). Structural and kinematic evolution of the lower crust during continental extension: the resolution island shear zone, fiordland, new zealand. Master's thesis, The University of Vermont.
- Bird, P. (1988). Formation of the rocky mountains, western united states: A continuum computer model. *Science* 239(4847), 1501.
- Blake, S. and J. Fink (2000). On the deformation and freezing of enclaves during magma mixing. *Journal of Volcanology and Geothermal Research* 95(1-4), 1–8.
- Blumenfeld, P. and J. Bouchez (1988). Shear criteria in granite and migmatite deformed in the magmatic and solid states. *Journal of Structural Geology* 10(4), 361–372.

- Borradaile, G. (1984). Strain analysis of passive elliptical markers: success of de-straining methods. *Journal of structural geology* 6(4), 433–437.
- Brandon, M. (1995). Analysis of geologic strain data in strain-magnitude space. *Journal of Structural Geology* 17(10), 1375–1385.
- Brown, M. (1994). The generation, segregation, ascent and emplacement of granite magma: the migmatite-to-crustally-derived granite connection in thickened orogens. *Earth-Science Reviews* 36(1-2), 83–130.
- Brown, M. (2001). Orogeny, migmatites and leucogranites: a review. *Journal of Earth System Science* 110(4), 313–336.
- Brown, M. (2010). The spatial and temporal patterning of the deep crust and implications for the process of melt extraction. *Philosophical Transactions of the Royal Society A: Mathematical, Physical and Engineering Sciences* 368(1910), 11–51.
- Brown, M. and T. Rushmer (1997). The role of deformation in the movement of granitic melt: views from the laboratory and the field. In M. Holness (Ed.), *Deformation-enhanced fluid transport in the Earths crust and mantle*, pp. 111–144. Mineralogical Society Series vol. 8.
- Brown, M. and G. Solar (1998). Granite ascent and emplacement during contractional deformation in convergent orogens. *Journal of Structural Geology* 20(9), 1365–1393.
- Burger, H. and T. Harms (2006). *An introduction to structural methods*. Tasa graphical arts inc.
- Burger, H. and W. Skala (1976). Comparison of sieve and thin-section technique by a monte-carlo model. *Computers & Geosciences* 2(2), 123–139.
- Casquet, C., E. Baldo, R. Pankhurst, C. Rapela, C. Galindo, C. Fanning, and J. Saavedra (2001). Involvement of the argentine precordillera terrane in the famatinian mobile belt: U-pb shrimp and metamorphic evidence from the sierra de pie de palo. *Geology* 29(8), 703.
- Cembrano, J., A. Lavenu, G. Yáñez, R. Riquelme, M. García, G. González, and G. Hérail (2007). Neotectonics. *The geology of Chile (Moreno, T.; Gibbons, W.; editors)*. The Geological Society, London, 231–261.
- Charrier, R., L. Pinto, M. Rodríguez, T. Moreno, and W. Gibbons (2007). Tectonostratigraphic evolution of the andean orogen in chile. *The Geology of Chile (Moreno, T.; Gibbons, W.; editors)*. The Geological Society, 21–114.
- Chew, D. (2003). An excel spreadsheet for finite strain analysis using the rf/phi technique. *Computers & geosciences* 29(6), 795–799.
- Clemens, J. and C. Mawer (1992). Granitic magma transport by fracture propagation. *Tectonophysics* 204(3-4), 339–360.



- Clemens, J., N. Petford, and C. Mawer (1997). Ascent mechanisms of granitic magmas: causes and consequences. In M. Holness (Ed.), *Deformation-enhanced fluid transport in the Earths crust and mantle*, pp. 145–172. Mineralogical Society Series vol. 8.
- Cockett, R. (2012). *Visible Geology*.
- Coira, B., J. Davidson, C. Mpodozis, and V. Ramos (1982). Tectonic and magmatic evolution of the andes of northern argentina and chile. *Earth-Science Reviews* 18(3-4), 303–332.
- Collins, W. and E. Sawyer (1996). Pervasive granitoid magma transfer through the lower–middle crust during non-coaxial compressional deformation. *Journal of Metamorphic Geology* 14(5), 565–579.
- Coney, P. and S. Reynolds (1977). Cordilleran benioff zones. *Nature* 270, 403–406.
- Cordani, U., F. Munizaga, F. Hervé, and M. Hervé (1976). Edades radiométricas provenientes del basamento cristalino de la cordillera de la costa de las provincias de valparaíso y santiago, chile. In *Congreso Geológico Chileno*, Number 1, pp. F213–F222.
- Creixell, C., M. Parada, D. Morata, P. Roperch, and C. Arriagada (2009). The genetic relationship between mafic dike swarms and plutonic reservoirs in the mesozoic of central chile (30°–33° 45' s): insights from ams and geochemistry. *International Journal of Earth Sciences* 98(1), 177–201.
- Creixell, C., M. Parada, D. Morata, P. Vásquez, C. Pérez de Arce, and C. Arriagada (2011). Middle-late jurassic to early cretaceous transtension and transpression during arc building in central chile: evidence from mafic dike swarms. *Andean geology* 38(1), 37–63.
- Czeck, D., D. Fissler, E. Horsman, and B. Tikoff (2009). Strain analysis and rheology contrasts in polymictic conglomerates: An example from the seine metaconglomerates, superior province, canada. *Journal of Structural Geology* 31(11), 1365–1376.
- Dalziel, I. (1997). Overview: Neoproterozoic-paleozoic geography and tectonics: Review, hypothesis, environmental speculation. *Geological Society of America Bulletin* 109(1), 16–42.
- Dalziel, I., L. Dalla Salda, and L. Gahagan (1994). Paleozoic laurentia-gondwana interaction and the origin of the appalachian-andean mountain system. *Bulletin of the Geological Society of America* 106(2), 243.
- Dewey, J. and J. Bird (1970). Mountain belts and the new global tectonics. *Journal of Geophysical Research* 75(14), 2625–2647.
- Dickinson, W. and W. Snyder (1978). Plate tectonics of the laramide orogeny. *Geological Society of America Memoir* 151, 355–366.

- Dlugogorski, B., M. Grmela, P. Carreau, and G. Lebon (1994). Rheology of several hundred rigid bodies. *Journal of non-newtonian fluid mechanics* 53, 25–64.
- Do Campo, M. and S. Guevara (2005). Provenance analysis and tectonic setting of late neoproterozoic metasedimentary successions in nw argentina. *Journal of South American Earth Sciences* 19(2), 143–153.
- Dunnet, D. (1969). A technique of finite strain analysis using elliptical particles. *Tectonophysics* 7(2), 117–136.
- Durand, F. (1996). La transición precámbrico-cámbrico en el sur de sudamérica. *Early Paleozoic evolution in NW Gondwana. Universidad Nacional de Tucumán, Argentina, Serie Correlación Geológica* 12, 195–205.
- Elgueta, S., O. Baeza, R. Aguirre, R. Charrier, N. Muñoz, and P. Gans (2000). Mecanismos de la depositación volcanoclástica oligo–miocena del cajón del maipo, chile central. 2, 21–25.
- English, J., S. Johnston, and K. Wang (2003). Thermal modelling of the laramide orogeny: testing the flat-slab subduction hypothesis. *Earth and Planetary Science Letters* 214(3), 619–632.
- Erslev, E. (1988). Normalized center-to-center strain analysis of packed aggregates. *Journal of Structural Geology* 10(2), 201–209.
- Erslev, E. and H. Ge (1990). Least-squares center-to-center and mean object ellipse fabric analysis. *Journal of Structural Geology* 12(8), 1047–1059.
- Farías, M., R. Charrier, A. Fock, D. Campbell, J. Martinod, and D. Comte (2005). Rapid late cenozoic surface uplift of the central chile andes (33–35 s). In *International Symposium on Andean Geodynamics (ISAG)*, Number 6, pp. 261–265.
- Feng, D. and L. Tierney (2008). Computing and displaying isosurfaces in R. *Journal of Statistical Software* 28(1).
- Finney, S., J. Gleason, G. Gehrels, S. Peralta, and G. Acenolaza (2003). Early gondwanan connection for the argentine precordillera terrane. *Earth and Planetary Science Letters* 205(3–4), 349–359.
- Fisher, N. (1996). *Statistical analysis of circular data*. Cambridge Univ Pr.
- Flinn, D. (1956). On the deformation of the funzie conglomerate, fetlar, shetland. *The Journal of Geology* 64(5), 480–505.
- Flinn, D. (1962). On folding during three-dimensional progressive deformation. *Quarterly Journal of the Geological Society* 118(1–4), 385–428.
- Fock, A., R. Charrier, M. Farías, V. Makshev, M. Fanning, and P. Álvarez (2005). Exhumation and uplift of the western main cordillera between 33° and 34° s. In *Proceedings of International Symposium on Andean Geodynamics (ISAG)*, Number 6, pp. 273–276.

- Frost, T. and G. Mahood (1987). Field, chemical, and physical constraints on mafic-felsic magma interaction in the lamarck granodiorite, sierra nevada, california. *Geological Society of America Bulletin* 99(2), 272.
- Fry, N. (1979). Random point distributions and strain measurement in rocks. *Tectonophysics* 60(1-2), 89–105.
- Gana, P. and R. Tosdal (1996). Geocronología u-pb y k-ar en intrusivos del paleozoico y mesozoico de la cordillera de la costa, región de valparaíso, chile. *Andean Geology* 23(2), 151–164.
- Genier, F. and J. Epard (2007). The fry method applied to an augen orthogneiss: Problems and results. *Journal of structural geology* 29(2), 209–224.
- Godoy, E. and W. Loske (1988). Tectonismo sinplutónico de dioritas jurásicas al sur de valparaíso: datos u-pb sobre la 'fase quintay'. *Andean Geology* 15(2), 119–127.
- Grocott, J., M. Brown, R. Dallmeyer, G. Taylor, and P. Treloar (1994). Mechanisms of continental growth in extensional arcs: An example from the andean plate-boundary zone. *Geology* 22(5), 391.
- Grothendieck, G. (2010). *squidf: Perform SQL Selects on R Data Frames*. R package version 0.3-5.
- Gudmundsson, A. (1984). Formation of dykes, feeder-dykes, and the intrusion of dykes from magma chambers. *Bulletin of Volcanology* 47(3), 537–550.
- Gumbsch, P., J. Riedle, A. Hartmaier, and H. Fischmeister (1998). Controlling factors for the brittle-to-ductile transition in tungsten single crystals. *Science* 282(5392), 1293–1295.
- Hand, M. and P. Dirks (1992). The influence of deformation on the formation of axial-planar leucosomes and the segregation of small melt bodies within the migmatitic nappes by gneiss, central australia. *Journal of structural geology* 14(5), 591–604.
- Hervé, F., F. Munizaga, M. Parada, M. Brook, R. Pankhurst, N. Snelling, and R. Drake (1988). Granitoids of the coast range of central chile: geochronology and geologic setting. *Journal of South American Earth Sciences* 1(2), 185–194.
- Hossack, J. (1968). Pebble deformation and thrusting in the bygdin area (southern norway). *Tectonophysics* 5(4), 315–339.
- Hsu, T. (1966). The characteristics of coaxial and non-coaxial strain paths. *The Journal of Strain Analysis for Engineering Design* 1(3), 216–222.
- Hudleston, P. (1999). Strain compatibility and shear zones: is there a problem? *Journal of Structural Geology* 21(8-9), 923–932.
- Hutton, D., T. Dempster, P. Brown, and S. Becker (1990). A new mechanism of granite emplacement: intrusion in active extensional shear zones.

- Irwin, J., W. Sharp, R. Spangler, and R. Drake (1987). Some paleomagnetic constraints on the tectonic evolution of the coastal cordillera of central chile. *Journal of Geophysical Research* 92(B5), 3603–3614.
- John, B. and J. Blundy (1993). Emplacement-related deformation of granitoid magmas, southern adamello massif, italy. *Geological Society of America Bulletin* 105(12), 1517–1541.
- Johnson, S., R. Vernon, and P. Upton (2004). Foliation development and progressive strain-rate partitioning in the crystallizing carapace of a tonalite pluton: microstructural evidence and numerical modeling. *Journal of Structural Geology* 26(10), 1845–1865.
- Kalakay, T., B. John, and D. Lageson (2001). Fault-controlled pluton emplacement in the sevier fold-and-thrust belt of southwest montana, usa. *Journal of Structural Geology* 23(6-7), 1151–1165.
- Klepeis, K., D. King, M. De Paoli, G. Clarke, and G. Gehrels (2007). Interaction of strong lower and weak middle crust during lithospheric extension in western new zealand. *Tectonics* 26(4), TC4017.
- Lamb, S. and P. Davis (2003). Cenozoic climate change as a possible cause for the rise of the andes. *Nature* 425(6960), 792–797.
- Launeau, P. and P. Robin (1996). Fabric analysis using the intercept method. *Tectonophysics* 267(1-4), 91–119.
- Launeau, P. and P. Robin (2005). Determination of fabric and strain ellipsoids from measured sectional ellipses—implementation and applications. *Journal of structural geology* 27(12), 2223–2233.
- Lavenu, A. and J. Cembrano (1999). Compressional-and transpressional-stress pattern for pliocene and quaternary brittle deformation in fore arc and intra-arc zones (andes of central and southern chile). *Journal of Structural Geology* 21(12), 1669–1691.
- Lees, J. M. (2011). *RFOC: Graphics for Spherical Distributions and Earthquake Focal Mechanisms*. R package version 2.0-00.
- Lemon, J. (2006). Plotrix: a package in the red light district of r. *R-News* 6(4), 8–12.
- Levi, B. (1973). Eastward shift of mesozoic and early tertiary volcanic centers in the coast range of central chile. *Bulletin of the Geological Society of America* 84(12), 3901.
- Li, Z., S. Bogdanova, A. Collins, A. Davidson, B. De Waele, R. Ernst, I. Fitzsimons, R. Fuck, D. Gladkochub, J. Jacobs, et al. (2008). Assembly, configuration, and break-up history of rodinia: a synthesis. *Precambrian Research* 160(1-2), 179–210.

- Lira, R., H. Millone, A. Kirschbaum, and R. Moreno (1997). Calc-alkaline arc granitoid activity in the sierra norte-ambargasta ranges, central argentina. *Journal of South American Earth Sciences* 10(2), 157–177.
- Lisle, R. (1985). Geological strain analysis, a manual for the rf/phi method.
- Lisle, R. (2010). Strain analysis from point fabric patterns: An objective variant of the fry method. *Journal of Structural Geology* 32(7), 975–981.
- Lisle, R., H. Rondeel, D. Doorn, J. Brugge, and P. Van de Gaag (1983). Estimation of viscosity contrast and finite strain from deformed elliptical inclusions. *Journal of Structural Geology* 5(6), 603–609.
- Llambías, E. and A. Sato (1995). El batolito de colangüil: transición entre orogénesis y anorogénesis. *Revista de la Asociación Geológica Argentina* 50(1-4), 111–131.
- Lode, W. (1926). Versuche über den einfluß der mittleren hauptspannung auf das fließen der metalle eisen, kupfer und nickel. *Zeitschrift für Physik A Hadrons and Nuclei* 36(11), 913–939.
- Loewy, S., J. Connelly, and I. Dalziel (2004). An orphaned basement block: The arequipa-antofalla basement of the central andean margin of south america. *Geological Society of America Bulletin* 116(1-2), 171–187.
- Macdonald, P. D. M. (2007). Drawing an ellipse in splup or r. [http://www.math.mcmaster.ca/peter/s4m03/s4m03\\_0304/classnotes/ellipse.html](http://www.math.mcmaster.ca/peter/s4m03/s4m03_0304/classnotes/ellipse.html). [Online; accessed 11-June-2011].
- Mancktelow, N. (1995). Deviatoric stress and the interplay between deformation and metamorphism. In *Geological Society of Australia, Abstracts, Clare Valley Conference*, Volume 40, pp. 95–96.
- Miller, R. and S. Paterson (1999). In defense of magmatic diapirs. *Journal of Structural Geology* 21(8-9), 1161–1173.
- Molyneux, S. and D. Hutton (2000). Evidence for significant granite space creation by the ballooning mechanism: the example of the ardara pluton, ireland. *Geological Society of America Bulletin* 112(10), 1543.
- Mookerjee, M. and S. Nickleach (2011). Three-dimensional strain analysis using mathematica. *Journal of Structural Geology*.
- Mpodozis, C. and P. Cornejo (1988). *Hoja Pisco Elqui: IV region de Coquimbo*. Servicio nacional de geología y minería.
- Mpodozis, C. and S. Kay (1992). Late paleozoic to triassic evolution of the gondwana margin: Evidence from chilean frontal cordilleran batholiths (28 {degrees} s to 31 {degrees} s). *Bulletin of the Geological Society of America* 104(8), 999.
- Mulchrone, K. (2003). Application of delaunay triangulation to the nearest neighbour method of strain analysis. *Journal of Structural Geology* 25(5), 689–702.

- Mulchrone, K. (2005). Dtnnm: A windows program for strain analysis using the delaunay triangulation nearest neighbour method. *Computers & geosciences* 31(8), 978–988.
- Mulchrone, K. and P. Meere (2001). A windows program for the analysis of tectonic strain using deformed elliptical markers. *Computers & geosciences* 27(10), 1251–1255.
- Mulchrone, K., P. Meere, and K. Choudhury (2005). Sape: a program for semi-automatic parameter extraction for strain analysis. *Journal of structural geology* 27(11), 2084–2098.
- Murphy, J., S. Pisarevsky, R. Nance, and J. Keppie (2004). Neoproterozoic early paleozoic evolution of peri-gondwanan terranes: implications for laurentia-gondwana connections. *International Journal of Earth Sciences* 93(5), 659–682.
- Nadai, A. (1963). Theory of fracture and flow of solids. *Vol. II) McGraw-H111, New York.*
- Nasi, C., C. Mpodozis, P. Cornejo, R. Moscoso, and V. Maksaev (1985). El batolito elqui-limarí (paleozoico superior triásico): características petrográficas, geoquímicas y significado tectónico. *Revista geológica de Chile* 25, 26.
- Nicolas, A. (1992a). Kinematics in magmatic rocks with special reference to gabbros. *Journal of Petrology* 33(4), 891.
- Nicolas, A. (1992b). Kinematics in magmatic rocks with special reference to gabbros. *Journal of Petrology* 33(4), 891.
- Pankhurst, R., C. Rapela, J. Saavedra, E. Baldo, J. Dahlquist, I. Pascua, and C. Fanning (1998). The famatinian magmatic arc in the central sierras pampeanas: an early to mid-ordovician continental arc on the gondwana margin. *Geological Society, London, Special Publications* 142(1), 343–367.
- Panozzo, R. (1984). Two-dimensional strain from the orientation of lines in a plane. *Journal of structural geology* 6(1-2), 215–221.
- Parada, M., J. Nyström, and B. Levi (1999). Multiple sources for the coastal batholith of central chile (31-34 s): geochemical and sr-nd isotopic evidence and tectonic implications. *Lithos* 46(3), 505–521.
- Paterson, S. (1983). A comparison of methods used in measuring finite strains from ellipsoidal objects. *Journal of structural geology* 5(6), 611–618.
- Paterson, S., T. Fowler Jr, K. Schmidt, A. Yoshinobu, E. Yuan, and R. Miller (1998). Interpreting magmatic fabric patterns in plutons. *Lithos* 44(1-2), 53–82.
- Paterson, S., G. Pignotta, and R. Vernon (2004). The significance of microgranitoid enclave shapes and orientations. *Journal of Structural Geology* 26(8), 1465–1481.

- Paterson, S., P. Rönnlund, and H. Koyi (1989). Comment and reply on "fry spacing of deformed and undeformed modeled and natural salt domes". *Geology* 17(2), 193–195.
- Paterson, S. and R. Vernon (1995). Bursting the bubble of ballooning plutons: A return to nested diapirs emplaced by multiple processes. *Geological Society of America Bulletin* 107(11), 1356–1380.
- Paterson, S., R. Vernon, and O. Tobisch (1989). A review of criteria for the identification of magmatic and tectonic foliations in granitoids. *Journal of structural geology* 11(3), 349–363.
- Peach, C. and R. Lisle (1979). A fortran iv program for the analysis of tectonic strain using deformed elliptical markers. *Computers & Geosciences* 5(3-4), 325–334.
- Petford, N. (1996). Dykes or diapirs? *Geological Society of America Special Papers* 315, 105–114.
- Petford, N. (2003). Rheology of granitic magmas during ascent and emplacement. *Annual Review of Earth and Planetary Sciences* 31(1), 399–427.
- Petford, N., A. Cruden, K. McCaffrey, and J. Vigneresse (2000). Granite magma formation, transport and emplacement in the earth's crust. *Nature* 408(6813), 669–673.
- Petrini, K. and Y. Podladchikov (2000). Lithospheric pressure-depth relationship in compressive regions of thickened crust. *Journal of Metamorphic Geology* 18(1), 67–78.
- Piñán-Llamas, A. and C. Simpson (2006). Deformation of gondwana margin turbidites during the pampean orogeny, north-central argentina. *Geological Society of America Bulletin* 118(9-10), 1270–1279.
- Pitcher, W. (1991). Synplutonic dykes and mafic enclaves. *Enclaves and Granite Petrology*. Amsterdam: Elsevier, 383–391.
- R Development Core Team (2010). *R: A Language and Environment for Statistical Computing*. Vienna, Austria: R Foundation for Statistical Computing. ISBN 3-900051-07-0.
- Ramos, V. (2009). Anatomy and global context of the andes: Main geologic features and the andean orogenic cycle. *Backbone of the Americas: Shallow Subduction, Plateau Uplift, and Ridge and Terrane Collision: Geological Society of America Memoir* 204, 31–65.
- Ramsay, J. (1967). *Folding and fracturing of rocks*, Volume 56. McGraw-Hill ^ eNew York New York.
- Ramsay, J. and M. Huber (1983). *The techniques of modern structural geology*. Number v. 1 in *The Techniques of Modern Structural Geology*. Academic Press.

- Rapela, C., R. Pankhurst, C. Casquet, E. Baldo, J. Saavedra, and C. Galindo (1998). Early evolution of the proto-andean margin of south america. *Geology* 26(8), 707–710.
- Rapela, C., R. Pankhurst, C. Casquet, E. Baldo, J. Saavedra, C. Galindo, and C. Fanning (1998). The pampean orogeny of the southern proto-andes: Cambrian continental collision in the sierras de córdoba. *Geological Society, London, Special Publications* 142(1), 181–217.
- Rönnlund, P. and H. Koyi (1988). Fry spacing of deformed and undeformed modeled and natural salt domes. *Geology* 16(5), 465–468.
- Rowland, S., E. Duebendorfer, and I. Schiefelbein (2007). *Structural Analysis and Synthesis: a laboratory course in Structural Geology*. Wiley-Blackwell.
- Rutter, E. and D. Neumann (1995). Experimental deformation of partially molten westerly granite under fluid-absent conditions, with implications for the extraction of granitic magmas. *Journal of Geophysical Research* 100(B8), 15697–15.
- Sanderson, D. (1977). The analysis of finite strain using lines with an initial random orientation. *Tectonophysics* 43(3-4), 199–211.
- SERNAGEOMIN (2002). *Mapa Geológico de Chile. Servicio Nacional de Geología y Minería, Chile. Carta geológica de Chile. Serie Geología básica No. 75, 1 mapa en 3 hojas, escala 1:1.000.000.*
- Shaw, H. (1980). The fracture mechanisms of magma transport from the mantle to the surface. *Physics of magmatic processes*, 201–264.
- Siña, A. (1987). El batolito de la costa entre algarrobo y rocas de santo domingo (chile central, 33° 30' s): geología e interpretacionespetrogenéticas. *Comunicaciones* 38, 47–66.
- Siña, A. and M. Parada (1985). Los granitoides de rocas de santo domingo: antecedentes de terreno, petrográficos y de química de elementos mayores para una mezcla de magmas. In *Proc. Congreso Geológico Chileno, 4th, Antofagasta, Chile*, Volume 3, pp. 512–530.
- Sleep, N. (1988). Tapping of melt by veins and dikes. *Journal of Geophysical Research* 93(B9), 10255–10272.
- Sorby, H. (1908). On the application of quantitative methods to the study of the structure and history of rocks. *Quarterly Journal of the Geological Society* 64(1-4), 171.
- Strömgård, K. (1973). Stress distribution during formation of boudinage and pressure shadows. *Tectonophysics* 16(3-4), 215–248.
- Sullivan, W. (2006). Structural significance of 1 tectonites in the eastern-central laramie mountains, wyoming. *Journal of Geology* 114(5), 513–532.



- Thomas, W., R. Astini, and G. Bayona (2002). Ordovician collision of the argentine precordillera with gondwana, independent of laurentian taconic orogeny. *Tectonophysics* 345(1-4), 131–152.
- Thorpe, R. and P. Francis (1979). Variations in andean andesite compositions and their petrogenetic significance. *Tectonophysics* 57(1), 53–70.
- Tikoff, B. and H. Fossen (1995). The limitations of three-dimensional kinematic vorticity analysis. *Journal of Structural Geology* 17(12), 1771–1784.
- Tobisch, O., B. McNulty, and R. Vernon (1997). Microgranitoid enclave swarms in granitic plutons, central sierra nevada, california. *Lithos* 40(2-4), 321–339.
- Trayner, P. (1986). A comparison of sanderson's and panno's strain measurement methods using calcite grain boundaries from the variscan fold and thrust belt in ireland. *Journal of structural geology* 8(2), 205–207.
- Treagus, S. and J. Treagus (2002). Studies of strain and rheology of conglomerates. *Journal of Structural Geology* 24(10), 1541–1567.
- Turner, J. C. M. (1960). Estratigrafía de la sierra de santa victoria y adyacencias. *Boletín de la Academia Nacional de Ciencias* 41(2), 163–196.
- Twiss, R. and E. Moores (2007). *Structural geology second edition*. WH Freeman and Company.
- Uliana, M. and K. Biddle (1988). Mesozoic-cenozoic paleogeographic and geodynamic evolution of southern south america. *Revista Brasileira de Geociencias* 18(2), 172–190.
- Valentine, J. and E. Moores (1970). Plate-tectonic regulation of faunal diversity and sea level: a model.
- Van der Molen, I. and M. Paterson (1979). Experimental deformation of partially-melted granite. *Contributions to Mineralogy and Petrology* 70(3), 299–318.
- Vergara, M., B. Levi, J. Nyström, and A. Cancino (1995). Jurassic and early cretaceous island arc volcanism, extension, and subsidence in the coast range of central chile. *Geological Society of America Bulletin* 107(12), 1427.
- Vernon, R., M. Etheridge, and V. Wall (1988). Shape and microstructure of microgranitoid enclaves: indicators of magma mingling and flow. *Lithos* 22(1), 1–11.
- Vignerresse, J. and B. Tikoff (1999). Strain partitioning during partial melting and crystallizing felsic magmas. *Tectonophysics* 312(2-4), 117–132.
- Waldron, J. and K. Wallace (2007). Objective fitting of ellipses in the centre-to-centre (fry) method of strain analysis. *Journal of Structural Geology* 29(9), 1430–1444.
- Wall, R., P. Gana, and A. Gutiérrez (1996). *Mapa geológico del area de Valparaíso-Curacavi, Regiones de Valparaíso y Metropolitana*. Servicio Nacional de Geología y Minería.

- Warnes, G., B. Bolker, L. Bonebakker, R. Gentleman, W. Huber, A. Liaw, T. Lumley, M. Maechler, A. Magnusson, S. Moeller, M. Schwartz, and B. Venables (2010). *gplots: Various R programming tools for plotting data*. R package version 2.8.0.
- Webber, J. R. (2012). *StructR: Structural geology tools*. R package version 1.1.
- Wellman, H. (1962). A graphical method for analysing fossil distortion caused by tectonic deformation. *Geol. Mag* 99(4), 348–352.
- Wells, M. (2001). Rheological control on the initial geometry of the raft river detachment fault and shear zone, western united states. *Tectonics* 20(4), 435–457.
- Wells, M. and T. Hoisch (2008). The role of mantle delamination in widespread late cretaceous extension and magmatism in the cordilleran orogen, western united states. *Geological Society of America Bulletin* 120(5-6), 515–530.
- Wiebe, R., M. Jellinek, M. Markley, D. Hawkins, and D. Snyder (2007). Steep schlieren and associated enclaves in the vinalhaven granite, maine: possible indicators for granite rheology. *Contributions to Mineralogy and Petrology* 153(2), 121–138.
- Williams, M., S. Hanmer, C. Kopf, and M. Darrach (1995). Syntectonic generation and segregation of tonalitic melts from amphibolite dikes in the lower crust, striding-athabasca mylonite zone, northern saskatchewan. *Journal of Geophysical Research* 100(B8), 15717–15.
- Williams, Q. and O. Tobisch (1994). Microgranitic enclave shapes and magmatic strain histories: Constraints from drop deformation theory. *Journal of Geophysical Research* 99(B12), 24359–24.
- Winter, J., J. CHAVEZ, R. MERINO, J. CHAVEZ, R. MERINO, C. OCHOA, P. CARLOS, M. SALAZAR, M. MINDIOLA, S. RECALDE, et al. (2001). An introduction to igneous and metamorphic petrology. *Pearson Education, New Jersey* 1, F2.
- Wortel, M. (1984). Spatial and temporal variations in the andean subduction zone. *Journal of the Geological Society* 141(5), 783–791.
- Yáñez, G. and J. Cembrano (2004). Role of viscous plate coupling in the late tertiary andean tectonics. *Journal of Geophysical Research* 109(B02407).

## Appendix A

### Additional field data

#### A.1 Sample information

All samples<sup>1</sup> are given a period separated concatenated index code that corresponds to the last two digits of the year (i.e. 2011), a two digit alphabetic region code, a numeric value for the site location within that region, and a letter corresponding to the sample collected. The easting and northing coordinates are based on the WGS 1984 datum and correspond to timezone 19H. Photographic identification numbers correspond to digital images collected by the author and are available upon request pending approval. Orientation markings are in strike and dip format following the right hand rule convention. Polarity denotes the orientation of marked faces such that an upright face has a positive polarity and an overhung face is negative. Sample collector abbreviations denote individual's notebook for specific information: JRW: Jeffrey R. Webber; KAK: Keith A. Klepeis; LEW: Laura E. Webb. Samples are held under the auspices of Keith A. Klepeis, Department of Geology, The University of Vermont, Burlington, VT 05405.

---

<sup>1</sup>For location information please refer to the "SAMPLES.kmz" file in the accompanying digital materials (explained in Appendix F).

Index	Easting	Northing	Photo	Strike	Dip	Pol.	Collector
11.IN.02.A	0250894	6295798	1376	016	64	pos	JRW
11.IN.03.A	0250961	6295732	1377	325	25	pos	JRW
11.IN.03.B	0250963	6295733	1378	058	52	pos	JRW
11.IN.03.C	0250957	6295740	1379	315	54	pos	JRW
11.LC.01.A	0255949	6290089	1387	273	52	pos	JRW
11.LC.01.B	0255948	6290089	1388	334	44	pos	JRW
11.LC.01.C	0255948	6290089	1402	134	50	pos	JRW
11.LC.01.D	0255948	6290089	1403	074	57	pos	JRW
11.LC.02.A	0255197	6289955	1404	066	72	pos	JRW
11.LC.02.B	0255198	6289960	1407	031	40	pos	JRW
11.LC.02.C	0255198	6289960	1409	297	88	pos	JRW
11.LC.03.A	0254825	6290727	1429	132	02	pos	JRW
11.AS.02.A	0256273	6283176	null	076	84	neg	KAK
11.AS.02.B	0256273	6283176	null	082	64	pos	KAK
11.IN.01.A	0250925	6295894	1440	251	87	pos	JRW
11.IN.01.B	0250977	6295894	1441	192	61	pos	JRW
11.IN.01.C	0250925	6295891	1442	019	67	pos	JRW
11.IN.01.D	0250902	6295952	1443	null	null	null	JRW
11.IN.01.E	0250902	6295952	1444	345	42	pos	KAK
11.LC.02.D	0255187	6289973	1448	294	74	pos	JRW
11.LC.04.A	0255194	6290077	1453	214	25	pos	JRW
11.LC.04.B	0255257	6290313	1455	193	51	pos	JRW
11.LC.03.B	0254825	6290727	null	null	null	null	LEW
11.LC.03.C	0254825	6290727	1456	025	60	pos	KAK
11.LC.02.E	0255198	6289960	null	null	null	null	KAK
11.AS.01.A	0256404	6282774	1467	198	59	pos	JRW
11.AS.01.B	0256404	6282774	1468	174	36	pos	JRW
11.AS.01.C	0256407	6282744	1470	091	29	pos	JRW
11.AS.01.D	0256404	6282771	1471	202	61	pos	JRW
11.AS.01.E	0256403	6282761	1472	036	42	pos	JRW
11.AS.03.A	0256396	6283131	1476	074	40	pos	JRW
11.AS.03.B	0256396	6283140	1477	150	90	pos	JRW
11.QT.01.A	0247986	6324162	1489	318	77	pos	JRW

## A.2 Las Cruces mylonites

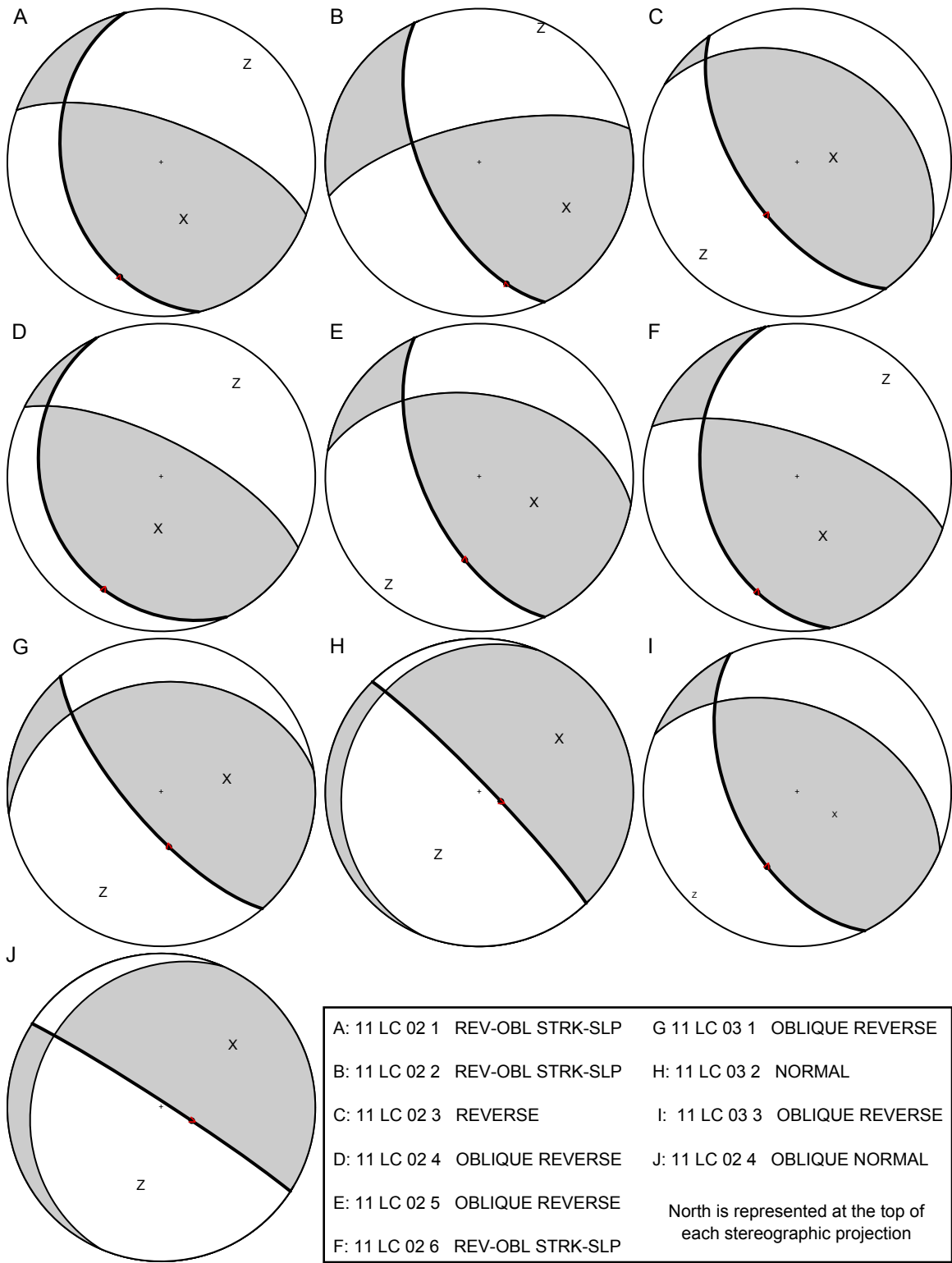
The following consist of stereographic projections constructed for discrete mylonitic shear zones developed within augen gneiss at Las Cruces. These projections follow the same conventions used in brittle fault plane solutions. Figure A.1 contains individual

mylonite plane solutions with shear zones plotted as thick great circles, extensional axes denoted by the “x” character, contractional axes plotted with the letter “z,” and the slip vector corresponding to lineation attitudes that point in the direction of motion. Figure A.2 is a composite solution of the individual plots shown in Figure A.1 and clearly defines a contractional and extensional . This analysis suggests that the formation of discrete mylonitic shear zones within the Las Cruces region are compatible with top to the north–north–west directed contraction.

My interpretation of these mylonites mimicking brittle faults is based on two observations: these mylonites exhibit low displacement and are highly localized (1–5 cm in width). This suggests that their orientation and sense of shear likely represent the initial state of strain and are not highly affected by progressive deformation. However, I must emphasize caution in applying this methodology to any given mylonite system as fault plane solutions are genetically assumed brittle in formation.

---

Figure A.1: Mylonite plane solutions for discrete shear zones documented in augen gneiss near Las Cruces.



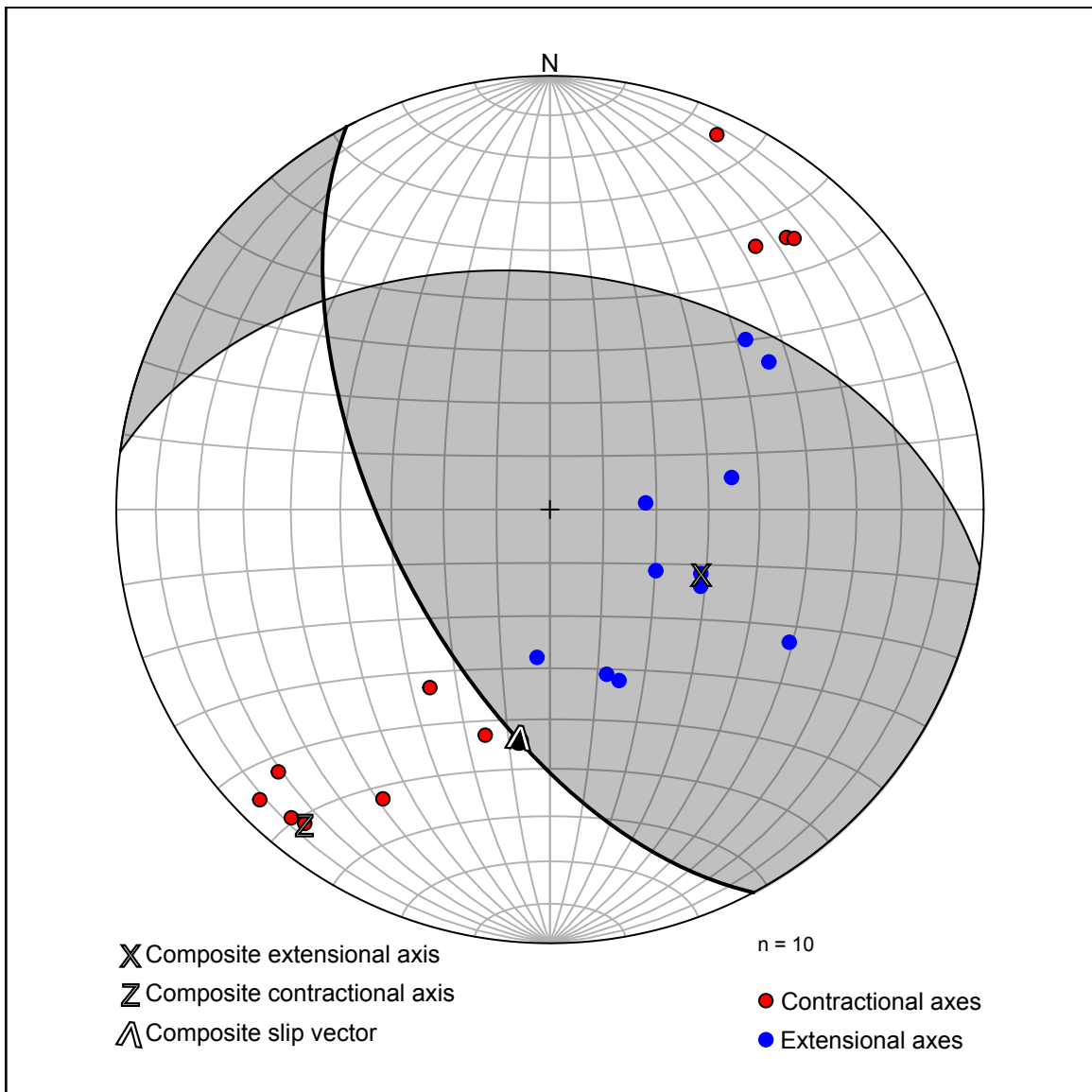


Figure A.2: Composite mylonite plane solution derived from the measurements shown in Figure A.1. Solution suggests mylonite zones are compatible with general top to the north–north–east directed contraction.

Table A.2: Overview of the primary geochronological constraints for the Isla Negra Igneous Complex.

Age (Ma)	Lithology	Method	Material	Locality	Reference
172.4±2.4	Mafic dike	$^{40}\text{Ar}/^{36}\text{Ar}$	Amphibole	Punta de Tralca	(Irwin et al. 1987)
214.0±1.0	Dioritic gneiss	U-Pb	Zircon	Cartagena	(Gana and Tosdal 1996)
278.0±6.0	Orthogneiss	K/Ar	Biotite	Las Cruces	(Cordani et al. 1976)
291.0±1.0	Tonalite	U-Pb	Zircon	Punta Gallo	(Godoy and Loske 1988)



### A.3 Structure orientations

The following is a series of tables containing structural orientation data from the central Chile field season of 2011. These measurements are tagged by a feature type and geometry. As such, planes correspond to strikes and dips following right hand rule. Linear features (“Lineations”) are presented with trends and plunges. The table caption provides location information based on the site index tag. For location information please refer to the “SAMPLES.kmz” file in the accompanying digital materials (explained in Appendix F).

Table A.3: Structural orientations from: 11–AS–01

Feature	Geometry	Strike/Trend	Dip/Plunge
Augen gneiss foliation	Plane	229	88
Augen gneiss foliation	Plane	210	79
Augen gneiss foliation	Plane	181	68
Augen gneiss foliation	Plane	213	50
Augen gneiss foliation	Plane	217	79
Augen gneiss foliation	Plane	309	87
Augen gneiss foliation	Plane	220	89
Augen gneiss foliation	Plane	200	67
Augen gneiss foliation	Plane	225	78
Augen gneiss foliation	Plane	210	74
Augen gneiss foliation	Plane	205	78
Augen gneiss lineation	Lineation	232	62
Augen gneiss lineation	Lineation	245	40
Augen gneiss lineation	Lineation	237	58
Augen gneiss lineation	Lineation	222	50
Augen gneiss lineation	Lineation	225	41
Augen gneiss lineation	Lineation	220	40
Axial plane	Plane	34	64
Axial plane	Plane	36	66
Axial plane	Plane	219	90
Axial plane	Plane	71	76
Axial plane	Plane	32	75
Axial plane	Plane	59	85
Axial plane	Plane	23	80
Axial plane	Plane	54	86

Table A.3: Structural orientations from: 11-AS-01

Feature	Geometry	Strike/Trend	Dip/Plunge
Axial plane	Plane	44	90
Axial plane	Plane	60	79
Dike or vein contact	Plane	18	85
Dike or vein contact	Plane	273	87
Dike or vein contact	Plane	238	82
Dike or vein contact	Plane	81	76
Dike or vein contact	Plane	182	50
Fold axis	Lineation	274	64
Fold axis	Lineation	271	70
Fold axis	Lineation	232	36
Fold axis	Lineation	207	33
Fold axis	Lineation	212	42
Fold axis	Lineation	234	49
Fold axis	Lineation	215	54
Fold axis	Lineation	211	42
Fold axis	Lineation	235	35
Fold axis	Lineation	213	52
Fold axis	Lineation	212	42
Fold axis	Lineation	230	33
Fold axis	Lineation	237	59
Fold axis	Lineation	248	60
Fold axis	Lineation	207	24
Fold axis	Lineation	243	40
Fold axis	Lineation	210	45
Fold axis	Lineation	54	40
Shear zone foliation	Plane	245	54
Shear zone lineation	Lineation	211	25
Migmatitic shear zone	Plane	145	66
Migmatitic shear zone	Plane	121	28
Migmatitic shear zone	Plane	133	85
Migmatitic shear zone	Plane	315	86
Migmatitic shear zone	Plane	216	84
Migmatitic shear zone	Plane	100	70
Migmatitic shear zone	Plane	114	64
Migmatitic shear zone	Plane	116	88
Migmatitic shear zone	Plane	125	48
Migmatitic shear zone	Plane	126	54
Migmatitic shear zone	Plane	138	50
Migmatitic shear zone	Plane	165	60

Table A.3: Structural orientations from: 11-AS-01

Feature	Geometry	Strike/Trend	Dip/Plunge
Migmatitic shear zone	Plane	144	70
Migmatitic shear zone	Plane	95	84
Migmatitic shear zone	Plane	318	57
Migmatitic shear zone	Plane	130	68
Migmatitic shear zone	Plane	126	56
Migmatitic shear zone	Plane	348	57

Table A.4: Structural orientations from: 11-AS-02

Feature	Geometry	Strike/Trend	Dip/Plunge
Augen gneiss foliation	Plane	84	60
Augen gneiss foliation	Plane	104	55
Augen gneiss foliation	Plane	90	66
Augen gneiss foliation	Plane	95	61
Augen gneiss foliation	Plane	89	65
Augen gneiss foliation	Plane	89	77
Augen gneiss foliation	Plane	76	84
Augen gneiss foliation	Plane	237	85
Augen gneiss foliation	Plane	75	78
Augen gneiss foliation	Plane	80	60
Augen gneiss lineation	Lineation	103	62
Augen gneiss lineation	Lineation	244	58
Augen gneiss lineation	Lineation	205	58
Augen gneiss lineation	Lineation	192	52
Augen gneiss lineation	Lineation	194	54
Augen gneiss lineation	Lineation	210	58
Augen gneiss lineation	Lineation	200	61
Augen gneiss lineation	Lineation	212	58

Table A.5: Structural orientations from: 11-AS-03

Feature	Geometry	Strike/Trend	Dip/Plunge
Augen gneiss foliation	Plane	96	71
Augen gneiss foliation	Plane	81	64
Augen gneiss foliation	Plane	89	62
Augen gneiss foliation	Plane	77	83
Augen gneiss foliation	Plane	85	85
Augen gneiss foliation	Plane	53	77
Augen gneiss foliation	Plane	257	81

Table A.5: Structural orientations from: 11-AS-03

Feature	Geometry	Strike/Trend	Dip/Plunge
Augen gneiss foliation	Plane	258	72
Augen gneiss foliation	Plane	79	72
Augen gneiss foliation	Plane	260	88
Augen gneiss foliation	Plane	66	76
Augen gneiss lineation	Lineation	213	69
Augen gneiss lineation	Lineation	223	46
Augen gneiss lineation	Lineation	242	53
Augen gneiss lineation	Lineation	258	59
Augen gneiss lineation	Lineation	225	55
Augen gneiss lineation	Lineation	212	55
Augen gneiss lineation	Lineation	287	50
Augen gneiss lineation	Lineation	230	63
Dike or vein contact	Plane	308	80

Table A.6: Structural orientations from: 11-IN-01

Feature	Geometry	Strike/Trend	Dip/Plunge
Magmatic flow foliation	Lineation	344	50
Magmatic flow foliation	Lineation	189	35
Magmatic flow foliation	Lineation	253	60
Magmatic flow foliation	Lineation	319	56
Magmatic flow foliation	Lineation	339	62
Magmatic flow foliation	Lineation	334	66
Magmatic flow foliation	Lineation	326	58
Magmatic flow foliation	Lineation	329	55
Magmatic flow foliation	Lineation	319	66
Magmatic flow foliation	Lineation	325	63
Magmatic flow foliation	Lineation	339	64
Magmatic flow foliation	Lineation	339	60
Magmatic flow foliation	Lineation	342	65
Magmatic flow foliation	Lineation	357	59
Magmatic flow foliation	Lineation	255	85
Magmatic flow foliation	Lineation	329	66
Magmatic flow foliation	Lineation	24	65
Magmatic flow foliation	Lineation	334	57
Magmatic flow foliation	Lineation	328	65
Magmatic flow foliation	Lineation	336	65
Magmatic flow foliation	Lineation	315	74
Magmatic flow foliation	Lineation	253	60
Magmatic flow foliation	Lineation	344	72

Table A.6: Structural orientations from: 11-IN-01

Feature	Geometry	Strike/Trend	Dip/Plunge
Magmatic flow foliation	Lineation	326	70
Magmatic flow foliation	Lineation	328	63
Magmatic flow foliation	Lineation	327	56
Magmatic flow foliation	Lineation	325	62
Magmatic flow lineation	Lineation	58	63
Magmatic flow lineation	Lineation	60	60
Magmatic flow lineation	Lineation	64	55
Magmatic flow lineation	Lineation	63	50
Magmatic flow lineation	Lineation	65	60
Magmatic flow lineation	Lineation	81	63
Magmatic flow lineation	Lineation	67	58
Magmatic flow lineation	Lineation	73	50
Magmatic flow lineation	Lineation	74	64
Magmatic flow lineation	Lineation	82	57
Magmatic flow lineation	Lineation	78	64
Magmatic flow lineation	Lineation	115	58
Magmatic flow lineation	Lineation	114	58

Table A.7: Structural orientations from: 11-IN-02

Feature	Geometry	Strike/Trend	Dip/Plunge
Dike or vein contact	Plane	242	66
Dike or vein contact	Plane	302	46
Enclave zone contact	Plane	315	64
Enclave zone contact	Plane	337	80
Enclave zone contact	Plane	330	45
Compositional gneissic foliation	Plane	327	65
Magmatic flow foliation	Lineation	318	50
Magmatic flow foliation	Lineation	315	44
Magmatic flow foliation	Lineation	300	44
Magmatic flow foliation	Lineation	315	40
Magmatic flow foliation	Lineation	298	41
Magmatic flow foliation	Lineation	305	44
Magmatic flow foliation	Lineation	325	50
Magmatic flow foliation	Lineation	308	43
Magmatic flow foliation	Lineation	315	46
Magmatic flow foliation	Lineation	330	45
Magmatic flow foliation	Lineation	321	45
Magmatic flow foliation	Lineation	320	48
Magmatic flow foliation	Lineation	333	40

Table A.7: Structural orientations from: 11-IN-02

Feature	Geometry	Strike/Trend	Dip/Plunge
Magmatic flow foliation	Lineation	307	44
Magmatic flow foliation	Lineation	325	46
Magmatic flow foliation	Lineation	317	58
Magmatic flow foliation	Lineation	300	52
Magmatic flow foliation	Lineation	315	40
Magmatic flow foliation	Lineation	311	61
Magmatic flow foliation	Lineation	309	62
Magmatic flow foliation	Lineation	331	46
Magmatic flow foliation	Lineation	317	52
Magmatic flow foliation	Lineation	306	62
Magmatic flow foliation	Lineation	298	52

Table A.8: Structural orientations from: 11-IN-03

Feature	Geometry	Strike/Trend	Dip/Plunge
Dike or vein contact	Plane	315	56
Dike or vein contact	Plane	306	45
Compositional gneissic foliation	Plane	305	58
Compositional gneissic foliation	Plane	329	41
Magmatic flow foliation	Lineation	315	54
Magmatic flow foliation	Lineation	303	58
Magmatic flow lineation	Lineation	75	42
Magmatic flow lineation	Lineation	73	54

Table A.9: Structural orientations from: 11-IN-04

Feature	Geometry	Strike/Trend	Dip/Plunge
Magmatic flow foliation	Lineation	315	40
Magmatic flow foliation	Lineation	341	55
Magmatic flow foliation	Lineation	345	38
Magmatic flow foliation	Lineation	325	56
Magmatic flow foliation	Lineation	312	45
Magmatic flow foliation	Lineation	332	52
Magmatic flow foliation	Lineation	350	50
Magmatic flow lineation	Lineation	75	38
Magmatic flow lineation	Lineation	58	53
Magmatic flow lineation	Lineation	109	28
Magmatic flow lineation	Lineation	90	44
Magmatic flow lineation	Lineation	76	36

Table A.9: Structural orientations from: 11-IN-04

Feature	Geometry	Strike/Trend	Dip/Plunge
Magmatic flow lineation	Lineation	95	58

Table A.10: Structural orientations from: 11-LC-01

Feature	Geometry	Strike/Trend	Dip/Plunge
Axial plane	Plane	145	75
Dike or vein contact	Plane	277	84
Fold axis	Lineation	275	32
Fold axis	Lineation	295	53
Fold axis	Lineation	135	55
Compositional gneissic foliation	Plane	125	75
Compositional gneissic foliation	Plane	122	75
Compositional gneissic foliation	Plane	120	74
Compositional gneissic foliation	Plane	84	72
Compositional gneissic foliation	Plane	104	72
Compositional gneissic foliation	Plane	105	86
Compositional gneissic foliation	Plane	95	72
Compositional gneissic foliation	Plane	105	84
Compositional gneissic foliation	Plane	290	80
Compositional gneissic foliation	Plane	287	82
Compositional gneissic foliation	Plane	292	80
Compositional gneissic foliation	Plane	284	71
Compositional gneissic foliation	Plane	274	89
Compositional gneissic lineation	Lineation	150	70
Compositional gneissic lineation	Lineation	100	64
Compositional gneissic lineation	Lineation	92	62
Compositional gneissic lineation	Lineation	150	70

Table A.11: Structural orientations from: 11-LC-02

Feature	Geometry	Strike/Trend	Dip/Plunge
Augen gneiss foliation	Plane	238	75
Augen gneiss foliation	Plane	116	64
Augen gneiss foliation	Plane	115	55
Augen gneiss foliation	Plane	285	71
Augen gneiss lineation	Lineation	137	58
Augen gneiss lineation	Lineation	146	48
Augen gneiss lineation	Lineation	141	84
Axial plane	Plane	193	65

Table A.11: Structural orientations from: 11-LC-02

Feature	Geometry	Strike/Trend	Dip/Plunge
Dike or vein contact	Plane	252	89
Dike or vein contact	Plane	13	85
Dike or vein contact	Plane	155	53
Dike or vein contact	Plane	164	58
Fold axis	Lineation	207	41
Fault zone foliation	Plane	286	80
Fault zone foliation	Plane	97	75
Gneissic foliation	Plane	68	79
Gneissic foliation	Plane	60	80
Shear zone foliation	Plane	141	54
Shear zone foliation	Plane	142	82
Shear zone foliation	Plane	123	81
Shear zone foliation	Plane	156	26
Shear zone foliation	Plane	141	54
Shear zone foliation	Plane	140	70
Shear zone foliation	Plane	285	64
Shear zone foliation	Plane	138	82
Shear zone foliation	Plane	145	32
Shear zone foliation	Plane	193	36
Shear zone foliation	Plane	175	36
Shear zone foliation	Plane	264	67
Shear zone foliation	Plane	267	85
Shear zone foliation	Plane	145	82
Shear zone foliation	Plane	144	54
Shear zone foliation	Plane	285	64
Shear zone foliation	Plane	155	60
Shear zone foliation	Plane	155	24
Shear zone foliation	Plane	155	60
Shear zone foliation	Plane	168	38
Shear zone lineation	Lineation	202	14
Shear zone lineation	Lineation	201	20
Shear zone lineation	Lineation	293	35
Shear zone lineation	Lineation	208	16
Shear zone lineation	Lineation	180	58
Shear zone lineation	Lineation	200	21
Shear zone lineation	Lineation	210	58
Shear zone lineation	Lineation	164	22
Shear zone lineation	Lineation	185	9



Table A.12: Structural orientations from: 11-LC-03

Feature	Geometry	Strike/Trend	Dip/Plunge
Augen gneiss foliation	Plane	296	76
Augen gneiss foliation	Plane	273	82
Augen gneiss foliation	Plane	297	75
Augen gneiss foliation	Plane	274	71
Augen gneiss foliation	Plane	284	80
Augen gneiss foliation	Plane	282	76
Augen gneiss foliation	Plane	284	74
Augen gneiss foliation	Plane	252	79
Augen gneiss foliation	Plane	267	67
Augen gneiss foliation	Plane	289	56
Augen gneiss foliation	Plane	269	70
Augen gneiss foliation	Plane	125	87
Augen gneiss foliation	Plane	356	32
Augen gneiss foliation	Plane	287	72
Augen gneiss lineation	Lineation	76	50
Augen gneiss lineation	Lineation	94	56
Augen gneiss lineation	Lineation	104	55
Augen gneiss lineation	Lineation	174	68
Augen gneiss lineation	Lineation	96	64
Augen gneiss lineation	Lineation	97	67
Augen gneiss lineation	Lineation	92	72
Augen gneiss lineation	Lineation	55	66
Augen gneiss lineation	Lineation	70	50
Augen gneiss lineation	Lineation	71	50
Augen gneiss lineation	Lineation	78	49
Augen gneiss lineation	Lineation	135	68
Augen gneiss lineation	Lineation	205	86
Augen gneiss lineation	Lineation	120	70
Augen gneiss lineation	Lineation	80	56
Augen gneiss lineation	Lineation	108	70
Shear zone foliation	Plane	290	72
Shear zone foliation	Plane	296	86
Shear zone foliation	Plane	154	55
Shear zone foliation	Plane	139	73
Shear zone foliation	Plane	279	83
Shear zone foliation	Plane	70	65
Shear zone foliation	Plane	140	71
Shear zone foliation	Plane	303	87
Shear zone foliation	Plane	116	85

Table A.12: Structural orientations from: 11-LC-03

Feature	Geometry	Strike/Trend	Dip/Plunge
Shear zone foliation	Plane	313	84
Shear zone foliation	Plane	304	24
Shear zone lineation	Lineation	202	47
Shear zone lineation	Lineation	174	60
Shear zone lineation	Lineation	92	57
Shear zone lineation	Lineation	107	72

Table A.13: Structural orientations from: 11-LC-04

Feature	Geometry	Strike/Trend	Dip/Plunge
Augen gneiss foliation	Plane	274	70
Augen gneiss foliation	Plane	291	65
Augen gneiss foliation	Plane	265	66
Augen gneiss foliation	Plane	290	62
Augen gneiss foliation	Plane	280	79
Augen gneiss foliation	Plane	292	65
Augen gneiss foliation	Plane	125	88
Augen gneiss foliation	Plane	111	75
Augen gneiss foliation	Plane	292	78
Augen gneiss foliation	Plane	274	78
Augen gneiss lineation	Lineation	114	57
Augen gneiss lineation	Lineation	90	40
Augen gneiss lineation	Lineation	125	42
Augen gneiss lineation	Lineation	51	44
Augen gneiss lineation	Lineation	90	36
Augen gneiss lineation	Lineation	52	66
Augen gneiss lineation	Lineation	67	56
Augen gneiss lineation	Lineation	95	32
Gneissic foliation	Plane	305	85
Shear zone foliation	Plane	77	89

Table A.14: Structural orientations from: 11-QT-01

Feature	Geometry	Strike/Trend	Dip/Plunge
Augen gneiss foliation	Plane	168	79
Augen gneiss foliation	Plane	147	80
Augen gneiss foliation	Plane	334	64
Augen gneiss foliation	Plane	159	74
Augen gneiss foliation	Plane	170	80

Table A.14: Structural orientations from: 11–QT–01

Feature	Geometry	Strike/Trend	Dip/Plunge
Augen gneiss foliation	Plane	155	84
Augen gneiss foliation	Plane	324	83
Augen gneiss foliation	Plane	158	74
Augen gneiss foliation	Plane	159	70
Augen gneiss foliation	Plane	152	80
Augen gneiss lineation	Lineation	255	76
Augen gneiss lineation	Lineation	67	64
Dike magmatic foliation	Plane	165	88
Dike magmatic lineation	Lineation	345	70
Dike or vein contact	Plane	154	66
Shear zone foliation	Plane	152	79
Shear zone foliation	Plane	156	60
Shear zone foliation	Plane	143	81
Shear zone foliation	Plane	140	88
Shear zone foliation	Plane	165	47
Shear zone foliation	Plane	144	84
Shear zone foliation	Plane	152	60
Shear zone foliation	Plane	163	88
Shear zone foliation	Plane	151	84
Shear zone foliation	Plane	144	79
Shear zone foliation	Plane	160	72
Shear zone lineation	Lineation	280	58
Shear zone lineation	Lineation	152	84
Shear zone lineation	Lineation	178	77
Shear zone lineation	Lineation	216	80
Shear zone lineation	Lineation	225	67
Shear zone lineation	Lineation	220	70
Shear zone lineation	Lineation	175	35
Shear zone lineation	Lineation	180	45
Shear zone lineation	Lineation	166	50
Shear zone lineation	Lineation	165	73
Shear zone lineation	Lineation	313	55
Shear zone lineation	Lineation	311	60

Table A.15: Structural orientations from: 11–QT–02

Feature	Geometry	Strike/Trend	Dip/Plunge
Augen gneiss foliation	Plane	327	82
Augen gneiss foliation	Plane	300	78

Table A.15: Structural orientations from: 11–QT–02

Feature	Geometry	Strike/Trend	Dip/Plunge
Augen gneiss foliation	Plane	151	70
Augen gneiss foliation	Plane	132	71
Augen gneiss foliation	Plane	328	85
Augen gneiss foliation	Plane	137	85
Augen gneiss foliation	Plane	145	86
Augen gneiss foliation	Plane	298	87
Dike or vein contact	Plane	158	33
Dike or vein contact	Plane	133	44
Dike or vein contact	Plane	145	65
Fault zone foliation	Plane	154	80
Fault zone lineation	Lineation	158	23
Shear zone foliation	Plane	306	66
Shear zone foliation	Plane	321	47
Shear zone foliation	Plane	180	86
Shear zone foliation	Plane	80	54
Shear zone foliation	Plane	198	81
Shear zone foliation	Plane	218	89
Shear zone foliation	Plane	187	71
Shear zone foliation	Plane	157	88
Shear zone foliation	Plane	22	77
Shear zone foliation	Plane	202	84
Shear zone foliation	Plane	312	45
Shear zone lineation	Lineation	312	5
Shear zone lineation	Lineation	324	70
Shear zone lineation	Lineation	312	5
Shear zone lineation	Lineation	12	10

## Appendix B

# Fabric quantification

### B.1 Preface

The purpose of this manual is to outline in detail, the process of obtaining and analyzing fabric data from a variety of deformed rocks at different scales. As such, different scenarios will present different challenges and may result in research avenues not explicitly discussed within the tutorial. It is of the utmost importance that this manual is applied with the notion of a working process, rather than an automated procedure (i.e. no “black box” technology). Numerous stages throughout the tutorial will require input and decisions from the operator which may have important consequences, and can result in geologically meaningless and completely erroneous results if not applied correctly. Therefore, I highly encourage you to review the references cited throughout this document, and fully understand the required inputs and generated outputs of each analytical stage. This task may seem daunting, but the ability to understand the processes involved within this methodology will provide an invaluable asset in describing deformation.

The fundamental requirement of this procedure is the recognition of a situation worthy of fabric analysis. Given the banality of this statement, it is still surprising

the number of workers who apply a strain analysis to rocks without a generalized conceptual goal. Although we may not have the ability to foresee the significance of our results prior to the embarkation of a new method or application, we must first address the validity of the questions we ask. The method outlined in this manual requires a fairly significant time investment, with no guarantee that the results will suit the intended research questions. This investment must be weighed against the allocation of time in other avenues, such that the specific goals of workers are met without unproductive distractions.

I fully acknowledge the general evolution of most computer based analytical procedures, in that the advancement of technology will undoubtedly leave the exact details of this manual obsolete. Therefore, an attempt to highlight the principles behind the operations, as opposed to the exact operations themselves, is made. Although the means by which data will be obtained, formatted, and manipulated within the computer environment, is bound to change as technology evolves, the principles behind the mathematics and algorithms implemented herein will remain through that transformation. Ultimately, the rationale behind a geologist's desire to quantitatively address the geometries of deformed rocks, cannot be replaced by a computer. Therefore, use this procedure only as a tool from which some answers may be obtained, and more frequently, questions will be asked. I would like to invite the courageous and patient to adapt, manipulate, adjust, or full on rewrite this procedure and apply it to exciting new research in structural geology.

## **B.2 Getting Started**

### **B.2.1 Understanding the manual**

This manual is organized as guide to help establish the basic procedure of conducting a fabric analysis using scanned or standardized photographic data. In order to effec-

tively complete this task, the manual is set up as a tutorial, based on a synthetically deformed conglomerate model with a known magnitude and shape. This synthetic data set will allow you to check your results with the expected values, and will hopefully enable the correction of mistakes, if any arise. From this tutorial, you will learn the general analytical fabric quantification process, as well as potential considerations and issues that may arise with the application of this method to deformed earth materials. This manual uses entirely open source software with the single exception of two Microsoft® Excelbased spreadsheets. Unfortunately, I have not found the time or motivation to “reinvent the wheel” and attempt to write the two critical Excel macros into the statistical environment R.

Section B.2 documents the necessary steps to create a working environment on a personal computer. This section is initially the most difficult and time consuming phase, due to the large number of programs and packages needed for the various components of data extraction, analysis, synthesis, and documentation. However, once the programs are properly installed, additional analyses will effectively bi-pass this section. Obviously, if you switch computers, or experience an unfortunate hard drive failure, you will need to reestablish the working environment.

Section B.3 outlines the nitty-gritty details of extracting geometric data from digital scans or images. In general, this is the least entertaining phase of a given analysis, yet it is likely the most important. Here, you will use several programs outlined in section B.2 to digitize the traces of deformed (or undeformed) markers, and generate a plethora of numbers that will form the bases of all subsequent analyses. Although this stage is somewhat analogous to point-counting in terms of excitement, I can assure you the data are worth it.

Section B.4 is a general procedure to set up and retrieve data used by two Microsoft® Excelfeatures. This is not intended as a comprehensive set of instruc-

tions on how to use these tools, but rather a simple list to help remind you (and myself) of the basic required steps to complete an analysis. For more information on these tools consult the original documentation as outlined in this manual. This section implements only the two most widely used analytical strain techniques ( $R_f/\phi$  and Fry methods). If you wish to combine your data with other techniques such as the normalized / least squares center-to-center method (Erslev 1988; Erslev and Ge 1990), the DTNNM method (Mulchrone 2005), the Sanderson / projection method (Sanderson 1977; Panozzo 1984; Trayner 1986), and/or the intercept method (Launeau and Robin 1996), I encourage you to do so. However, an endeavor like that is quite beyond any documentation found in this manual.

Section B.5 will guide you through the most entertaining phase of the entire procedure. This section documents how to obtain fitted ellipsoid data from the processed two dimensional data, how to generate 3D computer models the oriented ellipsoids, and how to calculate/plot various fabric parameters. I hope you enjoy this phase as I have included 3D rendering and stereographic projection capabilities into the R scripts to better standardize and visualize the calculated rock fabrics.

Finally, the last section describes some considerations for the application of this procedure to tectonically deformed rocks. In general, these are only suggestions and hints. I cannot personally determine the validity of the results you obtain from this procedure, nor can I provide the best methodology for every potential scenario; however, I do wish you patience and good luck.

### **B.2.2 Requirements**

The basic requirements for this tutorial include a geologic entity of interest, tools to extract raw data from that entity (e.g. rock saw, scanner, photographic aperture device, etc.), a P.C. with a Microsoft Windows<sup>®</sup> operating system (Windows<sup>®</sup> 7



is preferred), several open source software programs (Table B.1), the general folder structure and conversion scripts for the analysis (see Fig. B.1), and a good sense of humor. This chapter is designed to help establish the means of data processing within the computer environment which is generally adapted from Betka (2008). Heartbreak and frustration is greatly reduced by collecting data based on the conventions established by the individual programs and conversions supplied. It will, therefore, behoove you to establish the working environment prior to data collection. However, if you are dealing with pre-existing data sets, a conversion may be required prior to analysis.

As previously mentioned, this procedure is accompanied by a set of standardized photographic data for a synthetically generated, and deformed, conglomerate model. These images were taken with a photographic aperture device (PAD) which allows the orientation of the section to be measured and later processed. The synthetic conglomerate model is obviously uncharacteristic of any geologic medium in that all assumptions of finite strain are valid for both the  $R_f/\phi$  or Fry methods. Stated simply, this is the most idealistic dataset possible which cannot be expected from reality. However, following this procedure with the provided dataset will allow you check your calculations against the expected values, and will form a good foundation for use in deformed earth materials. For details on the construction of the deformed conglomerate model, or the Photographic Aperture Device, contact me at the address listed in Table B.1.

### **B.2.3 Establishing the computer environment**

Obtain the folder structure listed in B.1 by contacting me (in the future I hope to make this available online). Place the directory in a desired location from which you will work. Each folder structure is designed for one sample analysis. If multiple samples or outcrops are processed, you will need to rename the "FABRIC" folder to

Table B.1: List of available software resources used within the tutorial.

Feature	Usage
Folder Structure	All folders, scripts, and templates
R	Statistical computing environment
Inkscape	Software for vector graphics
Gimp	Software for raster graphics
Blender	3D modeling software
SAPE	Parameter extraction software
$R_f/\phi$	Excel worksheet for $R_f/\phi$ analysis
Fry	Excel worksheet for Fry analysis
Ellipsoid	Statistical ellipsoid fitting
Notepad++	Fabulous text editor
Mulchone $R_f/\phi$	Program for $R_f/\phi$ analysis
Meshlab	3D object conversion

a unique title such as the specific sample ID or location station; *however, this manual will continue to refer to this master folder as the ‘FABRIC’ folder.* The ‘FABRIC’ folder contains 27 nested folders which are required for proper data operation of the supplied R-scripts (fig. B.1). Although the master folder can be renamed, changing any sub-folder names is unwise, and will likely result in a myriad of errors. As a first order organizational hierarchy, the project is divided into sections which will contain the analytical data, digitization data, model data, extracted parameter data, conversion and plotting scripts, raw scan or photo data, and various templates for several processes. This hierarchy allows for specific locations to work and save data that the supplied scripts will utilize in the procedure.

#### B.2.4 Software

Download each of the programs listed in Table B.1. As mentioned earlier, all of these programs are free to use and distribute with the two exceptions of the  $R_f/\phi$  and Fry worksheets. Although other programs are available for the automating the  $R_f/\phi$  technique (Peach and Lisle 1979; Mulchrone and Meere 2001), the Fry method (Lisle

<table border="1"> <tr> <td>FABRIC</td> <td colspan="2">Encompassing master folder (renamed to specific analysis index)</td> <td></td> </tr> <tr> <td>ANALYSIS</td> <td colspan="2"></td> <td rowspan="10">Components of several analytical strain/fabric techniques</td> </tr> <tr> <td>FRY</td> <td colspan="2"></td> </tr> <tr> <td>FILES</td> <td>FryXFit files</td> <td rowspan="3">Files associated with a Fry analysis</td> </tr> <tr> <td>INPUT</td> <td>Converted input data</td> </tr> <tr> <td>OUTPUT</td> <td>Planar fabric data</td> </tr> <tr> <td>RPHI</td> <td colspan="2"></td> </tr> <tr> <td>FILES</td> <td>Chew (2003) Excel files</td> <td rowspan="3">Files associated with an Rf/Phi analysis</td> </tr> <tr> <td>INPUT</td> <td>Converted input data</td> </tr> <tr> <td>OUTPUT</td> <td>Planar fabric data</td> </tr> </table>	FABRIC	Encompassing master folder (renamed to specific analysis index)			ANALYSIS			Components of several analytical strain/fabric techniques	FRY			FILES	FryXFit files	Files associated with a Fry analysis	INPUT	Converted input data	OUTPUT	Planar fabric data	RPHI			FILES	Chew (2003) Excel files	Files associated with an Rf/Phi analysis	INPUT	Converted input data	OUTPUT	Planar fabric data			
FABRIC	Encompassing master folder (renamed to specific analysis index)																														
ANALYSIS			Components of several analytical strain/fabric techniques																												
FRY																															
FILES	FryXFit files	Files associated with a Fry analysis																													
INPUT	Converted input data																														
OUTPUT	Planar fabric data																														
RPHI																															
FILES	Chew (2003) Excel files	Files associated with an Rf/Phi analysis																													
INPUT	Converted input data																														
OUTPUT	Planar fabric data																														
DIGITIZATION				Files associated with the digitization process																											
BMP	Converted bitmap images																														
PNG	Exported raster traces																														
SVG	Vector based object trace files																														
MODEL			Files associated with three-dimensional analysis of calculated two-dimensional fabric data.																												
BLENDER																															
INPUT	Orientation data	Files associated with the 3D model in Blender™																													
WORK	Construction files																														
BLEND	Project																														
RENDER	Images																														
ELLIPSOID																															
INPUT	Planar shape data	Files associated with ellipsoid fitting and documentation																													
OUTPUT	Fabric output data																														
NADAI																															
INPUT	Orientation data	Files associated with displaying strain magnitude space																													
OUTPUT	Nadai Plot and data																														
PAR_EX	Extracted geometric parameters from SAPE																														
R_SCRIPTS	Conversion and plotting scripts for use in R																														
RAW_DATA	Raw scan or photographic data																														
TEMPLATES	Templates for various steps throughout the procedure																														

Figure B.1: Basic organizational description of the various components to the folder structure implemented in each three-dimensional analysis

2010), and image analysis (Abràmoff et al. 2004), they are not discussed within this manual. Follow the directions associated with each program to successfully install and operate the software.

#### **B.2.4.1 R: Statistical Computing**

The language and environment "R" forms the basis of data conversion and plotting within this tutorial. This program forms the heart of this procedure as it will effectively take you from one program to another and will help standardize data output.

1. Download R from the URL listed in Table B.1 following the general installation procedure associated with the program. I recommend creating a desktop shortcut, as this will allow the working directory to be changed to the fabric analysis folders. Once the program is installed, double click the desktop icon. Two windows should appear, the RGui and the R Console. Most first impressions of R are typically less than exciting; however, the computing power of R surely warrants the time investment needed to fully learn the program; however, do not let this stop you from continuing, you don't have to know too much about R to process fabric data. If everything is in working order, you may close the program.
2. In order to correctly use the conversion and data formatting operations within this tutorial, we need to establish the working directory. Simply put, we need to tell R where the files and folders that it needs to read and write are located on the computer. To do this, right-click on the desktop icon and open the properties. A window similar to that shown in Figure B.2 should appear. Change the folder location under the 'Start in:' field to the desired working location. That is, the location of the 'FABRIC' folder. If you are working from your desktop, the directory will look something like this: 'C:\USER NAME\DESKTOP\FABRIC.'

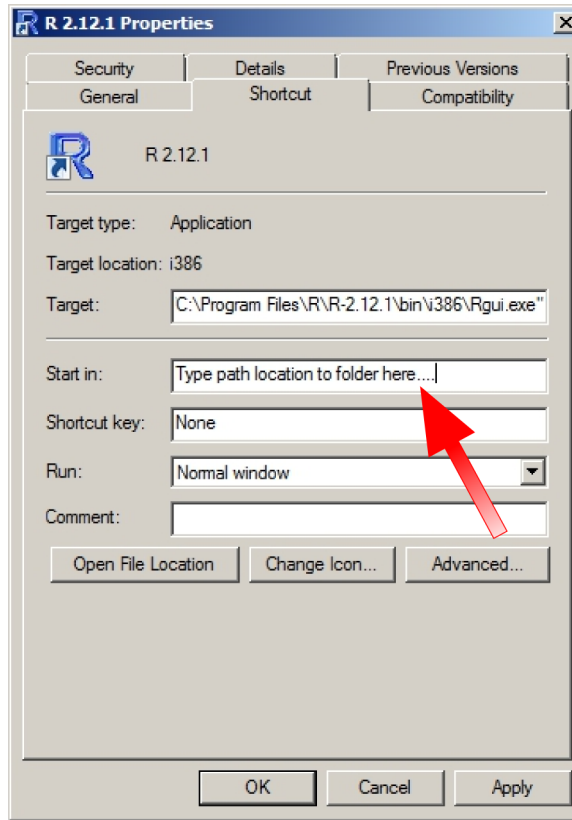


Figure B.2: How to change the working directory for R.

3. One of the best aspects of R, is the ability to download specialized packages for a variety of computational and graphical operations. These are specific to an enormous variety of disciplines ranging from three-dimensional MRI medical image analyses to GIS datum conversion applications. In order for the supplied scripts to operate, several packages must be downloaded and installed. This task is quite easy with the RGui. Simply click on the 'Packages' menu → 'Install packages(s)...' and select the location nearest to you (see Fig. B.3). This is called a mirror, and it is simply the nearest server from which you can download the desired packages.
4. Scroll through the extensive list of packages and select those listed in Table B.2. This table contains the package names, a brief description of usage, and the citation.

For more information on these packages, descriptions can be found from the CRAN website (R Development Core Team 2010). As a side note, several of the scripts implemented within this procedure use an ellipse plotting code created by Dr. Peter Macdonald (Professor Emeritus of Mathematics and Statistics at McMaster University) to whom I am grateful for permission to utilize the code within my scripts (Macdonald 2007). I would also like to thank Dr. David Chew who also helped with a ‘Vector Mean’ correction within one of the scripts.

Table B.2: Required R Packages.

<b>Package</b>	<b>Description</b>	<b>Citation</b>
sqldf	Enables SQL operations.	(Grothendieck 2010)
gplots	Formatted tables for data output.	(Warnes et al. 2010)
rgl	Provides 3D visualization.	(Adler and Murdoch 2011)
misc3d	Output of 3D objects.	(Feng and Tierney 2008)
plotrix	Plotting of arcs for Nadai plots.	(Lemon 2006)
RFOC	Plotting of stereographic projections.	(Lees 2011)

#### **B.2.4.2 Graphics programs**

I personally prefer the two open source graphics programs Inkscape and Gimp which collectively provide extensive vector and raster capabilities. If you enjoy the expensive proprietary equivalents (e.g. Illustrator<sup>TM</sup> and Photoshop<sup>TM</sup>) feel free to use them, just be warned that the operations will be different than explained in this tutorial. The use of specific graphics programs does not matter, as long as the end result is a file that SAPE is capable of processing, as explained in section B.3. Nevertheless, I will caution anyone who would like to use the Inkscape templates in a different program as this might become “fussy;” you will likely need to create your own. Finally, Blender<sup>TM</sup> is an excellent open source three dimensional modeling program that is

specifically integrated into this procedure because of the program’s splendid rendering capabilities and ability to fully attribute a three-dimensional scene.

### **B.2.4.3 Analytical software**

The “heavy lifting” in terms of data computation comes from four available programs specifically designed for use in strain analysis. These programs allow for the extraction of object trace parameters ‘SAPE’(Mulchrone et al. 2005); the objective, central void fitting of a Fry plot ‘FryXFit’(Waldron and Wallace 2007); the  $R_f/\phi$  processing macro(Chew 2003); and an ellipsoid fitting program ‘Ellipsoid’(Launeau and Robin 2005). Additionally, I have incorporated an output file within this procedure that enables use of the program rfphi (Mulchrone and Meere 2001). Please cite these programs if you use them in your research. All the other wizbangs and gizmos produced during this procedure were created to help standardize, plot, and visualize fabric data within the environment R. Please see the specific sources in Table B.2

## **B.3 Parameter extraction**

### **B.3.1 Preparing the data**

Once all the initial fuss setting up the various programs and packages is complete, a few minor, yet critically important, steps must be made. All the conversion and plotting scripts used in the procedure read and write from text files that must be appropriately labeled. This manual attempts to highlight file nomenclature as a potential source for calamity if not executed properly. Therefore, follow the procedure accordingly, and abide to the cases of characters within filenames (yes I know... it’s picky, but the file names are case sensitive) and folder locations (don’t change any of the folder names except for the master folder originally entitled ‘FABRIC’. Along this note, you must also establish the field data file, which contains orientation information

pertaining to the three mutually perpendicular sections. Unfortunately, the order of this data file matters as it will be read by the scripts in sequential order. The following list documents how to properly update this data file.

1. Open the text file 'FIELD\_DAT.txt' in 'TEMPLATES' folder with a standard text editor. If you use 'Notepad,' make sure that word wrapping is turned off.
2. Enter the correct data into each field separated by a 'tab' character and a hard return for each new line. The photo\_id field will correspond to the three entries 'A, B, and C' in sequential descending order; however, you do not need to type the names 'A, B, C' specifically, as long as you understand that the computer will think of them as just described, and that you do have some id name filled in. The 'strike' field is the strike of each section following right hand rule convention as an azimuth (not quadrant). The 'dip' is simply the dip also following right hand rule, while the field 'dd' is just a reminder to check the data, put in 'RHR' if you don't care. Add in the polarity for each section. This is explained in greater detail in the next section, but essentially denotes overhung faces; if the polarity is positive, it means the scan or photograph came from an upright surface. Finally, add any brief notes you desire about each section and add a single blank line at the end of the document. See Table B.3 for an example.

Table B.3: Example field data text file. Each field is separated with a tab character.

photo_id	strike	dip	dd	polarity	notes
A	035	64	RHR	pos	none
B	123	90	RHR	pos	none
C	214	26	RHR	pos	none

3. Once all the data is entered into the text file, save the document 'FIELD\_DAT.txt'



in the ‘RAW\_DATA’ folder and close the text editor. The data file for the deformed conglomerate is contained within the example folder also available upon contact.

### **B.3.2 Digitization**

The digitization process requires the manual selection and tracing of markers within the standardized photographs. Care must be taken to accurately follow the outlines of the markers, as repetitive inconsistencies in tracing may cause an unwanted deviation from the true object geometries. In general, three parameters are needed from each object, which include the long axis orientation, long axis length, and the short axis length. The location where the axes intersect marks the object centroid, which is necessary for a Fry plot. These attributes enable the application of both the  $R_f/\phi$  and Fry methods with relative ease compared to classic strain analyses. In general, the  $R_f/\phi$  technique requires 50 to 75 objects to produce a statistically valid plot (Borradaile 1984), while the Fry method classically requires greater than 260 centroids (Fry 1979); however, fry analyses with vastly fewer centroids (as low as 25) are reported in the literature with acceptable results (Treagus and Treagus 2002). Nevertheless, samples with less than 50 markers should generally be avoided.

1. Open the Inkscape template ‘STAND\_PHOTO.svg’ in the ‘TEMPLATES’ folder and save as ‘A.svg’ (you will need to type the file extension) under the location FABRIC/ DIGITIZATION/ SVG. This will preserve the template for use on the other sections.
2. The basic Inkscape lay out consists of the canvas, a black rectangle and a yellow grid. The blue lines are guides which allow the photographic data to ‘snap’ into the correct placement. Before we begin the digitization process, we need to set up the screen. First, the template uses a series of layers to organize the various

components of the process. Use the shortcut [Ctrl+Shift+L] to view the layers. The two important features of the layer panel are the 'eyeball' and the 'lock.' These features will allow us to toggle the visibility on and off, and will keep certain layers locked that we do not wish to edit. Make sure the 'PHOTODATA' layer is highlighted (in blue), visible (open eye icon), and unlocked. The other layers should remain locked for now.

3. Set up the other tool panels such as the transform [Ctrl+Shift+M], fill and stroke [Ctrl+Shift+F], and the align and distribute panels [Ctrl+Shift+A]. The transform panel will allow precise adjustments of objects, the fill and stroke will change the aspects of polygons, and the align and distribute panel will provide the means for accurately adjusting object locations on the canvas.
4. Import the file 'A.jpg' from the FABRIC/ RAW\_DATA folder by pressing [Ctrl+I] or File →Import. Make sure to 'link' the image, as embedding will create an excessively large file. Just note that if the location of the photo file changes, you will need to manually edit the image properties in Inkscape to the new location. Save the document.
5. Use the select tool (this one looks like a standard pointer) and move the image so the upper right hand corner snaps to the intersecting guides on the upper right portion of the canvas. Lock the 'PHOTODATA' layer and unlock the 'GRID' layer. This grid is based on the dimensions of the camera aperture device which is 25 cm by 25 cm. The grid is not a crucial part of the process, but may come in handy for additional research questions later on. Adjust the yellow grid so that it is approximately aligned to the inside margin of the Plexiglas frame. Lock the 'GRID' layer and turn off the visibility. Save the document.

6. We are now ready begin the exciting task of digitization, which conjures emotions similar to those experienced while grading assignments. Nevertheless, this tedious process is the most limiting step of the procedure in terms of data quality. By rushing this phase, you are limiting the accuracy of the entire project, in short, take your time. Begin by highlighting and unlocking the ‘DIGITIZATION’ layer, and make sure all other layers are locked. Select the pencil tool and toggle the ‘smoothing’ bar to 30. This is my personal preference, but feel free to experiment. Find an ellipse located near the center of the image, and accurately trace the outline. This is done by dragging the pencil along the ellipse outline until finished by releasing the tool within the small start box that denotes the beginning of the path. Save the document.
7. The extraction process works best with white objects on a black background. Therefore, we need to set the pencil tool to create filled white objects. Select the ellipse with the ‘selection’ tool and left-click the white color palette, typically located at the bottom of the screen, and repeat the motion while holding the shift key (this sets the outline color). Also, move the cursor over to the ‘fill and stroke, stroke style’ panel, and set the width to 1 pt. Make sure the ellipse is now completely white and selected. In order automatically set this object style for future ellipses, go to ‘File’→‘Inkscape Preferences’ (or use the shortcut [Ctrl+Shit+P]), select ‘Pencil’ from the ‘Tools’ category, and click on ‘Take from selection.’ Exit the preferences, and we are now ready to digitize the rest of the objects (see Fig. B.4). Remember to save frequently as Inkscape does crash from time to time.
8. Finish digitizing the ellipses so that there are at least 50 objects as previously mentioned. This may require some of the ellipses under the camera frame to be used; however, avoid this when there is a sufficient population within the frame.

Once again, save often. In order to view the number of objects digitized, press [Ctrl+A] and click the ‘selection’ tool; the number of objects selected should be displayed on the information bar at the bottom of the screen.

9. Once all the objects are traced, lock the ‘DIGITIZATION’ layer and save the document. Turn off the ‘PHOTO\_DATA’ visibility and unlock the ‘BACKGROUND’ layer. You may need to adjust the black box within the ‘BACKGROUND’ layer so that it completely incorporates the white ellipses. All layers other than ‘DIGITIZATION’ and ‘BACKGROUND’ should be hidden. Use the ‘selection’ tool to select the black box and click ‘file’→‘Export Bitmap’ or [Ctrl+Shift+E]. Set the ‘Export Area’ to ‘Selection’, Bitmap size to 100 dpi resolution which should reset the dimensions to 2629 by 2629 pixels, and change the file name to the location FABRIC/ DIGITIZATION/ PNG/ A.png.
10. Close Inkscape and repeat the digitization process for each of the three standardized photographs, while maintaining file nomenclature (i.e B.jpg→B.svg→B.png within the respective folders).

### **B.3.3 Raster requirements**

We have now established three exported raster files from our digitization process. However, this file type (portable network graphics .png) is not compatible with the program SAPE(Mulchrone, Meere, and Choudhury 2005), which requires a simple conversion using the program Gimp<sup>TM</sup> to a bitmap (.bmp) image. Also, SAPE can only handle black and white images, so we must convert the image from gray scale.

1. Start the program Gimp<sup>TM</sup> and open the file ‘A.png’ exported from the digitization process. Zoom into the boundary and notice that the image is not entirely black and white. In fact there are many gray values which will confuse SAPE. Therefore

it is wise to adjust the colors so that only black and white pixels exist as shown in Figure B.5.

2. Click on 'Colors' → 'Brightness-Contrast' and move the 'Contrast' bar to the maximum value possible. Select 'OK' and the pixels are now composed of only black and white values.
3. Finally, we need to export the image as a Windows<sup>®</sup> Bitmap image (.bmp). To do this simply click on 'File' → 'Save As', change the file location to FABRIC/DIGITIZATION/PNG, and name the file 'A.bmp.' Select 'Save' and close Gimp<sup>™</sup>.
4. Repeat the raster conversion process for each of the three standardized photographs, while maintaining file nomenclature (i.e B.jpg, B.svg, B.png, B.bmp within the respective folders).

#### **B.3.4 SAPE**

The program SAPE (Mulchrone, Meere, and Choudhury 2005) is a powerful tool which will statistically fit ellipses to individual digitized objects. With this tool, massive quantities of data can be obtained including the relative lengths of all major and minor ellipse axes, the location in cartesian space for the ellipse centroids, and the orientations of the major axes. This data set will therefore, provide all the necessary components required in both Fry and  $R_f/\phi$  analyses. For more information on the internal processes of SAPE, the reader is directed to (Mulchrone, Meere, and Choudhury 2005).

1. Open SAPE and edit the extraction parameters by clicking on 'Process' → 'Set Parameters' and changing the 'Bottom Tail %' and 'Top Tail %' to zero. Press 'OK'. However, if you do not intend to manually check the individual SAPE results,

which is highly discouraged (as SAPE will occasionally misidentify an object), do not adjust the default ‘Data Reduction’ parameters and leave to 5% tail cutoff.

2. Import the image ‘A.bmp’ into SAPE by clicking ‘File’ → ‘Import Image.’ Once the image is loaded click on ‘Process’ → ‘Run Analysis’ [Ctrl+R] and wait till the analysis is finished. This may take a few seconds.
3. In order to prevent the acceptance of erroneous fitted ellipses, and to insure all valid data is collected, a manual inspection is required. Change the ‘View’ to ‘Processed Data and Fitted Ellipses’ which will display the approximate outline of the fitted ellipses in red. Notice that most of the numbered tags are colored white (see Fig. B.6). When an object is rejected by SAPE, it will color the tag red. Manually inspect each tag to ensure that no valid data is rejected and no erroneous objects are accepted.
4. Once the dataset is satisfactory, export the parameters into the correct file location by clicking ‘File’ → ‘Export Parameters’ → ‘All Data’. The file location and name is crucial at this point, as all the subsequent scripts will process the data based on these attributes. Furthermore, always export ‘All Data’ even if you only intend to run an  $R_f/\phi$  analysis because all the scripts are written for this data format. Save the (.sda) file as FABRIC/ PAR\_EX/ A.sda. Once this is completed you may close SAPE.
5. Repeat the parameter extraction process for each of the remaining bitmap images, while maintaining file nomenclature.

## B.4 Analytical methods

### B.4.1 Setup

Before the Fry or  $R_f/\phi$  methods can be applied to the extracted dataset from SAPE, several conversions must be made. First, the program FryXFit needs the coordinates of a fry plot generated from the dataset and reduced to less than 3,000 data points. Secondly, SAPE uses a different origin for the coordinates than what is desired for plotting in the Cartesian grid. Finally, the  $R_f/\phi$  program (Chew 2003) requires the long, short, and  $\phi$  orientations arranged in subsequent columns. This format is not quite the same as produced in the SAPE export file so we must rearrange and convert these data. Fortunately, I have written conversion scripts for use in the program R (R Development Core Team 2010) to automatically execute the above operations and produce nice text based data files. Additionally, I have incorporated a new output file for direct use in the program written by Mulchrone and Meere (2001) that can directly bypass the Microsoft<sup>®</sup> Excel macro. This is the new recommended usage for rfphi analysis as newer versions of Microsoft<sup>®</sup> Excel have difficulties in executing the Chew 2003 macro. Assuming the previous steps outlined in this manual were followed closely, the conversions are very simply done. If however, you have deviated from the established nomenclature and folder structure, you will need to severely edit the scripts. I do not recommend changing the conversion scripts unless you are fluent in R and fully understand the inputs and outputs of each process in detail, but the world is yours, so do as you may.

1. Open the R Console from the desktop icon (this is the location for which the working directory has been changed and will correctly read and write the data files).

2. Open the script entitled “FRY\_SETUP” found in the “R\_SCRIPTS” folder with a text editor (I prefer notepad ++; however, simple notepad will work fine, but it’s a little more finicky). If you are using notepad, make sure the ‘Word Wrap’ option is not selected under ‘Format’. Select the entire script by using the shortcut: [Ctrl+A] and copy with [Ctrl+C].
3. Paste the entire script in to the R Console by using the command [Ctrl+V]. Let the machine do it’s thing and hopefully everything is produced without a hitch!
4. Scroll through the R Console and check for serious errors (don’t worry about warnings that deal with the specific version of R). If there are any, I suggest checking the working directory for the console and all file names and folder locations. Good Luck, this can become a nightmare if things are misplaced. However, if working properly, the program R will provide an incredible environment which cannot be matched by Microsoft<sup>®</sup> Excel. This point will be addressed further when producing graphs and figures directly from the data.
5. Close the R Console and don’t save the ‘Workspace Image’ as the scripts are the only things needed to processes the data again.
6. Check to make sure the output files were generated within the location FABRIC/ ANALYSIS/ FRY/ INPUT. There should now exist six text files titled ‘A.txt’, ‘B.txt’, ‘C.txt.’ These correspond to the respectively titled photographic data and SAPE parameter exports but are formatted for use in FryXFit.
7. Complete the same process for the  $R_f/\phi$  data by running the script entitled ‘RF-PHI\_SETUP’ within the R Console and checking the converted text files in FABRIC/ ANALYSIS/ RFPHI/ INPUT.



## **B.4.2 $R_f/\phi$ technique**

### **B.4.2.1 Mulchrone and Meere 2001 method**

1. Open the program rfphi by (Mulchrone and Meere 2001).
2. Open the sectional “.rfp” files directly in this program and three new windows should appear.
3. Simply press the “Run analysis” button and check the results.
4. In order to extract the section results, simply open the template ‘RFPHI.DAT.txt’ found in the ‘TEMPLATES’ folder and complete each column for each section (i.e. A, B, and C) with the specific attributes directly from the Rfphi.xls document, and separated by hitting the ‘Tab’ button once to denote a column change (this is the same style as the ‘FIELD.DAT.txt’ file you previously completed). Save the data file as ‘RF\_PHI.txt’ in the folder location FABRIC/ ANALYSIS/ RFPHI/ OUTPUT. Only the section names A,B, and C (listed as rows in that order) and the calculated  $R_s$  values are required for the subsequent stages of this procedure. The R-based scripts used in section B.5 will re-plot the data in a standardized manner for each section and will calculate the vector mean based on a geographic rake convention used in subsequent steps.

### **B.4.2.2 Chew 2003 method**

If you have used the program rfphi, there is no need to follow the subsequent steps.

1. Open the Microsoft<sup>®</sup> Excelbased macro (Chew 2003) titled ‘Rfphi.xls.’
2. Open the converted text data file titled ‘A.txt’ from FABRIC/ ANALYSIS/ RF-PHI/ INPUT. Select the entire text file by using the shortcut: [Ctrl+A] and copy with [Ctrl+C].

3. Paste the data into the Microsoft<sup>®</sup> Excelwork sheet 'Enter data' by right clicking the upper-left cell and selecting the 'Paste Special' option, choose 'text' and click 'OK'. Both the vector and harmonic means will be displayed to the right of the purple data cells, as well an Index of symmetry after Lisle (1985). The worksheet 'ln Rf vs. phi' will plot the data in standard Microsoft<sup>®</sup> Exceldefault colors with the  $R_f/\phi$  axis oriented horizontal. Note that the data is reentered such that the vector mean is now equal to  $0^\circ$ .
4. The  $R_s$  value will be calculated using a  $\chi^2$  statistical test from an iterative process which will essentially "hone" in on a precise value. To do this, open the 'Calculate Rs' worksheet. There will be three groups of cells colored yellow, purple, and red respectively from left to right. The yellow cells will allow us to set a range of values and a resolution from which the best  $R_s$  value will be determined. Because we are somewhat limited by the range and resolution of each calculation, I find it wise to hypothesize a general strain range for which the data will likely fall within (this estimation can be aided by visually examining the  $R_f/\phi$  plots and the calculated harmonic mean as suggested by Lisle (1985, page: 18).
5. Begin by changing the 'increment cell' to a value of '0.1' which will test a series of  $R_s$  values over a range of 1 to roughly 8.5. If you believe the strain exceeds this range, you may increase the 'Start Rs' cell to a value that will center the strain range over your hypothesis. Hit the return key to exit the current cell, and press the 'Calculate' button. Switch to the ' $\chi^2$  vs.  $R_s$ ' worksheet and notice the generated graph. The minimum  $\chi^2$  value produced for the  $R_s$  range is accepted as the best fit "strain" ratio.
6. In order to obtain a more precise  $R_s$  value, we will increase the resolution of the test range, and thereby, decrease the width of the test range. This is best done by

subtracting an  $R_s$  value of one from the first calculated  $R_s$  (assuming this is greater than 1), and enter this into the 'Start  $R_s$ ' cell. Change the 'Increment' value to '.05,' hit enter, and press 'Calculate'. The range is now centered on the original value and at a higher resolution. Repeat this process one more time; however, subtract an  $R_s$  value of .5 and change the 'Increment' cell to '.01.' Press 'Calculate' and the worksheet has now effectively produced a best fit  $\chi^2$  test of the extracted parameter data.

7. Before enjoying a cold beverage, you must compile the results into a standardized tab-separated text-based data table. Don't worry, this isn't as scary as it sounds. Simply open the template 'RFPHI.DAT.txt' found in the 'TEMPLATES' folder and complete each column for each section (i.e. A, B, and C) with the specific attributes directly from the Rfphi.xls document, and separated by hitting the 'Tab' button once to denote a column change (this is the same style as the 'FIELD.DAT.txt' file you previously completed). Save the data file as 'RF\_PHI.txt' in the folder location FABRIC/ ANALYSIS/ RFPHI/ OUTPUT. Only the section names A,B, and C (listed as rows in that order) and the calculated  $R_s$  values are required for the subsequent stages of this procedure. The R-based scripts used in section B.5 will re-plot the data in a standardized manner for each section and will calculate the vector mean based on a geographic rake convention used in subsequent steps. Please note, however, if you desire to have marker deformation grids accompany plots, use the graphs produced in the Microsoft<sup>®</sup> Excelmacro as the R plots will not produce deformation marker grids.
8. Complete the same process for the remaining sections. Do not forget to compile the fitted parameters and add a final blank line to the text document.

### B.4.3 Fry method

1. Open the Microsoft<sup>®</sup> Excelwork sheet by Waldron and Wallace (2007) titled ‘FryXFit.’
2. Open the converted text data file titled ‘A.txt’ from FABRIC/ ANALYSIS/ FRY/ INPUT. Select the entire text file by using the shortcut: [Ctrl+A] and copy with [Ctrl+C].
3. Paste the data into the Microsoft<sup>®</sup> Excelworksheet ‘Data’ by right clicking the upper-left cell and selecting the ‘Paste Special’ option, choose ‘text’ and click ‘OK’. Now that the data is correctly placed within the Excel environment, you can use another worksheet to fit an ellipse.
4. Switch to the ‘Plot’ worksheet and you should see the Fry plot in the typically ugly Microsoft<sup>®</sup> Excel colors. Visually estimate the central void and form a couple hypotheses for possible minimum and maximum “strain” values. Also postulate the orientation of the long axis in degrees with increasing positive values counter-clockwise from the positive x-axis (standard high school math convention). Estimate Phi values between -90 and +90, with negative values indicating a clockwise rotation from the positive x-axis. Enter these general estimates into the ‘R<sub>s</sub>,’ ‘Phi,’ and ‘Radius’ cells. The super hot pink ellipse should automatically update with the new values.
5. Attempt to objectively fit the Fry-ellipse by using the Microsoft<sup>®</sup> Excel ‘solver’ function. This is found under ‘Tools’→‘Solver’ (see the instructions worksheet for more help and details). Click the numerical cell to the right of the ‘fit statistic’ text and check to see if this is updated within the ‘set target cell’ box. Click solve and wait for the machine to run it’s course. Hopefully the produced values are satis-

factory and fall within your hypothesized “strain range”. If an obviously erroneous ellipse is created, do not accept the solved parameters and toggle the estimated parameters to obtain a reasonable result. For more detail on this procedure consult Waldron and Wallace (2007), and review the ‘Instructions’ worksheet provided directly within ‘FryXFit.’

6. Save the Microsoft<sup>®</sup> Excelfile as ‘A.xls’ in FABRIC/ ANALYSIS/ FRY/ FILES.
7. Compile the results for the fitted ellipse in a tab separated text file using the provided template ‘FRY\_DAT.txt’ found in the ‘TEMPLATES’ folder. Make sure each column is filled in for each section (i.e. A, B, and C) with the specific attributes directly from FryXFit, and separated by hitting the ‘tab’ button once.
8. Save the compiled data file as ‘FRY\_DAT.txt’ in FABRIC/ ANALYSIS/ FRY/ OUTPUT. Close the Excel document without modifying the original content.
9. Complete the same process for the remaining sections. Do not forget to compile the fitted parameters and add a final blank line to the text document.

#### **B.4.4 Data Compilation**

Congratulations, you have now analyzed a tremendous quantity of data in a relatively short amount of time. Additionally, you have utilized multiple methods on the same markers which may provide interesting insight to deformation mechanisms later on. However, we should take a moment to compile the sectional data into standardized plots. These plots could easily go into a publication if they are completed with enough data and care. I personally prefer  $R_f/\phi$  plots without marker deformation grids, unless the plots have been manually fitted. Manual plots require deformation marker grids so that the audience can judge the degree of fit. However, when a  $\chi^2$  test is used, I feel the grids tend to distract from the data. I have no problem if you

disagree with this statement, feel free to use the plots generated from the 'Rfphi.xls' document. The following few steps will automatically plot and synthesize the data generated from the  $R_f/\phi$  and Fry methods for use in ellipsoid fitting.

1. Open the R Console from the desktop icon (once again, this is the location for which the working directory has been changed and will correctly read and write the data files).
2. Open the script entitled 'FRY\_PLOT.r' found in the 'R\_SCRIPTS' folder with notepad ++ or notepad. Select the entire script by using the shortcut: [Ctrl+A] and copy with [Ctrl+C].
3. Simply paste [Ctrl+V] the script into the R-Console and wait until a nifty looking plot of the sectional data appears in a second window. Hopefully you do not encounter any errors! Scroll through the R Console and check for errors and warnings. If there are any, I suggest checking the working directory for the console and all file names and folder locations. As I mentioned earlier, this can easily become a nightmare if the file nomenclature and folder structure is not maintained.
4. Assuming the script has successfully executed and a plot of all the  $R_f/\phi$  sectional data is produced, you may exit the R-Console. Don't worry about saving anything, the script has already produced a PDF document of the plots within the FABRIC/ANALYSIS/ RFPHI/ OUTPUT folder, entitled 'RFPHI.pdf.' Pretty neat. If you would like to change the layout or colors of the plot, this can easily be done in Inkscape. If you wish to directly change the direct outputs of the 'RFPHI\_PLOT' script, I suggest learning the R-language if you are not already proficient.
5. A similar script for compiling the Fry data is available in the 'R\_SCRIPTS' folder titled 'FRY\_PLOT.' Execute this script in the same manner as before, and a PDF

plot should be generated with the name 'FRY.pdf' within the FABRIC/ ANALYSIS/ FRY/ OUTPUT folder. You will also notice that I have included a 3d Fry plotting functionality to better assess the sectional data and fitted ellipses.

## B.5 Ellipsoid construction

### B.5.1 Ellipsoid

At this point, you have successfully analyzed the two dimensional fabric of three mutually perpendicular faces with two different methods. In order to extrapolate these data into a fabric ellipsoid you will need to run a program entitled 'Ellipsoid2003' created by Launeau and Robin (2005). This program will directly read in a file generated by the previously executed R-scripts that utilizes the 'FIELD\_DAT.txt' file for geographical orientation information.

1. Open the program 'Ellipsoid2003' and click 'OK' on the startup credit screen. Four boxes will appear on the screen. We will only use the 'main' and 'table' frames for the ellipsoid fitting process.
2. As mentioned above, the previous R-scripts have auto generated an ellipsoid raw data file (.elli) which is saved in the folder FABRIC/ MODEL/ ELLIPSOID/ INPUT. If you have executed both an  $R_f/\phi$  and Fry analysis there will be two such files entitled 'RFPHI\_RAW.elli' and 'FRY\_RAW.elli' respectively. Also within this folder are two PDF files that show the compiled parameters in a nice table format that you can easily refer to later.
3. Within the main 'Ellipsoid 2003' window, check the 'shape ratio r' parameter in the 'Data format' field. This will change the columns in the data window to match those produced in the RFPHI\_RAW.elli file. To import the data, simply click

‘File’→‘Load ASCII file (\*.elli)’ and direct the browser to the RFPHI\_RAW.elli file location in the FABRIC/ MODEL/ ELLIPSOID/ INPUT folder. Press ‘Open’ and click ‘OK’ on the new dialog box. The data will automatically load into the Ellipsoid2003 table window. If this is too easy, feel free to manually enter the data from the exported PDF files.

4. Once finished, hit the bright green Ellipsoid button, and the two dimensional data will be statistically fitted with an ellipsoid! I recommend spending some time looking through the output panel to make sure no mistakes have been made.
5. If everything appears in order, you may export the fitted data for the three dimensional modeling phase. This is done by saving the ELLIPSOID project, ‘File’→‘Export results in ASCII file (\*.txt)’, as FABRIC/ MODEL/ ELLIPSOID/ OUTPUT/ RFPHI.elli. Make sure to use the default ‘.elli’ file extension as the next phase will extract the necessary data from these files. If you like the output stereographic projection produced in Ellipsoid 2003, save the image; however, I personally prefer the plotting capabilities I have incorporated into the next set of R-scripts which are vector based and easily imported into Inkscape (or Illustrator<sup>TM</sup> ... or Canvass<sup>TM</sup> ... or etc.).
6. Repeat the process for the Fry method data with the compiled data in FABRIC/ MODEL/ ELLIPSOID/ OUTPUT/ FRY.elli, while maintaining file nomenclature.

### **B.5.2 Visualization**

This stage of the fabric quantification process combines many aspects of art with science, and is a superb way of communicating the geometry of fabrics within deformed mediums. I have found that an excellent way to produce three-dimensional models of publishable quality is through the open source program Blender<sup>TM</sup>, which is described



in the following sections. Moreover, I have also included three-dimensional real-time modeling capabilities into the R-scripts that help aid in shape and orientation visualization. Unfortunately, recent versions of Blender<sup>TM</sup> no longer support the file format “.off.” As such, you will need to use the program Mesh lab to convert R output object to blender recognized files.

1. Before modeling the fabric ellipsoid, a few conversions must be made to the Ellipsoid2003 outputs. Once again, the program ‘R’ will be used for this process. Open the R-Console and the script ‘ELLIP2BLEND\_RFPHI.r’ in the location FABRIC/R\_SCRIPTS/. Select all, copy, and paste the script into the Console as described previously. Check for errors. If everything works correctly, you will see an interactive modeled ellipsoid in the ‘RGL’ window, as well as a plotted stereonet similar to the one shown in Figure B.7.
2. Close R, and repeat the previous step with the script ‘R\_SCRIPTS/ ELLIP2BLEND \_FRY.r.’ These two scripts have completed five basic tasks each: 1.) the ‘.elli’ files were scanned, and the desired ellipsoid parameters were extracted; 2.) the scripts converted the geographic orientation data into a series of parameters which Blender<sup>TM</sup> will use to orient the modeled ellipsoids; 3.) the scripts also produced and rendered oriented ellipsoid objects in three dimensions with real-time viewing capabilities; 4.) stereographic projections of the ellipsoid major axes and foliation planes were generated; and 5.) the scripts have written a text file of parameters which will be used in calculating the Octahedral Shear Strain ( $\bar{\epsilon}_s$ ) and Lode’s parameter ( $\nu$ ). Each time the script is fed into the R-Console, the new outputs will be appended to the former outputs within the  $\bar{\epsilon}_s$  and  $\nu$  parameter text file entitled ‘AXIAL\_DAT.txt.’ This will effectively create additional data points that allows multiple analyses to be plotted on the same graph. However, if the same

‘ELLI2BLEND’ script is processed multiple times, numerous duplicates of the same outputs will be stacked in subsequent steps. To avoid this duplication issue, only process the desired ‘ELLIP2BLEND’ scripts once in a correct manner. If errors arise during the conversion, close the R-Console, check all folder names, file names, and delete the output file ‘MODEL/ NADAI/ INPUT/ AXIAL\_DAT.r.’ Fix the errors, and reprocess the scripts. Once this is completed, you are ready to begin the Blender<sup>TM</sup> phase.

3. The most simplistic method to generate an ellipsoid will utilize a file generated by the ‘ELLIP2BLEND’ scripts. The down side to this method, is that the object axes will not be generated. If you are from the quick and easy crowd, simply open the Blender<sup>TM</sup> template file ‘ELLIPMOD\_BASIC.blend,’ and add the generated object by File→Import →DEC Object File Format (.off). Open the ‘RFPHI.off’ file in the ‘FABRIC’ folder, and save the file as ‘RFPHI.blend’ within the FABRIC/ MODEL/ BLENDER/ WORK/ BLEND folder. If you are using a new version of Blender, you will need to convert the .OFF file into a .PLY file in Meshlab. To do this simply open Mesh lab and import to .OFF file. Next click “Export mesh as” and select the Stanford polygon file format (\*.ply). Then open this file in Blender. Skip to step 10.
4. If you prefer axes, then skip the previous method and use the following procedure.
5. Open the Blender<sup>TM</sup> template file ‘ELLIPMOD.blend’ located in the ‘TEMPLATES’ folder and save the file as ‘RFPHI.blend’ within the FABRIC/ MODEL/ BLENDER/ WORK/ BLEND folder. The Blender<sup>TM</sup> graphical user interface is quite incredible and extensive in the ability to complete a plethora of operations. If you wish to learn the details of this program, I suggest working through a number of the many tutorials available online. Furthermore, several Blender<sup>TM</sup> manuals are

available for purchase which are quite comprehensive. Nevertheless, the procedure outlined within this section is designed to provide the beginner Blender<sup>TM</sup> user with the minimum number of tools necessary to accurately model the calculated fabric ellipsoids.

6. Check to make sure both the ‘BUTTONS’ and ‘3D VIEW’ windows are open. The screen should contain a horizontal reference frame with abbreviations for the azimuthal directions labeled, and a red sphere. Projecting from the sphere, are three axes, which will eventually define the principle fabric or strain axes.
7. Open the ‘Transform Properties’ dialog box if it is not already open by pressing the letter ‘n’ on the keyboard and with the cursor positioned within the ‘3D VIEW’ window.
8. Open the output PDF file from the previous conversion script (FABRIC/ MODEL/ BLENDER/ INPUT/ ELLIP2BLEND\_RFPHI.pdf) and enter the six parameters directly into the ‘Transform Properties’ window. This will successfully distort and orient the sphere according to the calculated fabric ellipsoid.
9. The camera view can be adjusted several ways. The most precise, yet finicky, method is to directly change the camera properties by right clicking on the black frame which surrounds the ellipsoid (you may need to zoom out to see this) and manually editing the ‘Transform Properties.’ A more entertaining method involves the ‘Fly Mode’ feature which is entered by pressing the shortcut [Shift+l+f] and maneuvering by the commands listed on the screen. Alternatively, use the number pad key to navigate based on the shortcuts listed under ‘View’→‘View Navigation.’
10. Finally, render a high quality image of the model by entering the ‘Scene’ panel [F10] and changing the ‘OSA’ parameter to ‘16.’ You can also change the render

image type and quality in dpi under the ‘Format’ frame. Press the large ‘RENDER’ button and save the image [F3] as ‘RFPHI.jpeg’ in the FABRIC/ MODEL/ BLENDER/ WORK/ RENDER folder (see Fig. B.8).

11. Repeat the same process for the calculated ellipsoid using the Fry method.

### **B.5.3 Quantifying shape and magnitude**

The comparison of multiple fabric analyses can be an extremely powerful tool in understanding the architecture of deformation through time. For this reason, several methods have been developed to graphically display various parameters of the calculated fabric ellipsoid. The two most widely implemented diagrams include the Flinn diagram (Flinn 1956) and the Nadai diagram (Nadai 1963) which are designed to illustrate both the strain symmetry and the deviatoric component of deformation (Brandon 1995). Unlike the Flinn diagram, the Nadai diagram forms an undistorted representation of the deviatoric section (Brandon 1995), yet is often more difficult to construct. As a utility of this procedure, another R based script will automatically set up a Nadai plot and tabulate the calculated Octahedral Shear Strain ( $\bar{\epsilon}_s$ ) and Lode’s parameter ( $\nu$ ) for both the  $R_f/\phi$  and Fry analyses. For a complete discussion on the use of strain magnitude space diagrams see Brandon (1995).

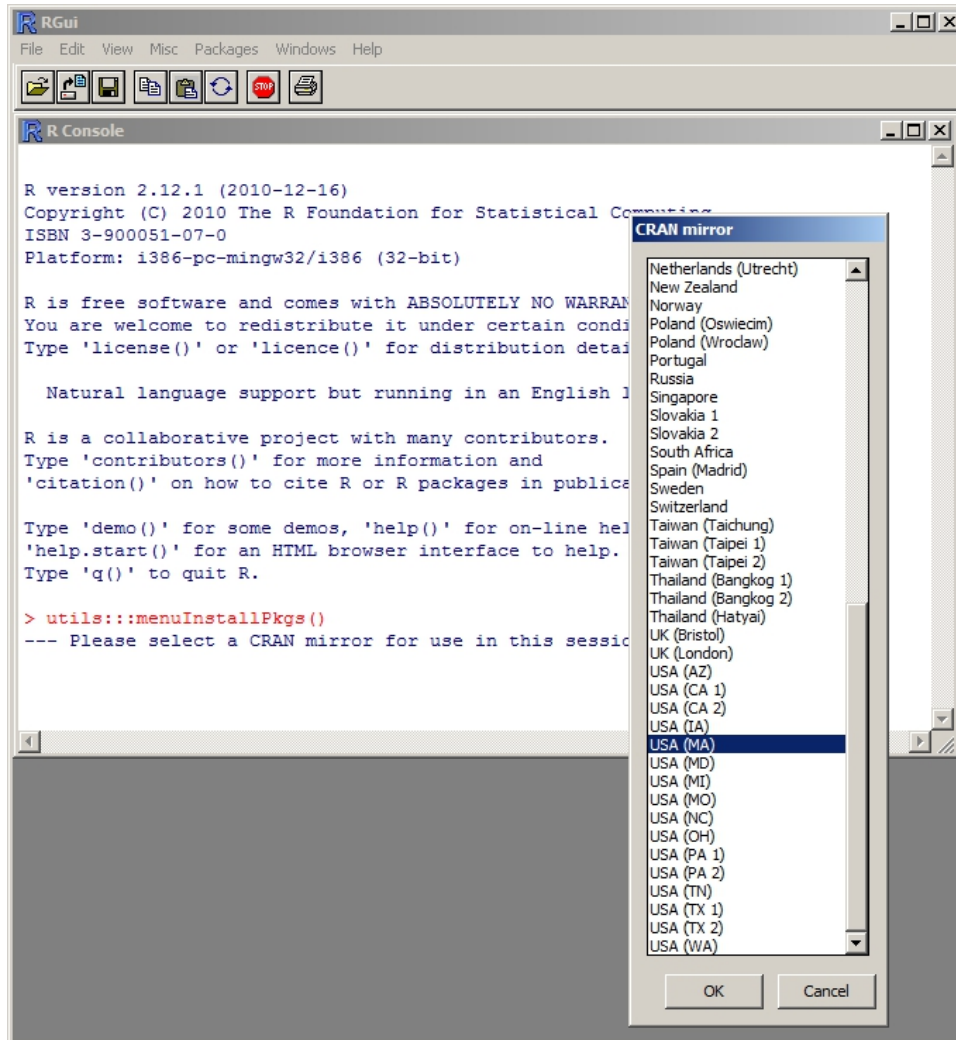


Figure B.3: Selecting a mirror to download R-packages.

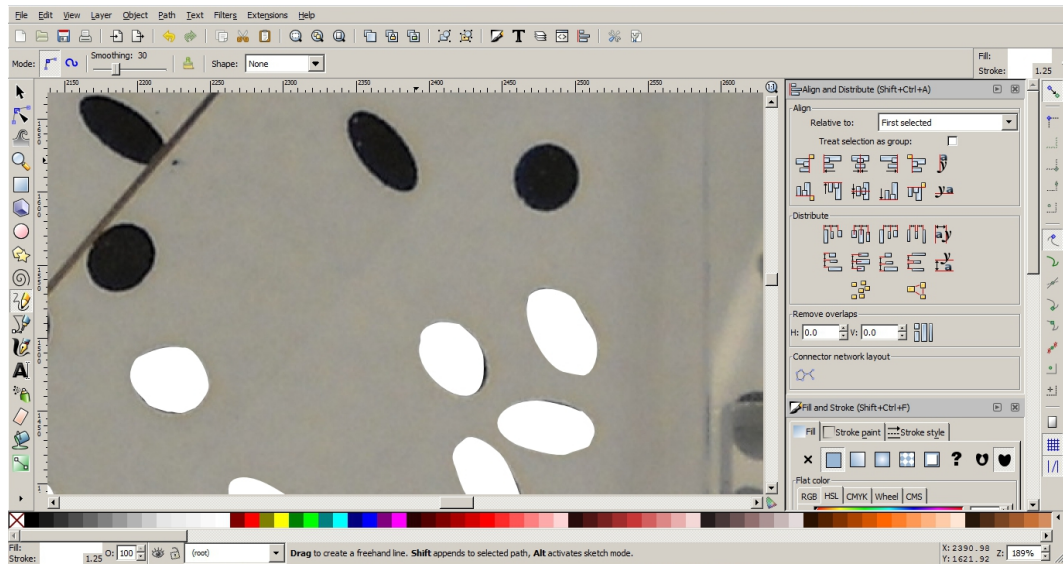


Figure B.4: Digitization of objects with Inkscape.

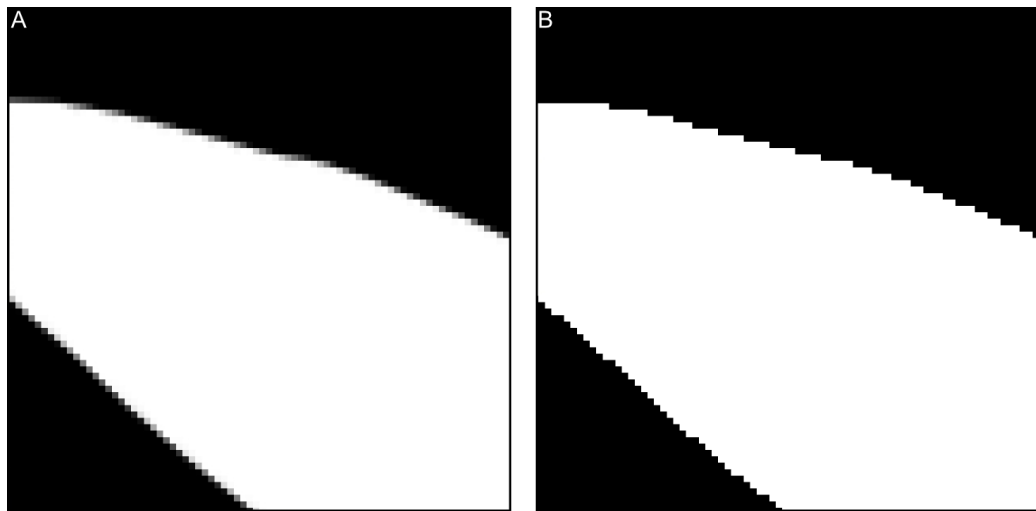


Figure B.5: Difference between gray scale (A) objects and two color objects (B).

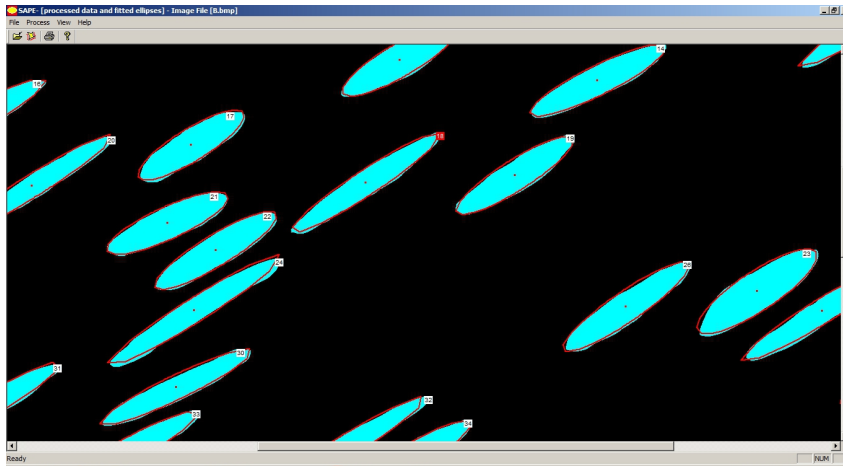


Figure B.6: Manual inspection of fitted ellipses in SAPE.

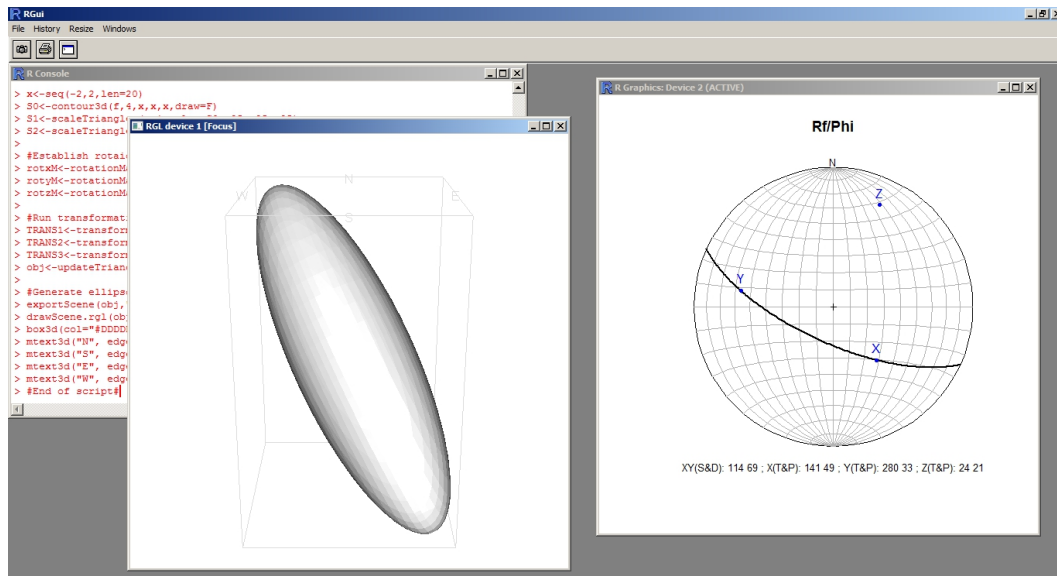


Figure B.7: R console output for the ELLIP2BLEND scripts.

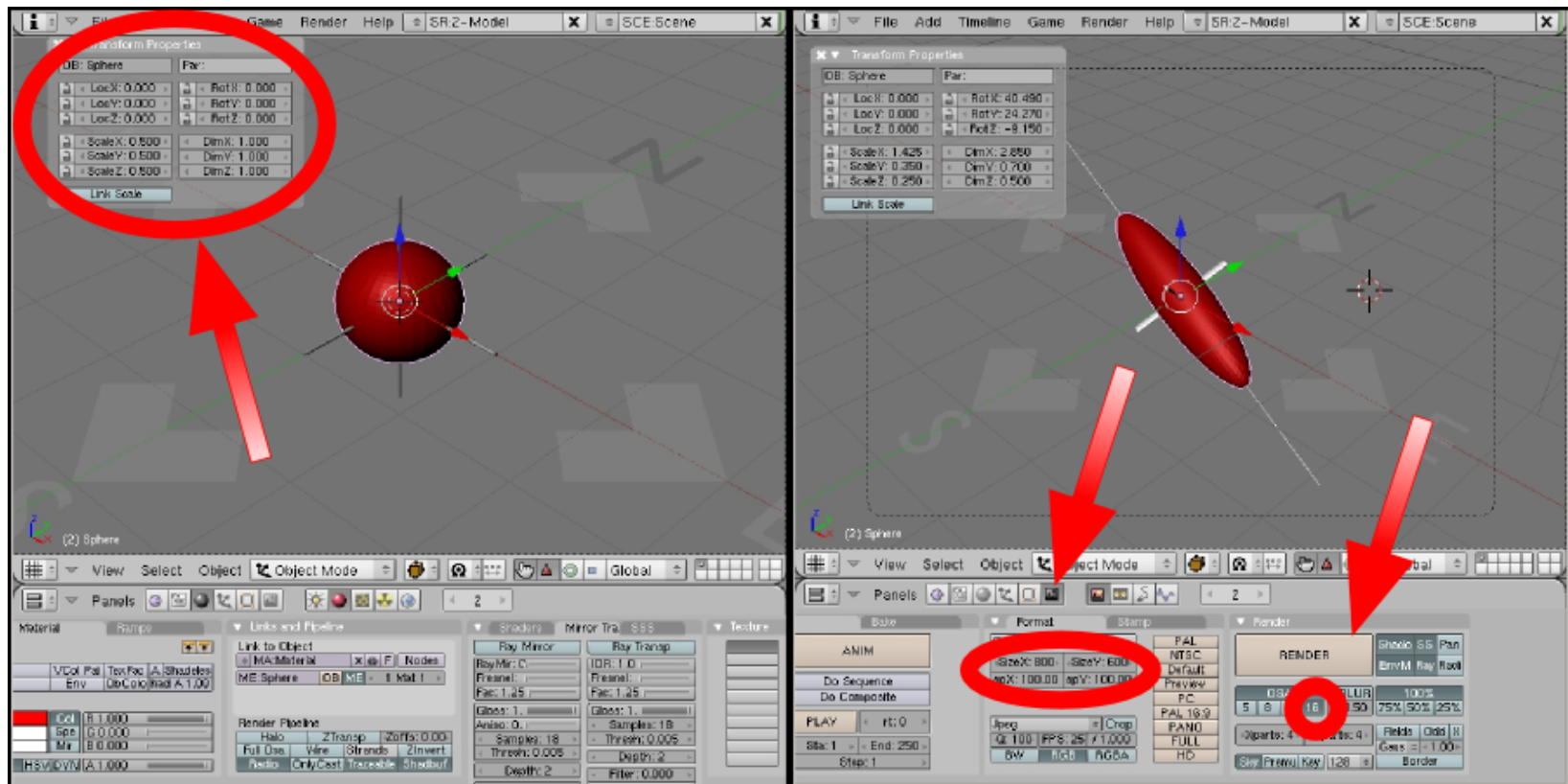


Figure B.8: Basic use of the Blender GUI.



1. Open the R console and the script 'R\_SCRIPTS/ NADAI\_PLOT.r'. Select all, copy, and paste the script into the Console as described previously. This will generate a Nadai plot and the calculated parameters(see Fig. B.9), and will also automatically save a PDF version of the plot found in FABRIC/ MODEL/ NADAI/ OUTPUT/ NADAI\_PLOT.pdf.

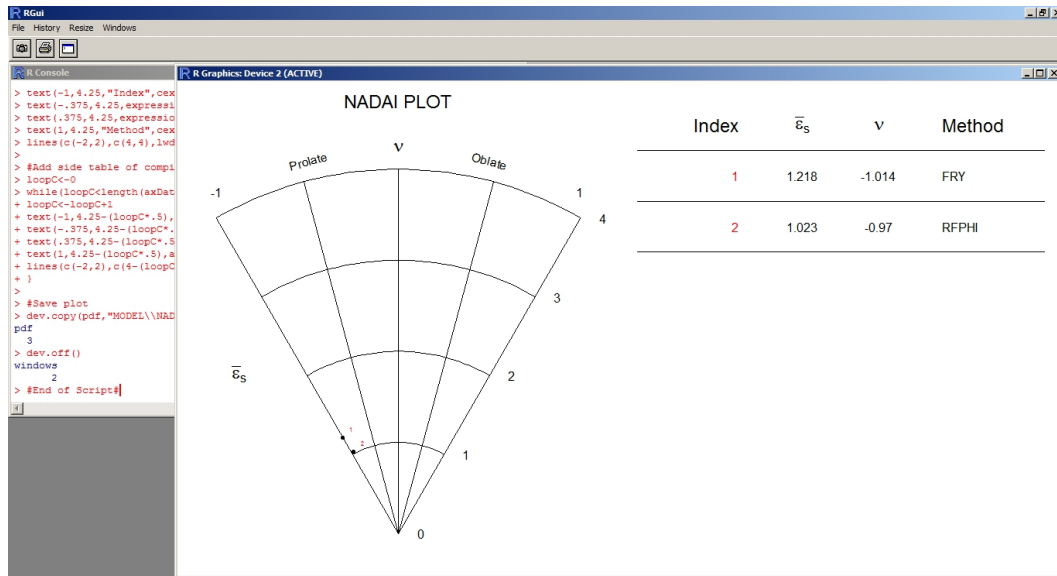


Figure B.9: R console display of the NADAI plotting utility.

2. Check the Console for errors and problems such as the stacking of identical data points. As briefly addressed earlier, this problem likely arises from running the ELLIP2BLEND scripts more than once. To correct this problem, delete the 'AXIAL\_DAT.txt' file, and rerun the 'ELLIP2BLEND' scripts.
3. Once the script is correctly executed you may close the Console without saving anything. Check the output file 'FABRIC/ MODEL/ NADAI/ OUTPUT/ NADAI\_PLOT.pdf' to ensure proper plotting.

## B.6 Data Collection

### B.6.1 Manual field measurement

The use of manual field measurements will work fine within this tutorial once all measurements have been compiled and formatted according to several key conventions. The best place to integrate a manually collected data set is within the Parameter Extraction phase. Obviously, you will not run the program SAPE. However, you must produce a tab delimited text file with an ‘.sda’ file extension that is formatted exactly like the the output files produced in SAPE. Table B.4 shows the basic structure of this file type, note however, the header names will not be produced within the ‘.sda’ file. The next sections will explain the necessary fields to processes manual data. As a side note, manually collected data must also be grouped into three mutually perpendicular planes and the orientations entered within the ‘FIELD\_DAT.txt’ file.

Table B.4: Basic file structure for a .sda file, columns from left to right in output file.

<b>Column</b>	<b>Description</b>
Column 1	Unconverted x-coordinates
Column 2	Unconverted y-coordinates
Column 3	Length of ellipse major axis
Column 4	Length of ellipse minor axis
Column 5	Orientation of the major axis
Column 6	Unknown extracted data

#### B.6.1.1 Manual $R_f/\phi$ data

To process manual  $R_f/\phi$  data you will need to create a spread sheet without coulumn headers. I prefer work in the Open Office suite as opposed to Microsoft<sup>®</sup> Excelsimply because this software is open source. If you wish to work in Microsoft<sup>®</sup> Excel, the process will essentially remain the same.

1. Populate the first two columns with the text 'NA.' Copy and paste this text for as many rows as data points.
2. Add the lengths of all recorded major axes in column two. If you only collected ratio data, simply place the ratio in this column and populate the next column with the value '1.'
3. Add the minor ellipse axes in column four (see above note about collected ratio data).
4. Populate the 5<sup>th</sup> column with the orientation of the long ellipse axis. The convention required for this field is in respect to the line of strike following right hand rule. To clarify, all  $\phi$  values are measured as the acute angle produced from the intersection of the strike line and the marker's long axis, as read from the direction of strike according to right hand rule convention (i.e. the right side of the strike line on an upright surface, or the left side of the strike line on an overhanging surface). Positive values denote acute angles that fall above the line of strike and negative values denote acute angles that are measured below the line of strike.
5. Populate the final field with the text 'NA' in each row and check for errors in the spread sheet.
6. Copy all the populated cells in the spreadsheet, open either 'Notepad++' or regular 'Notepad' and click paste. The data should now be entered within the program as tab delimited columns and row separated by hard returns.
7. Finally, save the file as 'A.sda' in the folder FABRIC/ PAR\_EX/. You may need to change the file type to 'All Types.'
8. Repeat this process for the other two sections and maintain file nomenclature as

discussed earlier in this manual. You may now complete the analytical process as outlined in this procedure.

### **B.6.1.2 Manual Fry data**

The manual collection of mesoscopic scale analyses is rather unlikely to occur considering the difficulty in defining a Cartesian coordinate system in the field. However, if the locations of object centroids can be identified from GPS data or any other source, this conversion will need to occur. This procedure will operate exactly the same as described in section B.6.1.1, however, you will only populate the first two columns with data and all others will be filled with the text string ‘NA.’ Unfortunately, SAPE utilizes a different quadrant to calculate the origin coordinates than is used for the program FryXFit. As such, the provided conversion scripts are written to correct for this discrepancy and will erroneously change the orientation of your data set. Use Equations B.1 and B.2 to correct for this correction (silly, but necessary) before running any subsequent steps.

$$\text{Column 1} = (\text{Maximum Value of } Y) - Y_n \quad (\text{B.1})$$

$$\text{Column 1} = X_n - (\text{Minimum Value of } X) \quad (\text{B.2})$$

An alternative method to this conversion would involve plotting the coordinates without a conversion, converting the plot (with large white circles and a black background) to a 1.bmp’ file and running this through SAPE. You could also disable the conversion code directly in the R-scripts and enter the SAPE data as is; however, I suspect this might lead to more problems than it solves.

### B.6.2 Standardized photographs

The use of photographic data to calculate rock fabrics has generally been avoided based on recommendations presented in Paterson (1983); however, recent studies have effectively applied digital imagery for strain analysis (Treagus and Treagus 2002). Advances in the resolution of digital cameras allowing for workers to easily zoom in on pictures from the field makes the reevaluation of this process a worth while endeavor. Nevertheless, several key limitations to this application involve: 1.) photo distortion due to changes in the line-of-sight distance from the center of the image to the periphery; 2.) oblique view distortion causing ‘foreshortening’ of objects; and 3.) the lack of orientation information associated with images.

In order to remove these limitations, I have constructed a Photographic Aperture Device (see Fig B.6.2) that attaches to a digital camera and positions the line of sight orthogonally onto a 25 cm X 25 cm Plexiglas frame.

Due to the close distance of the camera to the section of interest ( 50 cm), peripheral distortion is negligible. Foreshortening is removed on roughly planar surfaces because the line-of-sight is forced orthogonal to the basal frame. Finally, the orientation of the frame is easily measured and recoded in a standard table similar to Figure B.11.

The implementation of this device on outcrop surfaces, grouped into three approximately perpendicular sections, allows for the collection of an incredible quantity of data that can be later processed in the lab. Furthermore, multiple photos can be tiled and analyzed if objects are too large or spread apart to obtain a statistically significant population size in one image. In general, a few conventions must be followed to easily incorporate this kind of data into a fabric analysis.

- Identify outcrop faces that contain fabric markers of interest and that can be

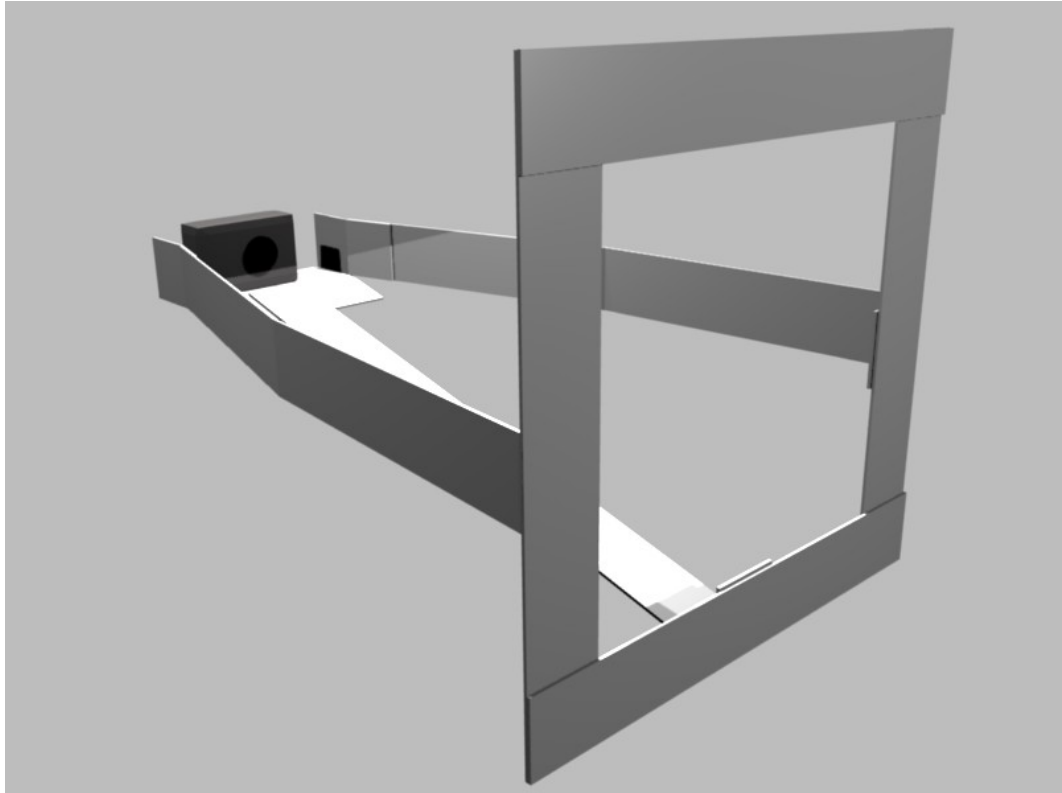


Figure B.10: Photographic Aperture Device for the collection of standardized digital images.

grouped in three approximately perpendicular planes (limit angular variances to  $\sim > 10^\circ$ ). Make sure faces are accessible for the PAD and sufficient lighting is available to recognize objects in the digital images. Some objects will need to be outlined in chalk for later recognition if the color contrast between objects and the matrix is low.

- Record the bulk orientations of the three sections in the table shown in Figure B.11 and denote the general locations of the sections to be digitized.
- Place the frame on the outcrop surface with the top of the frame aligned exactly parallel to the line of strike, orient the camera such that the image margins are aligned to the frame, and take the image.
- Fill out the table in B.11 with all necessary fields paying special attention to the ‘polarity’ of the outcrop surface (OH/UP). As noted previously, this simply refers to upright surfaces as ‘positive’ and overhung surfaces as ‘negative.’

Once back in the laboratory, the images can be digitized and synthesized into a fabric ellipsoid, just remember to correct for faces with a negative polarity.

### **B.6.3 Scanned slabs**

Numerous sources of error can occur when extracting scanned sections from hand samples. This is due to a variety of logistical issues that need to be addressed prior to scanning. Several key considerations in hand sample preparation include: 1.) the use of proper rock cutting equipment with planar cutting tables; 2.) aligned saw blades; and 3.) correctly positioned fences; as well as the correct orientation marks on each face. Unlike standardized photographic data where angular variance is

---

Figure B.11: Basic table for collection of standardized photographic field data.

**Photographic Fabric Analysis Data Sheet**

**Page#**

**Project:**

<b>Name:</b>	<b>Location:</b>		
<b>Date:</b>	<b>Zone:</b>	<b>E:</b>	<b>N:</b>

#	PHOTO ID	STRIKE	DIP	DD	OH/UP	NOTES
1						
2						
3						
4						
5						
6						
7						
8						
9						
10						
11						
12						
13						
14						
15						
16						
17						
18						
19						
20						
21						
22						
23						
24						
25						

Use one sheet per outcrop region with location nomenclature corresponding to notes written in the individual's field book. UTM coordinates need to be collected using the WGS84 datum and should represent a central location within the outcrop region. All attitudes need to use right hand rule standards with the upper frame edge parallel to strike and upright or overhung orientation indicated. Issues with measurements need to be recorded in the notes section. If more than one sheet is used per outcrop, indicate page number.



expected due to the inability to extract information from three precisely perpendicular mesoscopic outcrop faces, hand samples can easily be cut to within a few degrees of this requirement. As such they can provide high quality fabric data if properly cut and aligned. By following the steps recommended within this procedure, accurate, high quality data can be extracted on a variety of samples within the comfort of the laboratory (although many of us prefer the comfort of the field). The following steps require an oriented sample suitable for analysis, rock preparation equipment, and a quality scanner (preferably dedicated solely to use on rocks). Also, a little knowledge of stereographic projections is useful (then again, I always think stereonet are useful).

1. In order to properly execute a fabric analysis at the hand sample scale, proper cuts must be made on a sample with a sufficient number of markers to be statistically significant. This statement is easier said than done, and experience is highly beneficial. If you are new to rock preparation, I recommend testing a few cuts on several toss pieces. Of course, this is in addition to proper training and knowledge of the necessary tools and safety procedures required for cutting. I recommend attempting to mimic the principle fabric planes, such that plane A is parallel to the mineral foliation, plane B is perpendicular to foliation and parallel to the bulk mineral trace lineation, and plane C is orthogonal to the bulk mineral trace lineation.
2. Section the hand sample and use a goniometer to check the faces for accuracy. Hopefully the sections are within a few degrees of the desired  $90^\circ$ .
3. Reconstruct and properly orient the sample using a sand box or clay base. I have personally constructed an adjustable platform to aid in this step which is highly recommended to save patience and time.
4. Record the strike and dip of the most easily accessible sectioned face and lightly

- draw an arrow with a colored pencil parallel to strike such that the head points in the direction of strike following right hand rule convention. Also, add a tick in the down dip direction. This will properly orient face A in a geographic sense.
5. Orientation marks on faces B and C will be calculated directly from a simple stereonet procedure.
  6. First, plot the great circle and pole to face A on an equal area stereonet. Measure the rake of the edge between face A and B on face A using a goniometer. Plot this rake from the correct side of the primitive circle along the great circle for plane A.
  7. Because all three planes are  $90^\circ$  apart from each other, and plane A and B must share the line formed from the intersection of these two planes along their great circles, the orientation of plane B can easily be calculated. Plane B will contain the lines formed by the edge of A&B, and the pole to A. Rotate the stereonet until these two lines fall along the same great circle. Draw in the great circle and plot the pole to this plane. This is the orientation of plane B. Record the strike and dip of face B and determine the polarity.
  8. Count the angular distance between the cut edge made from faces A&B and the primitive circle along the great circle for face B. Set the goniometer to this value and measure in the strike line. To clarify, the measured angle is effectively the rake of the cut edge between faces A and B within face B. Therefore, this rake will allow you to reconstruct the the strike line without directly measuring the orientation on the sample (this method of direct measurement is logistical nightmare as the samples tend to move and faces are frequently obscured within the setup). Note the ambiguity of this measurement in that it can be made from two directions along the cut edge. However, a quick examination of the sample should clarify the

- ambiguity. Also, add an arrow in the direction of strike following right hand rule convention and a down dip tick as mentioned before. However, if the polarity is negative, remember the arrow will point to the left.
9. Repeat this process for Plane C using either plane A or B (which ever face creates the best edge to measure the rake). Determine the polarity and add the strike line, arrow and down dip tick.
  10. Place face A onto a sheet of transparency film and trace the outline of the sample on the film with a sharpie. Cut the transparency along the trace line so it will neatly cover the section without too much extra.
  11. Lightly coat face A with mineral oil and gently apply the transparency cover. With a stirring straw “squeegee” extra oil out from under the slip. Clean up any extra oil and wipe down the surface of the transparency film with a non-abrasive fabric or tissue.
  12. Scan face A on a high quality flatbed scanner at a resolution of 600 dpi. Save the image as ‘A.jpeg’ in the folder FABRIC/ RAW\_DATA. Open image ‘A.jpeg’ with Gimp<sup>TM</sup> and use the rotate tool to align the strike line parallel to horizontal (note, you may need to adjust the canvas size for images with long aspect ratios so that the image corners are not cutoff). If the face has a negative polarity (i.e. the arrow head is located to the left of the strike line when upright following right hand rule convention), you will need to flip the image about a vertical axis. This is accomplished with the mirror image tool in Gimp<sup>TM</sup>. Crop the image to size, and save at the highest quality. This will maintain the proper resolution.
  13. Repeat this process for the two remaining sections while maintaining file nomenclature and proper the folder structure.

14. Check the dimensions of each section scan by right clicking on the image icon and going to ‘properties’→‘details.’ Find the image with the largest dimension and record the number in pixels. In order to preserve scale information from the scanned sections, we will need to resize each image by the same percentage. This is easily done by sizing the largest dimension to the digitization template and calculating the scale. The scale will then be applied to the other two sections prior to digitization.
15. Following Equation (B.3), calculate the scale percentage. This is the proportional scale percentage that will be applied to each scanned image within the digitization phase.

$$Scale\ Percentage = \left( \frac{1000\ px}{Longest\ dimension\ in\ px} \right) \times 100 \quad (B.3)$$

16. Complete the analysis by following the general procedure outlined within the manual beginning with section B.3. However, open the Inkscape template ‘SCAN.svg’ in the ‘TEMPLATES’ folder and save as ‘SECTION\_A.svg’ (you will need to type the file extension) under the location FABRIC/ DIGITIZATION/ SVG. Also, remember to scale each imported image by the calculated *Scale Percentage* and update the field data file. The completed digitization process should result in scaled images similar to those shown in Figure B.6.3.

#### **B.6.4 Fabric from thin sections**

The use of thin sections to determine the three-dimensional fabric of a rock is relatively straight forward, following the procedure listed in section B.6.3. However, several key logistical issues may need consideration. By now, you may have realized the reference frame used in all measurements is based on azimuthal strike and dip following right hand rule convention. This convention is dependent on the nature of the section in

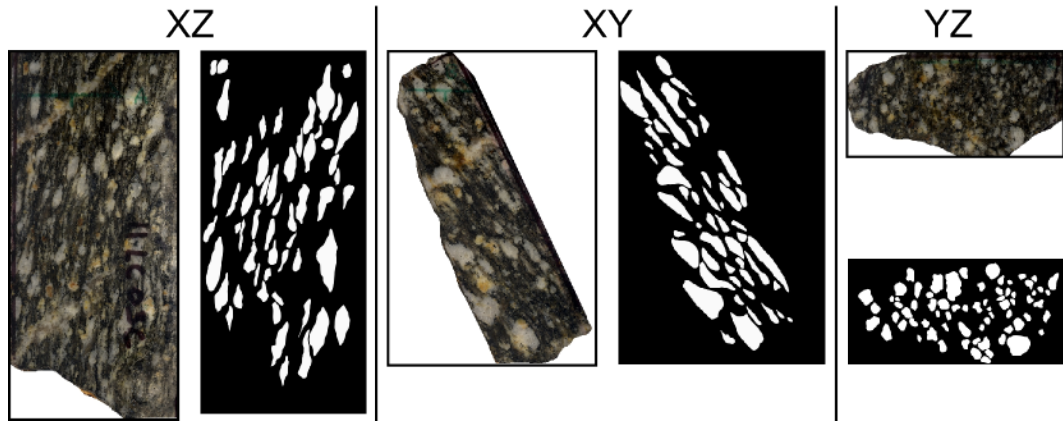


Figure B.12: Scanned, oriented, and traced images for three mutually perpendicular faces on a deformed granite augen gneiss.

terms of polarity. In the digitization of scanned slabs or standardized photographs originating from overhung sections, a simple image reflection is required to re-orient the direction to the right of the screen. Not only does this also apply to images of thin sections, an additional complication is the fact that a thin section can be viewed from both sides. As such, the direction of sight is a critical component when orienting photomicrographs (see Fig. B.6.4).

Although there is no procedure outlined in this manual for thin section preparation, I recommend follow the general guidelines for collecting oriented samples found in most structural or field geology texts. Always document the locations of the thin on slabbed surfaces, and keep all pieces of the sample so that reconstruction may be easier in the future. In general, photomicrographs may be tiled together, or thin sections may be scanned at high resolution in order to create a base image for object tracing. Follow the guidelines in section B.6.3 and factor in the relative orientations of the thin section and the line of strike on each face.

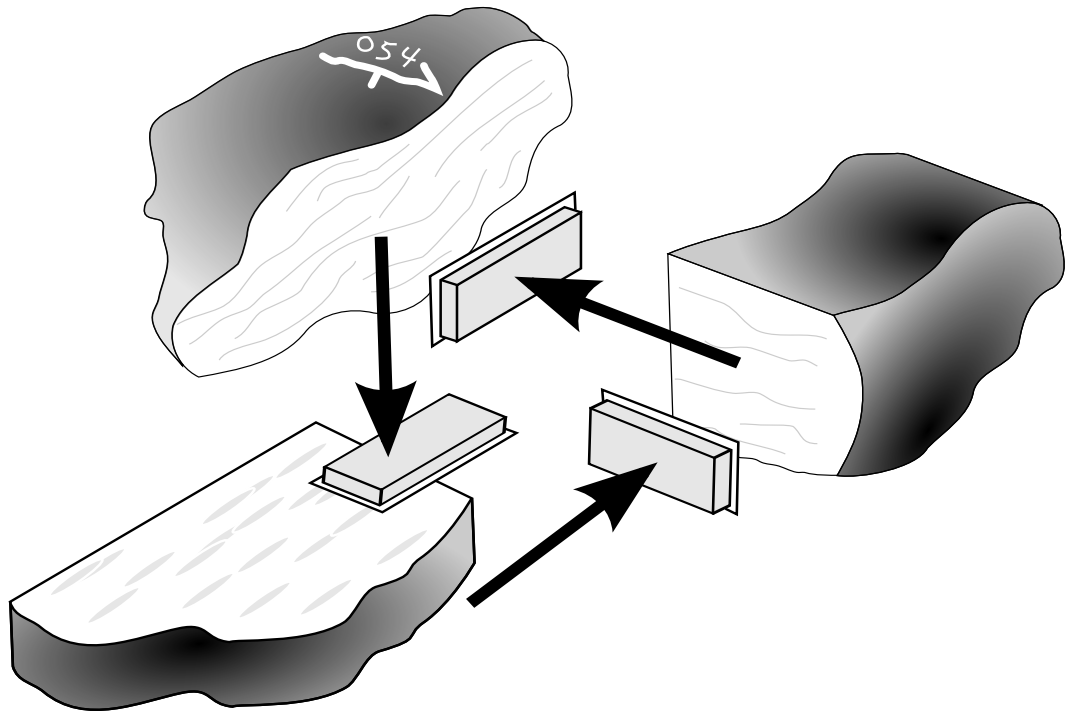


Figure B.13: The use of thin sections in a fabric analysis requires the documentation of the direction of sight in order for photomicrographs to be correctly oriented.

## B.7 Concluding remarks

Congratulations, you have now processed a tremendous quantity of data and reduced the results into a series of standardized plots. The visualization of three dimensional fabric data or 'strain' data is the one of the hardest concepts to convey. By combining stereographic projections, Nadai plots, and location information within the context of a known scale and representative object population; all the properties of fabric, with respect to the defining objects at the scale of analysis, can be effectively conveyed. Although this procedure, as applied only to a single analysis will essentially produce a rather meaningless number, the application to numerous samples within a region, may provide the means to quantify gradients in fabric development, and eventually in deformation partitioning.

In a semi-qualitative approach, this method could enable a field geologist to establish known fabric parameters at several key locations within a terrain, from which changes in fabric could be successfully mapped directly in the field. This holds great promise for the documentation of fabric development as it effectively enables the user to apply a standardized method to numerous samples, in a relatively time-efficient manner. Nevertheless, I must emphasize the recognition that none of the techniques presented within this manual are new. In fact, most originate from the heyday of the analytical strain revolution spawned by individuals like Ramsay, Dunnet, Fry, and Lisle (not to mention numerous others). The only new concepts presented herein are those which pertain to the nature of data manipulation, and presentation.

Throughout this documentation, I have made a concerted effort to avoid the implications of strain. Although the development of fabric may be inherently related to some component of a finite strain path, serious assumptions are required in the use of this terminology. As clearly documented in Paterson et al. (2004) the application of these methods to directly measure strain requires the following considerations:

1. At the scale of analysis, deformation is homogeneous.
2. Markers deform passively with the matrix, or some ductility contrast correction can be applied.
3. The initial properties of markers are reasonably understood with respect to population shapes and orientations.
4. Markers must be approximate ellipsoids in three-dimensional space.
5. Deformation within the region is not diachronous and affects the sample population with the same finite strain path such that marker objects are not introduced within the deforming medium at different times.

6. Population sizes are statistically significant.
7. The scale of interpretation is applied to the scale of analysis.
8. Specifically for the Fry method, object centroids and population distributions are reasonably understood.

In many circumstances, these assumptions may be impossible to constrain. This is the nature of science. However, the notion of fabric (and more importantly changes in fabric) can elucidate many great characteristics of deformation. The application of numerous analytical strain techniques to a single population of markers may unveil specific characteristics of the deforming markers, based on deviations in the analytical results. Nevertheless, the use of fabric quantification must be attributed to the scale of analysis, the specific population of markers, and the analytical method used. For instance, the development of fabric within an aguen gneiss, as defined by the shapes and orientations of feldspar porphyroclasts, using the  $R_f/\phi$  method, may be entirely different than the fabric produced by biotite grain centroids surrounding the feldspar porphyroclasts. It is from these nuances, however, that great insight may be obtained. As such, I wish any individuals good luck in their exploration of deformation.



## Appendix C

# FRY3D user guide

### C.1 Preface

The purpose of this tutorial is to guide structural geology students, at either the undergraduate or graduate level, through the procedure of three dimensional strain analysis using the Fry method. Traditionally, analytical strain techniques taught at the university level are restricted to two-dimensional sections. This limitation is not the product of poor course design, but rather a logistical issue of processing and maintaining the enormous quantity of data generated in such analyses. Although this is generally an accepted practice, I believe the lack of discussion on deformation in three-dimensions creates the misconception that a single two-dimensional analysis can effectively address the nature of pervasive deformation. Not only does a single section fail to accurately address the magnitude of strain, no information pertaining to the symmetry of strain can be gained as well.

In order to alleviate the logistical issues inherent to three-dimensional Fry analyses, this manual allows the user to interactively collect, process, and analyze data from both a synthetic data set and an actual rock sample.

Despite my best attempt to limit the user code interaction, some basic computer

knowledge is required. I do not recommend implementing this tutorial as an assignment without proper preparation, as some minor nuances are expected from time to time. Nonetheless, I am confident that with sufficient preparation this tutorial can be effectively used. Additionally, this application will provide students and instructors with an introduction to the extremely powerful language R. I hope you enjoy this tutorial, or at least learn something moderately interesting. Cheers!

## **C.2 Getting Started**

This general procedure will require only two programs to function completely. As mentioned in the preface, the statistical computing environment “R” is the primary program used. However, I have incorporated the program Ellipsoid2003 created by Launeau and Robin (2005) in order to synthesize the two-dimensional section data into a statistically fitted ellipsoid. Although the first portion of the tutorial will not require this ellipsoid fitting program, the second part will. Based on time constraints, you may opt to forgo the latter portion and focus only on combining three mutually perpendicular Fry plots. However, if time allows, I recommend downloading the program Ellipsoid2003 (see [hyperlink](#)) and incorporating this into the procedure.

### **C.2.1 R: Statistical Computing**

The language and environment R forms the basis of data collection, conversion and plotting within this tutorial. As such, it is essential that all components of this language are set up properly. The following steps will guide you through the basics of setting up R. Once this is established on your machine, you can skip this section for future runs. As a note, I have written these instructions based on Windows<sup>®</sup> 7, which may deviate slightly from the exact steps used on other platforms. Nevertheless, the general procedure should still work with minor procedural variations.

1. Download R from the Comprehensive R Archive Network following the general installation procedure associated with the program (see hyperlink). Once the program is installed, double click the desktop icon. The RGui should open with the R Console inside. Most first impressions of R are typically less than exciting; but what this program lacks in snazzy widow design, it makes up for in power and versatility.
2. One of the best aspects of R, is the ability to download specialized packages for a variety of computational and graphical operations. These are specific to an enormous variety of disciplines ranging from three-dimensional MRI medical image analyses to GIS datum conversion applications. In order for the supplied scripts to operate, the package StructR (Webber 2012) must be loaded.
3. To load the package “StructR,” click “Packages” within the RGui window and select “install package(s).” Find the CRAN mirror nearest to your location and press “OK” (Fig. C.1). Scroll through the extensive list and select the correct package. If you cannot find the “StructR” package, you can do a manual installation of the tar ball file available from CRAN by following the help pages associated with R.
4. Now that the package is installed on your computer, you must load the package into the current R session. Simply type: `library(StructR)` into the command line interface and press enter. This package is dependent on several other packages which may be dependent on other packages as well. Check the return messages and look for additional packages that need to be installed (e.g. package: “RFOC”). Repeat the steps above to install all required packages.
5. Once everything is installed correctly, you will be able to run the remainder of this

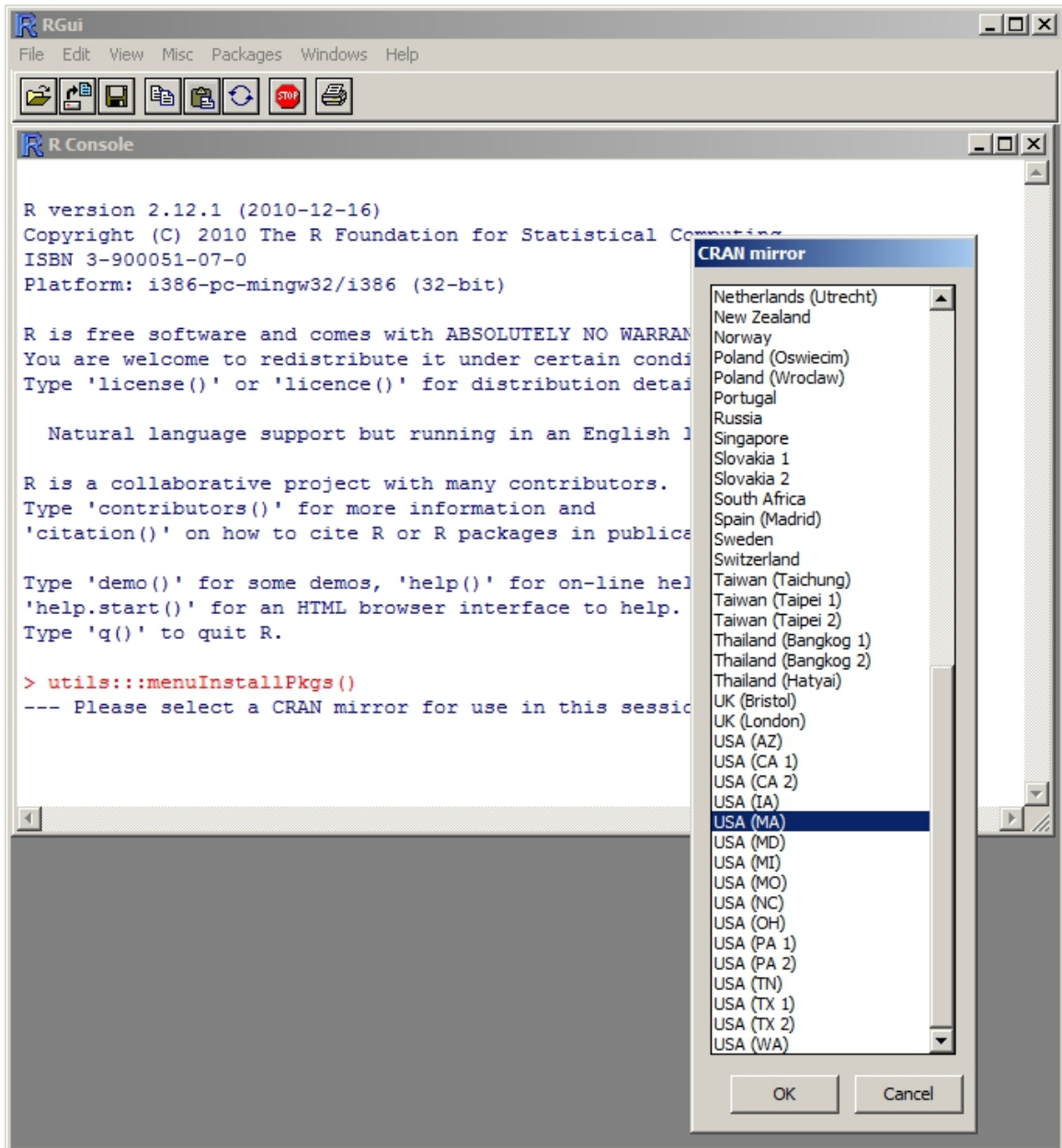


Figure C.1: Selecting a mirror to download R-packages.

tutorial with only a few minor modifications.

### C.2.2 Tutorial scripts and data

Now that R is correctly set up, you need to establish the general working environment to process the data accompanying this manual. This will require some minor editing of the supplied scripts such that the program will read and write data to and from your computer. The following steps will guide you through this process.

1. Make sure you have downloaded and extracted the data set accompanying this manual. The contents should be the same as illustrated in Figure C.2. The basic contents of the compressed folder include six image files that form the raw data to be analyzed. Additionally, there are four scripts associated with the synthetic and natural examples. Finally, there is another folder to organize input and output files.
2. Place the entire folder structure into a desired directory on your computer. This will be the location from which the image files are processed and the results are written.
3. In order for the script to correctly read in the image files and output the Ellipsoid2003 file you must configure the path locations directly in the script. This can be edited in two ways. First, you may edit the configuration header directly in a text editor (e.g. notepad) and save the file. However, some issues may arise from this if the text editor produces any auto formatting. The other method is explained in the following steps.
4. Open the RGui select “File” → “Open script...” and point the browser to the folder structure described above. Open the file entitled “SYNTHETIC.P1.R.”





 <b>FRY3D</b>	<b>Extracted master folder</b>
 <b>IMG_DAT</b>	<b>Folder containing image files</b>
<b>A_EX.png</b>	Synthetic section A image
<b>B_EX.png</b>	Synthetic section B image
<b>C_EX.png</b>	Synthetic section C image
<b>VT_A.png</b>	Vermont rock scan A
<b>VT_B.png</b>	Vermont rock scan B
<b>VT_C.png</b>	Vermont rock scan C
 <b>OUTPUT</b>	<b>Folder to contain Ellipsoid2003 files</b>
 <b>SCRIPTS</b>	<b>Folder containing R scripts</b>
<b>SYNTHETIC_P1.R</b>	Part one of the synthetic data script
<b>SYNTHETIC_P2.R</b>	Part two of the synthetic data script
<b>VT_P1.R</b>	Part one of the Vermont rock data script
<b>VT_P2.R</b>	Part two of the Vermont rock data script

Figure C.2: Folder structure and R scripts accompanying the manual.

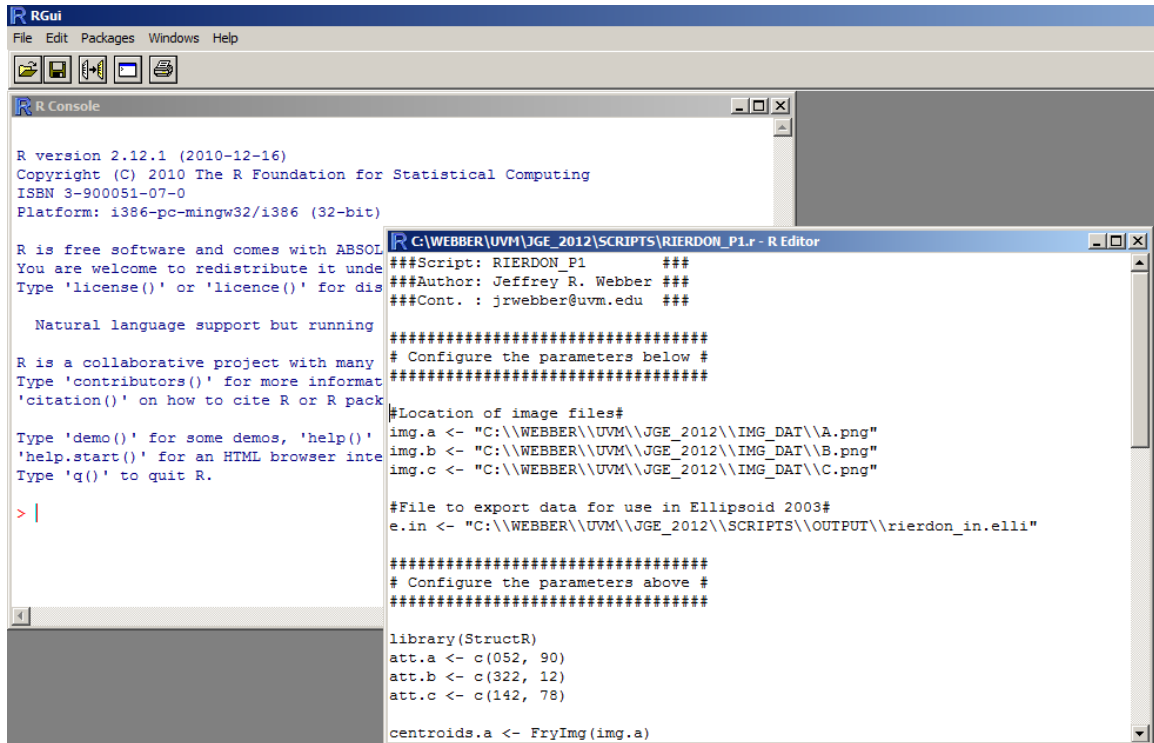


Figure C.3: Loaded R script from which the configuration parameters can be edited.

5. The RGui will load the script into a new window as shown in Figure C.3. Edit the location of the image files following the example syntax in the script. Note the use of the double “//” characters between folder locations.
6. Click on “File” → “Save” to save the edits you just made. This step will not need to be repeated for subsequent trials unless you change computers or re-download the accompanying data.
7. Double check to make sure the file location is correct for each image and the output location of the Ellipsoid file. Repeat this process for each of the remaining scripts and close the “RGui.” Now we are ready to begin the tutorial.

### C.3 Operating procedure

Once the correct programs and packages have been installed and the scripts edited to the correct directory, you can begin the FRY3D procedure.

1. Open the RGui and open the script “SYNTHETIC\_P1.R.” A new window should appear with the script code inside.
2. To run the script, simple click “Edit” → “Run all.” If the script fails to run correctly, you likely did not edit the directory location correctly. If so, close the RGui and repeat the previous steps.
3. If the script executes correctly, a new window will open with an image of a section of the synthetically deformed conglomerate. Use the cursor to select the center of each ellipse. A yellow dot will appear where clicked and is accompanied by a slightly annoying chime (Fig. C.4).
4. Once all of the ellipses are marked, right click with the mouse and press stop.
5. A new window will appear with the sectional Fry plot. Once again you will use the cursor, but this time you will need to estimate the central void apogee length. To clarify, simply click where you think the end of the central void’s long axis is. A red line will appear on the screen to denote your estimate of the long axis (Fig. C.5).
6. Repeat the previous step with the perigee (short axis). Note that the program will automatically plot the ellipse.
7. Once the ellipse is plotted, the program will move to the next section. Simply repeat the previous steps until all three mutually perpendicular sections are completed. The program will now plot an interactive three-dimensional Fry plot with



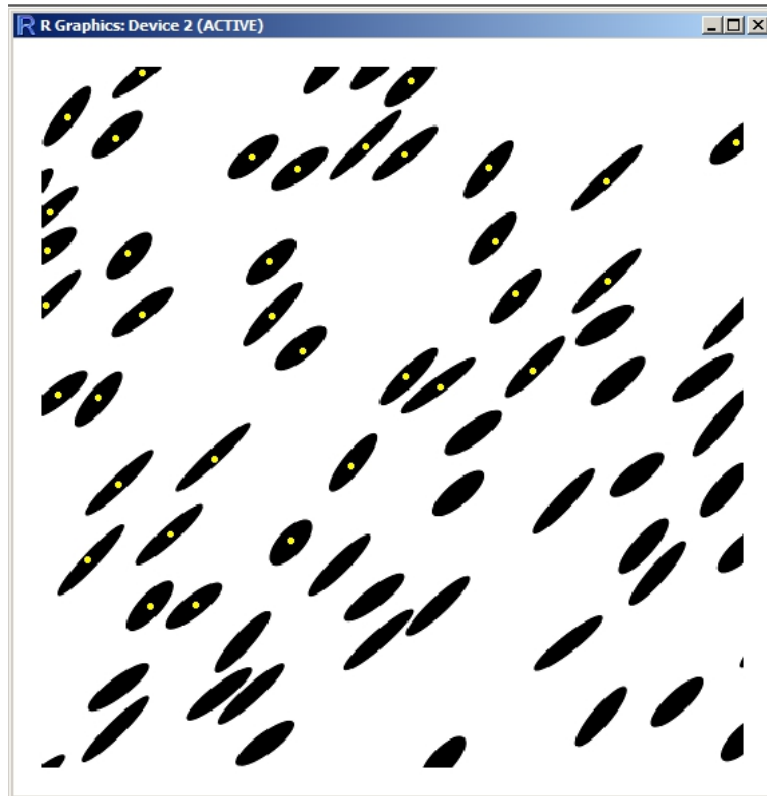


Figure C.4: Centroid locator tool in new window of sectional data.

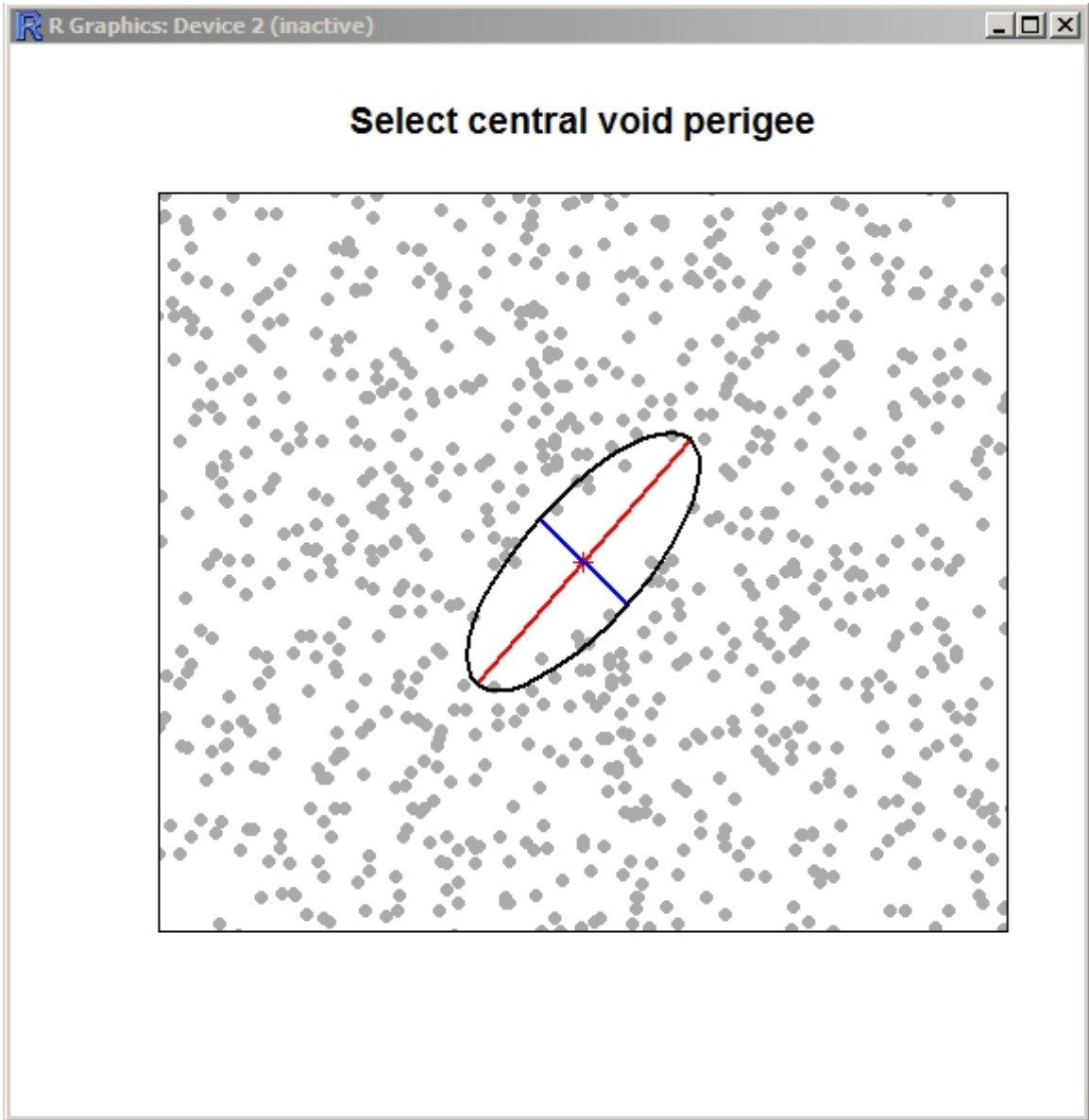


Figure C.5: Central void apogee and perigee locator tool.

- the fitted ellipses (Fig. C.6). Each color corresponds to each section such that red is the first section, blue the second, and green the third. Furthermore, the program has also written a file to be used in the program Ellipsoid2003 that is saved in the directory you specified at the beginning of the procedure.
8. In the 3D Fry plot window, use the left button on the mouse to spin the plot and the right to zoom in and out. With these controls, you will be able to see how the sectional strain data synthesizes into an ellipsoid. Furthermore, you will also be able to recognize the accuracy to which each ellipse represents the data and how closely they correspond.
  9. In order to complete the second main part of this tutorial, you will need to run the exported Ellipsoid 2003 file. Minimize the main RGui window and open the program Ellipsoid 2003. Press “OK” on the start up credit window.
  10. Load the exported file by clicking “File” → “Load ASCII file (\*.elli)” and directing the browser to the “synth\_in.elli” file. Press “Open” and “OK” in the new window. Now the file is successfully loaded.
  11. Click on the bright green button within the Ellipsoid 2003 graphical user interface entitled “Ellipsoid.” The program has now statistically fitted a strain ellipsoid to the two-dimensional Fry data.
  12. Now we must load in the fitted ellipsoid to R by saving the exported results. In order to do this, Click “File” → “Export results in ASCII file (.txt).” Change the name from “synth\_in.elli” to “synth\_out.elli” and press “OK.” You can now close the Ellipsoid program.
  13. Maximize the RGui. Open and run the second script entitled “SYNTHETIC\_P2.R.” If the script executes correctly (that is, if you have saved the data correctly and

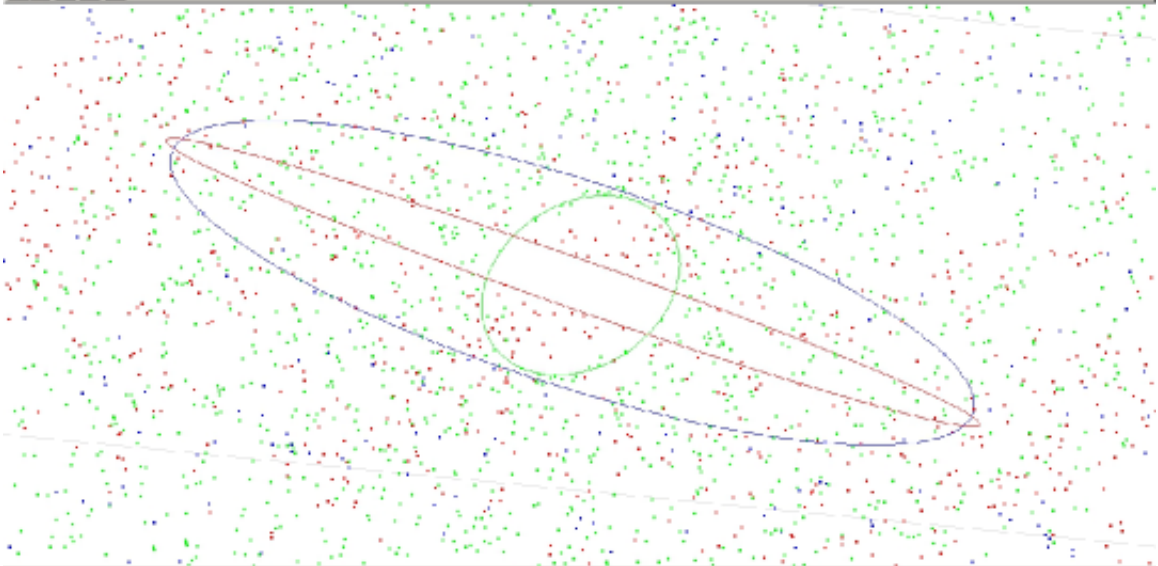
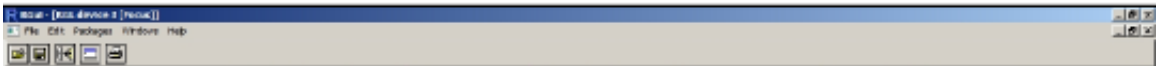
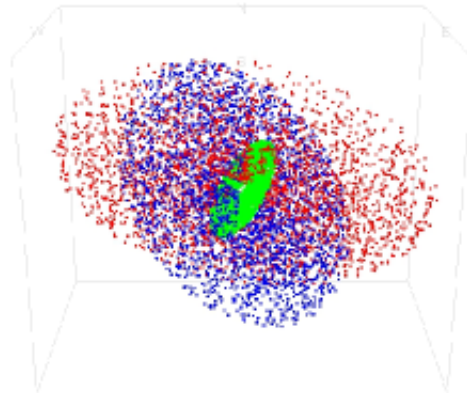
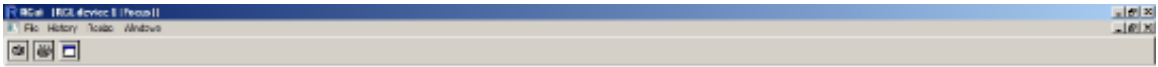


Figure C.6: Three-dimensional Fry plot with sectional fabric ellipses. Lower view is zoomed in from upper plot.

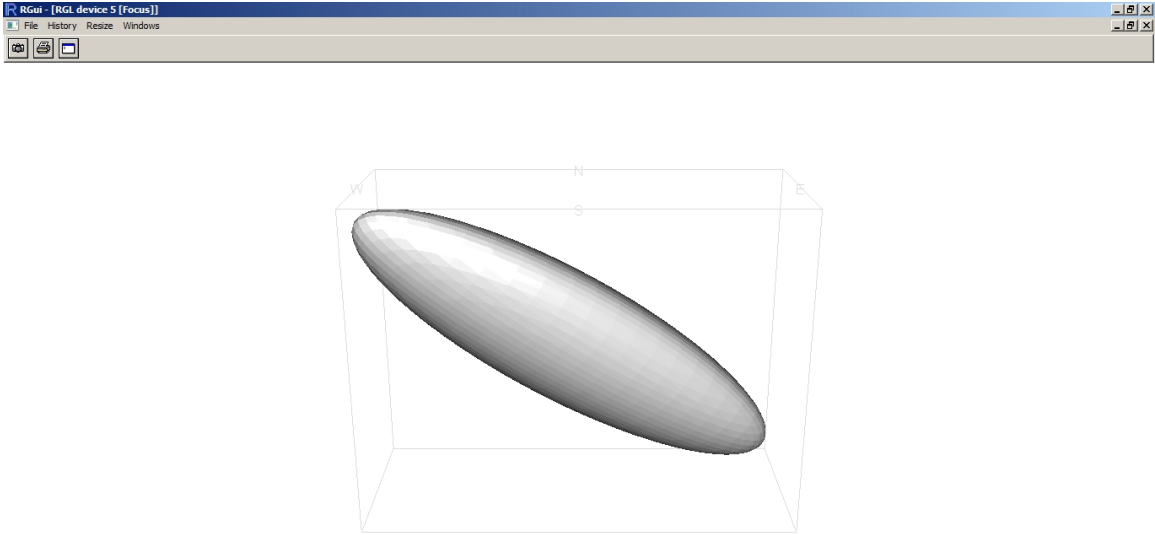


Figure C.7: Three-dimensional fitted ellipsoid calculated by the program Ellipsoid2003.

configured the scripts as outlined previously), a plethora of graphs and models will appear.

14. Activate the window containing the gray ellipsoid (Fig. C.7). You can use the mouse to navigate the ellipsoid and compare to the raw sectional data in the three dimensional Fry plot. Notice the geographic reference frame in both plots when comparing orientations.
15. Activate the window containing the Nadai plot (Fig. C.8). This diagram is generated by plotting the octahedral shear strain and Lode's parameter so that the ellipsoid distortion magnitude and shape (respectively) can be visualized. The synthetic data set is constructed from an idealized finite deformation corresponding to an octahedral shear strain of 1.33 and a Lode's parameter of -0.73. As such, the results presented in Figure C.8 are insignificantly less than the theoretical

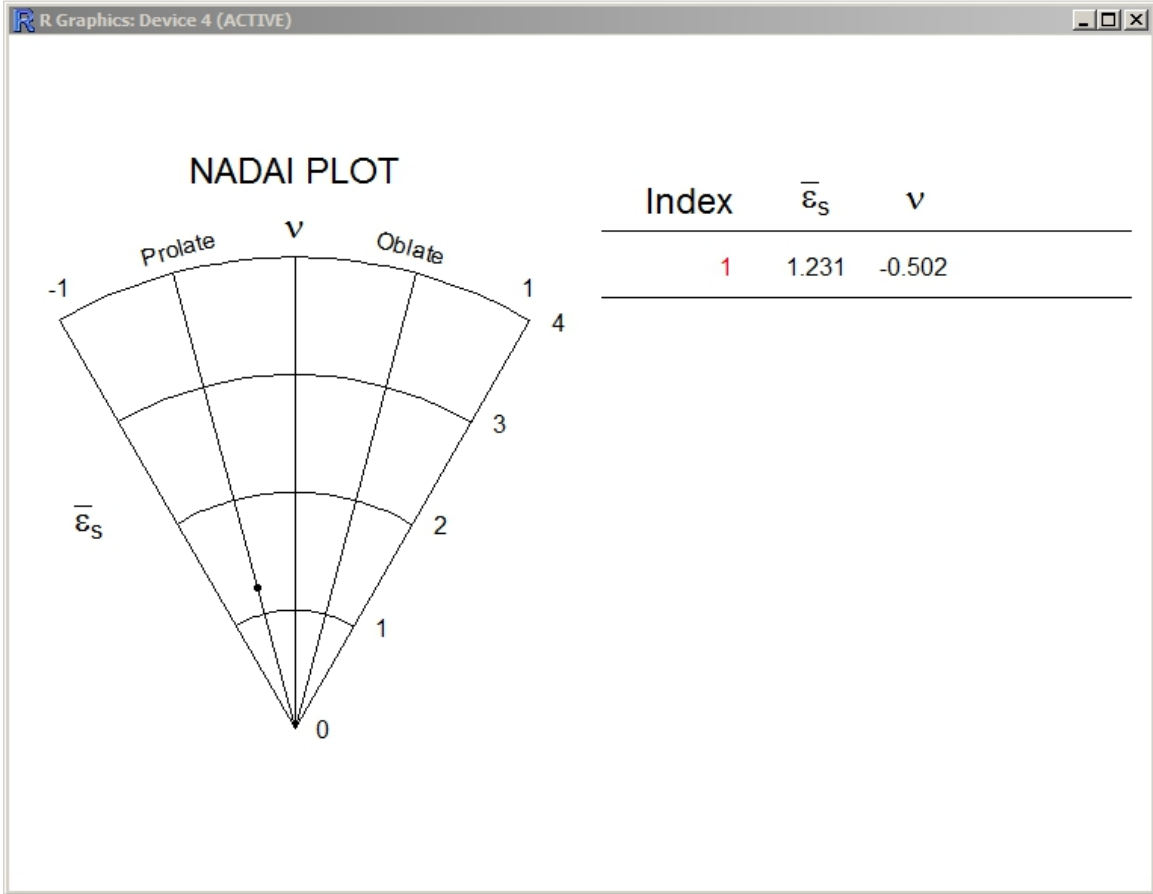


Figure C.8: Nadai plot corresponding to the fitted fabric ellipsoid.

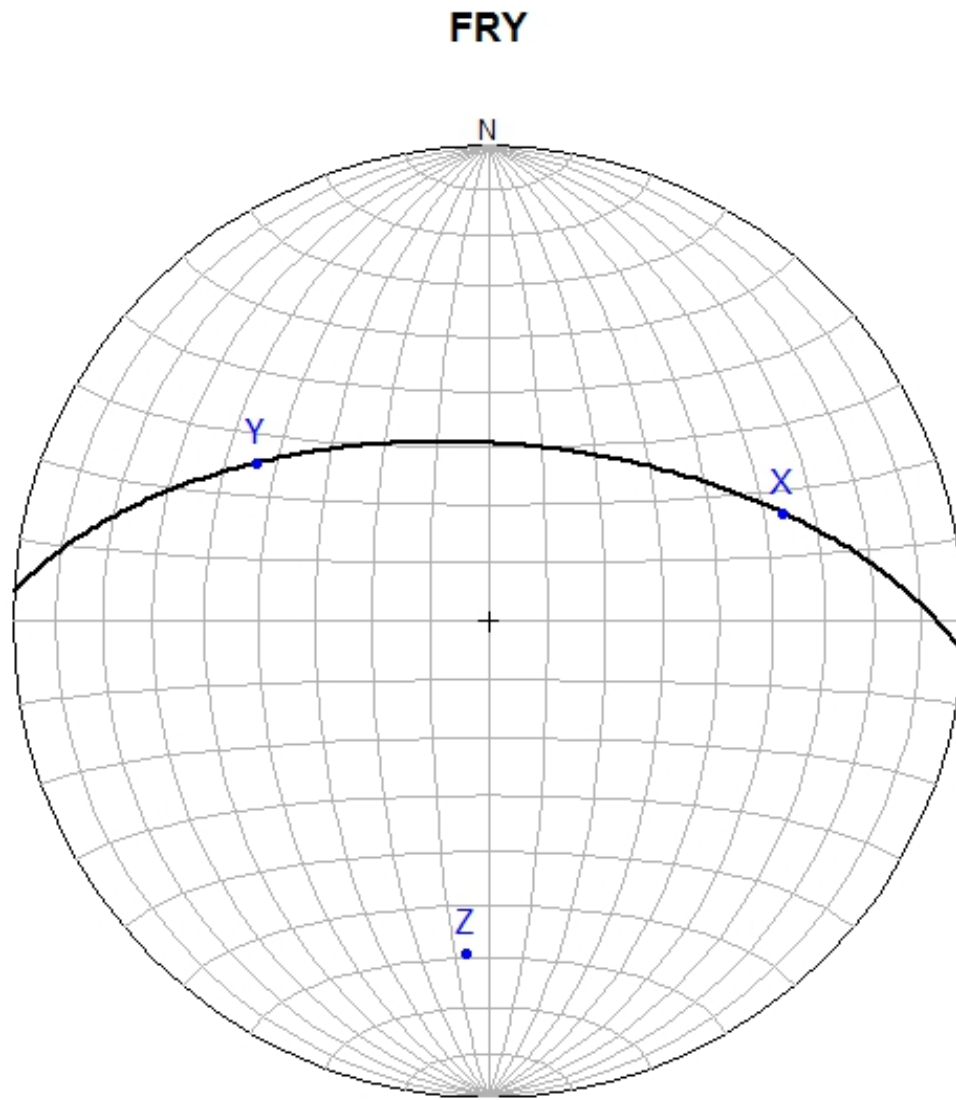
octahedral shear strain and slightly less prolate.

16. Finally, activate the window with the stereographic projection. This plot will contain four attitudes that correspond to the three principle ellipsoid axes and the XY principle plane. Furthermore, the numerical values to these points are listed at the bottom of the plot. In general, the XY plane should correspond to the fabric foliation. This may be less developed in more "L" dominated terrains with highly prolate strain symmetries. Therefore, cross checking this attitude to foliations measured in the field may be less reliable. However, the X axis (as a

proxy for the mineral stretching direction) should be much better constrained in prolate zones and may form a more robust measure of the discrepancy between measured fabric and calculated. The expected orientation of the XY plane for the synthetic data set is roughly  $281^\circ 55^\circ$  (strike and dip following right hand rule) and  $073^\circ 34^\circ$  (trend and plunge) for the X axis. Acceptable results should generally fall within the same quadrants. This plotting function depends heavily on code from the RFOC package (Lees 2011) and would not be possible without the tremendous effort of Jonathan M. Lees.

### **C.3.1 Concluding remarks**

As stated in the preface, the intention of this manual is twofold: allow users to better visualize three dimensional strain data; and introduce the statistical computing environment R. I must reiterate that the purpose of this procedure has never been, nor will likely ever be, designed to hide the code in a user friendly environment. By allowing the user to edit and run the scripts directly, I believe versatility and the potential for innovation is gained. I hope you see this as I do, and have attained some notion of the goals I have set to produce without too much frustration.



XY(S&D): 274 59 ; X(T&P): 70 34 ; Y(T&P): 304 40 ; Z(T&P): 184 31

Figure C.9: Stereographic projection of the principle fabric axes and XY plane for the fitted ellipsoid.



## Appendix D

# Three–dimensional synthetic model

### D.1 Introduction

This appendix contains raw tiles for the construction of a physical three–dimensional deformed conglomerate as modified from the synthetic dataset presented in Chapters 3 and 4. This model abides to the conservation of volume such that the section area of each ellipse was initially equal. This model represents a homogeneously deformed medium under general constrictional coaxial flow. This dataset is intended for use in error analysis of various strain techniques, as well as a general teaching tool such that students may better visualize three–dimensional deformation. Table D.1 contains the attitudes used in both the error analysis of Chapter 3 and the synthetic dataset in Chapter 4.

Table D.1: Sectional orientations following right hand rule convention to reorient a physical model of the synthetic dataset implemented in the FRY3D tutorial

<b>Section</b>	<b>Strike</b>	<b>Dip</b>
XY	281	55
XZ	041	53
YZ	162	57

## D.2 Construction procedure

1. Purchase a robust cubic cardboard box with a length dimension of 12 inches. Using packaging tape, securely close the box openings. Make sure each face is as planer as possible.
2. Print (or photocopy) two sets of Figures D.1–D.12 such that you have 24 pages to construct six faces of four tiles each. With scissors cut precisely along the tile border for each page. Do not cut the small section tab at the top of each tile until after the model is finished.
3. Find tile XYA (Fig. D.1) and paste to the lower left quarter section of a face of the cardboard box.
4. Paste tile XYB (Fig. D.2) to the lower right side of the same face and repeat for the other two XY tiles (Figs. D.3 and D.3) continuing in a counterclockwise fashion. Keep the box in the same orientation as you started with.
5. Rotate the box  $90^\circ$  either direction along the maximum stretching axis in the XY plane (i.e. rotate to the left or right). Spin the box  $90^\circ$  about a vertical axis and repeat steps 3 and 4 for the XZ tile (Figs. D.5 – D.8). Do not rotate the box during this step.
6. Flip the box  $90^\circ$  away from you about a horizontal axis then spin the box  $90^\circ$  about a vertical axis.
7. Repeat the procedure in steps 3 and 4 for the YZ tiles.
8. Finally complete the other three faces such that the corresponding principle plane of strain is on the opposite face.

### D.3 Sectional tiles

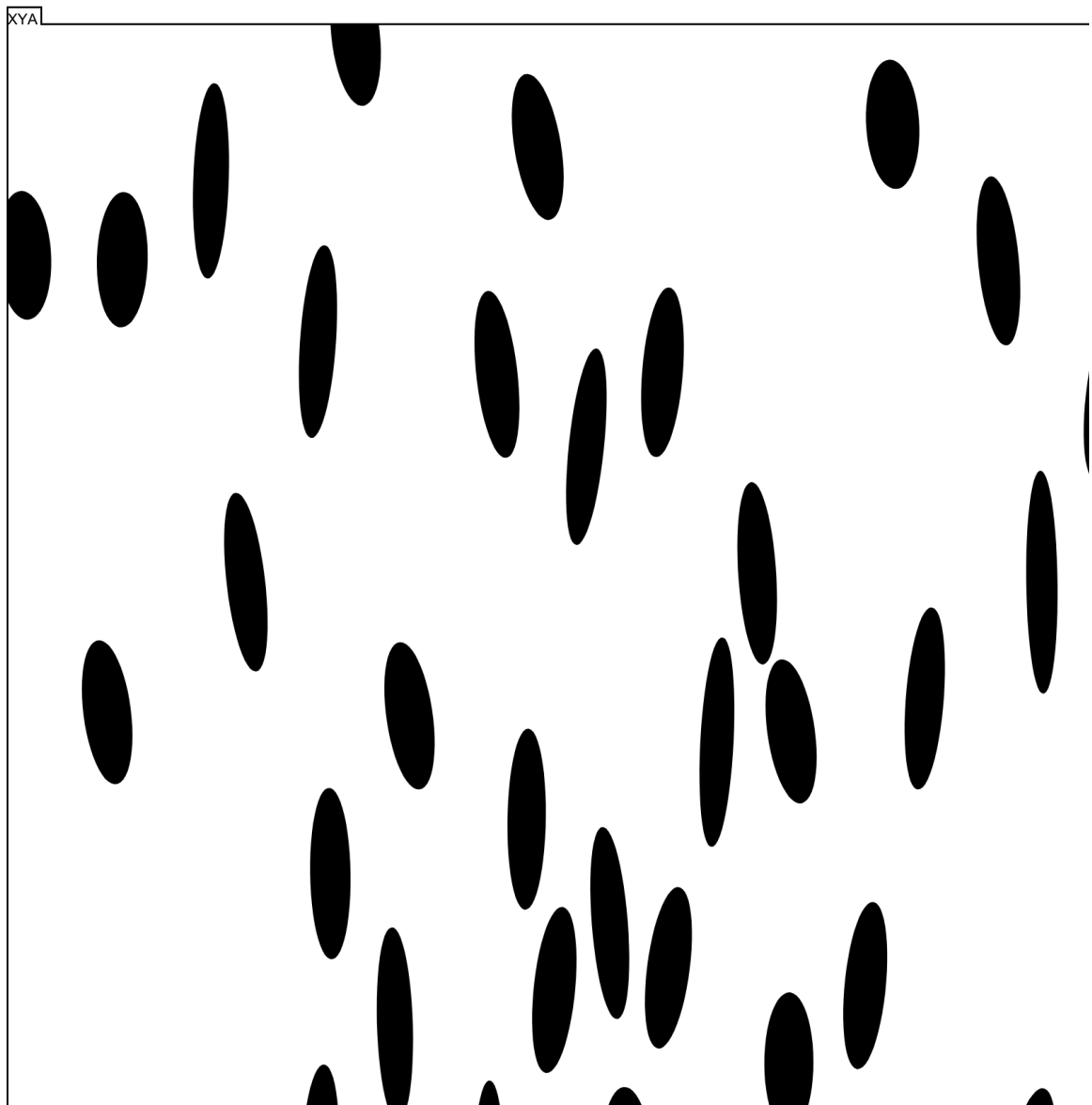


Figure D.1: Sectional tile A of the XY principle plane of strain.

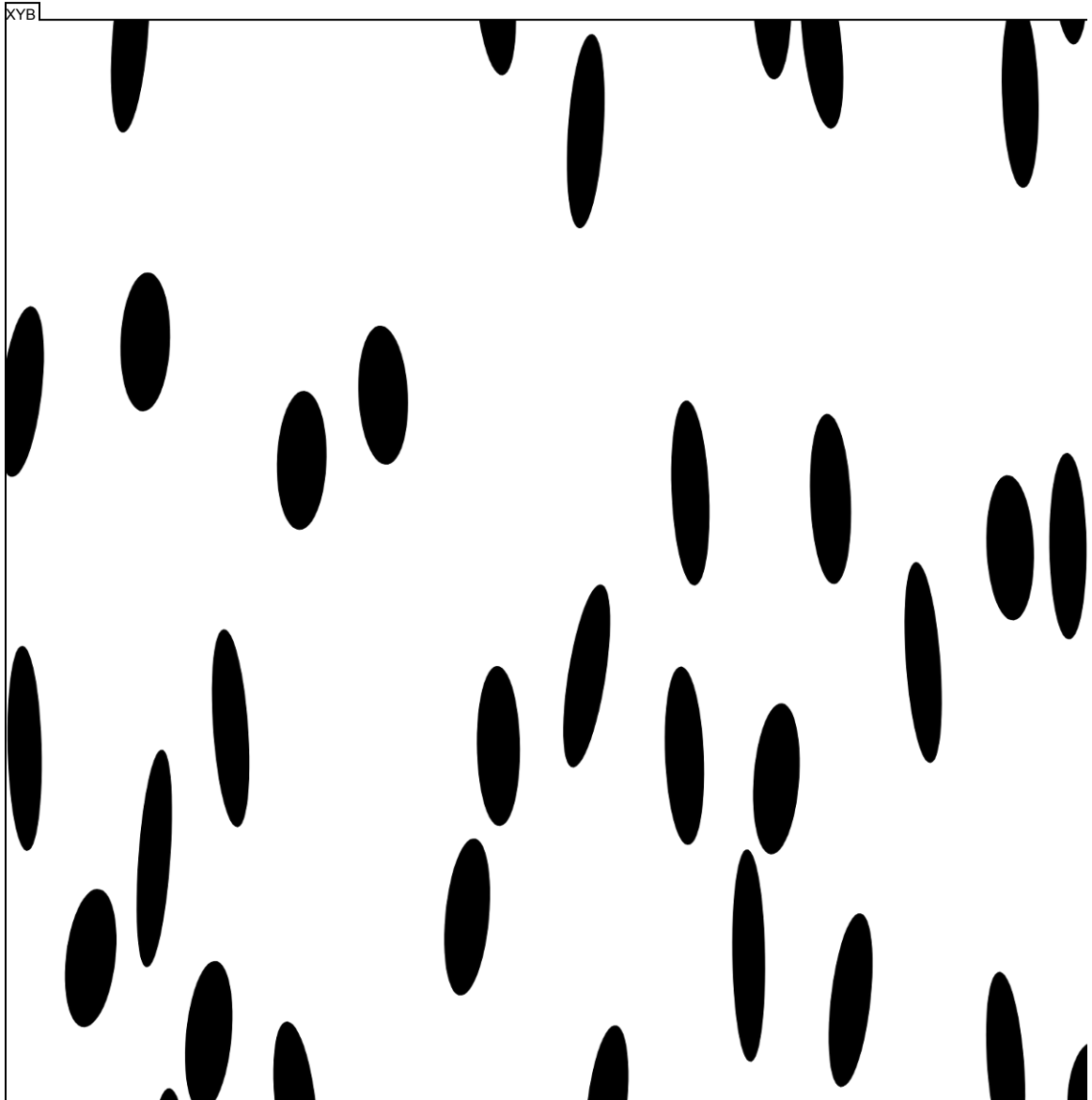


Figure D.2: Sectional tile B of the XY principle plane of strain.

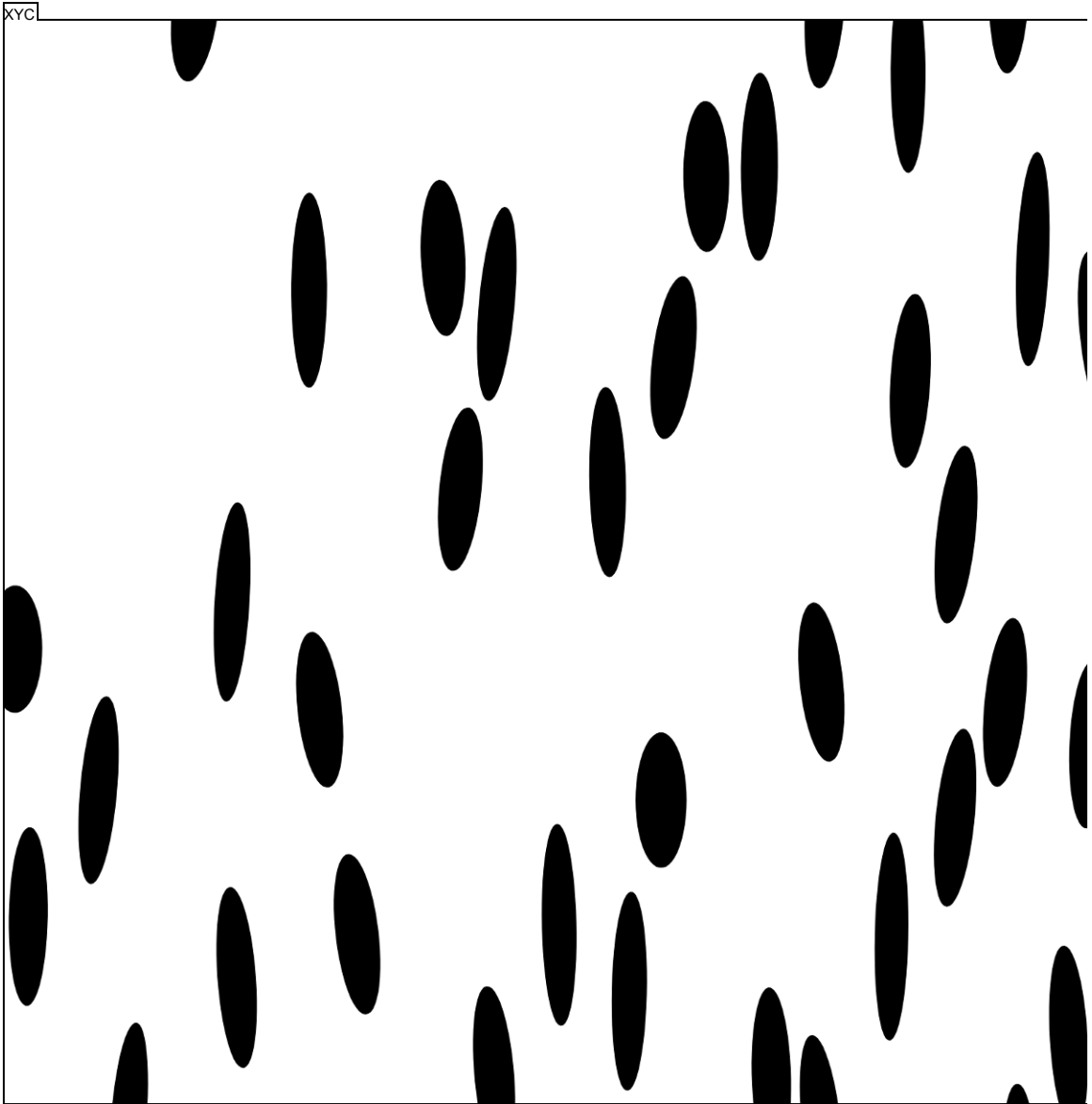


Figure D.3: Sectional tile C of the XY principle plane of strain.

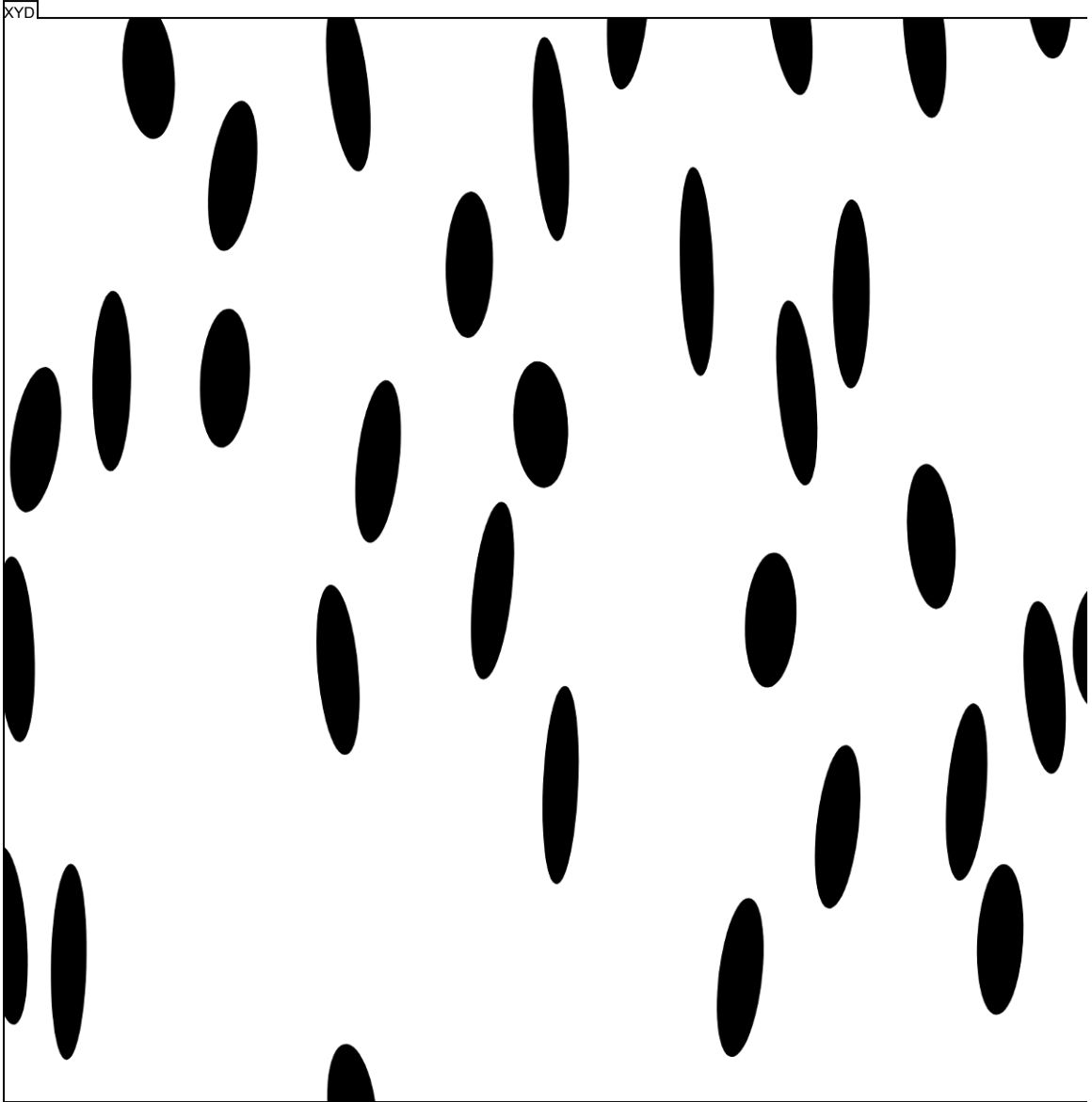


Figure D.4: Sectional tile D of the XY principle plane of strain.

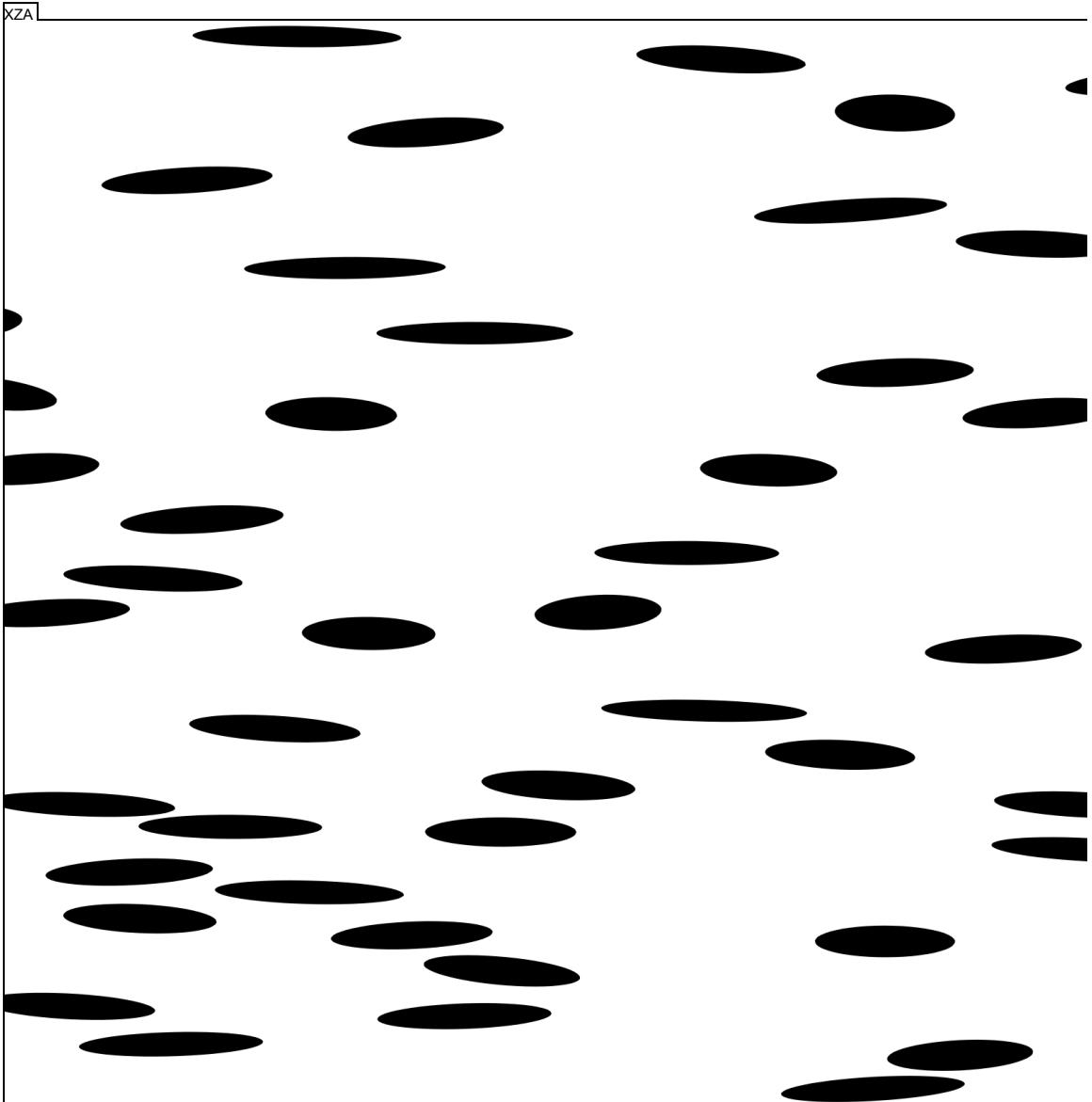


Figure D.5: Sectional tile A of the XZ principle plane of strain.

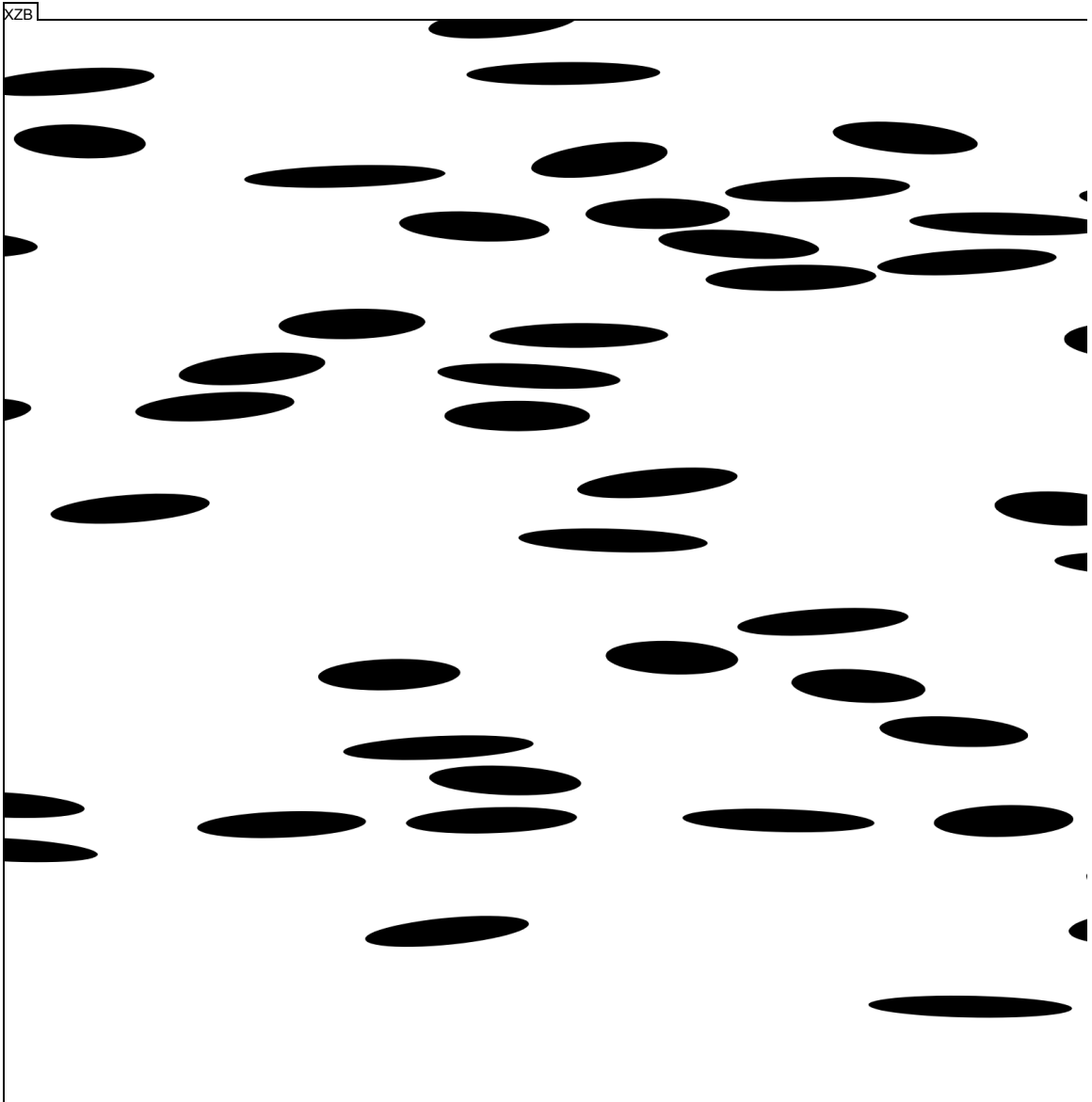


Figure D.6: Sectional tile B of the XZ principle plane of strain.



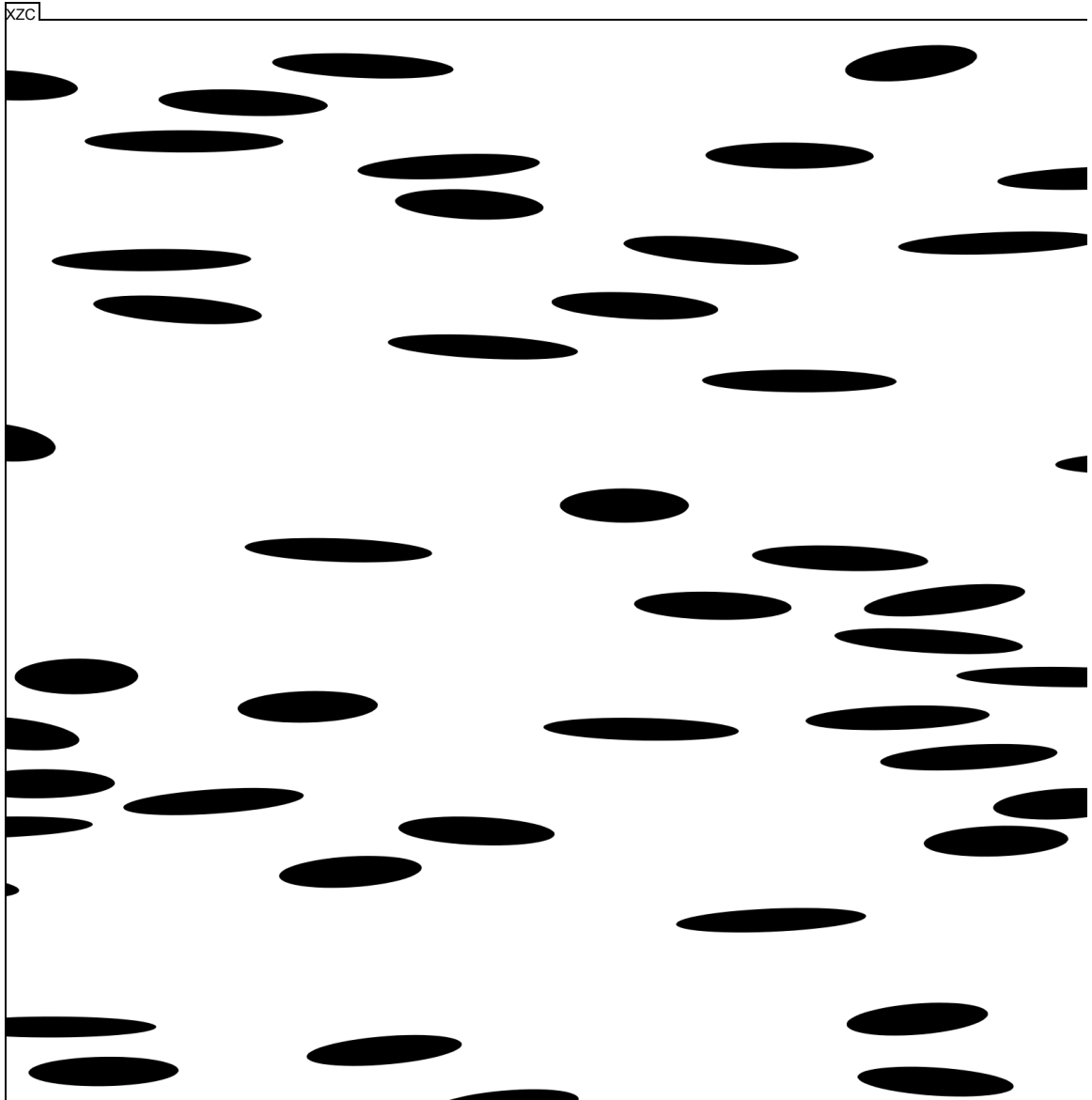


Figure D.7: Sectional tile C of the XZ principle plane of strain.

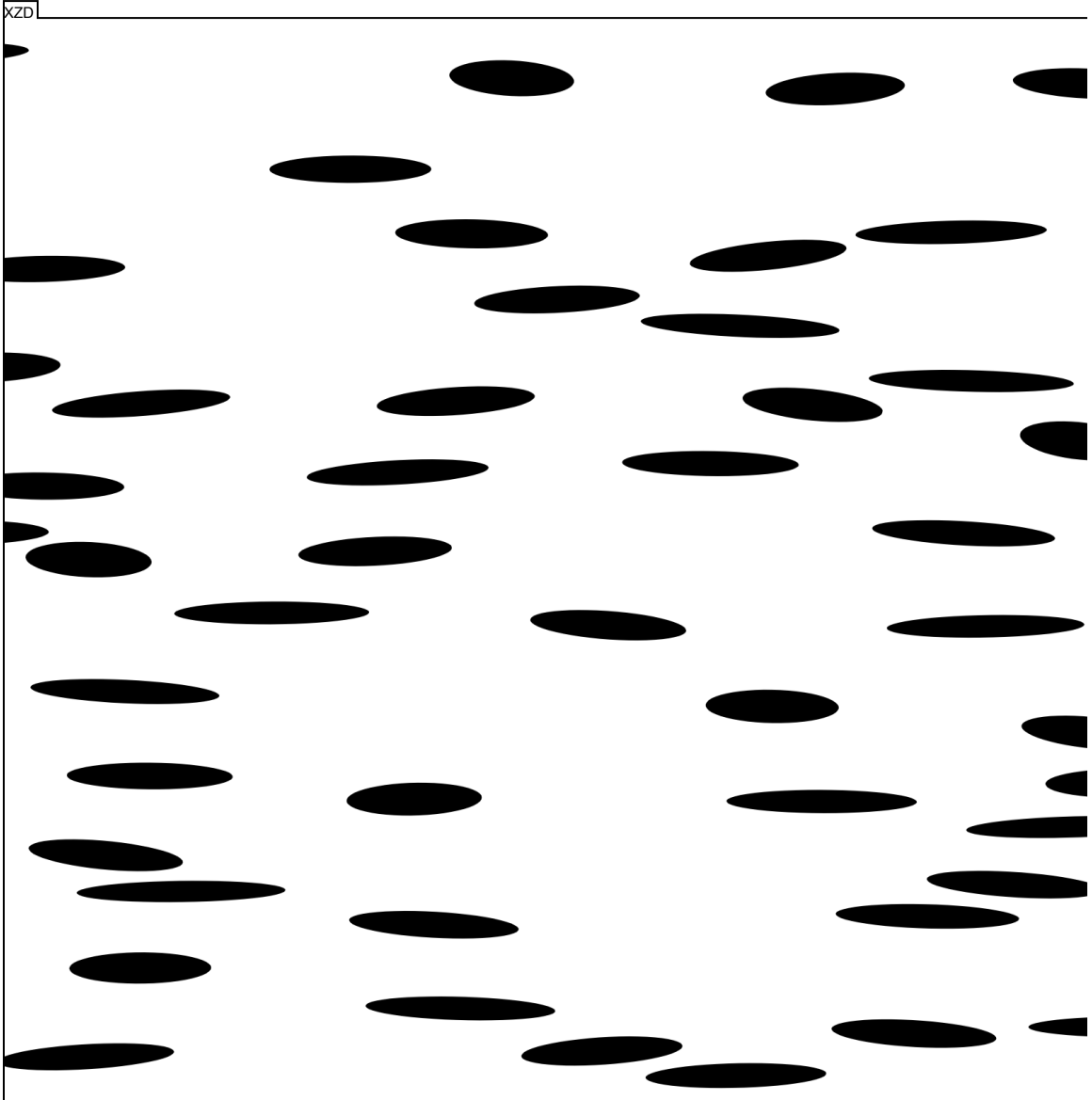


Figure D.8: Sectional tile D of the XZ principle plane of strain.

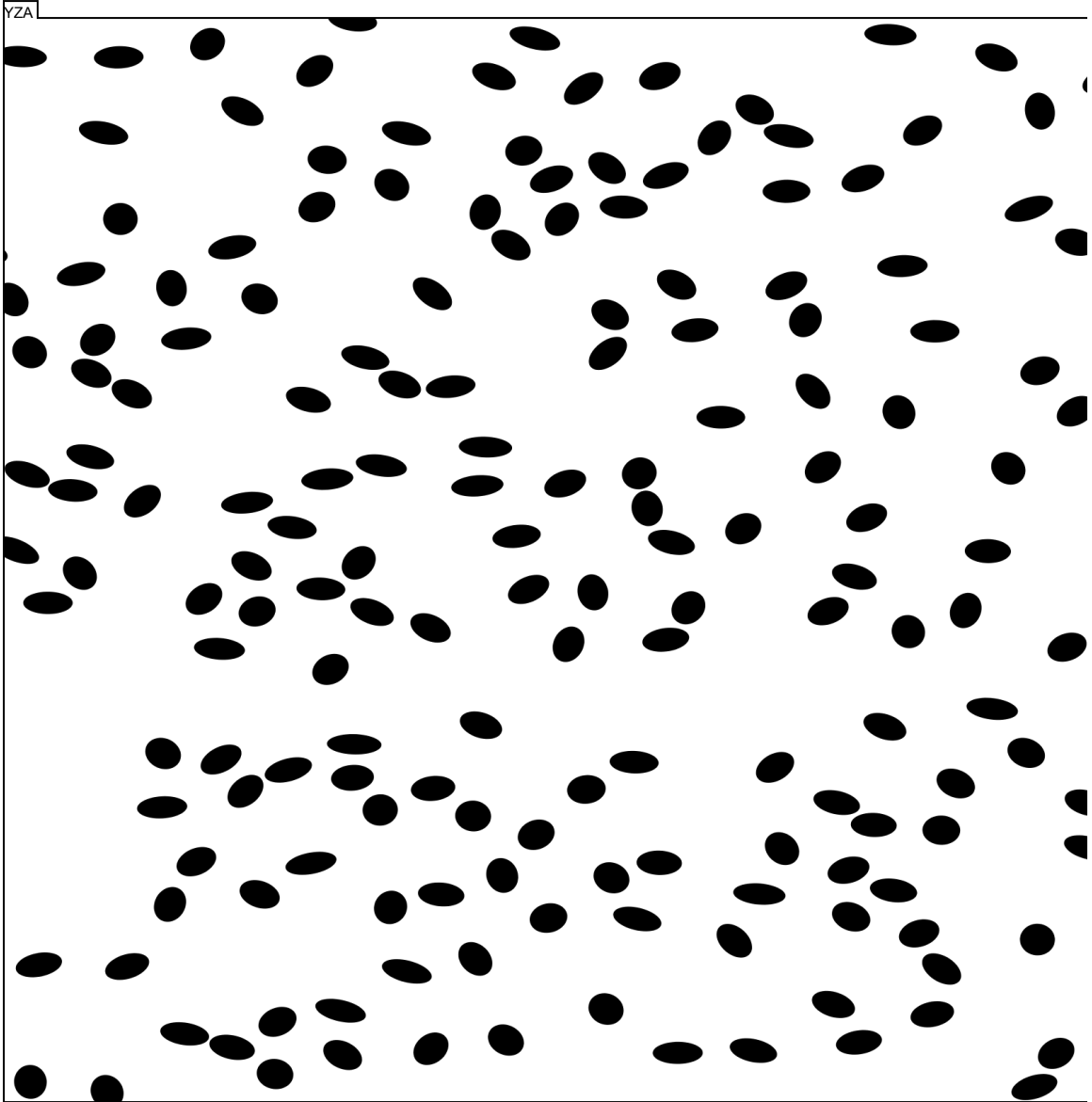


Figure D.9: Sectional tile A of the YZ principle plane of strain.

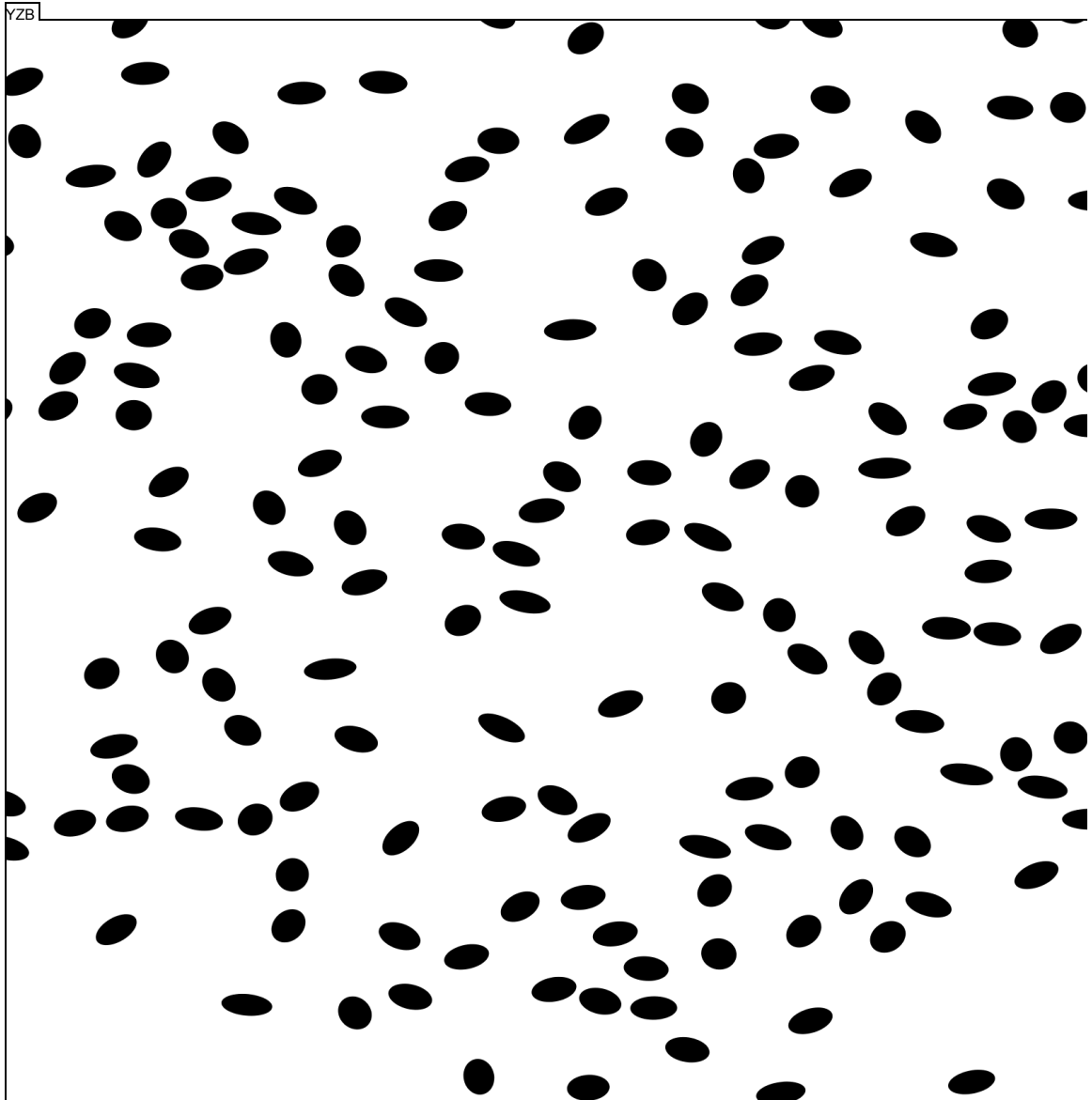


Figure D.10: Sectional tile B of the YZ principle plane of strain.

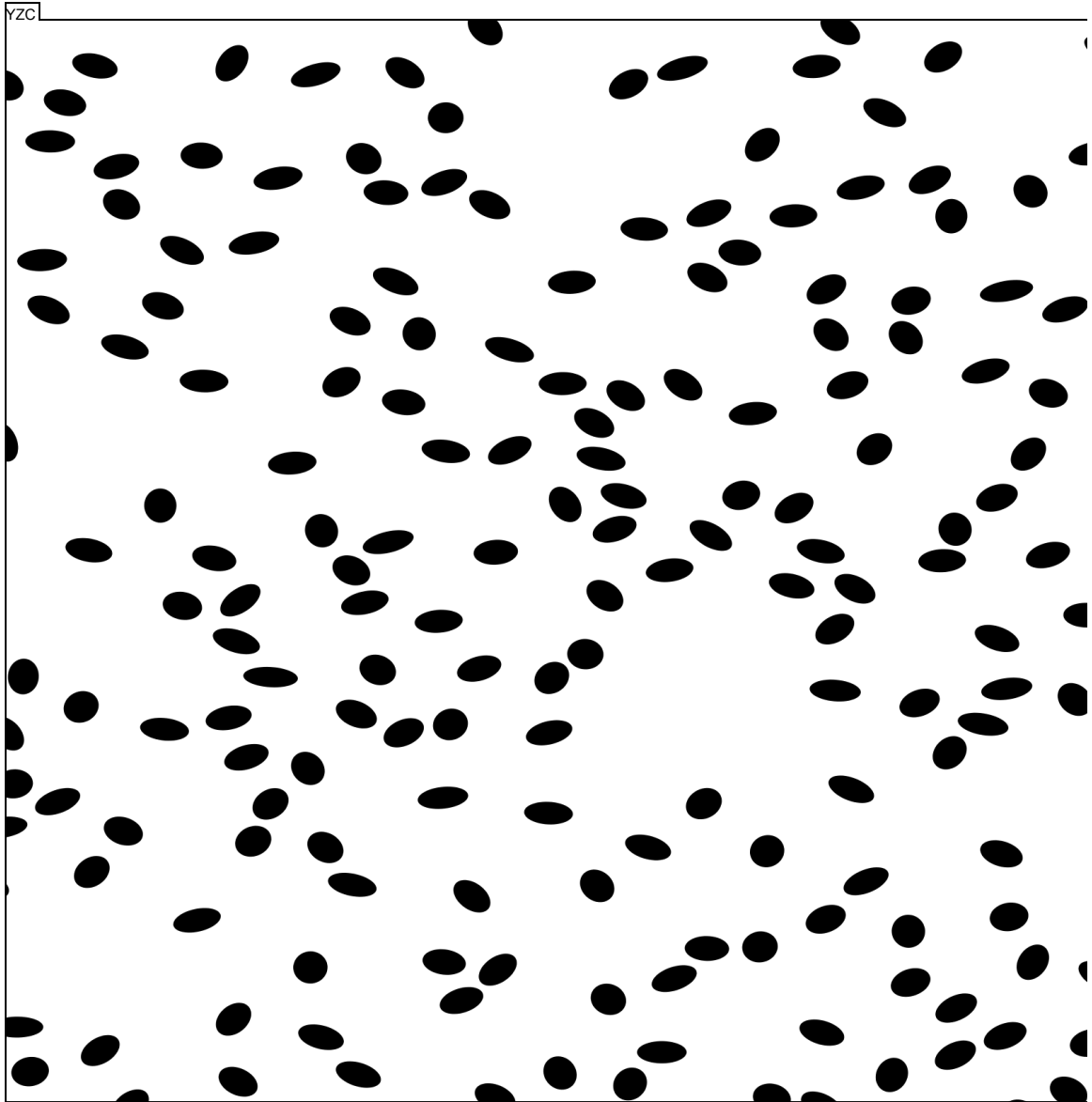


Figure D.11: Sectional tile C of the YZ principle plane of strain.

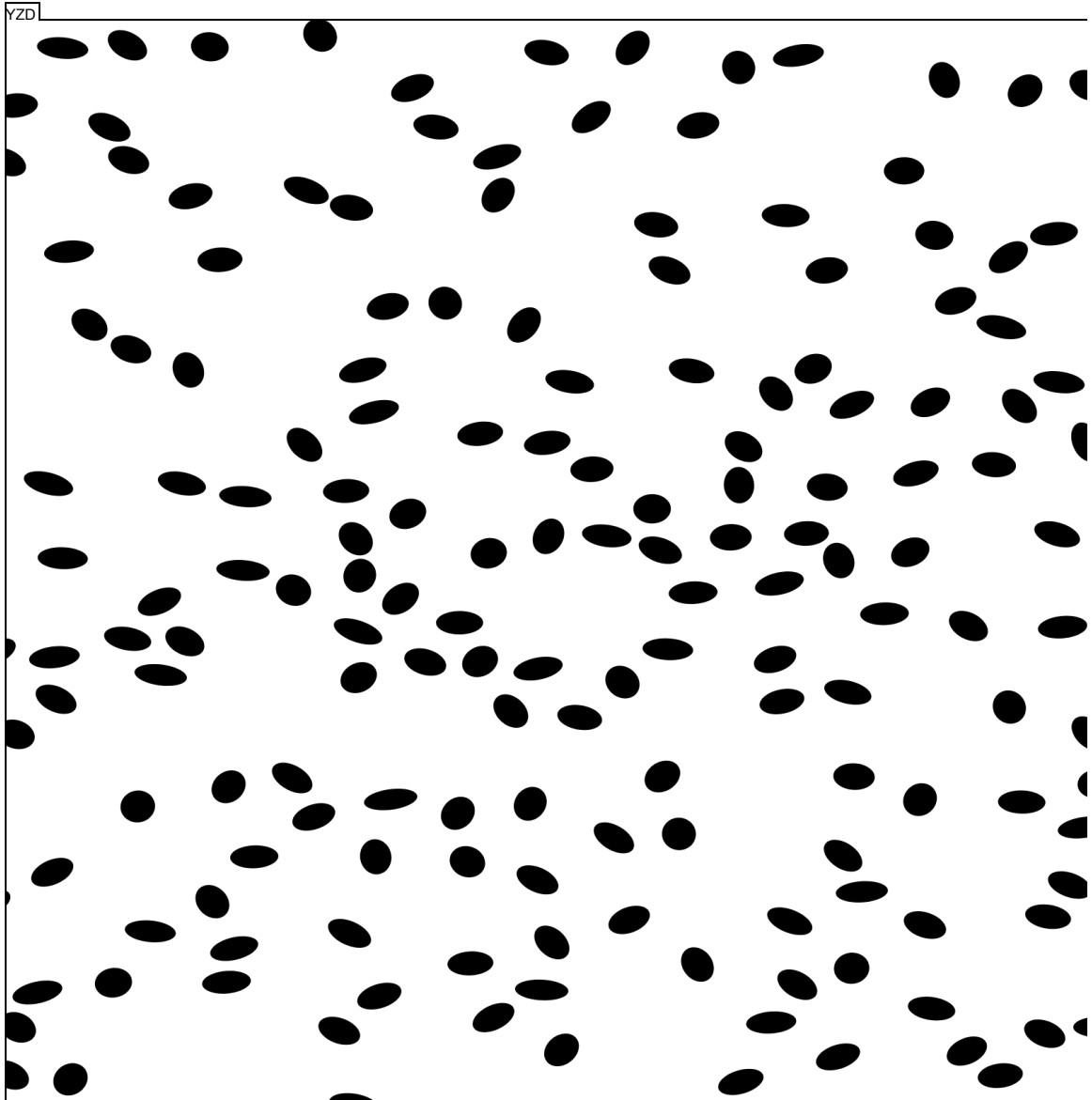


Figure D.12: Sectional tile D of the YZ principle plane of strain.

## Appendix E

# R Scripts

### E.1 Fry data setup and conversion

```
#####Script : FRY_SETUP
#####Author : Jeffrey R. Webber
#####Con : jrwebber@uvm.edu
###REQUIRED: Working directory set to the
master folder location
###Data : Extracted SAPE data,
location="PAR_EX"
###Data : Maintain hard return at end
of data list

#Set up libraries
library(sqldf)

#Define plot bound limitation factor
pBOUND<-2

#Load data into R from SAPE output: PLANE
A
raw1<-read.table(file="PAR_EX\\A.sda",
header=F)
names(raw1)=c("x","y","a","b","phi","
other")

#Load data into R from SAPE output: PLANE
B
raw2<-read.table(file="PAR_EX\\B.sda",
header=F)
names(raw2)=c("x","y","a","b","phi","
other")

#Load data into R from SAPE output: PLANE
C
raw3<-read.table(file="PAR_EX\\C.sda",
header=F)
names(raw3)=c("x","y","a","b","phi","
other")

###PLANE A CALCULATIONS
#Convert data to match cartesian coord.
from SAPE (origin correction)
xcoordA<-(raw1$y-min(raw1$y))
ycoordA<-(max(raw1$x)-raw1$x)

#Determine data length
lengthA<-length(xcoordA)

#Register variables for concatenation
xCatA<-NULL
yCatA<-NULL

#Run loop to create Fry coords.
loopCont<-0
while(loopCont<lengthA){
loopCont<-loopCont+1
#Center points based on iterative step
[loopCont] location=(0,0)
xA<-xcoordA [loopCont]-xcoordA
yA<-ycoordA [loopCont]-ycoordA

#Concatenate coord. lists
xCatA=c(xCatA,xA)
yCatA=c(yCatA,yA)
}

#Compile parameters into Waldron and
Wallace(2007) input
WaldWallA<-data.frame(xCatA,yCatA)
names(WaldWallA)=c("x","y")

#Remove stacked center values
WaldWallA<-sqldf("select *_ from _WaldWallA
_where_x_!=_'0'_and_y_!=_'0'")

#Calculate plot bounds
coordPosA<-round(max(c(max(xcoordA),max(
ycoordA)))/pBOUND,0)
```

```

coordNegA<-(-1)*coordPosA

#Run iterative loop to limit data
bufDat<-sqrt(2*((coordPosA)^2))
limDat<-length(WaldWallA$x)
while(limDat > 3000){
  #Create new radius such that field
  area is reduced by 10%
  bufDat<- sqrt(.9*(bufDat)^2)

  #Test coord distance WRT new radius
  VAL<-ifelse( sqrt((as.numeric(
    WaldWallA$x))^2+(as.numeric(
    WaldWallA$y))^2) < bufDat ,1,0)

  #Count number of valid values
  limDat<-sum(VAL)

  #Combine list of valid values with
  data set
  WaldWallA<-data.frame(WaldWallA$x,
    WaldWallA$y,VAL)
  names(WaldWallA)=c("x","y","val")

  #Select from data frame only valid
  coords.
  WaldWallA<-sqldf(" select *_from_
    WaldWallA_where_val_=1")
}

#Compile and name data frame
WaldWallA<-data.frame(WaldWallA$x,
  WaldWallA$y)
names(WaldWallA)=c("x","y")

WaldWallA$x<-as.numeric(WaldWallA$x)
WaldWallA$y<-as.numeric(WaldWallA$y)

##PLANE B CALCULATIONS
#Convert data to match cartesian coord.
from SAPE (origin correction)
xcoordB<-(raw2$y-min(raw2$y))
ycoordB<-(max(raw2$x)-raw2$x)

#Determine data length
lengthB<-length(xcoordB)

#Register variables for concatenation
xCatB<-NULL
yCatB<-NULL

#Run loop to create Fry coords.
loopCont<-0
while(loopCont<lengthB){
  loopCont<-loopCont+1
  #Center points based on iterative step
  [loopCont] location=(0,0)
  xB<-xcoordB [loopCont]-xcoordB
  yB<-ycoordB [loopCont]-ycoordB

  #Concatenate coord. lists
  xCatB=c(xCatB,xB)
  yCatB=c(yCatB,yB)
}

#Compile parameters into Waldron and
Wallace(2007) input
WaldWallB<-data.frame(xCatB,yCatB)
names(WaldWallB)=c("x","y")

#Remove stacked center values
WaldWallB<-sqldf(" select *_from_WaldWallB
  _where_x_!=_'0'_and_y_!=_'0'")

#Calculate plot bounds
coordPosB<-round(max(c(max(xcoordB),max(
  ycoordB)))/pBOUND,0)
coordNegB<-(-1)*coordPosB

#Run iterative loop to limit data
bufDat<-sqrt(2*((coordPosB)^2))
limDat<-length(WaldWallB$x)
while(limDat > 3000){
  #Create new radius such that field
  area is reduced by 10%
  bufDat<- sqrt(.9*(bufDat)^2)

  #Test coord distance WRT new radius
  VAL<-ifelse( sqrt((as.numeric(
    WaldWallB$x))^2+(as.numeric(
    WaldWallB$y))^2) < bufDat ,1,0)

  #Count number of valid values
  limDat<-sum(VAL)

  #Combine list of valid values with
  data set
  WaldWallB<-data.frame(WaldWallB$x,
    WaldWallB$y,VAL)
  names(WaldWallB)=c("x","y","val")

  #Select from data frame only valid
  coords.
  WaldWallB<-sqldf(" select *_from_
    WaldWallB_where_val_=1")
}

#Compile and name data frame
WaldWallB<-data.frame(WaldWallB$x,
  WaldWallB$y)
names(WaldWallB)=c("x","y")

WaldWallB$x<-as.numeric(WaldWallB$x)
WaldWallB$y<-as.numeric(WaldWallB$y)

##PLANE C CALCULATIONS
#Convert data to match cartesian coord.
from SAPE (origin correction)
xcoordC<-(raw3$y-min(raw3$y))
ycoordC<-(max(raw3$x)-raw3$x)

#Determine data length
lengthC<-length(xcoordC)

#Register variables for concatenation
xCatC<-NULL
yCatC<-NULL

#Run loop to create Fry coords.
loopCont<-0

```



```

while(loopCont<lengthC){
  loopCont<-loopCont+1
  #Center points based on iterative step
  [loopCont] location=(0,0)
  xC<-xcoordC[loopCont]-xcoordC
  yC<-ycoordC[loopCont]-ycoordC

  #Concatenate coord. lists
  xCatC=c(xCatC,xC)
  yCatC=c(yCatC,yC)
}

#Compile parameters into Waldron and
Wallace(2007) input
WaldWallC<-data.frame(xCatC,yCatC)
names(WaldWallC)=c("x","y")

#Remove stacked center values
WaldWallC<-sqldf("select *_ from _WaldWallC
  _where _x_!=_ '0' _and _y_!=_ '0'")

#Calculate plot bounds
coordPosC<-round(max(c(max(xcoordC),max(
  ycoordC)))/pBOUND,0)
coordNegC<-(-1)*coordPosC

#Run iterative loop to limit data
bufDat<-sqrt(2*((coordPosC)^2))
limDat<-length(WaldWallC$x)
while(limDat > 3000){
  #Create new radius such that field
  area is reduced by 10%
  bufDat<- sqrt(.9*(bufDat)^2)

  #Test coord distance WRT new radius
  VAL<-ifelse( sqrt((as.numeric(
    WaldWallC$x)^2+(as.numeric(
    WaldWallC$y)^2) < bufDat,1,0)

  #Count number of valid values
  limDat<-sum(VAL)

  #Combine list of valid values with
  data set

  WaldWallC<-data.frame(WaldWallC$x,
    WaldWallC$y,VAL)
  names(WaldWallC)=c("x","y","val")

  #Select from data frame only valid
  coords.
  WaldWallC<-sqldf("select *_ from _
    WaldWallC_where _val_=_1")
}

#Compile and name data frame
WaldWallC<-data.frame(WaldWallC$x,
  WaldWallC$y)
names(WaldWallC)=c("x","y")
WaldWallC$x<-as.numeric(WaldWallC$x)
WaldWallC$y<-as.numeric(WaldWallC$y)

#Save data for use in Fry Waldron and
Wallace(2007)

```

```

write.table(WaldWallA, file="ANALYSIS\\FRY
  \\INPUT\\A.txt", col.names = F, append=
  F, sep = "\t", quote=F, row.names=F)
write.table(WaldWallB, file="ANALYSIS\\FRY
  \\INPUT\\B.txt", col.names = F, append=
  F, sep = "\t", quote=F, row.names=F)
write.table(WaldWallC, file="ANALYSIS\\FRY
  \\INPUT\\C.txt", col.names = F, append=
  F, sep = "\t", quote=F, row.names=F)
#End of Script#

```

## E.2 $R_f/\phi$ data setup and con- version

```

####Script : RFPHI_SETUP
####Author : Jeffrey R. Webber
####Con : jrwebber@uwm.edu
###REQUIRED: Working directory set to the
master folder location
###Data : Extracted SAPE data,
location="PAR_EX"
###Data : Maintain hard return at end
of data list

#Load data into R from SAPE output: PLANE
A
raw1<-read.table(file="PAR_EX\\A.sda",
  header=F)
names(raw1)=c("x","y","a","b","phi","
  other")

#Load data into R from SAPE output: PLANE
B
raw2<-read.table(file="PAR_EX\\B.sda",
  header=F)
names(raw2)=c("x","y","a","b","phi","
  other")

#Load data into R from SAPE output: PLANE
C
raw3<-read.table(file="PAR_EX\\C.sda",
  header=F)
names(raw3)=c("x","y","a","b","phi","
  other")

###PLANE A CALCULATIONS
#Convert data to match cartesian coord.
from SAPE (origin correction)
xcoord1<-(raw1$y-min(raw1$y))
ycoord1<-(max(raw1$x)-raw1$x)

#Redefine fitted ellipse axes
aAxis1<-raw1$a
bAxis1<-raw1$b

#Calculate axial ratio
axRat1<-(aAxis1/bAxis1)

#Calculate phi in radians for standard
math convention
phiDeg1<-raw1$phi
phiRad1<-phiDeg1*(pi/180)

```

```

#Add Phi values in RHR clockwise positive
  convention (standard geographic (
    Ellipsoid) convention)
phiDegGEO1<-ifelse(raw1$phi>0, 180-raw1$
  phi, raw1$phi*-1)
phiRadGEO1<-phiDegGEO1*(pi/180)

#Compile parameters into Chew(2003) input
chewA<-data.frame(aAxis1 , bAxis1 , phiDeg1*
  (-1))

##PLANE B CALCULATIONS
#Convert data to match cartesian coord.
  from SAPE (origin correction)
xcoord2<-(raw2$y-min(raw2$y))
ycoord2<-((max(raw2$x)-raw2$x)

#Redefine fitted ellipse axes
aAxis2<-raw2$a
bAxis2<-raw2$b

#Calculate axial ratio
axRat2<-(aAxis2/bAxis2)

#Calculate phi in radians for standard
  math convention
phiDeg2<-raw2$phi
phiRad2<-phiDeg2*(pi/180)

#Add Phi values in RHR clockwise positive
  convention (standard geographic (
    Ellipsoid) convention)
phiDegGEO2<-ifelse(raw2$phi>0, (raw2$phi*
  -1)+180, raw2$phi*-1)
phiRadGEO2<-phiDegGEO2*(pi/180)

#Compile parameters into Chew(2003) input
chewB<-data.frame(aAxis2 , bAxis2 , phiDeg2*
  (-1))

##PLANE C CALCULATIONS
#Convert data to match cartesian coord.
  from SAPE (origin correction)
xcoord3<-(raw3$y-min(raw3$y))
ycoord3<-((max(raw3$x)-raw3$x)

#Redefine fitted ellipse axes
aAxis3<-raw3$a
bAxis3<-raw3$b

#Calculate axial ratio
axRat3<-(aAxis3/bAxis3)

#Calculate phi in radians for standard
  math convention
phiDeg3<-raw3$phi
phiRad3<-phiDeg3*(pi/180)

#Add Phi values in RHR clockwise positive
  convention (standard geographic (
    Ellipsoid) convention)
phiDegGEO3<-ifelse(raw3$phi>0, (raw3$phi*
  -1)+180, raw3$phi*-1)

```

```

phiRadGEO3<-phiDegGEO3*(pi/180)

#Compile parameters into Chew(2003) input
chewC<-data.frame(aAxis3 , bAxis3 , phiDeg3*
  (-1))

#Save data for use in Rf/Phi Chew (2003)
write.table(chewA, file="ANALYSIS\\RFPHI\\
  INPUT\\A.txt", col.names = F, append=F,
  sep = "\t", quote=F, row.names=F)
write.table(chewB, file="ANALYSIS\\RFPHI\\
  INPUT\\B.txt", col.names = F, append=F,
  sep = "\t", quote=F, row.names=F)
write.table(chewC, file="ANALYSIS\\RFPHI\\
  INPUT\\C.txt", col.names = F, append=F,
  sep = "\t", quote=F, row.names=F)
#End of Script#

```

## E.3 Standardized Fry plot

```

####Script : FRY_PLOT
####Author : Jeffrey R. Webber
####Con : jrwebber@uvm.edu
####REQUIRED: Working directory set to the
  master folder location
###Data : Extracted SAPE data,
  location="PAR_EX"
###Data : Compiled field data in file
  ="NOTES\\FIELD_DAT.txt"
###Data : Maintain hard return at end
  of data lists

##Set up libraries
library(sqldf)
library(gplots)
library(rgl)

#Load data into R from SAPE output: PLANE
  A
raw1<-read.table(file="PAR_EX\\A.sda",
  header=F)
names(raw1)=c("x", "y", "a", "b", "phi", "
  other")

#Load data into R from SAPE output: PLANE
  B
raw2<-read.table(file="PAR_EX\\B.sda",
  header=F)
names(raw2)=c("x", "y", "a", "b", "phi", "
  other")

#Load data into R from SAPE output: PLANE
  C
raw3<-read.table(file="PAR_EX\\C.sda",
  header=F)
names(raw3)=c("x", "y", "a", "b", "phi", "
  other")

#Load field data
fDat<-read.table(file="RAW_DATA\\FIELD_
  DAT.txt", header=T, sep='\\t')

##PLANE A CALCULATIONS

```

```

#Convert data to match cartesian coord.
  from SAPE (origin correction)
xcoordA<-(raw1$y-min(raw1$y))
ycoordA<-(max(raw1$x)-raw1$x)

#Determine data length
lengthA<-length(xcoordA)

#Register variables for concatenation
xCatA<-NULL
yCatA<-NULL

#Set loop control

#Run loop to create Fry coords.
loopCont<-0
while(loopCont<lengthA){
  loopCont<-loopCont+1
  #Center points based on iterative step
  [loopCont] location=(0,0)
  xA<-xcoordA [loopCont]-xcoordA
  yA<-ycoordA [loopCont]-ycoordA

  #Concatenate coord. lists
  xCatA=c(xCatA,xA)
  yCatA=c(yCatA,yA)
}

#Compile coords
fryA<-data.frame(xCatA,yCatA)
names(fryA)=c("x","y")

#Remove stacked center values
fryA<-sqldf("select *_ from fryA where x_!
  =_ '0' _and_ y_! =_ '0'")

##PLANE B CALCULATIONS
#Convert data to match cartesian coord.
  from SAPE (origin correction)
xcoordB<-(raw2$y-min(raw2$y))
ycoordB<-(max(raw2$x)-raw2$x)

#Determine data length
lengthB<-length(xcoordB)

#Register variables for concatenation
xCatB<-NULL
yCatB<-NULL

#Run loop to create Fry coords.
loopCont<-0
while(loopCont<lengthB){
  loopCont<-loopCont+1
  #Center points based on iterative step
  [loopCont] location=(0,0)
  xB<-xcoordB [loopCont]-xcoordB
  yB<-ycoordB [loopCont]-ycoordB

  #Concatenate coord. lists
  xCatB=c(xCatB,xB)
  yCatB=c(yCatB,yB)
}

#Compile coords
fryB<-data.frame(xCatB,yCatB)
names(fryB)=c("x","y")

#Remove stacked center values
fryB<-sqldf("select *_ from fryB where x_!
  =_ '0' _and_ y_! =_ '0'")

##PLANE C CALCULATIONS
#Convert data to match cartesian coord.
  from SAPE (origin correction)
xcoordC<-(raw3$y-min(raw3$y))
ycoordC<-(max(raw3$x)-raw3$x)

#Determine data length
lengthC<-length(xcoordC)

#Register variables for concatenation
xCatC<-NULL
yCatC<-NULL

#Run loop to create Fry coords.
loopCont<-0
while(loopCont<lengthC){
  loopCont<-loopCont+1
  #Center points based on iterative step
  [loopCont] location=(0,0)
  xC<-xcoordC [loopCont]-xcoordC
  yC<-ycoordC [loopCont]-ycoordC

  #Concatenate coord. lists
  xCatC=c(xCatC,xC)
  yCatC=c(yCatC,yC)
}

#Compile coords.
fryC<-data.frame(xCatC,yCatC)
names(fryC)=c("x","y")

#Remove stacked center values
fryC<-sqldf("select *_ from fryC where x_!
  =_ '0' _and_ y_! =_ '0'")

#Read in compiled parameters of the fitted
  ellipses
fitPar<-read.table(file="ANALYSIS\\FRY\\
  OUTPUT\\FRY_DAT.txt",header=T)

#Calculate each fitted ellipse max radius
winParA<-fitPar$rs[1] * fitPar$radius[1]
winParB<-fitPar$rs[2] * fitPar$radius[2]
winParC<-fitPar$rs[3] * fitPar$radius[3]

#Determine max radius and add a 25%
  buffer
winPar<-max(winParA, winParB, winParC)*1.25

#Establish tests
testA<-ifelse(sqrt((as.numeric(fryA$x))
  ^2+(as.numeric(fryA$y))^2)>winPar
  ,0,1)
testB<-ifelse(sqrt((as.numeric(fryB$x))
  ^2+(as.numeric(fryB$y))^2)>winPar
  ,0,1)

```



```

textplot(elliPar1 , halign="center" ,
  valign="top" ,show.rownames=F)
title (" Compiled_Parameters_for_ELLIPSOID_
  with_Ratios")
textplot(elliPar2 , halign="center" ,
  valign="top" ,show.rownames=F)
title (" Compiled_Parameters_for_ELLIPSOID_
  with_Lengths")

#Save compiled data
dev.copy(pdf,"MODEL\\ELLIPSOID\\INPUT\\
  FRY_COMPILE.pdf",useDingbats=F)
dev.off()

##Design cool plots of data
x11()
par(mfrow=c(2,3),mar=c(5.1,4.1,4.1,1))

#Plot Fry data while maintaining same
  scale between plots and add ellipses
plot(fryA,xlim=c(-winPar,winPar),ylim=c(-
  winPar,winPar),asp=1,pch=20,axes=F,
  main="A",
frame.plot=F,xlab=paste("phi_=",round(
  AgeoPhi,0)),ylab=NA)
ellipse(hlaxa=winParA,hlaxb=fitPar$radius
  [1],theta=(fitPar$phi[1])*(pi/180),n
  =100,sty="red")
ellipse(hlaxa=winPar*1.05,hlaxb=winPar*
  1.05,theta=0,n=100)
plot(fryB,xlim=c(-winPar,winPar),ylim=c(-
  winPar,winPar),asp=1,pch=20,axes=F,
  main="B",
frame.plot=F,xlab=paste("phi_=",round(
  BgeoPhi,0)),ylab=NA)
ellipse(hlaxa=winParB,hlaxb=fitPar$radius
  [2],theta=(fitPar$phi[2])*(pi/180),n
  =100,sty="red")
ellipse(hlaxa=winPar*1.05,hlaxb=winPar*
  1.05,theta=0,n=100,)
plot(fryC,xlim=c(-winPar,winPar),ylim=c(-
  winPar,winPar),asp=1,pch=20,axes=F,
  main="C",
frame.plot=F,xlab=paste("phi_=",round(
  CgeoPhi,0)),ylab=NA)
ellipse(hlaxa=winParC,hlaxb=fitPar$radius
  [3],theta=(fitPar$phi[3])*(pi/180),n
  =100,sty="red")
ellipse(hlaxa=winPar*1.05,hlaxb=winPar*
  1.05,theta=0,n=100)

#Add normalized ellipse A
plot(0,0,xlim=c(-2,2),ylim=c(-2,2),asp=1,
  axes=F,frame.plot=F,pch=20,xlab=NA,
  ylab=NA)
ellipse(hlaxa=sqrt(fitPar$rs[1])/2,hlaxb=
  sqrt(1/fitPar$rs[1])/2,theta=(fitPar$
  phi[1])*(pi/180),n=100)
text(0,-2,"Axial_Ratio:",adj=.5)
text(0,-2.5,fitPar$rs[1],adj=.5)
lines(x=c(-2,2),y=c(0,0))

#Add normalized ellipse B
plot(0,0,xlim=c(-2,2),ylim=c(-2,2),asp=1,
  axes=F,frame.plot=F,pch=20,xlab=NA,
  ylab=NA)
ellipse(hlaxa=sqrt(fitPar$rs[3])/2,hlaxb=
  sqrt(1/fitPar$rs[3])/2,theta=(fitPar$
  phi[3])*(pi/180),n=100)
text(0,-2,"Axial_Ratio:",adj=.5)
text(0,-2.5,fitPar$rs[3],adj=.5)
lines(x=c(-2,2),y=c(0,0))

#Save plot
dev.copy(pdf,"ANALYSIS\\FRY\\OUTPUT\\
  SECTIONAL_PLOT_FRY.pdf",useDingbats=F
  )
dev.off()

#Plot 3D Fry with fitted ellipses#
ellipse3d <-function(hlaxa = 1, hlaxb =
  1, theta = 0, xc = 0, yc = 0, npoints
  = 100, sty="black",
  ...)
{
  a <- seq(0, 2 * pi, length = npoints
  + 1)
  x <- hlaxa * cos(a)
  y <- hlaxb * sin(a)
  alpha <- angle(x, y)
  rad <- sqrt(x^2 + y^2)
  xp <- rad * cos(alpha + theta) + xc
  yp <- rad * sin(alpha + theta) + yc
  zp <- seq(0,0,len = npoints + 1)
  return(cbind(xp, yp, zp))
}
angle <-function(x, y)
{
  angle2 <- function(xy) {
    x <- xy[1]
    y <- xy[2]
    if (x > 0) {
      atan(y/x)
    }
    else {
      if (x < 0 & y != 0) {
        atan(y/x) + sign(y) * pi
      }
      else {
        if (x < 0 & y == 0) {
          pi
        }
        else {
          if (y != 0) {
            (sign(y) * pi)/2
          }
        }
      }
    }
  }
}

```



```

#Redefine fitted ellipse axes
aAxis1<-raw1$a
bAxis1<-raw1$b

#Calculate axial ratio
axRat1<-(aAxis1/bAxis1)

#Calculate phi in radians for standard
  math convention
phiDeg1<-raw1$phi
phiRad1<-phiDeg1*(pi/180)

#Add Phi values in RHR clockwise positive
  convention (standard geographic (
  Ellipsoid) convention)
phiDegGEO1<-ifelse(raw1$phi>0, 180-raw1$
  phi, raw1$phi*-1)
phiRadGEO1<-phiDegGEO1*(pi/180)

#Compile parameters into new data frame
exparam1<-data.frame(xcoord1, ycoord1,
  aAxis1, bAxis1, axRat1, phiDeg1, phiRad1,
  phiDegGEO1, phiRadGEO1)

#Calculate Vector Mean: Lisle (1985),
  page 14
vMeanRad1<-0.5*atan( sum(sin(2*exparam1$
  phiRad1)) /sum(cos(2*exparam1$phiRad1
  )))
vMeanDeg1<-vMeanRad1*(180/pi)
vMeanDeg1<-ifelse(sum(cos(2*exparam1$
  phiRad1))<0,vMeanDeg1+90,vMeanDeg1)

#Convert to ELLIPSOID rake convention
vMeanDegGEO1<-ifelse(vMeanDeg1 > 0, 180-
  vMeanDeg1, -1*vMeanDeg1)

#Calculate Harmonic mean: Lisle (1985),
  page 14
hMean1<-(length(axRat1))/(sum((axRat1)
  ^(-1)))

##PLANE B CALCULATIONS
#Convert data to match cartesian coord.
  from SAPE (origin correction)
xcoord2<-(raw2$y-min(raw2$y))
ycoord2<-(max(raw2$x)-raw2$x)

#Redefine fitted ellipse axes
aAxis2<-raw2$a
bAxis2<-raw2$b

#Calculate axial ratio
axRat2<-(aAxis2/bAxis2)

#Calculate phi in radians for standard
  math convention
phiDeg2<-raw2$phi
phiRad2<-phiDeg2*(pi/180)

#Add Phi values in RHR clockwise positive
  convention (standard geographic (
  Ellipsoid) convention)
phiDegGEO2<-ifelse(raw2$phi>0, (raw2$phi*
  -1)+180, raw2$phi*-1)
phiRadGEO2<-phiDegGEO2*(pi/180)

#Compile parameters into new data frame
exparam2<-data.frame(xcoord2, ycoord2,
  aAxis2, bAxis2, axRat2, phiDeg2, phiRad2,
  phiDegGEO2, phiRadGEO2)

#Calculate Vector Mean: Lisle (1985),
  page 14
vMeanRad2<-0.5*atan( sum(sin(2*exparam2$
  phiRad2)) /sum(cos(2*exparam2$phiRad2
  )))
vMeanDeg2<-vMeanRad2*(180/pi)
vMeanDeg2<-ifelse(sum(cos(2*exparam2$
  phiRad2))<0,vMeanDeg2+90,vMeanDeg2)

#Convert to ELLIPSOID rake convention
vMeanDegGEO2<-ifelse(vMeanDeg2 > 0, 180-
  vMeanDeg2, -1*vMeanDeg2)

#Calculate Harmonic mean: Lisle (1985),
  page 14
hMean2<-(length(axRat2))/(sum((axRat2)
  ^(-1)))

##PLANE C CALCULATIONS
#Convert data to match cartesian coord.
  from SAPE (origin correction)
xcoord3<-(raw3$y-min(raw3$y))
ycoord3<-(max(raw3$x)-raw3$x)

#Redefine fitted ellipse axes
aAxis3<-raw3$a
bAxis3<-raw3$b

#Calculate axial ratio
axRat3<-(aAxis3/bAxis3)

#Calculate phi in radians for standard
  math convention
phiDeg3<-raw3$phi
phiRad3<-phiDeg3*(pi/180)

#Add Phi values in RHR clockwise positive
  convention (standard geographic (
  Ellipsoid) convention)
phiDegGEO3<-ifelse(raw3$phi>0, (raw3$phi*
  -1)+180, raw3$phi*-1)
phiRadGEO3<-phiDegGEO3*(pi/180)

#Compile parameters into new data frame
exparam3<-data.frame(xcoord3, ycoord3,
  aAxis3, bAxis3, axRat3, phiDeg3, phiRad3,
  phiDegGEO3, phiRadGEO3)

#Calculate Vector Mean: Lisle (1985),
  page 14
vMeanRad3<-0.5*atan( sum(sin(2*exparam3$
  phiRad3)) /sum(cos(2*exparam3$phiRad3
  )))
vMeanDeg3<-vMeanRad3*(180/pi)

```

```

vMeanDeg3<-ifelse (sum(cos(2*exparam3$
  phiRad3)) <0,vMeanDeg3+90,vMeanDeg3)

#Convert to ELLIPSOID rake convention
vMeanDegGEO3<-ifelse (vMeanDeg3 > 0, 180-
  vMeanDeg3, -1*vMeanDeg3)

#Calculate Harmonic mean: Lisle (1985),
  page 14
hMean3<-(length(axRat3))/(sum((axRat3)
  ^(-1)))

##Define principle planes related to
  section data
#Read in Rf/Phi axial ratio data
RFPHI_DAT<-read.table(file="ANALYSIS\
  RFPHI\OUTPUT\RFPHI_DAT.txt",header=
  T)

#Plane A
Apar<-exparam1
names(Apar)=c("xcoord","ycoord","aAxis",
  "bAxis","axRat","phiDeg","phiRad",
  "phiDegGEO","phiRadGEO")
AvMean<-vMeanDegGEO1
AhMean<-hMean1
Ars<-RFPHI_DAT$rs[1]

#Plane B
Bpar<-exparam2
names(Bpar)=c("xcoord","ycoord","aAxis",
  "bAxis","axRat","phiDeg","phiRad",
  "phiDegGEO","phiRadGEO")
BvMean<-vMeanDegGEO2
BhMean<-hMean2
Brs<-RFPHI_DAT$rs[2]

#Plane C
Cpar<-exparam3
names(Cpar)=c("xcoord","ycoord","aAxis",
  "bAxis","axRat","phiDeg","phiRad",
  "phiDegGEO","phiRadGEO")
CvMean<-vMeanDegGEO3
ChMean<-hMean3
Crs<-RFPHI_DAT$rs[3]

##Recenter data for plotting and
  determine Isym
#A vMean center
Aphi<-Apar$phiDegGEO-AvMean
Aphi<-ifelse(Aphi>90,Aphi-180,Aphi)
Aphi<-ifelse(Aphi<(-90),Aphi+180,Aphi)
Aplot<-data.frame(Aphi,Apar$axRat)
names(Aplot)=c("Aphi","AaxRat")

#Calculate number of data points in each
  region
AQa<-ifelse(Aplot$AaxRat>AhMean & Aplot$
  Aphi<0,1,0)
AQa<-sum(AQa)
AQb<-ifelse(Aplot$AaxRat>AhMean & Aplot$
  Aphi>0,1,0)
AQb<-sum(AQb)

#Calculate Isym
AIsym<-1-((abs(AQa-AQb)+abs(AQc-AQd))/
  length(Aplot$Aphi))

#B vMean center
Bphi<-Bpar$phiDegGEO-BvMean
Bphi<-ifelse(Bphi>90,Bphi-180,Bphi)
Bphi<-ifelse(Bphi<(-90),Bphi+180,Bphi)
Bplot<-data.frame(Bphi,Bpar$axRat)
names(Bplot)=c("Bphi","BaxRat")

#Calculate number of data points in each
  region
BQa<-ifelse(Bplot$BaxRat>BhMean & Bplot$
  Bphi<0,1,0)
BQa<-sum(BQa)
BQb<-ifelse(Bplot$BaxRat>BhMean & Bplot$
  Bphi>0,1,0)
BQb<-sum(BQb)
BQc<-ifelse(Bplot$BaxRat<BhMean & Bplot$
  Bphi<0,1,0)
BQc<-sum(BQc)
BQd<-ifelse(Bplot$BaxRat<BhMean & Bplot$
  Bphi>0,1,0)
BQd<-sum(BQd)

#Calculate Isym
BIsym<-1-((abs(BQa-BQb)+abs(BQc-BQd))/
  length(Bplot$Bphi))

#C vMean center
Cphi<-Cpar$phiDegGEO-CvMean
Cphi<-ifelse(Cphi>90,Cphi-180,Cphi)
Cphi<-ifelse(Cphi<(-90),Cphi+180,Cphi)
Cplot<-data.frame(Cphi,Cpar$axRat)
names(Cplot)=c("Cphi","CaxRat")

#Calculate number of data points in each
  region
CQa<-ifelse(Cplot$CaxRat>ChMean & Cplot$
  Cphi<0,1,0)
CQa<-sum(CQa)
CQb<-ifelse(Cplot$CaxRat>ChMean & Cplot$
  Cphi>0,1,0)
CQb<-sum(CQb)
CQc<-ifelse(Cplot$CaxRat<ChMean & Cplot$
  Cphi<0,1,0)
CQc<-sum(CQc)
CQd<-ifelse(Cplot$CaxRat<ChMean & Cplot$
  Cphi>0,1,0)
CQd<-sum(CQd)

#Calculate Isym
CIsym<-1-((abs(CQa-CQb)+abs(CQc-CQd))/
  length(Cplot$Cphi))

##Compile values for ELLIPSOID

```



```

Number<-1:3
Strike<-c(round(fDat$strike[1],0),round(
  fDat$strike[2],0),round(fDat$strike
  [3],0))
Dip<-c(round(fDat$dip[1],0),round(fDat$
dip[2],0),round(fDat$dip[3],0))
Rake<-c(round(AvMean,2),round(BvMean,2),
  round(CvMean,2))
Ratio<-c(round(Ars,2),round(Brs,2),round(
  Crs,2))
Weight<-c(1,1,1)
elliPar<-data.frame(Number,Strike,Dip,
  Rake,Ratio,Weight)

#Write .elli file for parameters
sink(file="MODEL\\ELLIPSOID\\INPUT\\RFPHI
_RAW.elli")
cat("#","strike","dip","rake","shape_
ratio","","","","","","","\\n",sep=
"\\t")
cat("1",Strike[1],Dip[1],Rake[1],Ratio
[1],"","1\\n",sep="\\t")
cat("2",Strike[2],Dip[2],Rake[2],Ratio
[2],"","1\\n",sep="\\t")
cat("3",Strike[3],Dip[3],Rake[3],Ratio
[3],"","1\\n",sep="\\t")
cat("\\n")
sink()

#Plot compiled parameters
x11()
textplot(elliPar,halg="center",valign
="top",show.rownames=F)
textplot(elliPar,halg="center",valign
="top",show.rownames=F)
title("Compiled_Parameters_for_ELLIPSOID"
)

#Save file to input
dev.copy(pdf,"MODEL\\ELLIPSOID\\INPUT\\
RFPHI_COMPILE.pdf",useDingbats=F)
dev.off()

#Plot RF/PHI data while maintaining same
scale between plots and add ellipses
x11()
par(mfrow=c(2,3),mar=c(5.1,4.1,4.1,1))
plot(Aplot,main="A",log='y',xlab="
  Recentered_Phi",ylab="Rf",xlim=c
  (-90,90),
ylim=c(1,21),sub=paste("vm=",round(AvMean
,0),"/_hm=",round(AhMean,2)),pch=20,
xaxp=c(-90,90,2))
lines(x=c(0,0),y=c(1,20))
lines(x=c(-90,90),y=c(AhMean,AhMean),col=
"grey")
text(-90,21,paste("n_=",length(Aplot$
Aphi)),adj=0)
text(90,21,paste("s_=",round(AIsym,2)),
adj=1)
plot(Bplot,main="B",log='y',xlab="
  Recentered_Phi",ylab="Rf",xlim=c
  (-90,90),
ylim=c(1,21),sub=paste("vm=",round(
  BvMean,0),"/_hm=",round(BhMean,2)),
pch=20,xaxp=c(-90,90,2))
lines(x=c(0,0),y=c(1,20))
lines(x=c(-90,90),y=c(ChMean,ChMean),col=
"grey")
text(-90,21,paste("n_=",length(Cplot$Cphi
)),adj=0)
text(90,21,paste("s_=",round(CIsym,2)),
adj=1)

#Function for plotting ellipses(http://
www.math.mcmaster.ca/peter/s4m03/
s4m03_0304/classnotes/ellipse.html)
ellipse<-function(hlaxa=1,hlaxb=1,
  theta=0,xc=0,yc=0,npoints=
  100,
  ...)
{
  a<-seq(0,2*pi,length=npoints
  +1)
  x<-hlaxa*cos(a)
  y<-hlaxb*sin(a)
  alpha<-angle(x,y)
  rad<-sqrt(x^2+y^2)
  xp<-rad*cos(alpha+theta)+xc
  yp<-rad*sin(alpha+theta)+yc
  lines(xp,yp,...)
  invisible()
}

angle<-function(x,y)
{
  angle2<-function(xy){
    x<-xy[1]
    y<-xy[2]
    if(x>0){
      atan(y/x)
    }
    else{
      if(x<0&y!=0){
        atan(y/x)+sign(y)*pi
      }
      else{
        if(x<0&y==0){
          pi
        }
        else{
          if(y!=0){
            (sign(y)*pi)/2
          }
        }
      }
    }
  }
}

```



```

#Plot and export table of Blender values
textplot(blendPar, halign="center",
  valign="top", show.rownames=F, show.
  colnames=F)

#Save compiled data
dev.copy(pdf, "MODEL\\BLENDER\\INPUT\\
  ELLIP2BLEND_FR.Y.pdf", useDingbats=F)
dev.off()

##Plot stereonet of oriented ellipsoid
net()
XY<-faultplane(FolDat$V2, FolDat$V3, PLOT=F
)
lines(XY, lwd=2)
title("FRY")
text(0, 1.04, "N", cex=.8)
lab1<-focpoint(TX, PX, pch=20, col="blue")
lab2<-focpoint(TY, PY, pch=20, col="blue")
lab3<-focpoint(TZ, PZ, pch=20, col="blue")
info1<-paste("XY(S&D):", round(FolDat$V2
, 0), round(FolDat$V3, 0), "; X(T&P):",
  round(TX, 0), round(PX, 0), "; Y(T&P):",
  round(TY, 0), round(PY, 0), "; Z(T&P):",
  round(TZ, 0), round(PZ, 0), sep=" ")
mtext(info1, side=1, cex=.8)
text(lab1, "X", col="blue", pos=3)
text(lab2, "Y", col="blue", pos=3)
text(lab3, "Z", col="blue", pos=3)

#Save stereonet plot
dev.copy(pdf, "MODEL\\ELLIPSOID\\OUTPUT\\
  FRY_STEREO.pdf", useDingbats=F)
dev.off()

#Create non-oriented fabric ellipsoid
f<-function(x, y, z) x^2+y^2+z^2
x<-seq(-2, 2, len=20)
S0<-contour3d(f, 4, x, x, x, draw=F)
S1<-scaleTriangles(triangles=S0
, .25, .25, .25)
S2<-scaleTriangles(triangles=S1, XL, YL, ZL)

#Establish rotaion matrices
rotxM<-rotationMatrix((RX*(pi/180))
, 1, 0, 0)
rotyM<-rotationMatrix((RY*(pi/180))
, 0, 1, 0)
rotzM<-rotationMatrix((RZ*(pi/180))
, 0, 0, 1)

#Run transformations
TRANS1<-transformTriangles(triangles=S2,
  rotxM)
TRANS2<-transformTriangles(triangles=
  TRANS1, rotyM)
TRANS3<-transformTriangles(triangles=
  TRANS2, rotzM)
obj<-updateTriangles(TRANS3)

#Generate ellipsoid
exportScene(obj, "FRY", "OFF")
drawScene.rgl(obj)
box3d(col="#DDDDDD", lwd=.5)

```

```

mtext3d("N", edge='x+', col="#DDDDDD")
mtext3d("S", edge='x+', col="#DDDDDD")
mtext3d("E", edge='y+', col="#DDDDDD")
mtext3d("W", edge='y+', col="#DDDDDD")
#End of script#

```

## E.6 Ellipsoid to Blender conversion ( $R_f/\phi$ )

```

####Script : ELLIP2BLEND-RFPHI
####Author : Jeffrey R. Webber
####Con : jrwebber@uwm.edu
###REQUIRED: Working directory set to the
  master folder location
####Data : ELLIPSOID output ASCII file (
  MODEL\\ELLIPSOID\\OUTPUT\\RFY.elli)
###Data : Maintain hard return at end
  of data list

#Load required libraries
library(gplots)
library(misc3d)
library(rgl)
library(RFOC)

#Load data into R from ELLIPSOID OUTPUT
Lnorm<-read.table(file="MODEL\\ELLIPSOID
  \\OUTPUT\\RFPHI.elli", skip=17, sep='\t'
, nrow=1)
OrDat<-read.table(file="MODEL\\ELLIPSOID
  \\OUTPUT\\RFPHI.elli", skip=20, sep='\t'
, nrow=2)
FolDat<-read.table(file="MODEL\\ELLIPSOID
  \\OUTPUT\\RFPHI.elli", skip=23, sep='\t'
, nrow=1)

#Create orientation objects (L=length, P=
  plunge, T=trend)
XL<-Lnorm$V2
YL<-Lnorm$V3
ZL<-Lnorm$V4
TX<-round(OrDat$V2[1], 2)
TY<-round(OrDat$V3[1], 2)
TZ<-round(OrDat$V4[1], 2)
PX<-round(OrDat$V2[2], 2)
PY<-round(OrDat$V3[2], 2)
PZ<-round(OrDat$V4[2], 2)

#Calculate roation of principle axes
RX<-ifelse(TX<=180,
  ifelse(TY>TX,
    ifelse(TY<=(TX+180),
      PY/cos(PX*(pi/180)),
      PY/cos(PX*(pi/180))*(-1)),
    PY/cos(PX*(pi/180))*(-1)),
  ifelse(TY<TX,
    ifelse(TY<=(TX-180),
      PY/cos(PX*(pi/180))*(-1),
      PY/cos(PX*(pi/180))),
    PY/cos(PX*(pi/180)))
)
RX<-round(RX, 2)

```

```

RY<-round(PX,2)
RZ<-round((( -1)*TX+90) ,2)

#Compile parameters for Blender input
names<-c("RotX" ,"RotY" ,"RotZ" ,"DimX" ,"
DimY" ,"DimZ" )
values<-c(RX,RY,RZ,round(XL,2) ,round(YL
,2) ,round(ZL,2) )
blendPar<-data.frame(names, values)

##Write data file for appended axial
lengths
nadaiPar<-cbind(XL,YL,ZL,"RFPHI")
write.table(nadaiPar, file="MODEL\\NADAI\\
INPUT\\AXIAL_DAT.txt" ,append=T, col.
names=F, sep = "\t" ,quote=F,row.names=
F)

#Plot and export table of Blender values
textplot(blendPar, halign="center",
valign="top" ,show.rownames=F,show.
colnames=F)

#Save compiled data
dev.copy(pdf,"MODEL\\BLENDER\\INPUT\\
ELLIP2BLEND_RFPHI.pdf" ,useDingbats=F)
dev.off()

##Plot stereonet of oriented ellipsoid
net()
XY<-faultplane(FolDat$V2,FolDat$V3,PLOT=F)
)
lines(XY,lwd=2)
title("Rf/Phi")
text(0,1.04,"N" ,cex=.8)
lab1<-focpoint(TX,PX,pch=20,col="blue")
lab2<-focpoint(TY,PY,pch=20,col="blue")
lab3<-focpoint(TZ,PZ,pch=20,col="blue")
info1<-paste("XY(S&D):" ,round(FolDat$V2
,0) ,round(FolDat$V3,0) ," ; _X(T&P) : " ,
round(TX,0) ,round(PX,0) ," ; _Y(T&P) : " ,
round(TY,0) ,round(PY,0) ," ; _Z(T&P) : " ,
round(TZ,0) ,round(PZ,0) ,sep=" ")
mtext(info1,side=1,cex=.8)
text(lab1,"X" ,col="blue" ,pos=3)
text(lab2,"Y" ,col="blue" ,pos=3)
text(lab3,"Z" ,col="blue" ,pos=3)

#Save stereonet plot
dev.copy(pdf,"MODEL\\ELLIPSOID\\OUTPUT\\
RFPHI_STEREO.pdf" ,useDingbats=F)
dev.off()

#Create non-oriented fabric ellipsoid
f<-function(x,y,z) x^2+y^2+z^2
x<-seq(-2,2,len=20)
S0<-contour3d(f,4,x,x,x,draw=F)
S1<-scaleTriangles(triangles=S0
,.25,.25,.25)
S2<-scaleTriangles(triangles=S1,XL,YL,ZL)

#Establish rotaion matricies
rotxM<-rotationMatrix((RX*(pi/180))
,1,0,0)

```

```

rotyM<-rotationMatrix((RY*(pi/180))
,0,1,0)
rotzM<-rotationMatrix((RZ*(pi/180))
,0,0,1)

#Run transformations
TRANS1<-transformTriangles(triangles=S2,
rotxM)
TRANS2<-transformTriangles(triangles=
TRANS1,rotyM)
TRANS3<-transformTriangles(triangles=
TRANS2,rotzM)
obj<-updateTriangles(TRANS3)

#Generate ellipsoid
exportScene(obj,"RFPHI" ,"OFF")
drawScene.rgl(obj)
box3d(col="#DDDDDD" ,lwd=.5)
mtext3d("N" ,edge='x++' ,col="#DDDDDD")
mtext3d("S" ,edge='x-+' ,col="#DDDDDD")
mtext3d("E" ,edge='y++' ,col="#DDDDDD")
mtext3d("W" ,edge='y-+' ,col="#DDDDDD")
#End of script#

```

## E.7 SYNTHETIC\_P1

```

###Script: SYNTHETIC_P1 ###
###Author: Jeffrey R. Webber ###
###Cont. : jrwebber@uvm.edu ###

#####
# Configure the parameters below #
#####

#Location of image files#
img.a <- "C:\\WEBBER\\UVM\\JGE-2012\\
FRY3D\\IMG_DAT\\A.EX.png"
img.b <- "C:\\WEBBER\\UVM\\JGE-2012\\
FRY3D\\IMG_DAT\\B.EX.png"
img.c <- "C:\\WEBBER\\UVM\\JGE-2012\\
FRY3D\\IMG_DAT\\C.EX.png"

#File to export data for use in Ellipsoid
2003#
e.in <- "C:\\WEBBER\\UVM\\JGE-2012\\FRY3D
\\OUTPUT\\synth.in.elli"

#####
# Configure the parameters above #
#####

library(StructR)
att.a <- c(281, 55)
att.b <- c(041, 53)
att.c <- c(162, 57)
x11()
centroids.a <- FryImg(img.a)
fry.data.a<-FryPLOT(centroids.a)

centroids.b <- FryImg(img.b)
fry.data.b<-FryPLOT(centroids.b)

centroids.c <- FryImg(img.c)

```

```

fry.data.c<-FryPLOT(centroids.c)

Ellipse3D(hlaxa = fry.data.a$a.half.axis,
          hlaxb = fry.data.a$b.half.axis,
          theta = fry.data.a$elli.azimuth
          ,
          strike = att.a[1], dip = att.a
            [2],
          sty = "red")

Ellipse3D(hlaxa = fry.data.b$a.half.axis,
          hlaxb = fry.data.b$b.half.axis,
          theta = fry.data.b$elli.azimuth
          ,
          strike = att.b[1], dip = att.b
            [2],
          sty = "blue")

Ellipse3D(hlaxa = fry.data.c$a.half.axis,
          hlaxb = fry.data.c$b.half.axis,
          theta = fry.data.c$elli.azimuth
          ,
          strike = att.c[1], dip = att.c
            [2],
          sty = "green")

Fry3D(centroids.a, strike = att.a[1], dip
      = att.a[2], color = "red")
Fry3D(centroids.b, strike = att.b[1], dip
      = att.b[2], color = "blue")
Fry3D(centroids.c, strike = att.c[1], dip
      = att.c[2], color = "green")

RFrame()

ElliWrite(path = e.in,
          section.a = fry.data.a,
          section.b = fry.data.b,
          section.c = fry.data.c,
          ort.a = att.a,
          ort.b = att.b,
          ort.c = att.c)

#End of script#

```

## E.8 SYNTHETIC\_P2

```

##Script: SYNTHETIC_P2 ##
##Author: Jeffrey R. Webber ##
##Cont. : jrwebber@uvm.edu ##
library(StructR)
path <- "C:\\WEBBER\\UVM\\JGE_2012\\FRY3D
        \\OUTPUT\\synth_out.elli"

ElliRead(elli.file = path)

RFrame()
#End of script#

```

## E.9 VT\_P1

```

###Script: VERMONT_P1 ###

```

```

###Author: Jeffrey R. Webber ###
###Cont. : jrwebber@uvm.edu ###

#####
# Configure the parameters below #
#####

#Location of image files#
img.a <- "C:\\WEBBER\\UVM\\JGE_2012\\
        FRY3D\\IMG_DAT\\VT.A.png"
img.b <- "C:\\WEBBER\\UVM\\JGE_2012\\
        FRY3D\\IMG_DAT\\VT.B.png"
img.c <- "C:\\WEBBER\\UVM\\JGE_2012\\
        FRY3D\\IMG_DAT\\VT.C.png"

#File to export data for use in Ellipsoid
2003#
e.in <- "C:\\WEBBER\\UVM\\JGE_2012\\FRY3D
        \\OUTPUT\\vt_in.elli"

#####
# Configure the parameters above #
#####

library(StructR)
att.a <- c(011, 68)
att.b <- c(110, 71)
att.c <- c(235, 30)

centroids.a <- FryImg(img.a)
fry.data.a<-FryPLOT(centroids.a, .75)

centroids.b <- FryImg(img.b)
fry.data.b<-FryPLOT(centroids.b, .75)

centroids.c <- FryImg(img.c)
fry.data.c<-FryPLOT(centroids.c, .75)

Ellipse3D(hlaxa = fry.data.a$a.half.axis,
          hlaxb = fry.data.a$b.half.axis,
          theta = fry.data.a$elli.azimuth
          ,
          strike = att.a[1], dip = att.a
            [2],
          sty = "red")

Ellipse3D(hlaxa = fry.data.b$a.half.axis,
          hlaxb = fry.data.b$b.half.axis,
          theta = fry.data.b$elli.azimuth
          ,
          strike = att.b[1], dip = att.b
            [2],
          sty = "blue")

Ellipse3D(hlaxa = fry.data.c$a.half.axis,
          hlaxb = fry.data.c$b.half.axis,
          theta = fry.data.c$elli.azimuth
          ,
          strike = att.c[1], dip = att.c
            [2],
          sty = "green")

Fry3D(centroids.a, strike = att.a[1], dip
      = att.a[2], color = "red")

```

```
Fry3D(centroids.b, strike = att.b[1], dip
      = att.b[2], color = "blue")
Fry3D(centroids.c, strike = att.c[1], dip
      = att.c[2], color = "green")
```

```
RFrame()
```

```
ElliWrite(path = e.in,
          section.a = fry.data.a,
          section.b = fry.data.b,
          section.c = fry.data.c,
          ort.a = att.a,
          ort.b = att.b,
          ort.c = att.c)
```

```
#End of script#
```

## E.10 VT\_P2

```
##Script: VERMONT_P2 ##
##Author: Jeffrey R. Webber ##
##Cont. : jrwebber@uvm.edu ##
library(StructR)
path <- "C:\\WEBBER\\UVM\\JGE_2012\\FRY3D
        \\OUTPUT\\vt_out.elli"
```

```
ElliRead(elli.file = path)
```

```
RFrame()
```

```
#End of script#
```

## E.11 StructR functions

```
Ellipse2D <-
function(hlaxa = 1, hlaxb = 1, theta = 0,
        xc = 0, yc = 0, npoints = 50, sty="
red"){
  angle <- function(x, y){
    angle2 <- function(xy) {
      x <- xy[1]
      y <- xy[2]
      if (x > 0){
        atan(y / x)
      }
    }
  }
  else{
    if (x < 0 & y != 0){
      atan(y / x) + sign(y) * pi
    }
    else{
      if(x < 0 & y == 0){
        pi
      }
      else{
        if(y != 0){
          (sign(y) * pi) / 2
        }
        else{
          NA
        }
      }
    }
  }
}
```

```

}
  apply(cbind(x, y), 1, angle2)
}

a <- seq(0, 2 * pi, length = npoints +
1)
x <- hlaxa * cos(a)
y <- hlaxb * sin(a)
alpha <- angle(x, y)
rad <- sqrt(x^2 + y^2)
xp <- rad * cos(alpha + theta) + xc
yp <- rad * sin(alpha + theta) + yc
lines(xp, yp, col = sty, lwd =2)
invisible()
}
```

```
Ellipse3D <-
function(hlaxa = 1, hlaxb = 1, theta = 0,
        xc = 0, yc = 0, strike = 0, dip = 0,
        npoints = 50, sty="red"){
  angle <- function(x, y){
    angle2 <- function(xy) {
      x <- xy[1]
      y <- xy[2]
      if (x > 0){
        atan(y / x)
      }
    }
  }
  else{
    if (x < 0 & y != 0){
      atan(y / x) + sign(y) * pi
    }
    else{
      if(x < 0 & y == 0){
        pi
      }
      else{
        if(y != 0){
          (sign(y) * pi) / 2
        }
        else{
          NA
        }
      }
    }
  }
  apply(cbind(x, y), 1, angle2)
}
```

```
a <- seq(0, 2 * pi, length = npoints +
1)
x <- hlaxa * cos(a)
y <- hlaxb * sin(a)
alpha <- angle(x, y)
rad <- sqrt(x^2 + y^2)
xp <- rad * cos(alpha + theta) + xc
yp <- rad * sin(alpha + theta) + yc
zp <- seq(0, 0, len = npoints + 1)
elli3d.dat <- matrix(cbind(xp, yp, zp),
                    ncol = 3)
elli3d.dat <- rotate3d(elli3d.dat, dip
* (pi / 180), -1, 0, 0)
elli3d.dat <- rotate3d(elli3d.dat, (
strike - 90) * (pi / 180), 0, 0, 1)
```

```

lines3d(elli3d.dat, col = sty)
}

ElliRead <-
function(elli.file){
  Lnorm <- read.table(file = elli.file,
    skip=17,sep='\t',nrows=1)
  OrDat <- read.table(file = elli.file,
    skip=20,sep='\t',nrows=2)
  FolDat <- read.table(file = elli.file,
    skip=23,sep='\t',nrows=1)

  XL<-Lnorm$V2
  YL<-Lnorm$V3
  ZL<-Lnorm$V4
  TX<-round(OrDat$V2[1],2)
  TY<-round(OrDat$V3[1],2)
  TZ<-round(OrDat$V4[1],2)
  PX<-round(OrDat$V2[2],2)
  PY<-round(OrDat$V3[2],2)
  PZ<-round(OrDat$V4[2],2)

  #Calculate roation of principle axes#
  RX<-ifelse(TX<=180,
    ifelse(TY>TX,
      ifelse(TY<=(TX+180),
        PY/cos(PX*(pi/180)),
        PY/cos(PX*(pi/180))*(-1)),
      PY/cos(PX*(pi/180))*(-1)),
    ifelse(TY<TX,
      ifelse(TY<=(TX-180),
        PY/cos(PX*(pi/180))*(-1),
        PY/cos(PX*(pi/180))),
      PY/cos(PX*(pi/180)))
    )
  RX<-round(RX,2)
  RY<-round(PX,2)
  RZ<-round(((-1)*TX+90),2)

  #Plot stereonet of oriented ellipsoid#
  net()
  XY<-faultplane(FolDat$V2,FolDat$V3,PLOT
    =FALSE)
  lines(XY,lwd=2)
  title("FRY")
  text(0,1.04,"N",cex=.8)
  lab1<-focpoint(TX,PX,pch=20,col="blue")
  lab2<-focpoint(TY,PY,pch=20,col="blue")
  lab3<-focpoint(TZ,PZ,pch=20,col="blue")
  info1<-paste("XY(S&D):",round(FolDat$V2
    ,0),round(FolDat$V3,0),";_X(T&P):",
    round(TX,0),round(PX,0),";_Y(T&P):",
    round(TY,0),round(PY,0),";_Z(T&P):",
    round(TZ,0),round(PZ,0),sep=" ")
  mtext(info1,side=1,cex=.8)
  text(lab1,"X",col="blue",pos=3)
  text(lab2,"Y",col="blue",pos=3)
  text(lab3,"Z",col="blue",pos=3)

  #Create non-oriented fabric ellipsoid#
  f<-function(x,y,z) x^2+y^2+z^2
  x<-seq(-2,2,len=20)
  S0<-contour3d(f,4,x,x,x,draw=FALSE)

```

```

S1<-scaleTriangles(triangles=S0
  ,.25,.25,.25)
S2<-scaleTriangles(triangles=S1,XL,YL,
  ZL)

#Establish rotaion matrices#
rotxM<-rotationMatrix((RX*(pi/180))
  ,1,0,0)
rotyM<-rotationMatrix((RY*(pi/180))
  ,0,1,0)
rotzM<-rotationMatrix((RZ*(pi/180))
  ,0,0,1)

#Run transformations#
TRANS1<-transformTriangles(triangles=S2
  ,rotxM)
TRANS2<-transformTriangles(triangles=
  TRANS1,rotyM)
TRANS3<-transformTriangles(triangles=
  TRANS2,rotzM)
obj<-updateTriangles(TRANS3)

#Generate ellipsoid#
open3d()
drawScene.rgl(obj)

#Function for drawing arcs from package
:plotrix#
draw.arc <- function(x = 1, y = NULL,
  radius = 1, angle1 = deg1 * pi/180,
  angle2 = deg2 * pi/180, deg1 = 0,
  deg2 = 45, n = 35, col = 1, ...) {
  draw.arc.0 <- function(x, y, radius,
    angle1, angle2, n, col = col,
    ...) {
    xylim <- par("usr")
    plotdim <- par("pin")
    ymult <- (xylim[4] - xylim[3])/((
      xylim[2] - xylim[1]) * plotdim
      [1]/plotdim[2])
    angle <- angle1 + seq(0, length = n
      ) * (angle2 - angle1)/n
    p1x <- x + radius * cos(angle)
    ply <- y + radius * sin(angle) *
      ymult
    angle <- angle1 + seq(length = n) *
      (angle2 - angle1)/n
    p2x <- x + radius * cos(angle)
    p2y <- y + radius * sin(angle) *
      ymult
    segments(p1x, ply, p2x, p2y, col =
      col, ...)
  }
  xy <- xy.coords(x, y)
  x <- xy$x
  y <- xy$y
  a1 <- pmin(angle1, angle2)
  a2 <- pmax(angle1, angle2)
  angle1 <- a1
  angle2 <- a2
  args <- data.frame(x, y, radius,
    angle1, angle2, n, col,
    stringsAsFactors = FALSE)

```





```

cat("1", "\t", strike.a, "\t", dip.a, "
\t", rake.a, "\t", l.a, "\t", s.a,
"\t", 1, "\n", sep="")
cat("2", "\t", strike.b, "\t", dip.b, "
\t", rake.b, "\t", l.b, "\t", s.b,
"\t", 1, "\n", sep="")
cat("3", "\t", strike.c, "\t", dip.c, "
\t", rake.c, "\t", l.c, "\t", s.c,
"\t", 1, "\n\n", sep="")
sink()
}

Fry3D <-
function(fry.data, strike = 0, dip = 0,
color = "black"){
fry3d <- matrix(cbind(fry.data$x, fry.
data$y, seq(0, 0, len = length(fry.
data$x))), ncol = 3)
fry3d <- rotate3d(fry3d, dip * (pi /
180), -1, 0, 0)
fry3d <- rotate3d(fry3d, (strike - 90)
* (pi / 180), 0, 0, 1)
points3d(fry3d, col = color)
}

FryImg <-
function(img.path = NULL, limit = 3000){
#Plot image and create point locator#
img <-readPNG(source = img.path)

x11(xpos=25, ypos=0)
par(mar=c(0,0,0,0))
plot.new()
rasterImage(img,0,0,1,1,interpolate=
FALSE)
coords <- locator(type="p",pch=20, col
="yellow")
dev.off()

#Run loop to create Fry coords.#
x.fry <- NULL
y.fry <- NULL
i <- 0

while(i < length(coords$x)){
i<-i+1

#Center points based on iterative
step [i] location=(0,0)#
x.raw<-coords$x[i] - coords$x
y.raw<-coords$y[i] - coords$y

#Concatenate coord. lists#
x.fry <- c(x.fry,x.raw)
y.fry <- c(y.fry,y.raw)
}

coords.fry <- data.frame(x.fry, y.fry)

#Calculate center distance and limit
data size#
coords.fry$distance <- sqrt((coords.fry
$x.fry)^2 + (coords.fry$y.fry)^2)

coords.fry <- coords.fry[with(coords.
fry, order(distance)), ]
x <- coords.fry$x[(length(coords$x) +
1):length(coords.fry$x)]
y <- coords.fry$y[(length(coords$x) +
1):length(coords.fry$y)]

if( length(x) > limit){
x <- x[1:limit]
y <- y[1:limit]
}

coords.fry.lim <- data.frame(x, y)
return(coords.fry.lim)
}

FryPLOT <-
function(fry.data, zoom = 1){
#Determine plot window parameters#
x.range <- summary(fry.data$x)
x.range <- x.range[5]
y.range <- summary(fry.data$y)
y.range <- y.range[5]

#Plot data and estimate apogee#
x11(xpos=-25, ypos=0)
plot(fry.data,
xlim = c((-1 * x.range) * zoom, x.
range * zoom),
ylim = c((-1 * y.range) * zoom, y.
range * zoom),
asp = 1, ann = FALSE, axes = FALSE
,
pch = 19, col = "#AAAAAA")
box()
title(main = "Select_central_void_
apogee")
points(0, 0, pch = 3, col = "red")
apogee <- locator(n = 1, type="n")

#Plot data and estimate perigee#
plot(fry.data,
xlim = c((-1 * x.range) * zoom, x.
range * zoom),
ylim = c((-1 * y.range) * zoom, y.
range * zoom),
asp = 1, ann = FALSE, axes = FALSE
,
pch = 19, col = "#AAAAAA")
box()
title(main = "Select_central_void_
perigee")
points(0, 0, pch = 3, col = "red")

lines(x = c(-1 * as.numeric(apogee[1]),
as.numeric(apogee[1])),
y = c(-1 * as.numeric(apogee[2]),
as.numeric(apogee[2])),
col = "red", lwd = 2)

perigee <- locator(n = 1, type="n")

lines(x = c(-1 * as.numeric(perigee[1])
, as.numeric(perigee[1])),

```

```

y = c(-1 * as.numeric(perigee[2])
      , as.numeric(perigee[2])),
col = "blue", lwd = 2)

#Create data frame of central void
parameters#
elli.coords <- matrix(rbind(apogee ,
perigee , deparse.level = 0), ncol =
2)

a.half.axis <- sqrt(as.numeric(elli.
coords[1,1])^2 + as.numeric(elli.
coords[1,2])^2)
b.half.axis <- sqrt(as.numeric(elli.
coords[2,1])^2 + as.numeric(elli.
coords[2,2])^2)

#Run algorithm to determine dip
direction azimuth#
if(as.numeric(elli.coords[1,1]) >= 0 &
as.numeric(elli.coords[1,2]) > 0){
rake.azimuth<-abs(atan(as.numeric(
elli.coords[1,1]) / as.numeric(
elli.coords[1,2])))
}
if(as.numeric(elli.coords[1,1]) >= 0
& as.numeric(elli.coords[1,2]) <=
0){
rake.azimuth<-(pi / 2) + abs(atan(as.
numeric(elli.coords[1,2]) / as.
numeric(elli.coords[1,1])))
}
if(as.numeric(elli.coords[1,1]) < 0 &
as.numeric(elli.coords[1,2]) <=
0){
rake.azimuth<-(pi) + abs(atan(as.
numeric(elli.coords[1,1]) / as.
numeric(elli.coords[1,2])))
}
if(as.numeric(elli.coords[1,1]) < 0 &
as.numeric(elli.coords[1,2]) >
0){
rake.azimuth<-((3 / 2) * pi) + abs(
atan(as.numeric(elli.coords[1,2])
/ as.numeric(elli.coords[1,1])))
}

elli.azimuth <- ((5 / 2) * pi - rake.
azimuth) %% pi

#Plot fitted ellipse#
Ellipse2D(a.half.axis , b.half.axis ,
theta = elli.azimuth, sty = "black"
)
elli.par <- data.frame(a.half.axis , b.
half.axis , elli.azimuth)
return(elli.par)
}

Nadai <-
function(Lx = 2, Ly = 1, Lz = .5, Plot=
TRUE){
axDat<-data.frame(Lx, Ly, Lz)
names(axDat)=c("X" ,"Y" ,"Z")
#Calculate Lode's parameter#
lodes<-(2*(log(axDat$Y)-log(axDat$X)-
log(axDat$Z)))/(log(axDat$X)-log(
axDat$Z))

#Calculate the octahedral shear strain#
octSS<-(sqrt((log(axDat$X)-log(axDat$Y)
)^2+(log(axDat$Y)-log(axDat$Z))^2+(
log(axDat$Z)-log(axDat$X))^2)/sqrt
(3))

if(Plot == FALSE){
parameters<-data.frame(lodes , octSS)
names(parameters) = c("lodes" ,"octSS"
)
return(parameters)
}
if(Plot == TRUE){
#Calculate cartesian coords#
xcoord<-octSS*sin((pi/6)*lodes)
ycoord<-octSS*cos((pi/6)*lodes)

#Function for drawing arcs from
package:plotrix#
draw.arc <- function(x = 1, y = NULL
, radius = 1, angle1 = deg1 * pi/
180, angle2 = deg2 * pi/180, deg1
= 0, deg2 = 45, n = 35, col = 1,
...){
draw.arc.0 <- function(x, y, radius
, angle1, angle2, n, col = col,
...){
xylim <- par("usr")
plotdim <- par("pin")
ymult <- (xylim[4] - xyylim[3])/
(xyylim[2] - xyylim[1]) *
plotdim[1]/plotdim[2]
angle <- angle1 + seq(0, length =
n) * (angle2 - angle1)/n
plx <- x + radius * cos(angle)
ply <- y + radius * sin(angle) *
ymult
angle <- angle1 + seq(length = n)
* (angle2 - angle1)/n
p2x <- x + radius * cos(angle)
p2y <- y + radius * sin(angle) *
ymult
segments(plx, ply, p2x, p2y, col
= col, ...)
}
xy <- xy.coords(x, y)
x <- xy$x
y <- xy$y
a1 <- pmin(angle1, angle2)
a2 <- pmax(angle1, angle2)
angle1 <- a1
angle2 <- a2
args <- data.frame(x, y, radius ,
angle1, angle2, n, col,
stringsAsFactors = FALSE)
for(i in 1:nrow(args)) do.call("
draw.arc.0", c(args[i, ], ...))
invisible(args)
}
}

```

```

}

#Create standardized plot#
x11(width=10,height=7.5)
par(mfrow=c(1,2),mar=c(0,0,0,0))
plot(0,0, pch=NA,xlab=NA,ylab=NA,xlim
      =c(-2.25,2.25),ylim=c(0,4.5),asp
      =1,xaxt='n',yaxt='n',frame.plot=
      FALSE)
text(0,4.75,"NADAL_PLOT",cex=1.5)
text(0,4.25,expression(nu),cex=1.5)
text(-2,3.75,"-1")
text(2,3.75,"1")
text(-1,4.1,"Prolate",srt=15)
text(1,4.1,"Oblate",srt=345)
text(-1.75,1.75,expression(bar(
  epsilon)[s]),cex=1.5)
text(.25,0,"0")
text(.75,.866,"1")
text(1.25,1.732,"2")
text(1.75,2.598,"3")
text(2.25,3.464,"4")
lines(c(0,0),c(0,4),lwd=1.5)
lines(c(0,2),c(0,3.46),lwd=1.5)
lines(c(0,-2),c(0,3.46),lwd=1.5)
lines(c(0,1.04),c(0,3.86),lwd=1)
lines(c(0,-1.04),c(0,3.86),lwd=1)
draw.arc(x=0,y=0,radius=4,angle=(pi)/
  3,angle2=(2*pi)/3,lwd = 1.5)
draw.arc(x=0,y=0,radius=3,angle=(pi)/
  3,angle2=(2*pi)/3,lwd = 1)
draw.arc(x=0,y=0,radius=2,angle=(pi)/
  3,angle2=(2*pi)/3,lwd = 1)
draw.arc(x=0,y=0,radius=1,angle=(pi)/
  3,angle2=(2*pi)/3,lwd = 1)
points(xcoord,ycoord,pch=20)
index<-1:(length(axDat$X))

#Create data table#
nadPar<-data.frame(index,octSS,lodes)
plot(0,0, pch=NA,xlab=NA,ylab=NA,xlim
      =c(-2,2),ylim=c(0,4.5),asp=1,xaxt
      ='n',yaxt='n',frame.plot=FALSE)
text(-1,4.25,"Index",cex=1.5,adj=1)
text(-.375,4.25,expression(bar(
  epsilon)[s]),cex=1.5)
text(.375,4.25,expression(nu),cex
      =1.5)
lines(c(-2,2),c(4,4),lwd=1.5)

#Add side table of compiled data#
i<-0
while(i<length(axDat$X)){
  i<-i+1
  text(-1,4.25-(i*.5),index[i],col='
    red',adj=1)
  text(-.375,4.25-(i*.5),round(octSS[
    i],3))
  text(.375,4.25-(i*.5),round(lodes[
    i],3))
  lines(c(-2,2),c(4-(i*.5),4-(i*.5)))
}
}
}

```

```

RFrame <-
function(color = "#DDDDDD", lweight = .5)
{
  box3d(col = color, lwd = lweight)
  mtext3d("N", edge = 'x++', col = color)
  mtext3d("S", edge = 'x+', col = color)
  mtext3d("E", edge = 'y++', col = color)
  mtext3d("W", edge = 'y+', col = color)
}

```

## E.12 Panozzo functions

```

### PANOZZO_FIT.R ###
### Jeffrey R. Webber ###
### May 2012 ###

#Function to create undeformed line data
set.
#n.lines, number of lines.
#width, general width of region to plot
lines.
#PLOT, Boolean expression to plot
undeformed lines.
#Returns data frame of x1y1 x2y2
coordinates for tie line pairs.
LineGenerator <- function(n.lines = 100,
  width = 50, PLOT = TRUE, r.norm =
  TRUE){
  #Define object my.data
  my.data <- NULL

  #Create normal distribution of lines
  with average length .5 width
  length.l <- abs(rnorm(n = n.lines, mean
    = width / 2, sd = width / 2))

  if(r.norm == TRUE){
    #Set line coordinates along the x-axis
    my.data$x.1 <- -1 * length.l / 2
    my.data$y.1 <- seq(0, 0, length = n.
      lines)
    my.data$x.2 <- length.l / 2
    my.data$y.2 <- seq(0, 0, length = n.
      lines)

    #Create uniform vector of theta angles
    for rotation
    theta <- runif(n = n.lines, min = 0,
      max = pi)
  }

  if(r.norm == FALSE){
    #Set line coordinates along the x-
    axis
    my.data$x.1 <- seq(-12.5, -12.5,
      length = n.lines)
    my.data$y.1 <- seq(0, 0, length = n.
      lines)
    my.data$x.2 <- seq(12.5, 12.5, length
      = n.lines)
    my.data$y.2 <- seq(0, 0, length = n.
      lines)
  }
}

```

```

#Create uniform vector of theta
  angles for rotation
  theta <- seq(0, pi, length = n.lines)
}

#Loop to rotate material lines into
  uniform distribution
i <- 0
while(i < n.lines){
  i <- i + 1

  #Create rotation matrix for line [i]
  roation
  rot.matrix <- matrix(c(cos(theta[i]),
    -1 * sin(theta[i]), sin(theta[i]
    ]), cos(theta[i])), ncol = 2,
    byrow = TRUE)

  #Apply matrix transformation
  temp.matrix.a <- rot.matrix %*%
    matrix(c(my.data[[1]][i], my.data
    [[2]][i]), ncol = 1)
  temp.matrix.b <- rot.matrix %*%
    matrix(c(my.data[[3]][i], my.data
    [[4]][i]), ncol = 1)

  #Overwrite data frame element [i]
  my.data$x.1[i] <- temp.matrix.a[1]
  my.data$y.1[i] <- temp.matrix.a[2]
  my.data$x.2[i] <- temp.matrix.b[1]
  my.data$y.2[i] <- temp.matrix.b[2]
  remove(temp.matrix.a, temp.matrix.b)
}

#Plotting routine
if(PLOT){
  plot(0, 0, pch = "", xlim = c(-1 *
    width, width), ylim = c(-1 *
    width, width), ann = FALSE, axes
    = FALSE, asp = 1)

  i <- 0
  while(i < n.lines){
    i <- i + 1
    lines(c(my.data$x.1[i],my.data$x.2[
    i]), c(my.data$y.1[i],my.data$y
    .2[i]), lwd = 2, col = "#009900
    ")
  }
}

#Return undeformed line data frame
return(my.data)
}

#Function to shear line parallel to x—
  axis.
#l.nodes, data frame containing
  material line node pairs.
#e.s, shear strain value following e.s
  = tan(Psi).

#PLOT, Boolean expression to plot
  undeformed lines.
#plot.width, if PLOT = TRUE the width
  of the plot.
#Returns data frame of x1y1 x2y2
  coordinates fot tie line pairs.
LineShear <- function(l.nodes, e.s = 1,
  PLOT = TRUE, plot.width = 100){
  #Define object my.data
  my.data <- NULL

  #Run loop to translate x—coordinate
    based on shear strain.
  i <- 0
  while(i < length(l.nodes[[1]])){
    i <- i + 1

    #Overwrite data frame element [i]
    my.data$x.1[i] <- l.nodes[[1]][i] + 1
      .nodes[[2]][i] * e.s
    my.data$y.1[i] <- l.nodes[[2]][i]
    my.data$x.2[i] <- l.nodes[[3]][i] + 1
      .nodes[[4]][i] * e.s
    my.data$y.2[i] <- l.nodes[[4]][i]
  }

  #Plotting routine
  if(PLOT){
    plot(0, 0, pch = "", xlim = c(-1 *
      plot.width / 2, plot.width / 2),
      ylim = c(-1 * plot.width / 2,
      plot.width / 2), ann = FALSE,
      axes = FALSE, asp = 1)

    i <- 0
    while(i < length(l.nodes[[1]])){
      i <- i + 1
      lines(c(my.data$x.1[i],my.data$x.2[
      i]), c(my.data$y.1[i],my.data$y
      .2[i]), lwd = 2, col = "#009900
      ")
    }
  }

  #Return undeformed line data frame
  return(my.data)
}

#Function to calculate projected line
  data frame following Panozzo
#n.lines, number of lines.
#res, number of rotations (e.g. 180 = 1
  degree increments.
#Returns data frame of step rotation
  and line lengths.
Panozzo <- function(l.nodes, res = 180){
  #Calculate angular step in radians
    based on resolution
  angle.step <- pi / res

  #Establish initial rotation angle of 0
  angle.tot <- 0

```

```

#Define object projected
projected <- NULL

#Add step index in projected data frame
#
projected$rad <- seq(0, pi, length =
  res)

#Run loop to rotate line data stepwise
i <- 0
while(i < res){
  i <- 1 + i

  #Define object temp.data
  temp.data <- NULL

  #Determine set rotation angle for
  iteration [i]
  angle.tot <- angle.tot + angle.step

  #Create rotation matrix based step
  iteration rotation angle
  rot.matrix <- matrix(c(cos(angle.tot)
    , -1 * sin(angle.tot), sin(angle.
    tot), cos(angle.tot)), ncol = 2,
    byrow = TRUE)

  #Run loop to apply rotation matrix to
  each coordinate pair
  ii <- 0
  while(ii < length(1.nodes[[1]])){
    ii <- ii + 1

    #Multiply roatation matrix to line
    pairs
    temp.matrix.a <- rot.matrix %*%
      matrix(c(1.nodes[[1]][ii], 1.
        nodes[[2]][ii]), ncol = 1)
    temp.matrix.b <- rot.matrix %*%
      matrix(c(1.nodes[[3]][ii], 1.
        nodes[[4]][ii]), ncol = 1)

    #Populate temp.data data frame with
    coordinates
    temp.data$x.1[ii] <- temp.matrix.a
      [1]
    temp.data$y.1[ii] <- temp.matrix.a
      [2]
    temp.data$x.2[ii] <- temp.matrix.b
      [1]
    temp.data$y.2[ii] <- temp.matrix.b
      [2]
  }

  #Add projected x-lengths and
  concatenate for each iteration
  projected$len <- c(projected$len, sum
    (abs(temp.data$x.1 - temp.data$x
    .2)))
}
return(projected)
}

#Function to produce plot of ellipse
point perimeter
#panozzo, data frame of the panozzo
radian steps and corresponding
projected lengths
#Returns coordinates of projected
ellipse perimeter points
PanozzoEllipse <- function(panozzo, PLOT
  = TRUE){
  #Define object my.data
  my.data <- NULL

  #Determine step resolution
  res <- length(panozzo[[1]])

  #Determine radian step increment
  rot.step <- pi / res

  #Begin initial angle condition
  angle.tot <- pi / 2

  #Construct coords of lengths along x-
  axis
  ycoords <- seq(0, 0, res)

  #Set up length coords for rotation
  coord.matrix <- matrix(rbind(1 /
    panozzo[[2]], ycoords), nrow = 2)

  #Run lood to rotate length coords to
  create data.frame of Rs perimeter
  i <- 0
  while(i < res){
    i <- i + 1

    #Determine step [i] rotation angle
    angle.tot <- angle.tot - rot.step

    #Construct rotation matrix
    rot.matrix <- matrix(c(cos(angle.tot)
      , -1 * sin(angle.tot), sin(angle.
      tot), cos(angle.tot)), ncol = 2,
      byrow = TRUE)

    #Apply rotation matrix to panozzo
    coordinates
    temp.matrix <- rot.matrix %*% matrix(
      c(coord.matrix[1,i], coord.matrix
      [2,i]), ncol = 1)

    #Construct data frame of ellipse
    perimeter
    my.data$x[i] <- temp.matrix[1]
    my.data$x[i + res] <- temp.matrix[1]
      * -1
    my.data$y[i] <- temp.matrix[2]
    my.data$y[i + res] <- temp.matrix[2]
      * -1
  }

  if(PLOT){
    plot(my.data, asp = 1, pch = 21, cex
      = .5, axes = FALSE, ann = FALSE,

```

```

        col = "red")
    }
    return(my.data)
}

#Function to fit an ellipse to projected
length perimeter
#Modified code from Michael Bedward <
michael.bedward at gmail.com>
#Following algorithms described in:
# Radim Halir & Jan Flusser. 1998.
# Numerically stable direct least
squares fitting of ellipses.
# Proceedings of the 6th International
Conference in Central Europe
# on Computer Graphics and
Visualization. WSCG '98, p. 125-132
PanozzoFit <- function(p.ellipse){
  EPS <- 1.0e-8
  y <- NULL
  dat <- xy.coords(p.ellipse, y)

  D1 <- cbind(dat$x * dat$x, dat$x * dat$
y, dat$y * dat$y)
  D2 <- cbind(dat$x, dat$y, 1)
  S1 <- t(D1) %*% D1
  S2 <- t(D1) %*% D2
  S3 <- t(D2) %*% D2
  T <- -solve(S3) %*% t(S2)
  M <- S1 + S2 %*% T
  M <- rbind(M[3,] / 2, -M[2,], M[1,] /
2)
  evec <- eigen(M)$vec
  cond <- 4 * evec[1,] * evec[3,] - evec
[2,]^2
  a1 <- evec[, which(cond > 0)]
  f <- c(a1, T %*% a1)
  names(f) <- letters[1:6]

  # calculate the center and lengths of
the semi-axes
  b2 <- f[2]^2 / 4
  center <- c((f[3] * f[4] / 2 - b2 * f
[5]), (f[1] * f[5] / 2 - f[2] *
f[4] / 4)) / (b2 - f[1] * f[3])
  names(center) <- c("x", "y")

  num <- 2 * (f[1] * f[5]^2 / 4 + f[3] *
f[4]^2 / 4 + f[6] * b2 -
f[2]*f[4]*f[5]/4 - f[1]*f[3]*f[6])
  den1 <- (b2 - f[1]*f[3])
  den2 <- sqrt((f[1] - f[3])^2 + 4*b2)
  den3 <- f[1] + f[3]

  semi.axes <- sqrt(c( num / (den1 * (
den2 - den3)), num / (den1 *
(-den2 - den3)) ))

  # calculate the angle of rotation
  term <- (f[1] - f[3]) / f[2]
  angle <- atan(1 / term) / 2

  list(coef=f, center = center, major =
max(semi.axes), minor =
min(semi.axes), angle = unname(angle))
}

#Function to plot fitted ellipse from
PanozzoFit output
#Modified code from Michael Bedward <
michael.bedward at gmail.com>
get.ellipse <- function ( fit, n=360 ){
  tt <- seq(0, 2*pi, length=n)
  sa <- sin(fit$angle)
  ca <- cos(fit$angle)
  ct <- cos(tt)
  st <- sin(tt)

  x <- fit$center[1] + fit$maj * ct * ca
- fit$min * st * sa
  y <- fit$center[2] + fit$maj * ct * sa
+ fit$min * st * ca
  cbind(x=x, y=y)
}

#Function to calculate the true Rs from
shear strain
Es2R <- function(e.s = 1.5){
  1.1 <- sqrt((1/2) * (e.s^2 + 2 + e.s *
sqrt(e.s^2 + 4)))
  1.2 <- sqrt((1/2) * (e.s^2 + 2 - e.s *
sqrt(e.s^2 + 4)))

  rs <- 1.1 / 1.2
  return(rs)
}

#An empty function to run an example
PanozzoExample <- function(){
  lines.t1 <- LineGenerator(n.lines =
150, PLOT = TRUE)

  windows()
  lines.t2 <- LineShear(lines.t1, e.s =
1, PLOT = TRUE, plot.width = 100)

  panozzo <- Panozzo(lines.t2)

  windows()
  my.data <- PanozzoEllipse(panozzo, PLOT
= TRUE)
  ellip.fit <- PanozzoFit(my.data)
  ellip <- get.ellipse(ellip.fit)
  lines(ellip, col = "blue")
}

PanozzoExample()

```

## Appendix F

### Digital materials

This thesis includes an additional series of digital materials located on the accompanying compact disk. The following list briefly describes the contents of this compact disk. These files are also currently available at <http://www.uvm.edu/~jrwebber/resources.html> and are password protected (“webber2012”).

**UNDEFORMED.pdf** Portable document file containing vector based ellipses that are uniform in orientation and define a normal distribution of axial ratios.

**FABRIC.zip** Folder structure and scripts for the fabric quantification procedure presented in this thesis. Please visit my website for updated versions.

**FRY3D.zip** Folder structure and scripts for the FRY3D tutorial.

**CHILE2011.kmz** An SQLite3 database file containing structural orientation measurements and sample information.

**GEOCHRON.kml** Compiled geochronological ages throughout the Coastal Batholith of central Chile.

**11LC03C.kmz** A Google Earth File containing the oriented fabric ellipsoid calculated from the  $R_f/\phi$  method as presented in section 3.4.

**ISLA\_NEGRA.kmz** Oriented enclave swarm fabric ellipsoids from Isla Negra as explained in section 2.4.2.2.

**SAMPLES.kmz** A Google Earth file containing sample location information and field imagery of samples.